FLORIDA STATE UNIVERSITY

COLLEGE OF ARTS AND SCIENCES

A RATIONAL APPROACH TO HIGH ENTROPY MATERIALS FROM FIRST ROW TRANSITION METAL PRUSSIAN BLUE ANALOGUE (PBA) SINGLE SOURCE PRECURSORS

By

ISABELLA ANNE−JULIETTA BERTINI

A Dissertation submitted to the
Department of Chemistry and Biochemistry
in partial fulfillment of the
requirements for the degree of
Doctor of Philosophy

2024

Isabella Bertini defended this dissertation on June 21, 2024.
The members of the supervisory committee were:

Geoffrey Strouse
Professor Directing Dissertation

Bruce Locke
University Representative

Mykhailo Shatruk
Committee Member

Robert Lazenby
Committee Member

The Graduate School has verified and approved the above-named committee members and certifies that the dissertation has been approved in accordance with university requirements.

ACKNOWLEDGMENTS

First, I would like to thank my PI, Geoff Strouse for providing direction, inspiration, and opportunities for growth throughout my graduate school experience. I would not be the same scientist I am today without your influence, thank you for constantly challenging me and encouraging me to meet my own goals and expectations rather than those of others.

Next, I would like to thank my group mates past and current for their input in presentations and support. Specifically, I want to thank Dr. Carl Conti for his mentorship whilst our time in graduate school overlapped – thank you for teaching me how to critically think, problem solve, for answering my unending list of questions, and most of all how to properly google search topics. Thank you to Jason, Cat, Eddie and Raul for keeping the vibes up in lab, the laughs, the cries, and reminding me to not take things so seriously.

I would like to thank Dr. Eric Huddleston, and Dr. Megan Foley, my former research mentors for their constant mentorship, encouragement, and support personally and professionally throughout graduate school.

Further, I would like to thank my mom and dad for their long-distance support during this whole process. Thank you for helping me move (too many times), listening to my complaints and grievances, motivating me to continue, for instilling in me a great sense of work ethic and pride in my work, and most of all providing a safe haven to escape to when life threw curve balls at me.

I would be delusional if I did not thank my close friends who were my sanity throughout graduate school. Thank you, Dr. Erica Knorr, for being a constant shoulder to cry on, my bread making mentor, and fellow emo enthusiast. Thank you (soon to be) Dr. Gracie McCleod for encouraging me to live a healthy lifestyle, for giving me advice and support, and caring so deeply. Thank you, Dr. Brianna Coia, for reminding me that work life balance is important, to not be afraid of new opportunities, and to believe in myself. Thank you, Dr. Courtney Leo, for giving me a creative space to deal with life's struggles, my nature walk advocate, and most of all my role model. And lastly, I would like to thank Dr. Jason Kuszynski for helping me to realize my worth, helping me to become self-aware, and for being a wonderful support system for the majority of graduate school – no one understood my experience more than you. Additionally, all of my friends back home for encouraging me to continue and giving me perspective.

I would like to thank the love of my life, Joshua Scott Scarbary for the relentless support at home, constant encouragement, pushing me to be my best self, and being there to catch me when I fall.

And lastly, I want to thank myself for being stubborn enough to finish this degree. I am proud of myself for learning resilience, emotional regulation, and how to properly set boundaries. I couldn't be happier that this exceptional experience is coming to an end.

TABLE OF CONTENTS

LIST OF TABLES

LIST OF FIGURES

ABSTRACT

Chapter 1: Introduces the field of nanoscience including key concepts like important structure property – relationships, how nanomaterials are categorized, how nanomaterials are made, how nanoparticles are characterized, and what these nanomaterials can practically be used for. This chapter serves to provide foundational knowledge for the understanding of the remainder of this work.

Chapter 2: This chapter pertains to the bimetallic iron – cobalt carbide ($Fe_xCo_{1-x}C_y$) system. Specifically, this chapter serves to understand the effect of the iron and cobalt ratios on material properties (phase composition, size, and morphology), electrochemical performance of the $Fe_xCo_{1-x}C_y$ nanomaterials in the oxygen evolution reaction (OER), and material transformations under OER conditions.

Chapter 3: This chapter pertains to the bimetallic iron – nickel carbide ($Fe_xNi_{1-x}C_y$) and trimetallic iron – nickel – chromium carbide systems. Particularly, this chapter aims to gain insight into the effect of tuning iron and nickel ratios on material properties, electrochemical performance of the $Fe_xNi_{1-x}C_y$ nanomaterials in the oxygen evolution reaction (OER), and material transformations under OER and alkaline conditions. Furthermore, the addition of Cr to the bimetallic system is investigated for the enhancement of OER performance.

Chapter 4: This chapter pertains to the bimetallic iron – cobalt carbide ($Fe_xCo_{1-x}C_y$) system. As a follow up to the work completed in chapter 2, chapter 4 takes a closer look at synthetic control in the $Fe_xCo_{1-x}C_y$ system. Chapter 2 reveals a complex phase range that exists in these materials. In this chapter the effect of halide species, halide concentrations, and metal concentrations on $Fe_xCo_{1-x}C_y$ phase composition is investigated by coupling theoretical (density

functional theory) and experimental data to gain insight on how phase and metal compositions can be leveraged to produce targeted materials.

Chapter 5: This chapter expands the work from previous chapters by implementing Prussian Blue Analogues (PBAs) as single source precursors for the formation of nanocarbides from first row transition metals (Cr, Mn, Fe, Co, Ni) including monometallic (Ni_3C), bimetallic (FeNi), trimetallic (FeCoNiC), tetrametallic (CrFeCoNiC), and pentametallic (CrMnFeCoNiC) systems. This chapter focuses primarily on comparing these materials to the pentametallic (high entropy) PBA – derived materials as they are of increasing interest for applications in catalysis. We take a closer look at how the distribution of first row transition metals, the morphology, size, lattice planes, and crystal structure evolve from the monometallic carbide to the pentametallic carbide. Additionally, the nanocarbides are tested for water splitting performance under alkaline conditions.

Chapter 6: This chapter expands the work from chapter 5 by implementing Prussian Blue Analogues (PBAs) as single source precursors for the formation of nano MX-ides (oxides, sulfides, phosphides) from first row transition metals (Cr, Mn, Fe, Co, Ni) including monometallic, bimetallic, trimetallic, tetrametallic, and pentametallic systems. Preliminary pXRD and XRF data is reported showing the capability to expand this synthetic technique to other highly sought-after materials. This work serves to highlight the versatility of our synthetic approach as well as opportunities that exist to actualize PBA – derived nanomaterial synthesis.

Chapter 7: This chapter summarizes the findings reported in this thesis and describes future opportunities for further understanding of how PBAs can be implemented as robust, rational, scalable, cost effective, and tunable single source precursor for the production of next generation high entropy materials.

CHAPTER 1

INTRODUCTION

1.1 Nanoscience and Nanotechnology

Nanoscience is the study of the physical (color, crystal phase, morphology) and chemical (reactivity, electronic states) properties of nanoscale materials, whereas nanotechnology is the use and manipulation of nanomaterials for important applications in devices, catalysis, and medicine.[1] Nanotechnology was introduced in the 1950s by Richard Feynman, and the term was coined by Norio Taniguchi in 1974.[1] In general, materials are classified by size and composition. There are five main size regimes used to categorize materials; macroscopic materials which have one or more dimension between 1 cm to meters, bulk materials which have one or more dimension between 1 mm – 1 cm, microparticles which have one or more dimension between 1 μm – 1 mm, mesocrystals which have one or more dimension between 100 nm – 1 μm, and nanoparticles (NPs) which have one or more dimension between 1 nm – 100 nm in size. Likewise, materials can be further categorized by compositions. There are five main compositional classes of materials: organic (polymers), inorganic (polymers), inorganic (metals), inorganic (ceramics), and composites. A polymer can be defined as a homogeneous structure of repeating units called monomers; one can think of Legos as an example of monomers which come together to create a larger structure which is the polymer. Metals are materials that are made up of metallic elements and typically have high electrical and thermal conductivity due to the overlap of electron density. Ceramics are materials that are composed of inorganic elements with some metals incorporated like tetrels (carbides and silicates), pnictides (nitrides and phosphides), and chalcogenides (oxides, sulfides, selenides). Ceramics are known for their hardness, resistance to extreme conditions (corrosion, high temperature, and high pressure), and chemical inertness. The central dogma of

most applied science is that form follows function, meaning that in order to control a material's properties the structure must be thoroughly understood and well characterized. Materials scientist can then leverage a material's structure in order to target sought after mechanical, thermal, electrical, magnetic, optical, or chemical properties. This thesis will focus primarily on inorganic polymer mesocrystals and ceramic nanocrystal (NCs) materials.

1.1.1 Structure – Property Relations in Bulk, Meso, and Nanoscale Inorganic Materials

Nanoparticles exhibit unique chemical and physical properties as compared to their bulk counterparts because of the increased surface area to volume ratio in nanomaterials. Some examples of these properties include enhanced catalytic activity/stability or magnetic properties as well as allowed spin forbidden transitions due to quantum effects. Nanomaterials can be referred to as nanoparticles (NPs) or nanocrystals (NCs) in a general manner, but the material's properties depend on its composition and size. Inorganic nanomaterials can be further classified by their composition as metallic, semiconductors, or insulators. Likewise, nanomaterials come in a variety of morphologies with the most common being spherical particles, due to a stabilization of the surface that occurs to minimize surface energy along facets of a crystal, but they can also take on a variety of other 3D polyhedron crystal shapes. When NCs are confined in one direction, they take on a 2D morphology, for example a platelet is a common 2D structure where the crystal can grow in the x and y direction but not the z direction. When an NC is confined in two directions it is referred to as a 1D nanomaterial, nanorods are a common example. Similarly, when a nanomaterial is confined in all three x, y, and z directions, it is known as a 0D nanomaterial commonly called "quantum dots". Quantum dots are nanoparticles that specifically have a radius that is less than the Bohr radius (a constant that defines the most probable distance between an electron and nucleus for a ground state hydrogen atom) and are of interest because of their optical

and electronic tuneability based on size. This phenomenon of quantum confinement in quantum dots was most recently recognized by the Nobel prize in chemistry in 2023. The award was given to Aleksey Yekimov, Louis Brus, and Moungi Bawendi for the discovery and development of semiconductor quantum dots and their intriguing physical properties for applications in LEDs, OLED TVs, and histology due to quantum confinement effects.

1.2. Band Theory

1.2.1. From Atomic Orbitals to Bulk Materials. In an atom, electron density is characterized as discrete energy levels known as atomic orbitals which are adapted based on molecular symmetry. At the most basic level, electron density defines reactivity of an atom, molecule, or ion. When two atoms bond together, or share electron density, the energy levels of each atom within the bond combine and form a new set of discrete energy levels known as molecular orbitals. In a molecular orbital diagram, there is an energy gap that exists between the highest occupied molecular orbital (HOMO) and the lowest unoccupied molecular orbital (LUMO), this energy gap represents the amount of energy that is required to excite an electron from a filled state (HOMO) to an excited state. The energy gap between HOMO and LUMO is unique to every molecule that exists. This energy gap, or absorption, is important to note as it can be used to do work (optically or electronically). As a molecule gets more complex or becomes larger, the number of molecular orbital states that exist increases. Eventually, once a molecule has a repeating unit it has reached the point of a material, or polymer. Materials have so many molecular orbital states that are so close in energy that instead of describing them as discrete orbitals we describe the electron density in structures known as bands. These bands are a projection of atomic orbitals across electron momentum space (k – space) wherein the assumption of infinite orbitals contributes to their formation of a bulk band. Band**s** are commonly illustrated graphically

as a density of states model wherein the electron occupation is shown within the orbital framework. Similarly, bands are used to categorize the type of material.

1.2.2. Band Structures of Metals Semiconductors and Insulators. The band structure can be visualized similarly to the molecular orbital, however, differ in the fact that bands are a summarized form of all atomic orbital energy levels within a material. The bands and the electron density in the density of states for the bands allow the categorization of materials into three main groups: insulators, semiconductors, and metals, as depicted in Figure 1.1. The properties of these materials are closely related to their electronic structures. The metallic band diagram can be represented as one large band because the atomic orbitals within the conduction and valence bands are overlapping, which describes the free-flowing nature of electrons within these materials. Metals are electrically and thermally conductive due to the overlap of the band levels, which allows the ease of electrons to move through the energy states. A semiconductor has two distinct bands, the conduction band, which can be equated to the HOMO in a molecular system, and the valence band which can be equated to the LUMO in a molecular system. The valence band represents the

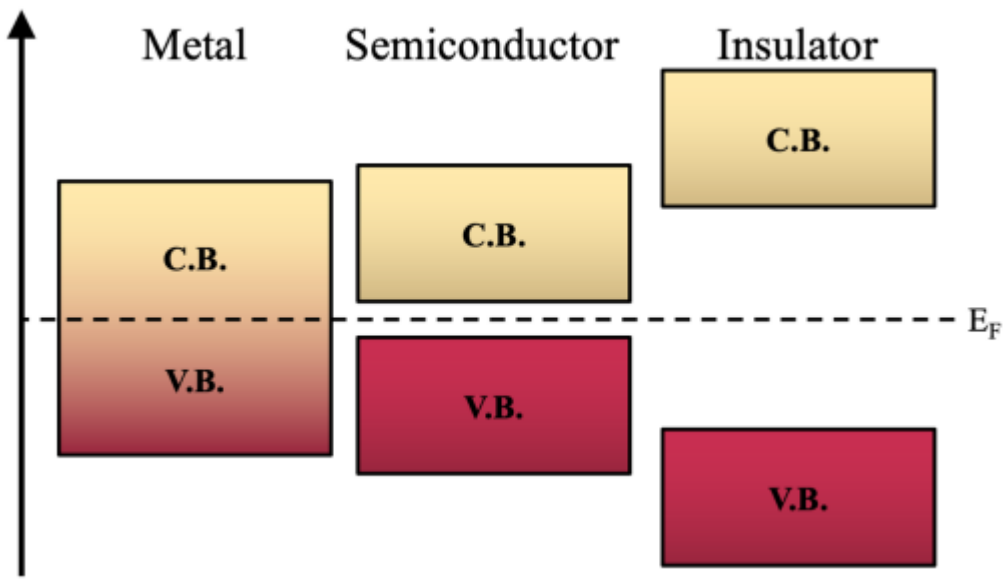

Figure 1.1. Band diagram schematic describing metal, semiconductor, and insulator

energy levels that are electron filled and the conduction band represents the energy levels that are empty. An energy gap exists between the bands in a semiconductor known as the band gap, the larger the band gap the more energy it takes to excite an electron from the ground to excited state. Similarly, an insulator also has a conduction and valence band. What separates an insulator from semiconductor is the distance of the bandgap. An insulator is characterized by having a band gap energy of 4 eV or greater. A semiconductor can have a band gap energy from 0.5 to 3.9 eV, and a metal is < 0.5 eV. The last feature in a band diagram that is important to note is the fermi level (E_f), which represents a value of thermodynamic work energy that is required to add one electron to the material. At 0 K, the Fermi level is the highest energy a population of electrons can reach. The relative location of the fermi level within the band diagram can provide insight into electronic properties like conduction.

1.3. Nucleation Theories

There are a number of nucleation theories of nanoparticle growth that have been proposed in the literature.[2]

1.3.1 Classical Nucleation Theory (CNT). Classical nucleation theory follows the LaMer model of nanoparticle growth which is dependent on precursor (monomer) concentration and reaction time as illustrated in figure 1.2.[3,4] CNT describes nucleation as a three stage process involving the formation of a critical nucleus followed by its growth into a stable nucleus. Stage I, the monomer concentration increases to the critical supersaturation concentration (C_{min}) required for nucleation. Stage II, the monomer saturation is partially relieved by the nucleation event. Stage III, the monomer concentration drops below the level required for nucleation, and particle growth proceeds by addition of the monomer to the particle surface. With a limited supply of monomer available, the monomer concentration approaches the lower solubility limit (Cs), and additional

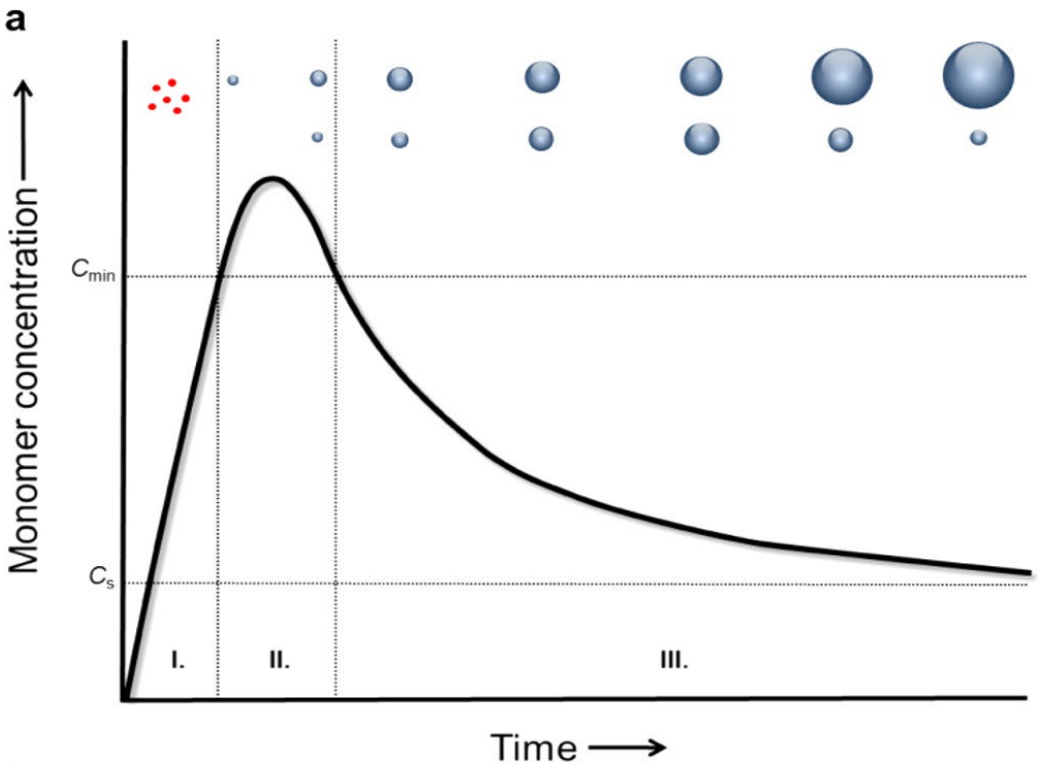

Figure 1.2. Classic LaMer mechanism for nanoparticle growth can be explained in three stages: saturation, nucleation, and growth. Reprinted with permission from Chem. Mater. 2015, 27, 17, 6059–6066.

growth proceeds by Ostwald ripening, which is the phenomenon observed in solutions that refers to dissolution of small particles in solution and redeposition of those onto the surface of larger crystals.[3,4] Ostwald ripening leads to the formation of heterogeneous particle size distribution and aggregation of particles. CNT assumes a constant rate of nucleation over time where nucleation occurs due to a balance between the free energy required to form new nuclei and the free energy released by this formation. CNT is most applicable to systems where the nucleation process is primarily driven by temperature, monomer supersaturation, and the presence of pre-existing nuclei is negligible.

1.3.2. Autocatalytic Nucleation Theory (ANT). Autocatalytic nucleation theory describes nanoparticle growth as an extension of the classical nucleation theory (LaMer) as it considers the role of existing nanoparticles as catalysts for the nucleation of new nanoparticles.

ANT assumes that the presence of nanoparticles enhances the rate of nucleation, leading to a self-perpetuating growth process that is typically seen in metallic or semi-metal nanoparticle systems. Autocatalytic nanoparticles follow the mechanism studied by Finke and Watsky as shown in figure 1.3. [5] ANT emphasizes the role of existing nanoparticles as active sites for the nucleation of new nanoparticles and assumes that the presence of these existing nanoparticles lowers the energy barrier for nucleation of new nanoparticles, leading to a faster nucleation rate resembling a sigmoidal growth function. ANT predicts a non-constant, increasing rate of nucleation over time.

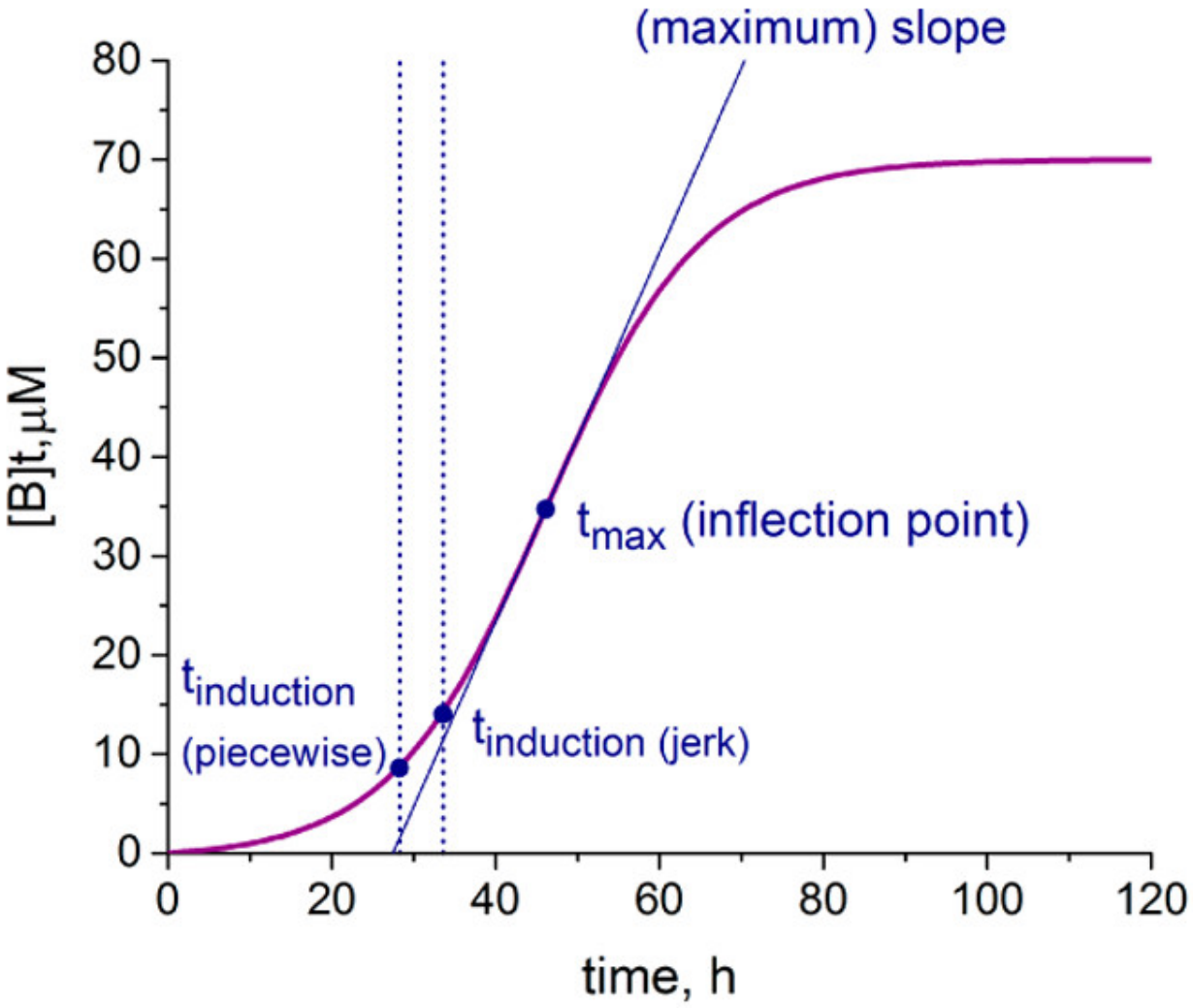

Figure 1.3. Autocatalytic growth kinetic model in three stages lag, growth, and plateau phases. Reprinted with permission from J. Phys. Chem. C 2017, 121, 9, 5302-5312.

The rate of nucleation and size of resultant nanoparticles are highly dependent on concentration and time.

1.3.3. Avrami Nucleation Theory. The Avrami theory describes how nanoparticles grow within a matrix or solution. This theory assumes that nanoparticle growth is governed by nucleation, similar to CNT. However, unlike CNT, it does not assume a constant rate of nucleation. Instead, the rate follows an exponential function (Eq. 1) where $f(t)$ is the fraction of transformed phase at time t, k is the rate constant, and n is the Avrami exponent, which depends on the dimensionality of the materials under study. For example, a value of n=1 indicates one-dimensional growth, while n=3 indicates three-dimensional growth as described in Avrami's works. [6–8] Avrami theory is a more universally applicable model as compare to the other nucleation theories as it can be used to describe bulk material growth as well as nanomaterials. However, the gold standard used in the nanoscience field to describe growth is the Finke-Watsky Autocatalytic growth model.

$$f(t) = 1 - \exp(-kt^n) \qquad \text{(Eq. 1)}$$

1.4. Methods of Nanoparticle Synthesis

1.4.1. Bottom – Up Methods. Bottom – up synthesis methods take atomic building blocks that form clusters which subsequently combine to construct a nanoparticle. Sol-gel, spinning, soft and hard templating, pyrolysis, chemical vapor deposition, solvothermal and hydrothermal, and reverse micelle are all examples of bottom – up methods.[9]

1.4.2. Top – Down Methods. Top – down synthesis methods take the opposite approach to bottom – up and rather than using building blocks to form the nanoparticle, a larger bulk material is destructed and transformed into smaller nanomaterials. Examples of top – down methods include

thermal decomposition, mechanical milling, laser ablation, sputtering, arc discharge, and nano lithography.[9] Thermal decomposition is one of the main top-down approaches taken in this work. Thermal decomposition works by actively heating a bulk material to a critical temperature needed for the formation of nanomaterials, the decomposition temperature is material dependent. Classically this is a solid-state chemistry synthetic approach and typically does not require solvent. However, in this work Prussian Blue Analogues (PBAs) are used as sacrificial templates to produce resultant nanomaterials, this method is executed in high boiling point organic solvents like octadecylamine, dodecanethiol, or trioctylphosphine.

1.4.2.1 Sacrificial Templated Nanomaterial Synthesis. Previous work in the Strouse group at FSU has uncovered a versatile synthetic technique to produce nanocarbides and nanoalloys as shown in Figure 1.4.[10] The work established in 2019 showed that the metal composition in the mesocrystal precursor is maintained in the resultant nanomaterials, the formation of the carbide is reliant on presence of the aminated solvent, and the PBA templates the growth of the nanomaterial by selective etching of the PBA as it decomposes under synthetic conditions. Figure 1.4. shows the proposed mechanism of the templated thermal decomposition where upon heating to 350°C, the cubic PBA releases NCN^- and $(CN)_2$ from the destabilization of the CN linkages between metal sites within the crystal structure as gas byproducts. After two hours of heating the PBA is decomposed fully and the carbide is formed, matching the thermodynamically most stable carbide, Fe_3C phase. Upon further heating, carbon is released from the carbide crystal through carbon diffusion and after heating for 6 hours the final structure of FeCo alloy is produced. Beneath the proposed mechanism schematic are electron images of the PBA, carbide, and alloy highlighting the morphology of the materials.

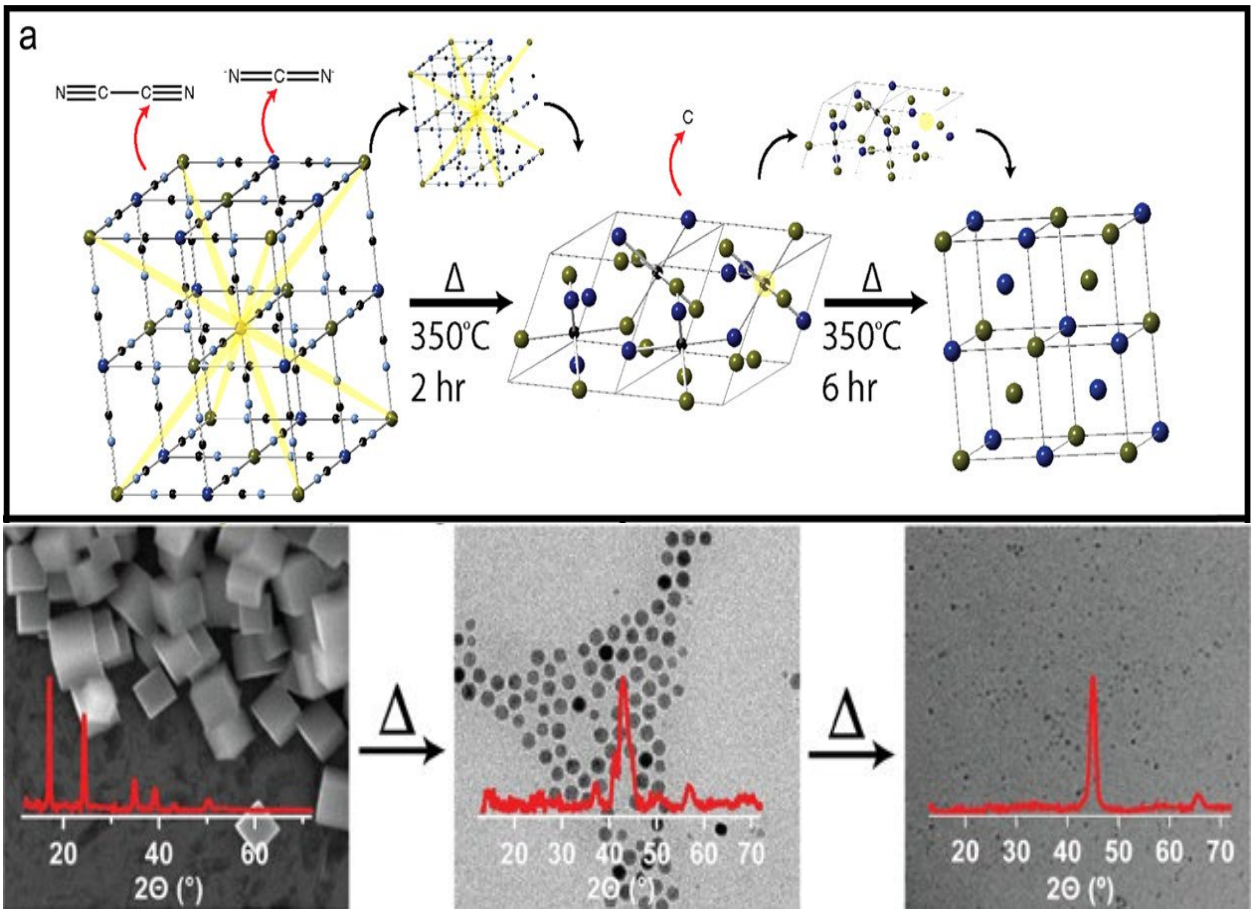

Figure 1.4. (a) Proposed interconversion of a $K[Fe_{2-x}Co_x(CN)_6]$ to $Fe_{3-x}Co_xC$ and $Fe_{2-x}Co_x$ nanoparticles. pXRD and TEM of each synthetic stem shown below. Reprinted with permission from Chem. Mater.2019,31,19,8163–8173.

A time dependent study of the PBA decomposition was done to take a closer look at the templated growth of the carbides. Figure 1.4. shows the time dependent etching along the (111), (010), and (001) facets and in between the facets where nucleation of the nanocarbide occurs. The facets found between the channels etched in the PBA were matched to the carbide crystal phase. Expansion of Hardy and coworkers work in this thesis illustrates this robust and versatile synthetic method can be translated to more complicated multimetallic and other various ceramic type nanomaterials such as phosphides, oxides, and sulfides.

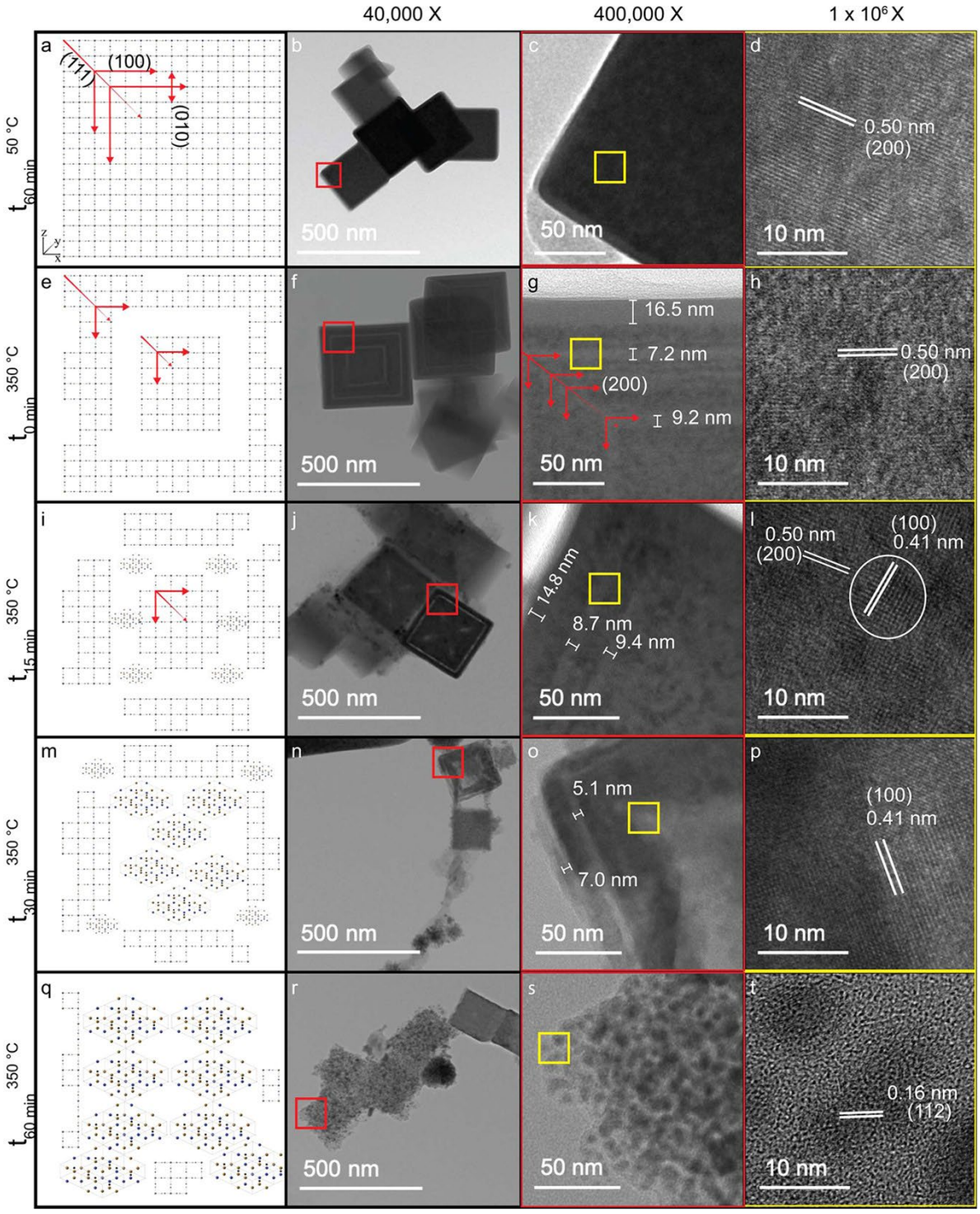

Figure 1.5. Time-dependent TEM images and the proposed PBA changes indicating the direction of etching during the interconversion process. The reaction aliquots are drawn after 60 min at 50 °C (b–d), 0 min (f–h), 15 min (j–l), 30 min (n–p), and 60 min (r–t) at 350 °C. The image magnifications from left to right are 40 000×, 400 000×, and 1 000 000×. Images a, e, i, m, and q are schematic representations at the specified time points. Reprinted with permission from Chem. Mater. 2019, 31, 19, 8163–8173.

1.5. Research Motivation

In this work a plethora of new materials have been synthesized, characterized, and tested in applications such as the water splitting reaction. The motivation behind this research is to design new advanced materials that are cost effective, globally accessible, sustainable, and scalable. Additionally, there is a focus on controlling complex material characteristics like crystal phase and elemental composition for the production of targeted materials because the structure of the material determines the function of the material.

Much research has been done on synthesizing nanomaterials; however, many studies focus on perfecting small batches of nanomaterials. For small scale academic applications this approach suffices but we aim to produce materials that could be manufactured in industrial proportions. Additionally, the materials produced should be low cost. There is a huge effort in the field of chemistry to find first or second row transition metal alternatives to state-of-the-art materials for many applications, especially in catalysis. The standard for catalysts in the organic division, for example, are ruthenium or platinum complexes. Likewise in the world of heterogeneous catalysis noble metals (Ir, Os, Ag, Au, Ru, Pt, Pd) remain the "gold standard" as they are very inert elements that are great hosts for electron transfer. Recently, there has been a huge effort to move away from noble metal-based materials and discover new cost effective alternatives.[11–15] Many scientists have specifically started testing first row transition metals for the same applications that noble metals have been used for as we now have better methods of controlling reactivities in structures made with these cheaper elements. Another benefit of using first row transition metals as opposed to nobles is that they are accessible with a few exceptions where there are some supply chain issues.

The water splitting reaction which is a green method (fully sustainable when powered by renewable resources) of producing hydrogen fuel. With the increase in fossil fuel-based gas prices, environmental impact of crude oil fracking, recent electric vehicle failure and safety concerns, and consistently increasing greenhouse gases in Earth's atmosphere, a new standard of energy production must be realized. Hydrogen fuel is a more efficient fuel because it can be produced sustainably, when burned creates no toxic byproducts, and can store almost three times as much energy as fossil fuels. (120 megajoules/kg vs 45 Mj/kg).[16] A sustainable future is accessible with the actualization of Hydrogen fuel.

1.6. Applications of Inorganic Nanomaterials as Water Splitting Electrocatalysts (OER and HER)

There are two half-cell reactions involved in the electrochemical water splitting reaction (WSR). The hydrogen evolution reaction (HER) which occurs at the cathode of the electrochemical cell (Eq. 2) and the oxygen evolution occurs at the anode of the electrochemical cell (Eq. 3). Each half cell reaction has a standard reduction potential (E°_{cell}) which represents the thermodynamic barrier of each half cell reaction. The E°_{cell} for HER (cathode) is 0 V, vs the standard hydrogen electrode (SHE) and 1.23 V for OER (anode). Using Eq. 4 the E°_{cell} for the total WSR becomes −1.23 V. When the standard reduction potential for the WSR is substituted into the Gibb's free energy equation (Eq. 5) a positive value for ΔG is obtained confirming that the WSR is an endergonic reaction and requires −1.23 V to drive the reaction forward. In this work we report all potentials against the reversible hydrogen electrode (RHE), to reflect the non-standard conditions of electrochemical measurements (see Eq. 10 and 11).

(Eq. 2) $2\ H_2O\ (l) + 4\ e^- \rightarrow 4\ OH^-\ (aq) + 2\ H_2\ (g)$ $E_{1/2\ cell} = -0.828$ V vs SHE

(Eq. 3) $2\ H_2O\ (l) + 4\ e^- + O_2\ (g) \rightarrow 4\ OH^-\ (aq)$ $E_{1/2\ cell} = 0.401$ V vs SHE

(Eq. 4) $E_{cell} = E_{cathode} - E_{anode} = -0.828 - 0.401 = -1.229$ V

(Eq. 5) $\Delta G = -nFE_{cell} = -(4)(86{,}485\ C/mol)(-1.229\ V) = 474$ kJ/mol

1.6.1. Rational Design of Electrocatalysts for Water Splitting. Currently, alkaline water electrolyzers use RuO_2 or IrO_2 and Pt as catalysts for the WSR due to their high OER and HER activities, respectively. Although they have high intrinsic activity under both alkaline and acidic conditions, these materials are limited by production costs as well as electrochemical instability. The current cost of Pt, Ir, and Ru metals \$32/g, \$154/g, and \$14/g respectively. However, first row transition metals like Ni, Co, and Fe cost several orders of magnitude less at \$0.02/g, \$0.03/g, and \$0.0001/g, respectively. Therefore, focusing on designing materials using earth abundant with ease of availability and cost is crucial for next generation catalysts. The motivation for this research is to create electrocatalysts for use in water electrolysis by driving the cost of catalyst synthesis down without compromising on performance. Not only is the goal to produce materials that perform comparably to the state-of-the-art, but also to make materials that compensate for the limitations of the state-of-the-art. Despite its high electrocatalytic performance for OER, RuO_2 is electrochemically unstable under the oxidative conditions at the anodic surface. RuO_2 readily oxidizes to RuO_4 under OER conditions which is problematic because RuO_4 has a higher dissolution rate than RuO_2 leading to a vast decrease in performance over time. Danilovic and coworkers found that the rate of dissolution of metal oxides from the surface of the electrode correlates to higher oxidation states. They established an inverse relationship of activity and stability for OER and correlated it to the "nobleness" of the material.[17] For example, the more noble a metal oxide is the more stable but less active it is for OER. Morphological factors were also considered, and they elucidated a correlation between stability and crystallinity; the less crystalline the metal oxide the less stable but more reactive in OER due to increased defect density.

Likewise, there is a correlation between defect density and activity. The higher the defect density, the higher the activity but the lower the stability.[17] Therefore, the trend for reactivity in OER for heterogenous catalysts from most reactive to least reactive should be metal > metal X-ide (MX-ide, X- carbide, phosphide, nitride, hydroxide)) > metal oxide. Transition metal carbides pose to be a great alternative to pure metal or metal oxide catalysts because they are resistant to dissolution under highly oxidative environments − like at the anode of a water electrolyzer. Metal carbides have carbon incorporated into the crystal lattice, which serves as a protective coating for metal centers against oxidation. Pure metal and metal oxide counterparts will either transform into an oxide material (partially or completely), or the metal will increase in oxidation state and consequently dissolve off the electrode surface over time.[18–21]

1.6.2. The Fe Effect. The "Fe effect": A synergistic effect of Fe concentration in metal X-ide materials on enhanced OER/HER performance has been frequently observed in the literature, where increased activity is reported upon Fe incorporation- even in trace amounts.[22–25] There are several hypotheses in the literature speculating the cause of the Fe effect; 1) Fe incorporation at the surface of a catalyst enhances conductivity so the rate of water splitting increases, 2) Addition of Fe in MX-ides changes metal-oxygen bond length/strength causing a shift to higher oxidation states which induces a better catalytic center, 3) The Fe impurity itself is the active site for OER.[24,26–28] By recognition of this phenomena, there should be an optimum ratio of metals intrinsic to every MX-ide for the optimum performance in OER and HER which motivates the study of these material types.

1.6.3. In-Situ Electrochemical Material Transformation in MX-ide Materials. There are several methods known in literature to enhance electrocatalytic activity including defect engineering, doping, supports, size, and morphology. Recently, the electrocatalysis field has been

focusing research efforts on understanding the chemistry of the electrocatalyst's surface for reactions like OER. MX-ides are an interesting class of materials to research as they all behave differently under alkaline OER conditions. A commonality in MX-ide literature is the tendency for these materials to transform under OER conditions. Sulfides typically undergo complete oxidation to oxyhydroxide/oxide when a potential is applied. Phosphides are unstable in alkaline solutions and start oxidizing before a potential is applied. They also have the propensity to form a metal phosphide core and metal oxide shell M_xP_y/M_xO_y structure and once a potential is applied the phosphide is typically transformed completely into oxyhydroxide/oxide. Metal nitrides (M_xN_y) and carbides (M_xC_y) are typically more resistant to corrosion due to their noble metal-like electronic structure (high electron density close to the Fermi level) and are therefore more stable under OER conditions. In literature, M_xC_y tend to outperform M_xN_y in OER because M_xC_y only partially oxidizes when a potential is applied whereas M_xN_y tend to form M_xO_y.[29,30] Although oxides are the current standard OER electrocatalysts, MX-ides perform better by comparison because of their intrinsically higher conductivity/charge transfer efficiency, higher surface area as in-situ transformations typically induce formation of amorphous structures, increased defects which allows for metal sites to reach higher valency to maintain lattice neutrality, and oxyanion formation that can mediate the ΔG of OER intermediate adsorption.[29–31] By modulating the composition and crystal phase of these materials, especially M_xC_y, water splitting enhancement is realistically attainable.

1.7. Inorganic Nanomaterial Characterization Methods

1.7.1. Imaging

In the realm of material science and nanotechnology, electron microscopy stands as an indispensable tool for the characterization of materials at the micro- and nano-scale. Among the

diverse array of electron microscopy techniques, Scanning Electron Microscopy (SEM) and Transmission Electron Microscopy (TEM) are widely utilized for their exceptional imaging capabilities and versatility in sample characterization.

1.7.1.1. Scanning Electron Microscopy (SEM). SEM employs a focused beam of electrons to scan the surface of a sample, generating high-resolution images of its topography and composition. The key components include an electron gun, condenser lenses, scanning coils, specimen chamber, and a detector system for signal collection. Upon energizing the electron gun, electrons are accelerated towards the sample through a series of electromagnetic lenses, forming a fine electron beam. The scanning coils steer the beam across the specimen surface in a raster pattern, while detectors capture various signals emitted from the sample, such as secondary electrons, backscattered electrons, and characteristic X-rays. SEM operates on the principles of electron-matter interactions, where the incident electron beam interacts with atoms near the sample surface, leading to the emission of secondary electrons and backscattered electrons. The intensity and distribution of these emitted electrons provide valuable information about the sample's topography, composition, and crystal structure. SEM is suitable for imaging a wide range of samples, including metals, ceramics, polymers, biological specimens, and nanomaterials. It enables detailed examination of surface morphology, particle size distribution, fracture surfaces, and elemental composition with resolutions ranging from nanometers to micrometers. In this work, SEM is utilized for the characterization of morphology (shape), particle size, and size dispersity in Prussian Blue Analogue (PBA) precursors and PBA-derived materials.

1.7.1.2. Transmission Electron Microscopy (TEM). TEM operates on a fundamentally different principle than SEM, where a beam of electrons transmitted through an ultra-thin sample generates high-resolution images of its internal structure. The key components comprise an

electron gun, condenser lenses, objective lens, specimen holder, and detectors for image formation. In TEM, electrons emitted from the electron gun are focused into a parallel beam by condenser lenses and directed towards the sample. As the electrons pass through the specimen, they interact with its atoms, undergoing scattering and diffraction processes. The objective lens forms a magnified image of the transmitted electrons onto a fluorescent screen or detector, producing a detailed representation of the sample's internal structure. TEM relies on the principles of wave-particle duality, diffraction, and interference of electrons passing through a thin specimen. The interaction of electrons with the sample's atomic arrangement results in the formation of a diffraction pattern, which contains information about the crystal lattice, defects, and phase composition of the material. TEM is well-suited for the analysis of thin samples, such as nanoparticles, thin films, biological tissues, and crystalline materials. It enables the visualization of atomic-scale features, including lattice fringes, dislocations, grain boundaries, and defects, providing invaluable insights into the structure-property relationships of diverse materials. In this work, TEM is used for the characterization of lattice planes (fringes), morphology (shape), particle size, and size dispersity PBA-derived materials.

1.7.2. X-ray Techniques

X-ray spectroscopy and diffraction techniques are critical in the characterization of nanomaterials, offering valuable insights into their elemental composition, crystal structure, and surface chemistry.

1.7.2.1. Energy Dispersive X-Ray Spectroscopy (EDS). Energy Dispersive X-ray Spectroscopy is a complementary technique often integrated with Scanning Electron Microscopy (SEM) and Transmission Electron Microscopy (TEM) for elemental analysis of materials. By detecting characteristic X-rays emitted from the sample upon interaction with the electron beam,

EDS provides valuable information about the chemical composition and elemental distribution within the specimen. In SEM and TEM systems equipped with EDS capabilities, an X-ray detector is positioned adjacent to the sample chamber. The detector consists of a semiconductor crystal, such as silicon or germanium, which generates electrical signals proportional to the energy of incoming X-rays. These signals are processed by a multichannel analyzer (MCA) to generate a spectrum representing the intensity of X-rays emitted at different energies. During SEM or TEM imaging, the electron beam interacts with the sample, causing excitation of inner-shell electrons within the atoms. Subsequently, these excited electrons transition to lower energy states, emitting characteristic X-rays with discrete energies specific to each element present in the sample. The EDS detector collects these X-rays, and the MCA analyzes their energy spectra to identify the elements and quantify their concentrations. Each element emits X-rays at unique characteristic energies corresponding to transitions between specific electron energy levels. By measuring the energy and intensity of these X-rays, EDS enables identification and quantification of elements present in the sample, typically ranging from atomic number 9 (Fluorine) upwards. EDS can be used on a wide range of materials, including metals, minerals, ceramics, polymers, semiconductors, and biological specimens. Typically, EDS is used to identify trace elements, analyze chemical compositions, and map elemental distributions within the sample. EDS is used in this work to verify chemical compositions of PBA precursors and PBA-derived nanomaterials.

1.7.2.2. X-ray Fluorescence Spectroscopy (XRF). X-ray Fluorescence Spectroscopy is a non-destructive analytical technique used for elemental analysis of materials. When irradiated with high-energy X-rays, atoms in a sample are excited to a higher energy state, causing inner-shell electrons to be ejected. Subsequently, outer-shell electrons transition to fill the vacancies, emitting characteristic fluorescent X-rays whose energy levels are indicative of the elemental composition

of the sample. The energy of the emitted X-rays corresponds to the energy differences between electronic energy levels, enabling element specific identification and quantification of the sample. Detectors collect these emitted X-rays, and the resulting spectra are analyzed to determine the elemental composition and concentration of elements present in the sample. XRF instruments typically consist of an X-ray source, sample chamber, detectors, and data acquisition system. The X-ray source emits high-energy X-rays, which irradiate the sample. Detectors measure the energy and intensity of emitted fluorescent X-rays, which are then processed to generate elemental spectra. XRF provides quantitative elemental analysis of solid, liquid, and powdered samples across a wide range of elements, Fluorine being the smallest detectable element. It can determine the concentrations of major, minor, and trace elements present in the sample, making it invaluable for applications in geology, environmental science, archaeology, and materials characterization. In this work, XRF is used to quantify the elemental composition in Prussian Blue Analogue (PBA) precursors and PBA-derived materials.

1.7.2.3. Powder X-ray Diffraction (pXRD). Powder X-ray Diffraction is a technique used to analyze the crystallographic structure of crystalline or polycrystalline materials. When irradiated with X-rays, atoms in the crystal lattice scatter the incident radiation, producing a diffraction pattern of constructive and destructive interference. pXRD operates on the principles of Bragg's law (Eq.6) and diffraction of X-rays by crystals. According to Bragg's law, constructive interference occurs when the path difference between scattered waves from adjacent crystal planes is equal to an integer multiple of the X-ray wavelength, leading to peak intensities at specific diffraction angles. By measuring the angles and intensities of diffracted X-rays, the crystal structure and phase composition of the sample can be determined. pXRD instruments include an X-ray source, sample holder, goniometer, and detector. The X-ray source emits monochromatic

X-rays, which are directed onto the sample. The goniometer rotates the sample to different angles, while the detector measures the intensity of diffracted X-rays as a function of scattering angle. pXRD provides detailed information about the crystal structure, lattice parameters, and phase composition of crystalline and polycrystalline materials. It enables identification of crystal phases, determination of crystal symmetry, and quantitative analysis of relative phase abundance in a material or nanomaterial. pXRD is used in this work to characterize the structure of pure phase (crystalline) and mixed phase (polycrystalline) meso and nanomaterials.

$$n\lambda = 2\,d\sin(\theta) \qquad \text{(Eq. 6)}$$

1.7.2.4. X-Ray Photoelectron Spectroscopy (XPS). X-ray Photoelectron Spectroscopy is a surface-sensitive technique used for elemental and chemical analysis of solid surfaces. XPS provides quantitative elemental analysis, chemical state analysis, and surface characterization of materials with high sensitivity and spatial resolution with a penetration depth of approximately 10 nm. It can identify elements present on the sample surface, determine their chemical bonding states (like oxidation state and coordination environment), and detect surface contaminants or functional groups. Similar to XRF, when atoms are irradiated with X-rays of sufficient energy, electrons in the sample are ejected from the inner-shell orbitals, resulting in the emission of photoelectrons instead of a characteristic x-ray. The kinetic energy and intensity of emitted photoelectrons provide information about the elemental composition and chemical bonding states of the sample. XPS operates by the "photoelectric effect" where X-ray photons transfer energy to inner-shell electrons, ejecting them from the sample surface. The binding energy of emitted photoelectrons is characteristic of the element and chemical environment, allowing for not only element specific but also chemical state analysis. XPS instruments typically consist of an X-ray source, sample chamber, electron analyzer, and detector. The X-ray source emits monochromatic X-rays onto the

sample, while the electron detector measures the energy and intensity of emitted photoelectrons. The information is collected and processed into a photoelectron spectrum, which is then analyzed to determine the elemental and chemical composition of the sample surface. XPS is widely applied in materials science, surface chemistry, catalysis, and semiconductor research for studying surface phenomena and interfaces. XPS is used in this work to determine surface chemistry in FeCo and FeNi nanocarbides.

1.7.3. Thermal Analysis

1.7.3.1. Simultaneous Differential Thermal Analysis (SDT). Simultaneous Differential Thermal Analysis is a technique used in materials science that offers insights into the thermal properties and behaviors of diverse materials such as thermal stability, phase transitions, and reaction kinetics. SDT combines the techniques of differential scanning calorimetry (DSC) and thermogravimetric analysis (TGA) within a single instrument. The simultaneous measurement of heat flow (DSC) and mass change (TGA) enables a comprehensive characterization of materials under controlled thermal conditions. DSC operates on the principle of comparing the heat flow to a reference material, typically an empty pan or an inert substance, as the sample and reference are subjected to identical thermal conditions. Temperature differentials between the sample and reference pans manifest as characteristic peaks in the heat flow curve, elucidating thermal events such as melting, crystallization, and chemical reactions. Conversely, TGA relies on monitoring the sample's mass as a function of temperature or time, revealing changes attributable to decomposition, volatilization, or oxidation processes. In an SDT experiment, the sample is subjected to a programmed temperature ramp while simultaneously measuring the heat flow and mass changes. The DSC component detects endothermic and exothermic events, providing insights into phase transitions, reactions, and heat capacities. Meanwhile, the TGA component monitors

changes in sample mass due to decomposition, desorption, or other thermal processes. By synchronizing these measurements, SDT offers a holistic understanding of material behavior under varying thermal stimuli. SDT can be performed on a wide array of sample types, including polymers, pharmaceuticals, ceramics, metals, and composites. In this work, SDT is used to identify phase transitions in PBA-derived nanocarbide materials, investigate thermal stability of PBA and PBA-derived materials, and gain insight into reaction kinetics of the PBA-decomposition mechanism as it pertains to compositional changes.

1.7.4. Electrochemical Analysis

Electrochemical techniques play a pivotal role in elucidating the redox behavior, electroactive species, and kinetic parameters of materials, thereby facilitating advancements in fields such as energy storage, corrosion science, and electrocatalysis.

1.7.4.1. Linear Sweep Voltammetry (LSV). LSV typically employs a three-electrode configuration comprising a working electrode (WE), reference electrode (RE), and counter electrode (CE) for larger currents. A potentiostat controls the applied potential between the WE and RE while measuring the resulting current response. The potential is scanned linearly between specified limits at a controlled scan rate. The resulting current response provides information about redox reactions, electron transfer kinetics, and electrochemical mechanisms. LSV is based on the principles of electrochemical kinetics and mass transport, wherein the current response is governed by Faraday's law of electrolysis, Ohm's law, and Fick's laws of diffusion. The observed current-potential profiles reveal information about electrode processes, reaction mechanisms, and electroactive species concentrations. In this work, LSV is used to test PBA-derived nanomaterial performance as potential OER and HER electrocatalysts.

1.7.4.2. Cyclic Voltammetry (CV). CV setups share similarities with LSV but involve cyclic potential sweeps between defined limits. The cyclic nature enables the investigation of reversible and irreversible redox processes. The potential is scanned cyclically between specified limits at a controlled scan rate. The resulting current response provides information about redox reactions, electron transfer kinetics, and electrochemical mechanisms. CV is also based on the principles of electrochemical kinetics and mass transport, wherein the current response is governed by Faraday's law of electrolysis, Ohm's law, and Fick's laws of diffusion. Similar to LSV, CV current-potential graphs reveal information about electrode processes, reaction mechanisms, and electroactive species concentrations. CV is used in this work to test the stability of PBA-derived nanomaterials for the OER, HER, and to measure the double layer capacitance for electrocatalyst electrochemical surface areas.

1.7.4.3. Tafel Analysis. Tafel analysis is a method to analyze the kinetics of an electrochemical rection. Linear regions of LSV or CV data (potential vs current) is replotted as overpotential and log of current density to produce the Tafel plot. A Tafel plot allows the determination of kinetic parameters such as exchange current density and Tafel slopes, providing insight into reaction mechanisms and electrocatalytic activity. Tafel analysis is based on the Tafel equation, which describes the relationship between the overpotential and the logarithm of the current density. Tafel analysis is used in this work to compare PBA-derived electrocatalysts catalyst efficiency.

1.7.4.4. Chronopotentiometry (CP). In chronopotentiometry, a constant current is applied to the electrochemical cell, and the resulting potential changes over time are monitored. The setup resembles LSV and CV configurations but operates under galvanostatic conditions. This technique enables the study of electrode kinetics, charge transfer processes, and diffusion-limited reactions.

Chronopotentiometry relies on the relationship between applied current, electrode potential, and time, as dictated by the Butler-Volmer equation and Nernst diffusion layer theory. By analyzing the potential-time curves, one can extract information about charge transfer kinetics, diffusion coefficients, and electrochemical reaction rates. Chronopotentiometry is used in this work as another method of evaluating electrochemical stability under OER and HER conditions.

CHAPTER 2

TUNING THE BIMETALLIC RATIO IN PRUSSIAN BLUE ANALOGUE (PBA) DERIVED FECO NANOCARBIDES FOR THE OXYGEN EVOLUTION REACTION (OER)

Reprinted with permission from Ritz, A.J.; Bertini, I.A.; Nguyen, E.T.; Strouse, G.F.; Lazenby, R.A. Electrocatalytic activity and surface oxide reconstruction of bimetallic iron-cobalt nanocarbide electrocatalysts for the oxygen evolution reaction. RSC Adv., 2023,13, 33413-33423. DOI: 10.1039/D3RA07003D. Copyright 2023 Royal Chemistry Society.

2.1 Introduction

For renewable energy technology to become ubiquitous, it is imperative to develop efficient oxygen evolution reaction (OER) electrocatalysts, which is challenging due to the kinetically and thermodynamically unfavorable OER mechanism. Transition metal carbides (TMCs) have recently been investigated as desirable OER pre-catalysts, but the ability to tune electrocatalytic performance of bimetallic catalysts and understand their transformation under electrochemical oxidation requires further study. In an effort to understand the tunable TMC material properties for enhancing electrocatalytic activity, we synthesized bimetallic FeCo nanocarbides with a complex mixture of FeCo carbide crystal phases. The synthesized FeCo nanocarbides were tuned by percent proportion Fe (i.e. % Fe), and analysis revealed a non-linear dependence of OER electrocatalytic activity on % Fe, with a minimum overpotential of 0.42 V (15-20% Fe) in alkaline conditions. In an effort to understand the effects of Fe composition on electrocatalytic performance of FeCo nanocarbides, we assessed the structural phase and electronic state of the carbides. Although we did not identify a single activity descriptor for tuning activity for FeCo nanocarbides, we found that surface reconstruction of the carbide surface to oxide during water oxidation plays a pivotal role in defining electrocatalytic activity over time. We observed

that a rapid increase of the $(Fe_xCo_{1-x})_2O_4$ phase on the carbide surface correlated with lower electrocatalytic activity (i.e. higher overpotential). We have demonstrated that the electrochemical performance of carbides under harsh alkaline conditions has the potential to be fine-tuned via Fe incorporation and with control, or suppression, of the growth of the oxide phase.

Electrochemical water splitting offers a promising route for sourcing green hydrogen, a renewable energy alternative to fossil fuels.[32] However, the anodic four-electron oxygen evolution reaction (OER) mechanism is kinetically sluggish and thermodynamically unfavorable under alkaline conditions. Despite tremendous efforts in the search for new catalysts to utilize in electrochemical water splitting systems[33,34] costly ruthenium and iridium oxide (RuO_2 and IrO_2) electrocatalysts persist as the only viable options for industrial implementation.[35–38] Therefore, the development of alternative highly efficient, earth-abundant and low cost electrocatalysts for the OER remains crucial.

Nanoparticle electrocatalysts have attracted considerable interest for the replacement of bulk noble metal oxide catalysts due to their increased surface area to volume ratio, exposure of more active sites to reduce the amount of material needed to undergo reactions like the OER,[39–41] and offering a high degree of physical and chemical property tunability for the modulation of catalytic performance.[41,42] In particular, earth-abundant transition metal (TM)-based nanocatalysts have been reported to have comparable electrochemical performance to noble metal-based catalysts.[40] Recent studies have investigated transition metal carbides (TMCs) as low-cost alternative electrocatalysts for the hydrogen evolution reaction (HER) in acidic conditions,[43,44] however, few reports have discussed their use for catalyzing the OER in alkaline conditions.[45,46] TMCs possess high electrical conductivity, high chemical stability, and are resistant to corrosion at both the bulk and surface levels, all properties that are advantageous for water splitting

electrocatalysts.[47,48] While TMCs often do not have competitive OER activity and kinetics in comparison to high-performance TM-based oxides and layered double hydroxide (LDH) materials,[49,50] carbon materials often have more potential for scalable, low-cost fabrication processes and high thermal stability and remarkable conductivity for potential use in water electrolysis applications.[44,51] Therefore, developing an in-depth understanding of these materials can aid in rational design of TMC materials with high OER electrocatalytic efficiency.

We recently investigated the electrocatalytic OER performance of monometallic TM-nanocarbides, finding that Co > Ni > Fe for both electrocatalytic activity and stability with Co being our best performer, while the oxide thickness layer for post-catalytic OER nanocarbides decreased in the order Fe > Co > Ni[52]. There have been efforts towards designing enhanced electronic properties of TMCs for OER catalysis[45,53]. In particular, the incorporation of Fe with another metal in a bimetallic system for improved electrocatalytic activity has been widely studied, and these materials often outperform monometallic catalysts as a result of synergistic effects due to various structure and composition-dependent enhancement in active sites.[53,54] In particular, studies claim that mixed crystalline phases and increased disorder that often result from multi-metal incorporation have been shown to modify local electronic structures, leading to enhancement in activity towards the OER.[55–57] These synergistic effects are not well understood for bimetallic carbide systems and could be potential activity predictors for designing future bimetallic carbide catalysts.

Non-oxide-based catalysts are often known for undergoing surface termination changes via in-situ electrochemical oxidation, to produce thin oxide/hydroxide surface layers that are known for enhancing electrocatalytic activity[46,58–61]. However, our previous study on monometallic TMCs revealed that the thickest oxide layer formed on the Fe carbide (as compared to Co and Ni), but

this material exhibited the lowest electrocatalytic activity and poor stability[52]. We are therefore motivated to understand how to tune electrocatalytic activity in bimetallic FeCo carbides, given that we previously observed that the monometallic Co carbide was the highest performing electrocatalyst, and to explore the phenomenon of oxide layer transformation on carbide surfaces. In this study, $Fe_xCo_{1-x}C_y$ nanocarbides were synthesized from a single-source Prussian blue analogue (PBA) precursor, using a previously established method, which offers a potential route to economical bimetallic carbides for use as industrial OER electrocatalysts. The percent proportion of Fe (to Fe and Co) was changed, herein referred to as % Fe (i.e. x × 100%), for a series of bimetallic $Fe_xCo_{1-x}C_y$ nanoparticles, which resulted in various crystal phases across the entire composition range. These bimetallic carbides, and the monometallic Fe and Co carbides, were analyzed to reveal that optimal OER electrocatalytic activity was achieved for the samples that were synthesized to contain 15 – 20% Fe with a geometric normalized overpotential of 0.4 V. Our results suggest that Fe content is not the sole contributor for tunability of electrocatalytic activity, rather it works in synergy with resulting structural and oxide surface layer composition changes of the $Fe_xCo_{1-x}C_y$ nanocarbides.

2.2 Experimental Methods

All commercially available reagents were used without further purification. Precursors for FeCo PBAs were $K_3Co(CN)_6$ and $K_3Fe(CN)_6$ (Sigma Aldrich, > 99%), KCl (Sigma Aldrich, 98%), $CoCl_2 \cdot 6H_2O$ (Thermo Fisher, > 99%), and $FeCl_2 \cdot 4H_2O$ (Thermo Fisher, > 99%). Solvents used for synthesis were ultrapure water (18.2 Ω cm-1 at 25.0 °C, Thermo Scientific Barnstead E-Pure ultrapure water purification system), octadecylamine (ODA) (Thermo Fisher, 90%), acetone (VWR, ACS Grade) and toluene (VWR, ACS Grade).

2.2.1. General Synthesis of Ratio Controlled Bimetallic FeCo PBA. Two precursor solutions were prepared, and upon combination a precipitation reaction occurred to form the PBA. Briefly, x mmol $K_3Fe(CN)_6$ and 1 - x mmol $K_3Co(CN)_6$ (where x = 0, 0.1, 0.3, 0.5, 0.7, 0.9, 1), and 5 mmol of KCl in 100 mL of ultrapure water, comprised solution 1. Solution 2 comprised 1 mmol of either $FeCl_2$ (to make PBAs of > 50% Fe) or $CoCl_2$ (to make PBAs of < 50% Fe) in 200 mL of ultrapure water. Solution 2 was added dropwise to solution 1 at a rate of 5 mL min-1 and vigorously stirred. The subsequent reaction solutions were left for 18 hrs while stirring to grow the PBAs. The PBAs were collected via centrifugation, washed with 300 mL of ultrapure water and dried on the benchtop at room temperature. The PBA precursors were characterized using SEM, pXRD, and XRF.

2.2.2. Thermal Decomposition of PBAs into FeCo Nanocarbides. Synthesis of FeCo Nanocarbides. 200 mg of solid PBA and 40 mL of ODA were heated to 330 °C, under inert atmosphere for 24 hrs. After 24 hrs, the reaction was quenched using toluene and the resultant nanocarbide was collected via magnetic separation. The nanoparticles were washed with toluene (3×), acetone (1×), ultrapure water (3×), and again with acetone (1×), then dried in an oven at 100 °C for 15 minutes. The nanoparticles were structurally characterized using pXRD (Rigaku Miniflex benchtop powder diffractometer, Cu Kα. Elemental composition was confirmed using XRF spectroscopy (Panalytical Epsilon X-ray florescence analyzer). Morphology and size analyses were executed using transmission electron microscopy (TEM, FEI CM300 FEG).

2.2.3. Thermal Decomposition of PBAs into FeCo Nano-oxides. Synthesis of FeCo Oxides. 200 mg of solid PBA was loaded into an aluminum boat and placed into a Lindberg tube furnace. The PBA was subsequently heated to 300 °C with a ramp rate of 60 °C min^{-1}, for 30 minutes. The resultant oxides were structurally characterized with pXRD.

2.2.4. Materials Characterization. PXRD patterns of PBAs, PBA derived carbides and PBA derived oxides were collected at room temperature on a Rigaku Miniflex powder diffractometer (Cu Kα source, λ = 1.54 Å). The contributions of various crystalline phases were fitted and calculated as a percentage for each $Fe_xCo_{1-x}C_y$. PXRD measurements on post-OER samples were performed on a Rigaku Synergy single crystal diffractometer running in powder diffraction mode (Mo Kα source, λ = 0.71 Å). The bimetallic ratios in both PBA and nanocarbide were confirmed using XRF on a Panalytical Epsilon XRF analyzer (Cu Kα source, Table 1). X-ray photoelectron spectroscopy (XPS) was performed on as-synthesized powders deposited on carbon tape using a PHI 5100 X-ray photoelectron spectrometer (Mg Kα source) with a pass energy of 22.36 eV. The XPS spectra were fitted using CasaXPS software. Samples were Ar+-sputtered using a sputtering gun at 5 keV and 1 μA for 15 minutes to reveal underlying carbide features. All samples were calibrated to the aliphatic carbon assignment (C1s, 284.8 eV). Size and morphology of PBA precursors were investigated via SEM imaging (FEI Nova 400, 15 keV, Figure S1). Size, size dispersity, and morphology of the nanocarbides were estimated using ImageJ software (sample size = 100 particles) via TEM images, collected on a Tecnai Osiris TEM operating at 200 kV.

2.2.5. Electrode Preparation. A catalyst ink suspension was prepared using catalyst powder (1.3 mg, 2 mL total volume) in a solution mixture of 10% Nafion (5% (w/w) in water/1-propanol, Beantown Chemical), 6% ethanol, and 84% deionized water. The mixture was then sonicated for 5 min, until a homogeneous black ink formed. Catalyst ink (31 μL) was drop casted onto the surface of a 5 mm diameter glassy carbon (GC) rotating disk electrode (RDE) (Pine Research Instrumentation) with a nanoparticle mass loading of 0.1 mg cm^{-2}. The samples were

dried for 1 – 2 hrs in air at room temperature to achieve a uniform thin film (shown in the SEM image in Figure S7).

2.2.6 Electrochemical Measurements. All electrochemical measurements were performed using a RDE setup equipped with an electrode rotator (WaveVortex 10, Pine Research Instrumentation) set to 1500 rpm, connected to a potentiostat (model CH 660E, CH instruments) within a compartmentalized electrochemical glass cell filled with approximately 250 mL of 1.0 M KOH. A three-electrode setup was used with a GC RDE as the working electrode, a Ag/AgCl reference electrode (1.0 M KCl internal filling solution), and a graphite rod counter electrode.

The electrochemical surface area (ECSA) was determined for each sample using the double layer capacitance, C_{dl}, measured by cyclic voltammetry (CV), so that current densities could be estimated (example shown in SI Figure S8)[42,43]. The charging current, i_c, is proportional to the potential scan rate, v, shown in Eq. 7.

$$i_c = v\, C_{dl} \qquad \text{(Eq. 7)}$$

By varying the scan rate (10, 20, 50 and 100 mV s-1), a plot of i_c as a function of v will yield a straight line where C_{dl} is the gradient, using CVs recorded in a designated potential window of the nonfaradaic region of the CV, shown in example CV in Figure S8 as 0.81 to 1.01 V vs. reversible hydrogen electrode (RHE). ECSA was calculated using the determined value of C_{dl} using Eq. 8.

$$ECSA = C_{dl} / C_s \qquad \text{(Eq. 8)}$$

where C_s is the specific capacitance of the material. We used a value for C_s of 45 μF cm-2 for the $Fe_xCo_{1-x}C_y$ samples, based on reported values in literature for TMs on GC electrodes in the range of 30 – 70 μF cm^{-2}.[62,63]

In 1.0 M KOH (pH = 13.8) electrolyte, the potentials against Ag/AgCl can be converted to potentials vs. the reversible hydrogen electrode (RHE) at 25˚C using Eq. 9.

(Eq. 9) $E_{vs.\ RHE} = E_{vs.Ag/AgCl} + 0.059\ pH$

which was used to calculate the overpotential, η, using Eq. 10.

(Eq. 10) $\eta = E_{vs.\ RHE} - 1.23\ V$

Additionally, a master reference electrode (not used in experiments) was compared against the Ag/AgCl reference electrode used experimentally and was observed to change no more than 5 mV to ensure a stable, well-defined electrochemical potential.

Tafel slopes were calculated from the linear kinetic region of the Tafel plot, i.e. log (current density) vs. overpotential, at the early onset current in the LSV curves. Electrochemical stability measurements were performed for 200 repetitive CV cycles, with a potential range of 1.0 to 1.8 V vs. RHE, using a scan rate of 5 mV s^{-1}. For the preparation of samples analyzed by pXRD post-OER, nanomaterial was drop casted onto a GC wafer electrode (glassy carbon plate, 2 mm thick, Thermo Fisher) setup with an estimated mass loading of 0.8 mg cm^{-2}.

2.3 Results and Discussion

2.3.1. Electrocatalytic Activity of $Fe_xCo_{1-x}C_y$ Exhibits Non-Linear Dependence on % Fe. Here, PBA derived FeCo nanocarbides were rationally designed using previously established synthetic conditions, and Fe and Co proportions were finely tuned for controlling OER activity. XRF was used to determine the elemental composition, and the ratio of Fe and Co was maintained from PBA precursor to carbide (Table 1). There was reasonable agreement between the measured Fe:Co ratio, and desired ratio based on synthesis, so all samples are referred to by the desired % Fe throughout this work. The electrocatalytic activity and stability of the nanocarbides towards the OER was evaluated in 1.0 M KOH, using a three-electrode set up and a mass loading of 0.1 mg cm^{-2}. Electrocatalytic activities of the FeCo nanocarbides were evaluated by extracting the

overpotential required to achieve a current density of 10 mA cm^{-2} from linear sweep voltammograms (LSVs). This value is the benchmarking standard for current density expected at the anode for an artificial photo-synthetic device yielding 10% efficiency at 1 sun illumination and serves as a useful comparison for our samples and literature.[40,64] The electrochemically active surface areas (ECSAs) were determined from the electrochemical double layer capacitance of the drop casted surface, to materials have both crystalline and amorphous features confirmed by XPS

Table 2.1. X-ray fluorescence (XRF) elemental composition for FeCo PBA precursors and FeCo carbides. Results show ratio of metals are maintained from precursor to resultant carbide.

Sample (PBA Precursors)	% Fe	% Co	Sample (FeCo Carbide)	% Fe	% Co
100% Fe	99	1	100% Fe	100	0
95% Fe	93	7	95% Fe	93	7
85% Fe	95	5	85% Fe	95	5
75% Fe	84	16	75% Fe	80	20
65% Fe	72	28	65% Fe	71	29
55% Fe	60	40	55% Fe	60	40
45% Fe	33	67	45% Fe	35	65
35% Fe	26	74	35% Fe	27	73
25% Fe	18	82	25% Fe	20	80
20% Fe	14	86	20% Fe	14	86
15% Fe	12	88	15% Fe	12	88
5% Fe	7	93	5% Fe	4	96
0% Fe	0	100	0% Fe	0	100

in Figure 2.8, the latter of which tend to have enhanced ECSAs.

Figure 2.1a shows representative LSVs of the nanocarbides, with their corresponding Tafel slopes in Figure 2.1b. FeCo nanocarbides containing 20% Fe exhibited lower overpotentials and steeper voltametric slopes than those below or above this % Fe (Figure 2.1a). Also, the more active OER carbide electrocatalysts, between 0 and 20% Fe, exhibited an exponential increase of current density as potential increased, which is to be expected based on the Butler-Volmer equation. However, the voltammetry in Figure 2.1a also shows that as % Fe increased above 20%, the rate of increase of current density was suppressed at the highest potentials and higher overpotentials allow for comparison of intrinsic activity between samples. This was necessary because the (lower activity) at 10 mA cm^{-2} were observed. It is important to mention that these catalysts have a low mass loading (0.1 mg cm^{-2}) compared to significantly higher loadings used in other catalyst studies, and it is well known that an increase in catalyst loading can be utilized to enhance electrocatalytic reaction rates. The voltammetry for carbide catalysts with higher % Fe exhibiting more diffusion-controlled behavior could suggest that the accessibility of the catalyst towards the electrolyte solution is hindered for nanocarbide compositions with higher Fe content and could require higher mass loadings to overcome diffusion effects.[65] Attempts to correct electrocatalytic voltammograms with mixed kinetic and mass transport control on a macroelectrode have been implemented using computational studies but are time-intensive to implement.[66] To consider solution resistance factors, iR drop compensation was performed on CoC and FeCoC (15% Fe). We found that the overpotentials extracted at a current density of 10 mA cm^{-2} yielded an inappreciable shift in overpotential of ~13 mV when iR corrected. These voltammetric differences warranted Tafel analysis to gain insight into the kinetics of the electrocatalytic OER reaction, shown in Figure 2.1b. The linear region of the Tafel plot was fitted from the kinetically controlled region of the voltammogram to provide Tafel slopes of nanocarbides with varying % Fe. The

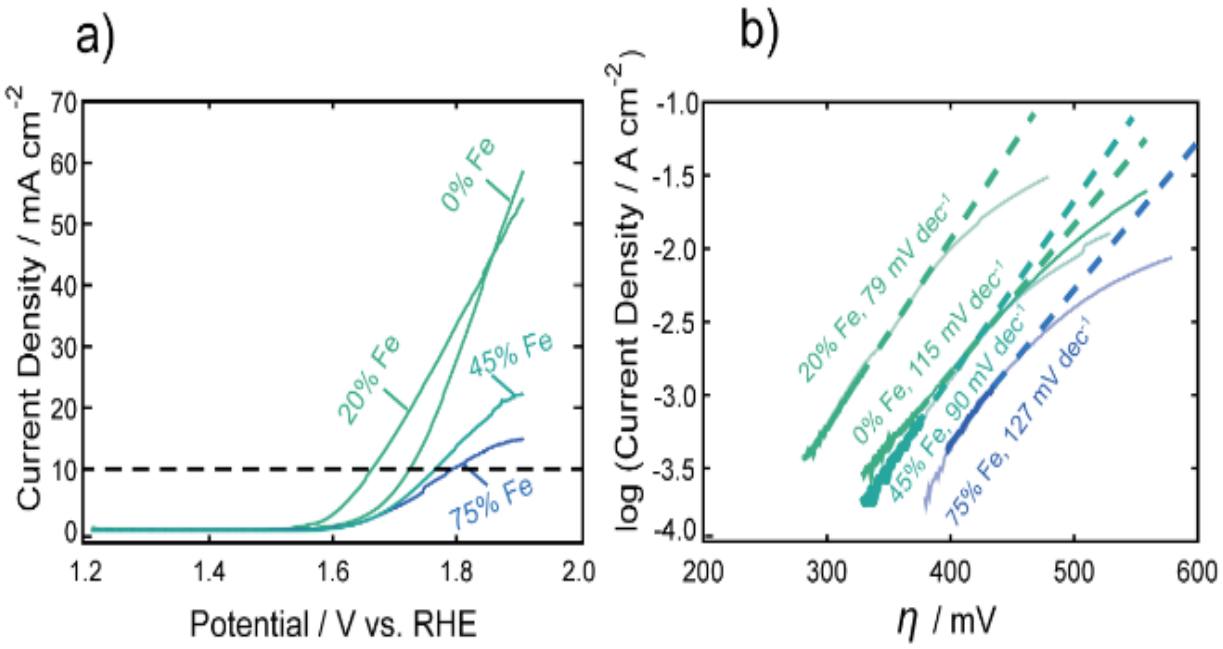

Figure 2.1. a) Representative linear sweep voltammograms of FeCo nanocarbides in 1.0 M KOH, with a dashed line denoting the benchmarking standard current density of 10 mA cm^{-2}. Note that RuO_2 achieved an overpotential of 0.36 V at 10 mA cm^{-2} (per geometric surface area). b) The linear regions of the Tafel plots were fitted, using the kinetically-controlled region of the voltammetry from part a) to determine Tafel slopes, indicated by the dashed lines. Note that the Tafel slope obtained for RuO_2 was 85 mV dec^{-1}.These fitted slopes are shown as dashed lines in Figure 2.1.b, which do not fit the portions of the voltammograms in which diffusion effects become significant. We can assume based on the lower Tafel slopes shown for nanocarbides with 45 and 75% Fe (90-127 mV dec^{-1}) in Figure 2.1b that these are poor performing catalysts as compared to nanocarbides with 20% Fe, without additional analysis.

monometallic Co nanocarbide (i.e. 0% Fe) achieved an overpotential of 0.53 V (at 10 mA cm^{-2}), and the 100% Fe carbide was unable achieve a current density of 10 mA cm-2 in this potential window. The best performing FeCo nanocarbide electrocatalysts, i.e. 15 – 20% Fe, yielded a lower, enhanced overpotential of 0.40 V (geometric corrected) and 0.42 V (ECSA corrected) compared to the monometallic Fe and Co carbides. For comparison, an industrial electrocatalyst RuO_2 was tested under the same electrochemical conditions and mass loading, which gave an overpotential of 0.36 V at 10 mA cm^{-2}, comparable to other RuO_2 values shown in literature (0.38 V).[39] Higher intrinsic activities are often predicted for catalysts with higher mass loadings. Electrocatalytic activity measurements were performed with higher mass loadings of 0.8 and 0.4 mg cm^{-2} using

one of our best performing FeCo nanocarbides with 15% Fe. Samples prepared with higher mass loadings resulted in a higher rate of OER current and slightly lower overpotentials, with the lowest geometric overpotential achieved with a mass loading of 0.8 mg cm^{-2} (0.38 ± 0.01 V) and current densities of ~105 mA cm^{-2}. Mechanical instabilities such as the thin nanomaterial film peeling from the surface and sample flaking off the electrode surface occurred in long-term electrochemical stability interrogation of samples with higher mass loading (>0.8 mg cm^{-2}), which motivated us to choose a lower mass loading of 0.1 mg cm^{-2} for this study. The overpotentials at 10 mA cm^{-2} were extracted from each voltammogram and are plotted against the % Fe in Figure 2.2a. A U-shaped curve (polynomial fit to guide the reader) is observed with a minimum overpotential between 15 – 20% Fe. In Figure 2.2b, the corresponding Tafel slopes showed a similar U-shaped curve, with a favorable minimum Tafel slope observed between 20 – 25% Fe. Tafel plots allow for the kinetic region of a voltammogram to be analyzed, although unlike for the HER, the value of the Tafel slope cannot be used for directly predicting the mechanism of the OER, given the multi-electron reaction and many possible intermediates.[67–69] When the reaction rate is limited by the charge transfer reaction, Tafel slopes of 120 mV dec^{-1}, 90 mV dec^{-1}, 60 mV dec^{-1}, and 30 mV dec^{-1} can be correlated to 1, 2, 3, and 4 electron transfer processes,[70] respectively, under alkaline conditions. Comparison of Tafel slopes, albeit without full interpretation, is useful to compare the relative kinetics of the various samples. The most favorable kinetics for the OER were observed at 20 – 25% Fe, with a Tafel slope of 79 mV dec^{-1}, comparable to a Tafel slope of 85 mV dec^{-1} for RuO_2 and suggesting a 2 electron-transfer rate determining step. FeCo nanocarbides with lower Fe content, i.e. 0 – 15% Fe, have Tafel slopes ranging from approximately 115 to 104 mV dec^{-1}, respectively, suggesting that the 0% Fe sample is closest to the 1 electron-transfer rate determining step. Similarly, 75% Fe has a high Tafel slope of 127 mV dec^{-1} that

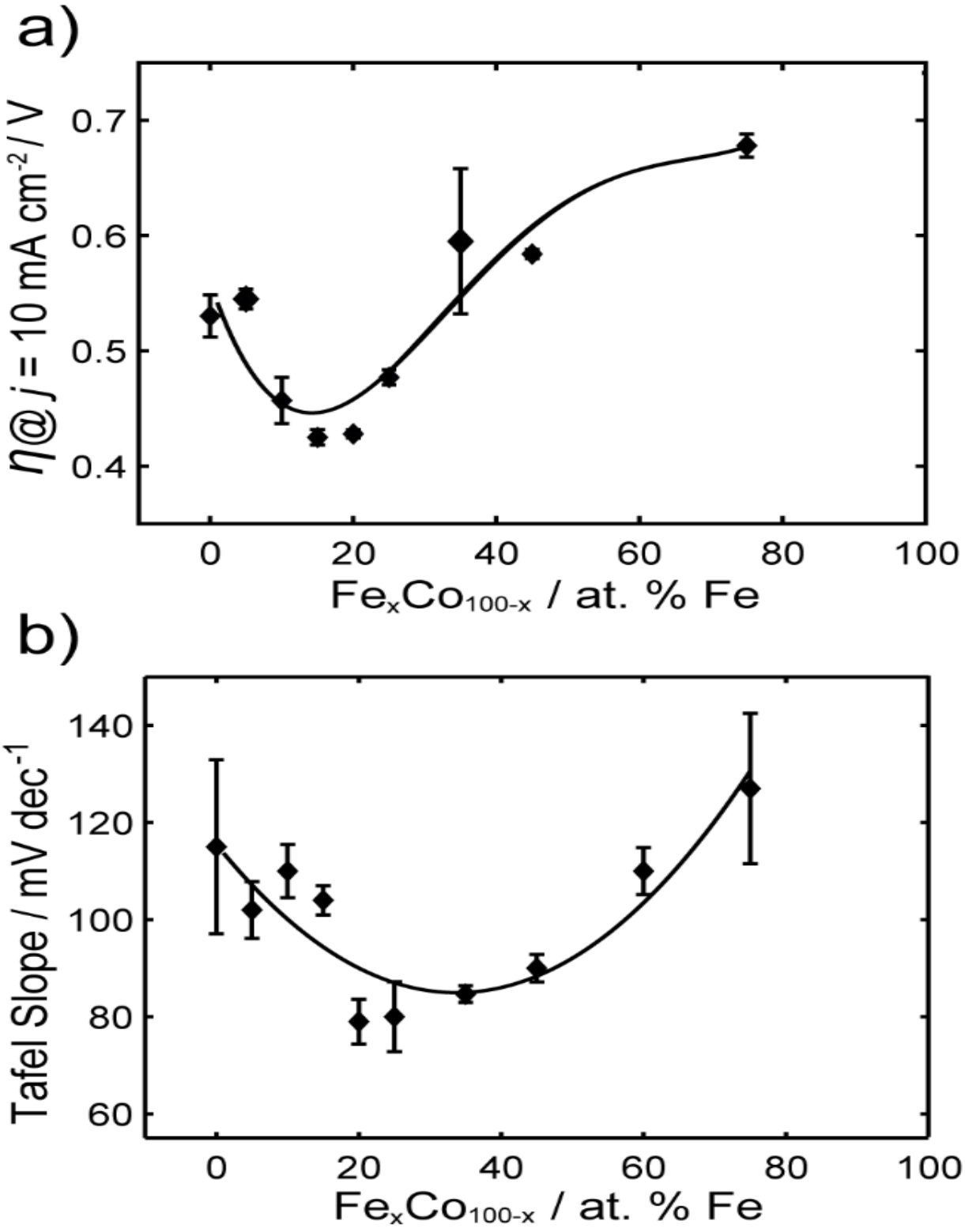

Figure 2.2. a) Overpotentials (n = 3) required to achieve 10 mA cm-2 (per ECSA) for FexCo1-xCy of varying % Fe, in 1.0 M KOH. b) Tafel slopes for FexCo1-xCy of varying % Fe.

corresponds to a 1 electron-transfer rate determining step, suggesting that <15% Fe and >75% Fe both have less favorable electron transfer kinetics.

The results from the FeCo nanocarbide system reveal optimal geometric and ECSA normalized overpotentials (for 15 – 20% Fe) of 0.40 V and 0.42 V, respectively, which are competitive to a geometric-normalized overpotential of a Co_2C OER pre-catalyst reported by Mullins and coworkers of 0.46 V.[46] When comparing electrocatalysts in literature, it is important to note that there are various methods by which the materials are attached to a substrate electrode. Electrode modification methods other than drop casting, such as electrodeposition and sputtering, will result in different film thicknesses and catalytic loading, which can influence the measured overpotentials. While our study is not motivated in simply lowering this benchmarking overpotential and is more concerned with understanding which (and how) material properties dictate the overpotential for carbides, it is nonetheless important to consider where the carbides lie in relation to the state-of-the-art and other competitive catalysts. Our best FeCo nanocarbide (for 15% Fe) had an overpotential of 0.38 V (j= 10 mA cm^{-2}) at a mass loading of 0.8 mg cm^{-2}, which is competitive to a geometric-normalized overpotential of a Co_2C OER pre-catalyst reported by Mullins and coworkers of 0.46 V.[71] Other examples in literature such as FeCo phosphide has an overpotential of 0.37 V (for 50% Fe),[72] and FeCo(OOH) has an overpotential of 0.35 V (60% Fe),[73] which are comparable to our system. The lowest overpotentials in the field have been demonstrated for FeCo-layered double hydroxide (LDH) nanosheets, with an overpotential of 0.28 V,[74] and FeCo- oxyhydroxide (OOH) nanosheet, with an overpotential of 0.21 V.[75]

Fe's role in regulating OER activity for multimetallic systems has been suggested to result from: the favorable binding energies of intermediate species in the OER inducing stabilization of the crystal lattice,[76] Fe^{3+} acts as the catalytic active site in both FeCo and FeNi materials,[55,73] Fe

has increased conductivity over other TMs,[73] and the regulation of charge transfer energies in a mixture of Co^{4+} and Fe^{4+} ions.[74] In this work, we attempted to identify the source of electrocatalytic enhancement that occurs when combining Fe and Co in the bimetallic carbide catalysts, exploring the role of key activity descriptors. In the following section, we have investigated the effects of tuning material composition and structure, such as crystal phase composition and surface chemical states, on regulating electrocatalytic activity.

2.3.2. Effects of Material Composition and Structural Properties on OER Electrocatalytic Activity. Carbides are known to have amorphous and graphitic-type carbon that could influence phase,[77] therefore impacting electrocatalytic activity as the carbide crystallinity and crystal structure is tuned.[78] The preparation of pure-phase Fe carbide materials is notoriously difficult to achieve under mild synthesis conditions, often resulting in mixed phase materials.[45,77,79] Strain in materials can often be the result of substitutional doping and disorder.[80–82] To investigate whether crystal phase composition of the nanocarbides plays a role in the electrochemical activity, pXRD phase analysis was used to reveal an evolution of crystal phases across the various percentages of Fe (Figure 2.4a,b). The simulated pXRD patterns of the four identified phases are shown in Figure 2.4a, which are overlaid on a contour plot of 2θ vs Fe percentage, in which the black intensity is normalized to most prominent peak in the pXRD pattern. Figure 2.4b represents approximate individual phase contributions, of the four unique phases identified in the $Fe_xCo_{1-x}C_y$ system, across the range of samples. However, identifying the amount of each phase present was deconvolute contributions of each phase towards the overall diffraction patterns, whole pattern fitting was executed using Rigaku SmartLab Studio II software (Figure 2.3). According to the fits, all samples are mixed phase, containing a minimum of two crystal phases. From 0 – 45% Fe, the carbides have approximately 60 – 85% M_3C (ICSD: 43521, hexagonal) phase and 15 – 40% M_2C

(COD: 1528415, orthorhombic) phase. From 55 – 65% Fe, the M_5C_2 persists as the major phase and decreases in abundance at 65% Fe, where the final phase M_7C_3 (ICSD: 76830) evolves in and a non-trivial task, due to diffraction pattern overlap and differences in diffraction intensity. To is mixed with M_5C_2, up to 100% Fe. There are key differences in electrocatalytic activity observed between different mixed-phase regions shown in Figures 2.1 and 2.2, such as 75% Fe (mixed M_5C_2/M_7C_3) and 0% Fe (mixed M_2C/M_3C), which exhibit an overpotential difference of 150 mV. Although phase may affect catalysis in conjunction with tuning Fe composition, this is not the only activity descriptor for the FeCo carbide catalysts. This is evidenced by nanocarbides between 0 – 20% Fe which have similar phase compositions, but differing overpotentials (Figure 2.2b). Another factor considered for optimizing electrocatalytic activity was the size of the nanocrystal, however our results showed that the size of the carbide nanoparticles could not be correlated to electrocatalytic activity. In agreement with previous studies[10,52] the resultant carbide size was proportional to the size of the mesocrystal precursor (SEM images shown in Figure 2.5). The size and morphology of the nanocarbide particles were analyzed using TEM analysis (Figure 2.4c-g). pXRD results for the entire ratio range of synthesized FeCo PBAs are shown in figure 2.6 and pXRD results for the entire range of synthesized FeCo nanocarbides are shown in figure 2.7. Figure 2.6 shows a clear shift from the Co PBA structure to the Fe PBA structure as the amount of Fe is amount of Fe increases as well. The shift to lower 2θ is correlative to the size of PBA decreasing as the amount of Fe increases as well. Figure 2.7 shows a mixture of carbide phases present with a general trend of cobalt structure types to Fe structure type as the amount of Fe increases.

However, due to the presence of significant amounts of amorphous carbon surrounding our nanocarbides, the images were only used to estimate particle size and shape. The monometallic

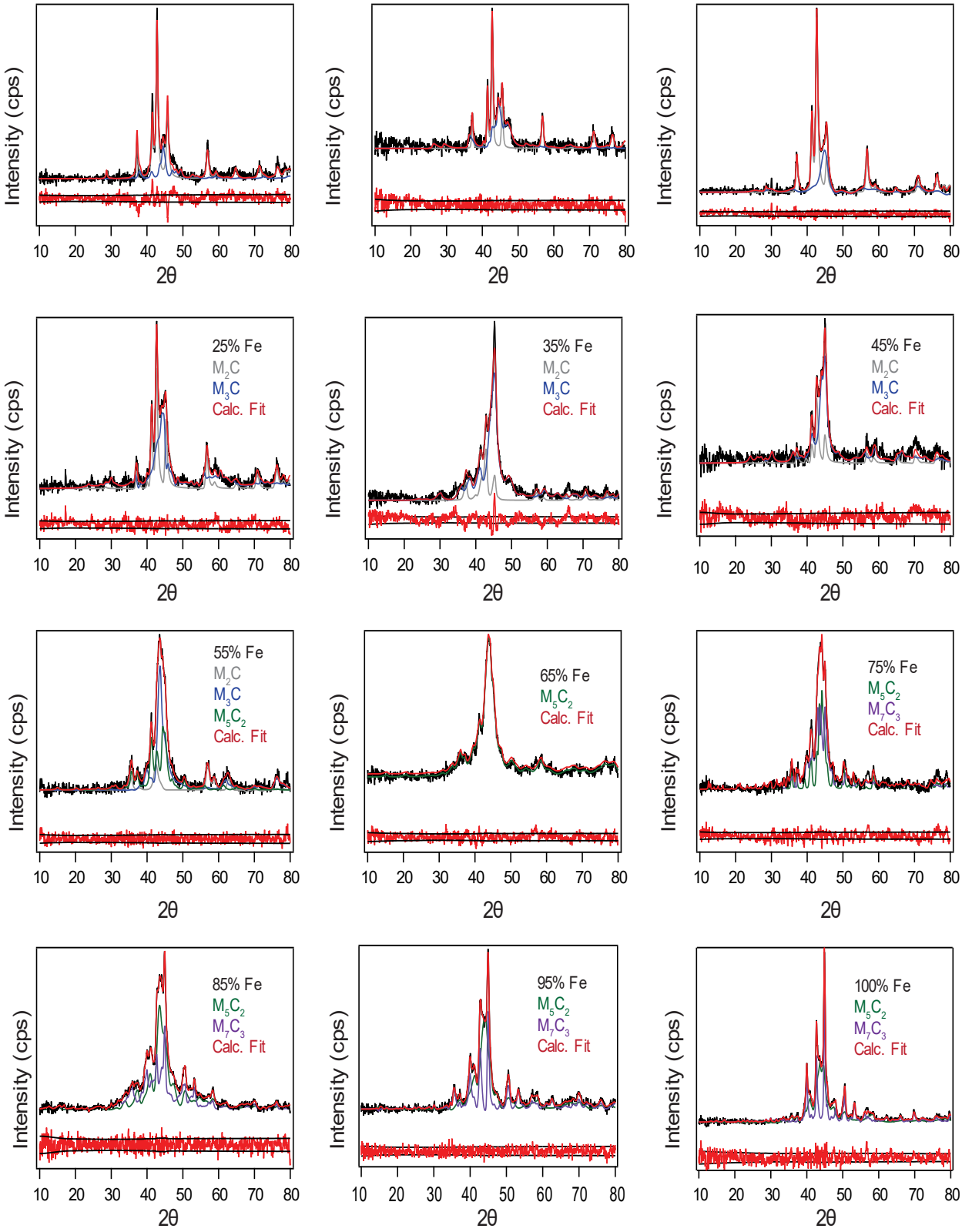

Figure 2.3. Contribution of varying phased fitted to each $Fe_xCo_{1-x}C_y$ pXRD patter. Residuals are plotted below each fit.

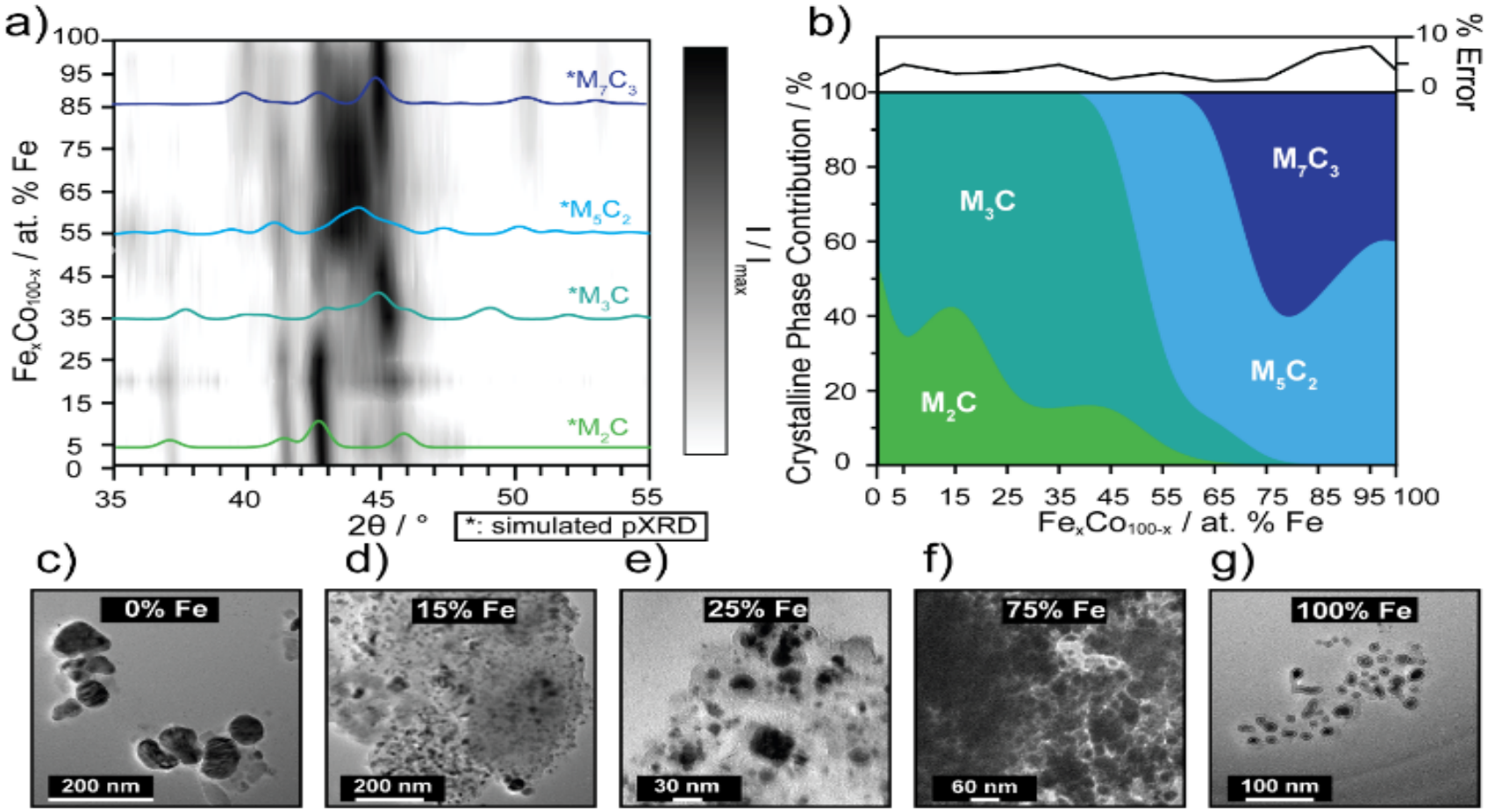

Figure 2.4. a) 3D contour plot tracking the evolution of the major carbide phase as a function of % Fe, using pXRD patterns. The black intensity represents the XRD signal, I, normalized to the maximum signal, Imax, where the most intense peaks appear darkest. Phase references are broadened to reflect 10 nm materials and overlaid (in color) to highlight differences. The references shown are for M7C3 (dark blue, ICSD: 76830), M5C2 (light blue, ICSD: 423885), M3C (blue-green, ICSD: 43521) and M2C (green, COD: 1528415). b) Proposed phase diagram of metastable bimetallic carbides, where relative phase contributions are plotted against % Fe. The error plot (top) represents the % error (±) in each fit. Fits for select samples are shown in SI Figure S4. TEM images of select FexCo1-xCy for c) 0% Fe, d) 15% Fe, e) 25% Fe, f) 75% Fe, and g) 100% Fe. Sizes of the nanocrystals increase, as the Fe content decreases, based on histogram size analysis (n = 50 – 100).

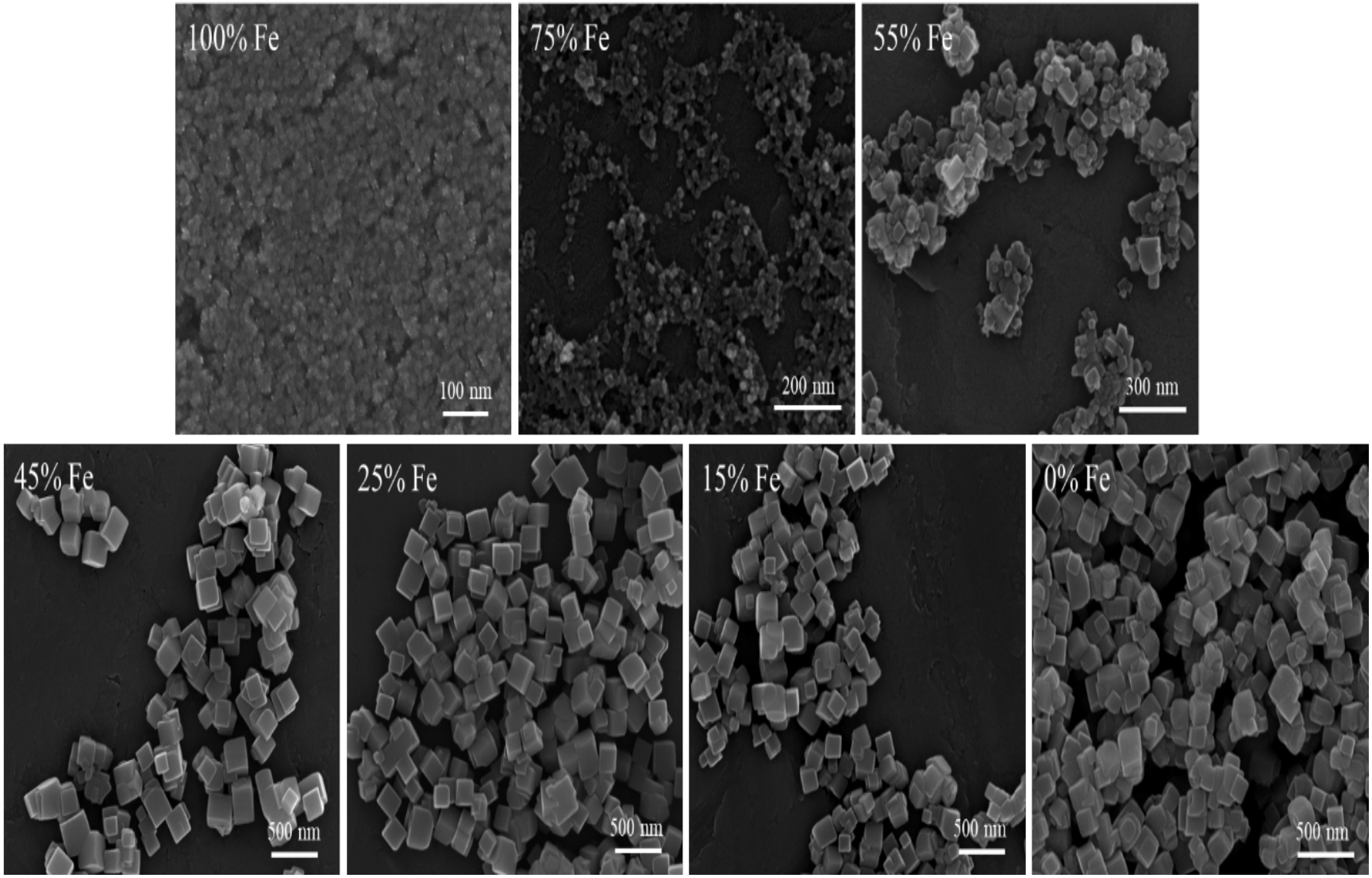

Figure 2.5. Scanning electron microscopy (SEM) images of FeCo Prussian blue analogue (PBA) precursors with increasing % Fe. Sizes range from < 20 nm – 150 nm.

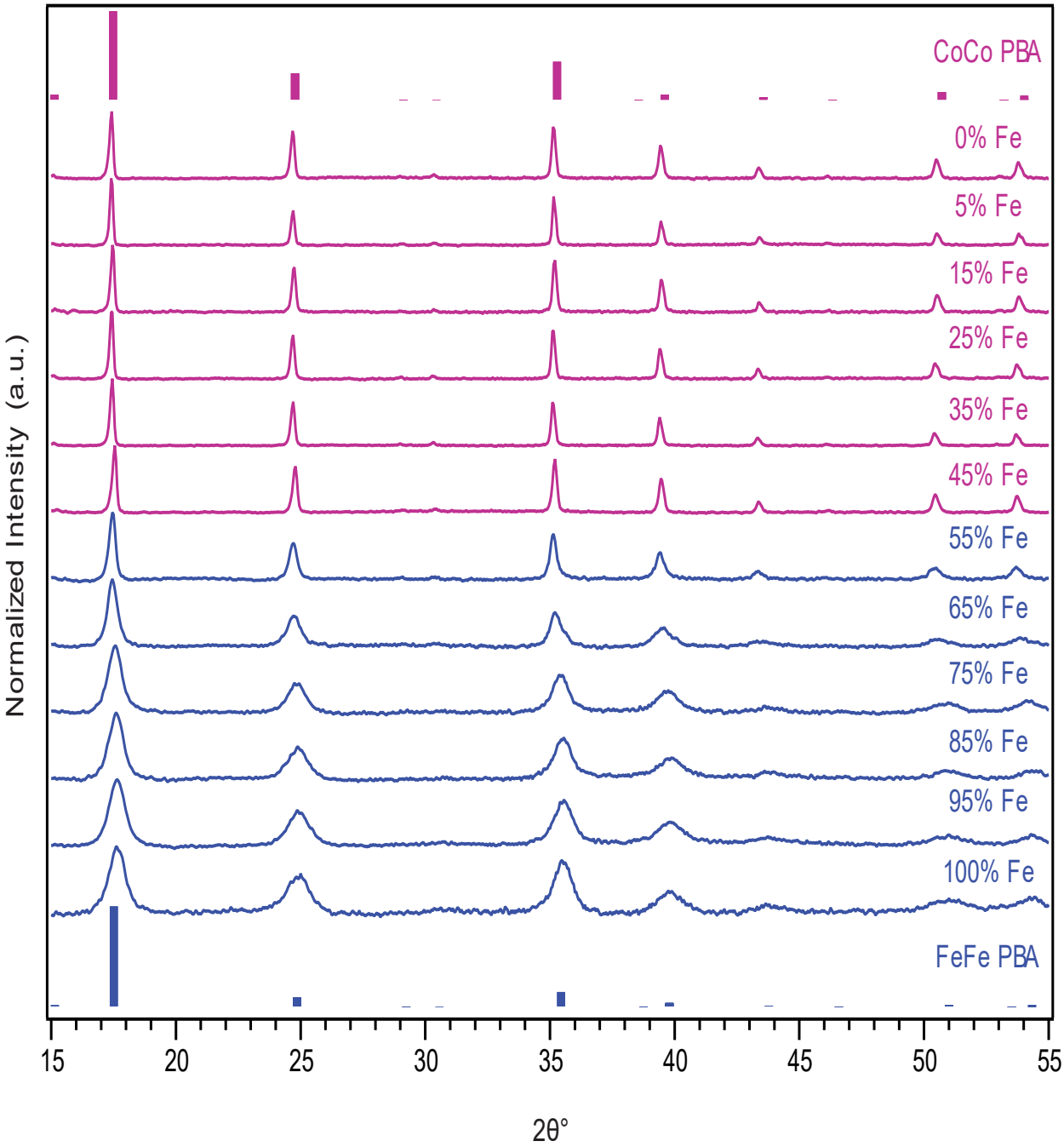

Figure 2.6. Powder X-ray diffraction patterns of FeCo PBA precursors. A transition from the $KCoCo(CN)_6 \cdot x\ H_2O$ PBA type to the $KFeFe(CN)_6 \cdot x\ H_2O$ is observed as the amount of Fe increases, corresponding to a Vegard shift towards lower 2θ and the space group of Fm-3m remains for both PBA forms. The pink reference card (ICSD 45154) represents the $KCoCo(CN)_6 \cdot x\ H_2O$ type and the blue reference card (ICSD 23102) represents the $KFeFe(CN)_6 \cdot x\ H_2O$ type.

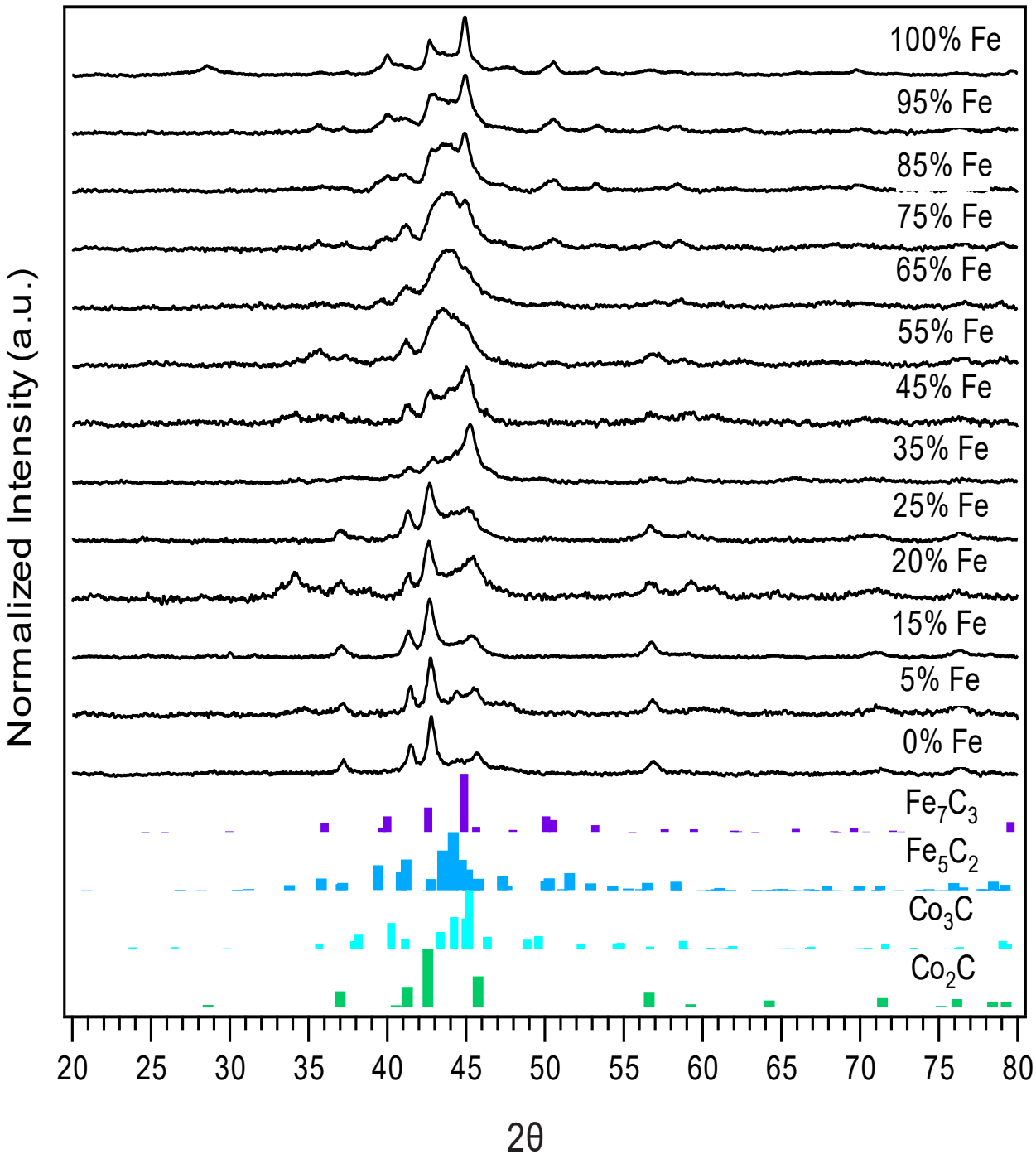

Figure 2.7. Powder X-ray diffraction (pXRD) patterns of all $Fe_xCo_{1-x}C_y$ samples produced for electrocatalytic study, of varying Fe content from 0 – 100%. Pure reference phases are shown for comparison, for M_2C (Green reference, COD: 1528415), M_3C (light blue reference, ICSD: 43521), M_5C_2 (dark blue reference, ICSD: 423885) and M_7C_3 (purple reference, ICSD: 76830).

Co (i.e. 0% Fe) carbide particles were significantly larger than the other bimetallic carbide nanocrystals, as shown in the TEM images in Figure 2.4 for 0% Fe (51 ± 6 nm), 15% Fe (9 ± 6 nm), 25% Fe (9 ± 3 nm), 75% Fe (14 ± 3 nm), and 100% Fe (8 ± 2 nm). Based on TEM images shown in Figures 2.6c-g, and in our previous study, the resulting carbide nanocrystals are highly disordered, with stacking faults likely present[52]. Although stacking faults[83] and NP size[42] are often linked to tuning electrocatalytic activity, our results show that the minimum overpotential of 0.42 V achieved cannot be attributed to differences in particle size or morphology, as particles containing 15-100% Fe the have similar nanocrystal sizes, yet the electrocatalytic activity changes significantly.

XPS was used to investigate the surface structure of the as-synthesized $Fe_xCo_{1-x}C_y$ materials with varying % Fe (Figure 2.8), with chemical shifts obtained from fits in Table 2. For the Co2p spectra in Figure 2.8a, three Co species were identified: Co^0 (778 eV 2p3/2), Co^{2+} (780-786 eV 2p3/2), and Co^{3+} (779-785 eV 2p3/2), indicative of the carbide and mixed valence oxide surface species, respectively.[84] The observed Co^{2+} and Co^{3+} species observed in as-synthesized samples are consistent with finding from Mullins and coworkers,[46] suggesting the presence of a thin-layer amorphous oxide on the surface. In particular, the evidence of a broadened 2p3/2 peak at ~795 eV from post-OER pXRD analysis. The Fe2p spectra revealed three Fe species: Fe^0 (707 eV 2p3/2) resulting from metal carbide, and Fe^{2+} (709 eV 2p3/2) and Fe^{3+} (711 eV 2p3/2) resulting from a mixed valence oxide at the surface. The C1s spectra revealed three unique species: metal to carbon bonding (M-C, 284.8 eV) present in the carbide material, carbon to carbon bonding (C-C, 286 eV) from ligand, carbide, and carbon tape support,

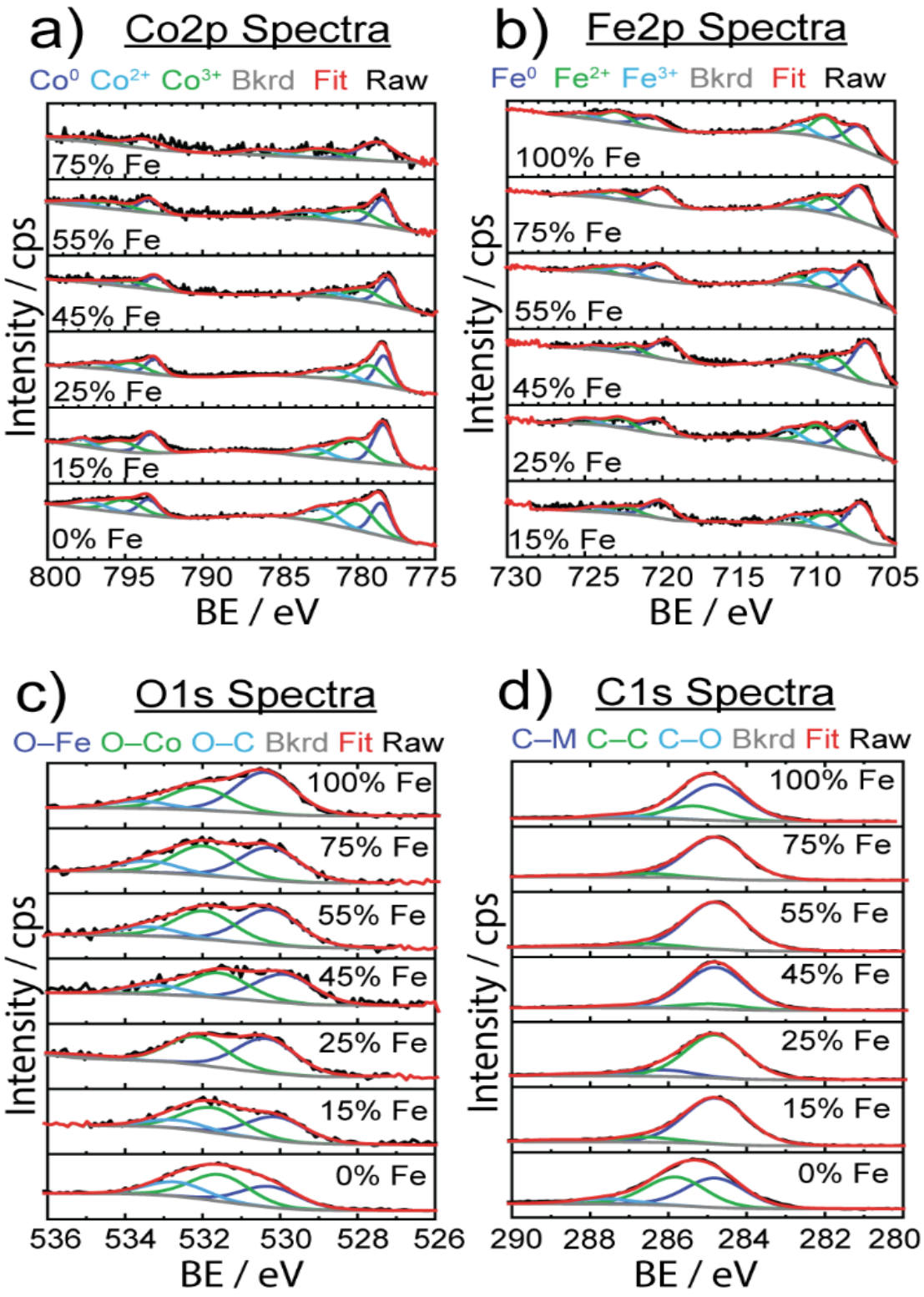

Figure 2.8. Stacked X-ray photoelectron spectra for FexCo1-xCy samples of varying Fe concentrations are shown for a) Co2p, b) Fe2p, c) O1s, and d) C1s with respective contributions of chemical species below. Black lines represent raw data, red lines represent overall fits, the gray lines show the background (bkrd) and specified chemical species are shown in dark blue, green and light blue lines.

and carbon to oxygen bonding (C-O, 288 eV) attributed to ligand and oxygen passivation via ambient conditions.

In the O1s spectra, three species were identified, and attributed to oxygen bonding to each of Fe and Co at the surface (O-Fe: 531 – 532 eV, O-Co: 530 eV), and oxygen to carbon bonding (O-C, 533 eV) due to ligand and amorphous surface oxide contributions. Although there was some variability in chemical shifts in the Co2p and Fe2p spectra, there were no detectable changes in electronic structure to explain electrocatalytic enhancement. A study on Fe-doped molybdenum carbide catalysts noted that although there were appreciable differences in the electrocatalytic

Table 2.2. Table of all XPS chemical shifts for selected $Fe_xCo_{1-x}C_y$ samples. All chemical shifts were calibrated to C1s = 284.8 eV. No clear trend is correlative to experimental electrocatalysis results, and minimal changes are seen in the overall electronic environment.

Sample	Co Chemical Shifts (eV)	Fe Chemical Shifts (eV)	C Chemical Shifts (eV)	O Chemical Shifts (eV)
0% Fe	Co^0: 778.5 Co^{2+}: 782.3 Co^{3+}: 780.0	N/A	C-M: 284.8 C-C: 285.8 C-O: 287.6	O-Fe: 530.3 O-Co: 531.6 O-C: 532.7
15% Fe	Co^0: 778.3 Co^{2+}: 782.7 Co^{3+}: 780.3	Fe^0: 707.0 Fe^{2+}: 709.3 Fe^{3+}: 711.3	M-C: 284.8 C-C: 286.6 C-O: 288.9	O-Fe: 530.1 O-Co: 531.8 O-C: 532.7
25% Fe	Co^0: 778.2 Co^{2+}: 781.4 Co^{3+}: 779.1	Fe^0: 707.5 Fe^{2+}: 709.9 Fe^{3+}: 711.8	M-C: 284.8 C-C: 286.1 C-O: 288.2	O-Fe: 530.4 O-Co: 532.1 O-C: 535.2
45% Fe	Co^0: 777.9 Co^{2+}: 781.8 Co^{3+}: 779.5	Fe^0: 706.7 Fe^{2+}: 708.8 Fe^{3+}: 710.7	M-C: 284.8 C-C: 284.9 C-O: 287.2	O-Fe: 529.9 O-Co: 531.6 O-C: 533.2
55% Fe	Co^0: 778.3 Co^{2+}: 783.3 Co^{3+}: 780.1	Fe^0: 707.1 Fe^{2+}: 709.3 Fe^{3+}: 711.2	M-C: 284.8 C-C: 286.5 C-O: 288.5	O-Fe: 530.3 O-Co: 532.0 O-C: 533.4
75% Fe	Co^0: 778.6 Co^{2+}: 786.0 Co^{3+}: 782.3	Fe^0: 707.1 Fe^{2+}: 709.3 Fe^{3+}: 711.2	M-C: 284.8 C-C: 286.6 C-O: 288.7	O-Fe: 530.3 O-Co: 532.0 O-C: 533.4
100% Fe	---	Fe^0: 707.3 Fe^{2+}: 709.5 Fe^{3+}: 711.2	M-C: 284.8 C-C: 285.3 C-O: 287.3	O-Fe: 530.4 O-Co: 532.1 O-C: 533.6

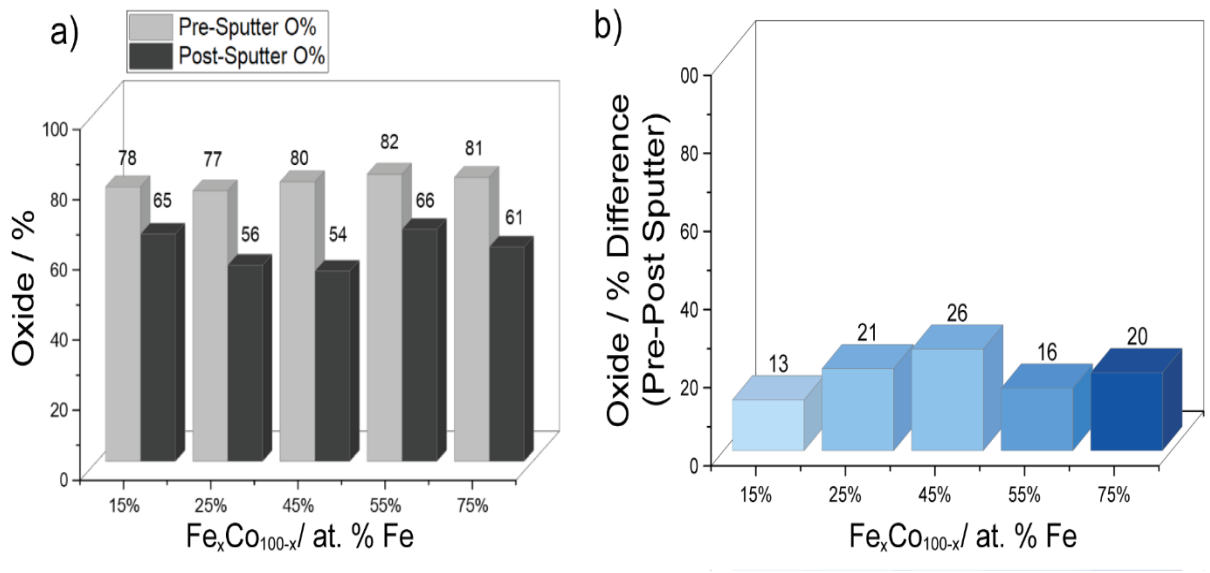

Figure 2.9. a) XPS quantification of oxide present in as synthesized $Fe_xCo_{1-x}C_y$ samples before (light gray) and after (dark gray) Ar ion sputtering at 5 keV/1 μA for 15 minutes. Note that carbon atomic percentages were not included as samples were run on a carbon puck, therefore the relative amount of only metal and oxygen can be accurately observed. b) Percent difference of oxide in various $Fe_xCo_{1-x}C_y$ samples. Interestingly, 15% shows the smallest oxide percent difference suggesting that minor oxide surface layers may enhance electrocatalysis.

activity of pure and Fe-doped molybdenum carbide, there was no significant difference in oxidation state shifts upon addition of Fe, similar to our data (Figure 2.8).[11] However, to better understand the thin amorphous oxide layer detected on the carbide samples, we implemented the difference in oxide before and after Ar^+ ion etching to quantify the amount of surface oxide, shown in Figure 2.9.

Interestingly, 15% Fe had the smallest change in oxide amount after sputtering, which could suggest a more stable, or possibly thinner, oxide surface in comparison to the other samples. In our previous studies on monometallic TMCs, it was observed that higher electrocatalytic activity was correlated to a thinner oxide surface layer.[52] Although we did not identify a key activity descriptor to explain the role of Fe composition in tuning OER activity, we are motivated to better understand the role of surface oxide for regulating electrocatalytic activity.

2.3.3. Electrochemical Transformation of $Fe_xCo_{1-x}C_y$ During Oxygen Evolution Reaction Under Alkaline Conditions. The electrocatalytic stability of one of the best performing FeCo nanocarbides, 15% Fe, was tested and compared against commercial RuO_2 nanoparticles. The $Fe_xCo_{1-x}C_y$ samples were tested using CV repetitive cycling (Figure 2.12a), so that overpotentials could be extracted at 10 mA cm-2 from each voltammogram (Figure 2.12b), in alkaline conditions using a RDE setup. It was evident that although the initial OER activity was greater for commercial RuO_2 than the nanocarbides in the first cycle, the electrocatalytic OER stability of the RuO_2 nanoparticles was greatly affected by harsh OER alkaline conditions upon further cycling (Figure 2.10). Given the rapid loss in activity, after ten cycles the current density no longer achieved the benchmarking current density of 10 mA cm^{-2}. Therefore, the maximum current density observed at 1.8 V was extracted from the CVs to show the loss of performance. The current density decreased by more than half after just ten cycles, and by 92% of the original value after 100 cycles (Figure 2.10).

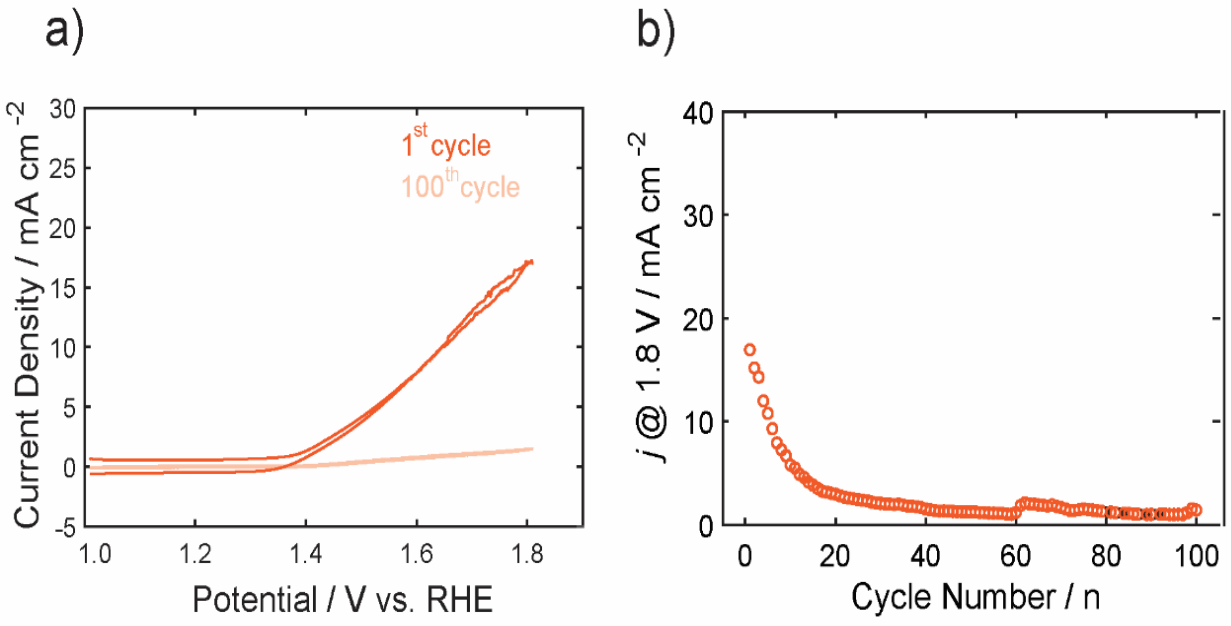

Figure 2.10. a) CVs of the 1st and 100th cycle of RuO_2 at a scan rate of 5 mV s^{-1}, and b) the decay of current density at a maximum potential of 1.8 V vs. RHE over the 100 CV cycles.

In our previous work, we found that the Co carbide resulted in robust electrochemical stability with < 2% increase of overpotential over 100 CV cycles.[52] In contrast, the 15% Fe nanocarbide from this study showed a ~110 mV increase in overpotential (loss of activity) in the first 30 cycles (Figure 2.12). Between 30 and 200 cycles the overpotential remained relatively stable, with <4% change in mV observed (Figure 2.12b). The near overlapping CVs of the 25th and 200th cycles in Figure 5a show that the current densities are relatively similar, suggesting similar electrochemical activity. In addition, we assessed the stability of FeCo nanocarbide (15% Fe) at a scan rate of 50 mV s^{-1} for 2000 CV cycles and found that a rapid increase of ~62 mV occurred in the first 500 cycles and remained stable for the rest of the measurement (Figure 2.11). electrochemical interrogation of FeCo nanocarbide (15% Fe) revealed this sample did not achieve the same magnitude of loss of activity as demonstrated for the lower scan rate, which is corroborated by previous works that observe larger changes in catalyst degradation at low scan rates.[85] While we investigated the source of the increase in overpotential, other factors were

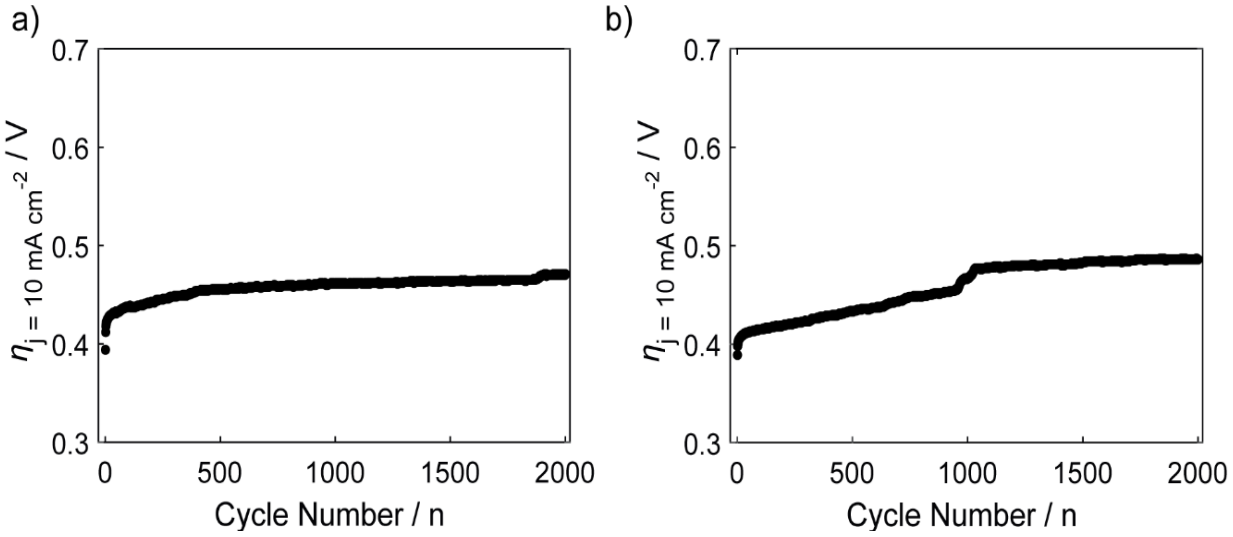

Figure 2.11. Stability measurement of FeCo nanocarbide (15% Fe) with overpotentials extracted from a current density of 10 mA cm^{-2}, collected at a scan rate of 50 mV s^{-1} in 1 M KOH with a) representing the first measurement and b) the second measurement collected.

considered which may decrease apparent electrochemical activity, such as the formation of bubbles that block active sites of the electrode surface, physical detachment of the nanomaterial, and hydrophobic/hydrophilic properties of the nanomaterial and the underlying electrode.[13,86] To avoid some of these deleterious effects, our measurements were monitored by visual inspection every five cycles and large bubbles were removed from the electrode surface when they appeared. Mullins and coworkers showed that their Co_2C transformed into an amorphous CoO, with an enhancement in OER activity after the first two LSV sweeps.[46] To determine whether the rapid increase in overpotential, observed in the first 30 cycles for the 15% Fe, was due to oxide reconstruction or other material transformation changes, the materials described in Figure 2.11

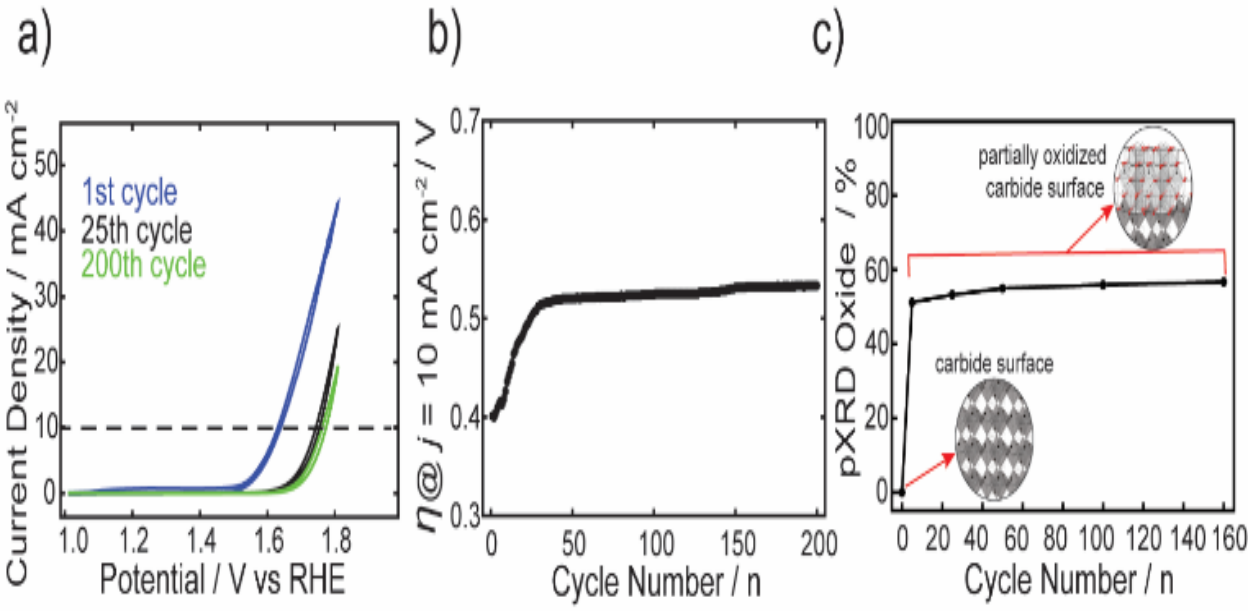

Figure 2.12. a) CVs of the 1st, 25th, and 200th cycles at a scan rate of 5 mV s-1 for the FeCo nanocarbide, containing 15% Fe. b) Overpotentials were extracted from CVs at a current density of 10 mA cm-2 over 200 cycles. c) Plot showing phase contributions from (Fe0.5Co0.5)2O4 (i.e. oxide) derived from XRD analysis of 15% FeCo post-electrocatalytic OER, with increasing CV cycles, using a Mo Kα source. Insets shown in c) depict a carbide surface with an M2C crystalline phase (orthorhombic lattice) and a partially oxidized carbide surface containing (Fe0.5Co0.5)2O4 (cubic lattice), embedded in the surface layer. These lattice structures were generated using CrystalMaker software.

were analyzed using pXRD before and after OER electrochemical conditioning at 0,5,25,50,100, and 160 cycles.

At zero cycles, an oxide layer was not detectable by pXRD, however there is evidence for a partial amorphous oxide layer present using XPS (Figure 2.9). After five cycles, an increase of up to 51% of $(Fe_{0.15}Co_{0.85})_2O_4$ was observed (identified by the Fe_2CoO_4 reference card) and the material analyzed after 5 or more cycles contributed 51-57% $(Fe_{0.15}Co_{0.85})_2O_4$ that remained relatively stable over 5 to 160 cycles (Figure 2.12c). Notably, the rapid formation of spinel oxide correlates with the decline of the OER activity (Figure 2.12c). The monometallic Co carbide was shown to not have a notable increase in crystalline oxide before and after 30 CV cycles and maintained robust electrochemical stability.[52] Therefore, we can infer that the initial electrochemical instability in the first 30 CV cycles we observe in the FeCo nanocarbide (15% Fe) reconstruction of 100% carbide to 57% spinel oxide (43% carbide) coverage in the nanomaterial after 160 CV cycles, we further analyzed how much total oxide contributed to the surface layer of the nanoparticle. To determine the surface layer thickness of the $(Fe_{0.15}\,Co_{0.85})_2O_4$ oxide material layer present in the as-synthesized carbide samples, all oxygen atoms were assumed to be present resulted from rapid surface oxide formation. To enhance our understanding of the rapid surface in the surface layer of the particle. We determined that 85% of the total surface layer was attributed to oxide after 160 cycles, suggesting that a portion of the surface layer is still attributed to carbide and there is not a complete transformation to oxide. PBA-derived FeCo oxides were synthesized (pXRD shown in Figure 2.13) to better understand the performance of FeCo oxide compared to FeCo carbide electrocatalysts. Both the in situ electrochemically oxidized FeCo carbides (post 30 OER cycles) and the PBA-derived FeCo oxides with 15% Fe, resulted in lower electrocatalytic OER activity than the 1st cycle of FeCo carbide. Figure 2.13 shows PBA-derived oxide (15% Fe)

yielded an average overpotential of 0.70 V at 10 mA cm^{-2} (per geometric area), approximately a 300 mV and 170 mV increase in overpotential in comparison to the in situ electrochemically oxidized 15% Fe nanocarbides at the 1st CV cycle (0.41 V) and even the 200th cycle (0.53 V). The 170 mV overpotential difference between the in situ electrochemically oxidized nanocarbides and

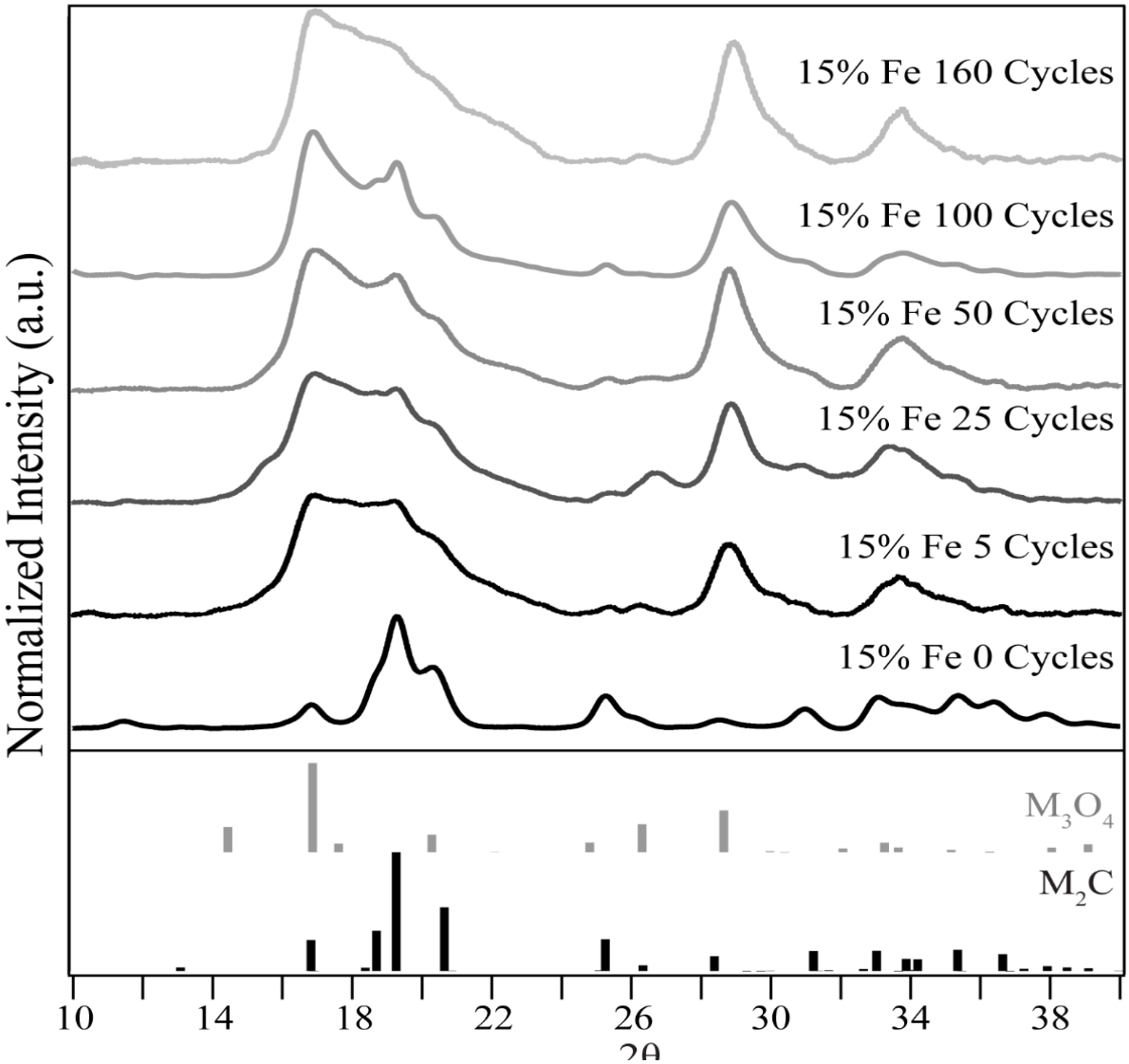

Figure 2.13. Powder X-ray diffraction of the 15% Fe sample, post OER cycling study. pXRD reference cards shown below, in grey M_3O_4 (Fe_2CoO_4 structure) and in black M_2C (Co_2C structure). The intensities of the M_2C peaks, I_{M2C}, are normalized to 1 in each spectrum The percentage of M_3O_4 in the sample was estimated using the relative intensities of the most prominent pXRD peak for M_3O_4 (16.88 2θ) and M_2C (19.26 2θ) using: % $M_3O_4 = (I_{M3O4}/(I_{M3O4} + I_{M2C})) \times 100$

the PBA-derived FeCo oxides could be explained by the difference in the amount of crystalline oxide phase present and possibly the influence of strain on metal surface-oxygen interactions.[87] Similar cobalt oxide nanocatalysts, such as CoO and Co_3O_4, exhibited geometric overpotentials achieved for a current density of 10 mA cm^{-2} of 0.45 V and 0.50 V, respectively,[39] significantly lower than the 0.70 V achieved for our PBA-derived 15% Fe nanocarbide electrocatalyst. Fe oxide nanocatalysts reported in literature exhibited higher overpotentials than the FeCo carbides, such as 1.23 V at 10 mA cm^{-2} for Fe_2O_3,[39] and 0.45 V at 1 mA cm-2 for Fe_3O_4.[88]

In contrast to other monometallic Co carbides in literature,[46] our FeCo carbide electrocatalysts differ in terms of electrocatalytic activity and oxide layer growth. We hypothesize

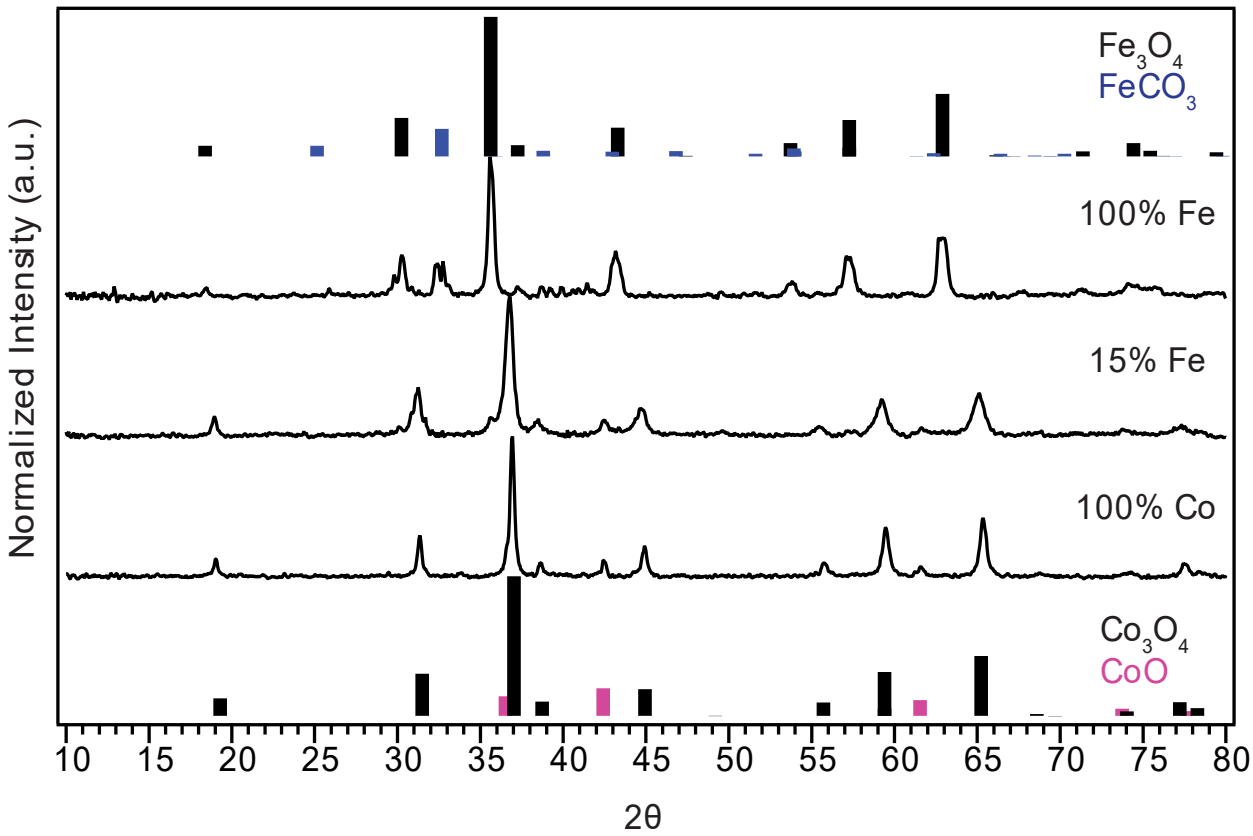

Figure 2.14. Powder XRD patterns of FeCo oxides, for 0% Fe (i.e. 100% Co), 15% Fe and 100% Fe. Pure phase references are shown for comparison for Co_3O_4 (bottom black, reference ICSD 24210), CoO (bottom pink, reference ICSD 174027), Fe_3O_4 (top blue, reference ICSD 75627) and $FeCO_3$ (top black, reference COD 9014728).

that OER activity can be dependent on material descriptors that result from the harsh oxidative environment, which include the active oxide phase,[89] phase crystallinity and disorder, and the amount of Fe_2CoO_4 oxide present in the surface layer. Previous studies of oxide surface reconstruction have ascribed both rapid OER activity increase[46,90] and decrease[91] to the evolution of oxide on the surface during electrocatalytic OER. Oxygen vacancies are another potential phenomenon to occur in reconstructed surface metal oxide catalysts, influencing the local environment and reaction rates of active sites.[92,93] To relate this to our work, a more in-depth analysis of oxygen vacancies on the surface of highly conductive carbon materials with surface oxide reconstruction. Further investigation of stability and oxide surface reconstruction in the carbide family and other non-oxide materials will be fundamental to improving knowledge of designing efficient earth-abundant, non-oxide electrocatalysts for the OER. Further investigation of stability and oxide surface reconstruction in the carbide family and other non-oxide materials will be fundamental to improving knowledge of designing efficient earth-abundant, non-oxide electrocatalysts for the OER.

2.4 Conclusions

In this work, various ratios of Fe:Co in $Fe_xCo_{1-x}C_y$ were controlled through a top-down templated synthetic route, and used to better understand the material composition and structure properties that tune the electrocatalytic activity of bimetallic carbides for the OER. FeCo nanocarbides containing 15 – 20% Fe resulted in an optimal overpotential of 0.42 V (at 10 mA cm^{-2} per ECSA), with a 100 mV enhancement from the monometallic Co_2C. Electrochemical stability and material properties of one of the best performing nanocarbides, $Fe_{0.15}Co_{0.85}C_y$, were monitored for 200 OER cycles using CV, and a series of samples were analyzed ex situ by pXRD. The overpotential achieved increased by ~110 mV within the first 30 cycles, which was attributed

to the growth of an oxide. From this work, it is shown that the $Fe_{0.15}Co_{0.85}C_y$ catalyst's oxygen coordinated surface likely undergoes a reconstruction to $(Fe_{0.15}Co_{0.85})_2O_4$, that represents 85% of the total surface layer after the first 5 OER CV cycles and is subsequently maintained. These results support the notion that OER activity is dependent on metal composition and the amount of surface oxide present. Tuning the elemental composition, i.e. proportion of Fe and Co present in $Fe_{0.15}Co_{0.85}C_y$, led to enhanced activity for the OER. This enhanced performance could have resulted from surface level oxide reconstruction, relative surface oxide stabilities, and the amount of oxide layer (post-OER) changing across the composition range. This study provides new insight on the performance of FeCo-based carbide materials for the OER as well as a new strategy for designing multi-metallic carbides as efficient OER electrocatalysts.

CHAPTER 3

TUNING THE BIMETALLIC AND TRIMETALLIC RATIO IN PRUSSIAN BLUE ANALOGUE (PBA) DERIVED FENI AND CRFENI NANOCARBIDES FOR THE OXYGEN EVOLUTION REACTION (OER)

Reprinted with permission from Ritz, A.J.; Bertini, I.A.; Strouse, G.F.; Lazenby, R.A. Tracking surface oxide formation in FeNi-containing nanocarbides: insights into carbide catalyst degradation in alkaline OER conditions.

3.1 Introduction

The production of hydrogen through alkaline water electrolysis serves as a highly promising avenue for fueling renewable energy production and storage technologies such as alkaline water electrolyzers and fuel cells.[94–96] Yet, the electrocatalytic oxygen evolution reaction (OER) presents a challenge for efficient electrochemical water splitting to occur with its sluggish four-electron transfer process, demanding low overpotentials to surmount the OER kinetic barrier.[67] It becomes imperative, therefore, to engineer cost-effective and highly efficient electrocatalysts for the OER. Notably, Ni-based electrocatalysts operating in alkaline media offer a promising alternative to the expensive benchmark catalysts, IrO_2 and RuO_2.[97–99] In particular, Ni-based oxides, oxy(hydroxides), and layered double hydroxides (LDHs) are well-studied and known to have enhanced OER activity with incorporation of Fe.[50,100] However, Ni-based oxides and oxy(hydroxides) have poor electrical conductivity,[73,101] and LDHs exhibit structural degradation under dynamic water-electrolyzer conditions.[102,103]

Ni-containing phosphides,[59,60,97,104,105] and carbides[51,106–108] are some of the most promising non-oxide-based catalyst alternatives with high electrical conductivity and corrosion resistance. Although carbides and phosphides exhibit similar physical and chemical properties, carbides stand

out due to their abundance of low-cost precursors and high thermal stability suitable for water electrolyzer applications.[51] However, one of the main drawbacks of carbides lies in the limited exploration of complex surface oxide degradation mechanisms of carbides during electrocatalytic OER.[29,71] Raman spectroscopy has been used as a non-destructive, and versatile technique for ex-situ and in-situ/operando characterization of metal oxide (MO) and metal oxyhydroxide (MOOH)-based electrocatalysts.[109–113] A comprehensive understanding of the OER active phase in NiO and $Ni(OH)_2$ catalyst materials under alkaline conditions using Raman spectroscopy is provided in literature, often identifying NiOOH as the electrocatalytically active OER phase. However, using this technique for studying structural oxide transformation and degradation in non-oxide-based catalysts is a relatively underexplored application.

The well-established Bode scheme highlights the transformation of NiO and $Ni(OH)_2$, undergoing oxidation to NiOOH, and the further oxidation of β-NiOOH to γ-NiOOH.[114,115] While long-standing debates have revolved around the question of which phases are more active for OER, the majority of recent studies contend that γ-NiOOH, with its higher oxidation state (>3+), exhibits superior catalytic activity.[116–118] However, recent research has posited that the heightened OER activity is not solely attributable to the formation of NiO to β-NiOOH or γ-NiOOH, but rather to the incorporation of Fe impurities into the NiOOH films.[119,120] While it is well-established that the incorporation of Fe enhances OER activity, recent efforts have been directed towards comprehending less well-known Fe activation and degradation mechanisms in OER catalysts. For instance, Valizadeh and Najafpour suggest that although the transformation of Ni phosphide to Ni (hydr)oxides is observable, the catalyst's activity remains low in the absence of Fe salt.[121] However, the incorporation of Fe salt after repetitive cyclic voltammetry (CV) cycling led to catalyst degradation.[122] Yang et al. suggest that Fe oxide aggregates may contribute to the degradation of

OER active FeNiOOH catalysts, highlighting the complexity of structural and morphological changes during electrochemical transformation of catalysts.[121]

In our prior investigations, bimetallic FeCo carbides[23], revealed that the formation of Fe_2CoO_4 led to catalyst degradation, despite the initial catalytic activity improvement with the incorporation of Fe. In this current study, our focus is on FeNi nanocarbides, aiming to assess the impact of Fe on electrocatalytic activity and explore the effects of Fe on the degradation mechanisms of carbide catalysts using electrochemical and Raman spectroscopy techniques. We introduce $Fe_{0.20}Ni_{0.70}Cr_{0.10}C$, a meticulously engineered carbide catalyst with synergistic effects of Fe and Ni to enhance electrocatalytic activity, and the inclusion of Cr to tailor the surface oxide composition for improved electrocatalytic stability in alkaline oxygen evolution reactions. Select $(Fe_xNi_{1-x})_yC_z$ nanomaterials with varying Fe content and the optimized $Fe_{0.20}Ni_{0.70}Cr_{0.10}C$ sample are evaluated in harsh alkaline conditions with a particular emphasis on studying the effects of the formation (or lack of) Fe oxide for OER activity and stability.

3.2 Experimental Methods

3.2.1. General Synthesis of Ratio Controlled Bimetallic FeNi and Trimetallic CrFeNi PBAs.

The synthesis used in this work for FeNi nanocarbides is similar to our previously described synthesis for FeCo nanocarbides, except that Ni-containing precursor solutions were used instead of Co-containing precursors, and modifications were made to the molar ratios and reaction times used.[94] Two precursor solutions were prepared and coprecipitated at room temperature, as described in our previous work. To control the metal ratio, x mmol $K_3Fe(CN)_6$ and 1 - x mmol $K_2Ni(CN)_4$ (Sigma Aldrich, >99%) (where x = 0, 0.1, 0.3, 0.5, 0.7, 0.9, 1), and 5 mmol of KCl (Sigma Aldrich, 98%) in 100 mL of ultrapure water, comprised solution 1. 1 mmol of either

$FeCl_2$ (Thermo Fisher, >99%) (to make PBAs of > 50% Fe) or $NiCl_2$ (J.T Baker, >97%) (to make PBAs of < 50% Fe) were combined in 200 mL of ultrapure water to form solution 2. Solution 2 was then added dropwise to solution 1 and stirred at a rate of 5 mL min^{-1} for 18 h, leading to the formation of the precursor PBA materials. For the synthesis of $Fe_{0.2}Ni_{0.7}Cr_{0.1}C$, 0.2 mmol $K_3Fe(CN)_6$, 0.7 mmol $K_2Ni(CN)_4$ and 0.1 mmol $K_3Cr(CN)_6$, and (i.e. 1 mmol total) and 5 mmol of KCl in 100 mL of ultrapure water, comprised solution 1. Equal parts $FeCl_2$, $NiCl_2$ and $CrCl_2$ were combined in 200 mL of ultrapure water to form solution 2. The aged PBAs were collected via centrifugation, purified with 300 mL of ultrapure water, and dried on the benchtop at room temperature. Subsequently, they were characterized using pXRD, XRF and SEM.

3.2.2. Thermal Decomposition of PBAs into Nanocarbides. 200 mg of solid PBA and 40 mL of octadecylamine (ODA) (Thermo Fisher, 90%) were heated to 330 °C under an inert atmosphere for 1 h and the resulting nanocarbides were collected through magnetic separation. The nanocarbides were purified with toluene (VWR, ACS Grade) (3×), acetone (VWR, ACS Grade) (1×), ultrapure water (18.2 Ω cm^{-1} at 25.0 °C, Thermo Fisher Barnstead E-Pure Ultrapure filtration system) (3×), and again with acetone (1×), then dried in an oven at 100 °C for 15 minutes.

3.2.3. Materials Characterization. PXRD patterns of PBAs, PBA derived carbides and oxides were collected at room temperature on a Rigaku Miniflex powder diffractometer (Cu K_α source, λ = 1.54 Å). The elemental compositions for both PBA and nanocarbide were confirmed using XRF on a Panalytical Epsilon X-ray florescence analyzer (Cu K_α source). X-ray photoelectron spectroscopy (XPS) was performed on as-synthesized FeNi carbide powders deposited on carbon tape using a PHI 5100 X-ray photoelectron spectrometer (Mg K_α source) with a pass energy of 22.36 eV. The XPS spectra were fitted using CasaXPS software. Samples were Ar^+-sputtered using a sputtering gun at 5 keV and 1 μA for 10 minutes to reveal underlying carbide

features. All samples were calibrated to the aliphatic carbon assignment (C1s, 284.8 eV). Size, size dispersity, and morphology of PBA precursors were investigated using ImageJ software (sample size = 300 particles) via SEM images (FEI Nova 400). Size, size dispersity, and morphology of the nanocarbides were estimated using ImageJ software (sample size = 100 particles) via TEM images, collected on a Tecnai Osiris TEM operating at 200 kV.

3.2.4. Preparation of Electrode Surfaces. Catalyst ink solutions were prepared using catalyst powder (varied between 1 and 5 mg depending on the desired mass loading) in a solution containing 6% (54 μL) of Nafion (5 wt. % solution in alcohol/water system, Aldrich), 84% (744 μL) ethanol, and 10% (92 μL) deionized water. This mixture was then sonicated for 3 – 5 min, until a homogeneous black solution formed. The catalyst ink solution (10 μL) was drop casted onto the glassy carbon (GC) electrode surface and dried in air at room temperature for 1 h. For all activity measurements, a mass loading of 0.1 mg cm^{-2} was used. Electrochemical stability measurements performed in Fig. 3.5 and Fig.3.6 implemented a mass loading of 0.3 mg cm^{-2}, with the addition of carbon black carbon (1 mg mL^{-1} in the catalyst ink, Alfa Aesar). This adjustment aimed not only to optimize electrochemical activity but also to enhance mechanical stability, ensuring the nanoparticles adhere effectively to the electrode surface for long-term measurements.

3.2.5. Electrochemical Methods. All OER activity and stability measurements were evaluated in 1.0 M KOH with a 5 mm diameter GC rotating disk electrode (RDE) with a rotation rate of 1500 rpm, connected to a potentiostat (model CH 660E, CH instruments). A graphite rod served as the counter electrode and all potentials were recorded vs. a Ag/AgCl reference electrode (filled with and stored in 1.0 M KCl) and routinely checked against a master reference electrode to ensure electrode stability and a potential difference of no more than 2.5 mV. Linear sweep voltammograms (LSVs) were recorded at a scan rate of 5 mV s^{-1} to evaluate activity, while cyclic

voltammograms (CVs) for stability measurements were conducted at a scan rate of 10 mV s^{-1}. Electrochemical surface area (ECSA) was determined by estimating the double-layer capacitance, with the assumption that the specific capacitance remains constant irrespective of material composition. These capacitance values were determined through cyclic voltammetry (CV) measurements performed within an optimized potential window in the non-faradaic region of the CV, employing scan rates of 0.01, 0.02, 0.05, and 0.1 V. Electrochemical impedance spectroscopy (EIS) was conducted in the frequency range of 10^{-1} to 10^{5} Hz at a potential of 1.6 V vs. RHE, using a 5-mV amplitude perturbation. To assess the turnover frequency (TOF) of these catalysts, all Fe and Ni catalytic sites were assumed to be equally active.

3.3 Results and Discussion

3.3.1. Physical Materials Characterization. Here, we have synthesized a library of PBA sourced FeNi nanocarbides ($Fe_xNi_{1-x})_yC_z$), ranging from 0% Fe (i.e. $x = 0$) to 100% Fe (i.e. $x = 1$), to investigate the effect of the ratio of Fe and Ni on electrocatalytic activity for the OER. Throughout this study, the molar ratios of the metal(s) will be represented as the theoretical molar ratios, rather than the actual molar ratio values obtained through XRF analysis. We confirmed that the molar metal composition remains well-controlled, as evidenced by XRF characterization (refer to XRF data in Table 3.1). The pXRD for selected $(Fe_xNi_{1-x})_yC_z$ nanomaterials with varying percentages of Fe are illustrated in Fig. 3.1. Across the range of $(Fe_xNi_{1-x})_yC_z$ nanomaterials studied, three major crystal phases were identified: Ni_3C, Fe_3C, and Fe_7C_3, with a clear evolution from the Ni_3C to Fe_7C_3 as the amount of Fe in the material is increased. While not all data are included in Fig. 3.1, it is observed that the Ni_3C phase appears in isolation from 0 – 25% Fe, and at 35% Fe the Fe_3C phase starts to appear until it becomes the dominant phase at 75% Fe, and the final Fe_7C_3 phase is only observed in the 100% Fe sample. Small impurities (< 1% of total material)

of PBA precursor in the 25% and 45% Fe samples were observed. A secondary phase of NiO (depicted with +) was observed in the $Fe_{0.65}Ni_{0.35}C$ sample. This is worth noting as the presence of crystalline oxide within the carbide sample has been shown to degrade catalytic activity in our previous work.[23]

Table 3. 1. XRF elemental analysis verifying the metal composition in PBA precursor and resultant nanocarbide

Target amount of Fe	Actual amount of Fe	Actual amount of Ni
0	0.16	99.8
1	0.37	99.6
2.5	2.38	97.6
5	5.80	94.2
15	14.8	85.2
25	27.1	73.0
35	33.6	66.4
45	49.0	51.1
55	57.1	43.0
65	64.1	35.9
75	82.8	17.2
85	89.6	10.4
100	99.97	0.03

STEM images were used to determine size, shape, and lattice fringe assignments of select $(Fe_xNi_{1-x})_yC_z$ nanomaterials as shown in Fig. 3.2. The nanoparticle sizes (n = 100) were evaluated, with the histograms available in the Supporting Information (Fig. S6). As depicted in Figure 3.2, monometallic Ni carbide (i.e. 0% Fe) particles exhibited an average diameter of 77 ± 36 nm, while $Fe_{0.01}Ni_{0.99}C$ showcased an average diameter of 55 ± 18 nm. The $Fe_{0.25}Ni_{0.75}C$ nanoparticles demonstrated the largest particles, with an average diameter of 77 +/- 22 nm, whereas $Fe_{0.65}Ni_{0.35}C$ displayed the smallest average diameter at 26 ± 14 nm. We found that there were no obvious relationship between Fe content and particle size. In Figure 3.2b, a distinct amorphous surface

oxide layer (thickness < 10 nm) was apparent for the $Fe_{0.01}Ni_{0.99}C$ and $Fe_{0.25}Ni_{0.75}C$. Interestingly, a similar amorphous oxide layer was not apparent in $Fe_{0.65}Ni_{0.35}C$ despite the presence of

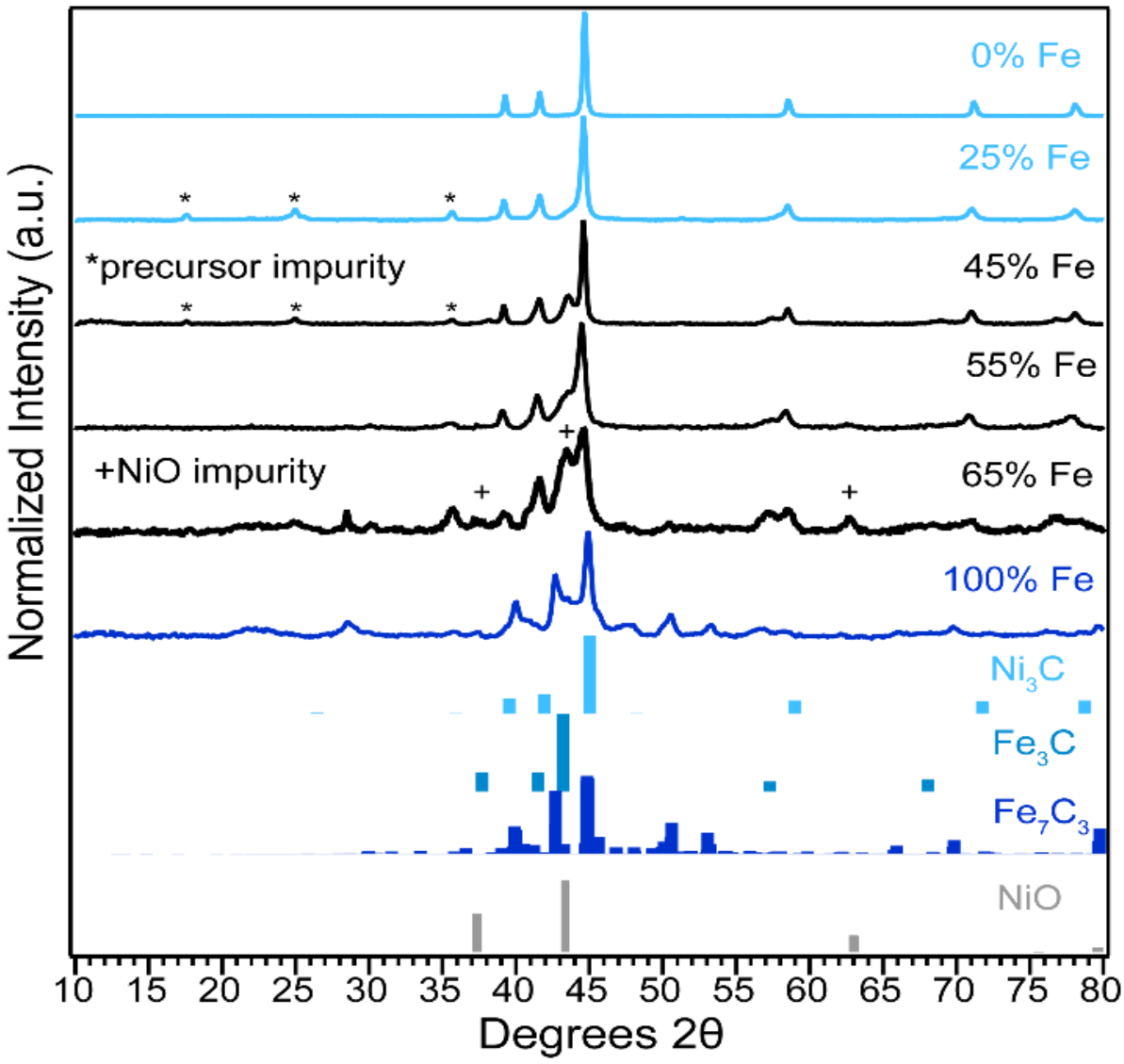

Figure 3.1. Powder X-ray diffraction (pRXD) patterns for select FeNi carbides are shown with varying Fe content from 0 – 100%. The spectra colored light blue were assigned to Ni_3C, while the spectra in black were assigned to a mixture of the Ni_3C and Fe_3C phases, and the dark blue spectrum was assigned to Fe_7C_3. Peaks assigned to PBA impurities and a secondary phase of NiO were observed in select samples, marked with an asterisk (*) or a plus sign (+), respectively. Pure reference phases of the carbide and oxide crystalline phases are shown for comparison, for Ni_3C (COD: 17005), Fe_3C (ICSD: 42542), Fe_7C_3 (ICSD: 76830) and NiO (ICSD:76669).

crystalline NiO shown via pXRD in Fig. 3.1. STEM lattice fringe analysis was also performed on select $(Fe_xNi_{1-x})_yC_z$ nanomaterials to assign Miller indices and d-spacing (Fig. 3.2b).

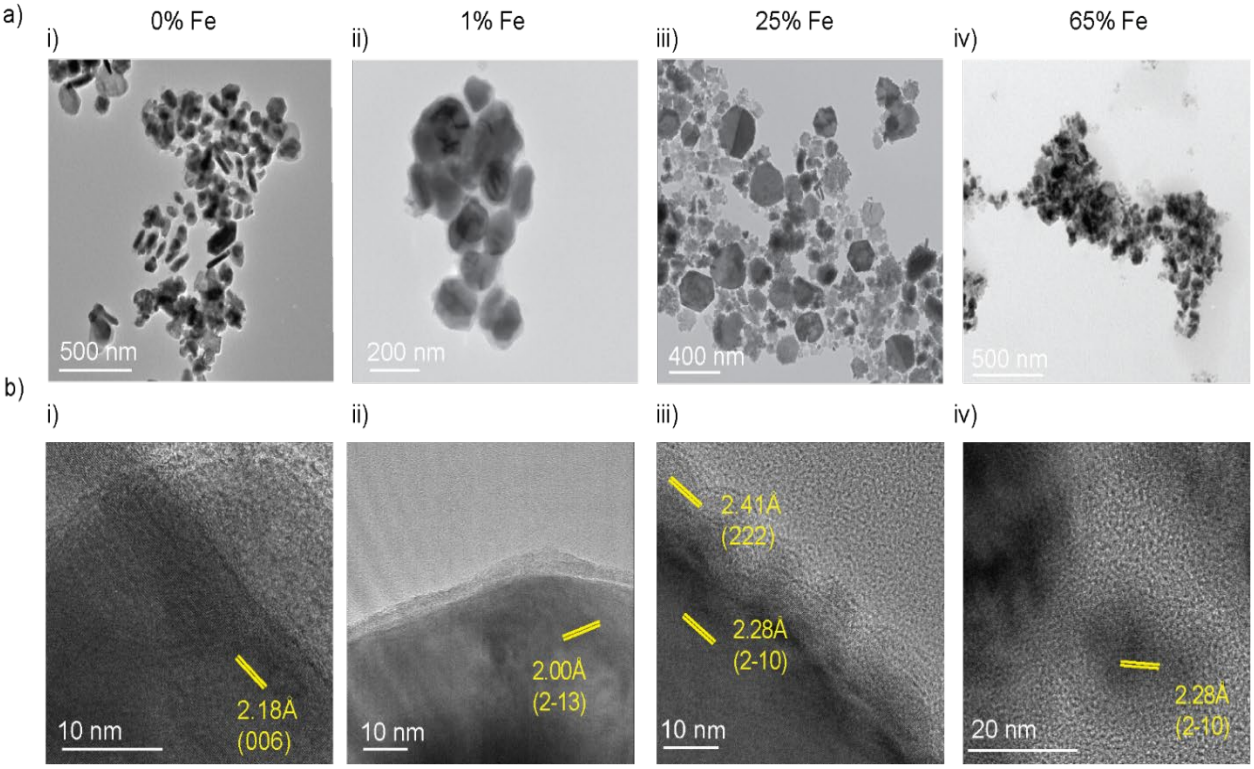

Figure 3.2. STEM images of select FeNi nanocarbides showing a) zoomed-out views of the particles, and b) higher magnification images in which lattice fringes were observed (yellow lines) which were used to obtain d-spacings and assign Miller indices, for i) 0% Fe, ii) 1% Fe, iii) 25% Fe, and iv) 65% Fe.

The lattice fringes were indexed to the (006) lattice plane with a d-spacing of 2.18 Å in the 100% Ni (0% Fe) sample. The $Fe_{0.01}Ni_{0.99}C$ sample lattice fringes matched the (2-13) lattice plane with a d-spacing of 2.00 Å. The $Fe_{0.25}Ni_{0.75}C$ and $Fe_{0.65}Ni_{0.35}C$ samples both matched the 2.28 Å (2-10) lattice plane. Therefore, all lattice fringe assignments are indexable to Ni_3C. Despite much of the outer-shell amorphous layer being non-indexable in the $(Fe_xNi_{1-x})_yC_z$ nanomaterials, we found exceptions where crystalline oxide was identified. In the outermost region of what appears to be a mostly amorphous oxide shell, the $Fe_{0.25}Ni_{0.75}C$ sample showcased a (222) lattice plane with a d-spacing of 2.41 Å, which is attributed to $NiFe_2O_4$ (Fig. 1b (iii)). The $Fe_{0.65}Ni_{0.35}C$

sample in a separate STEM image, also exhibited a (222) lattice with a d-spacing of 2.45 Å, which is attributed to $NiFe_2O_4$ (Table S-2), this is worth noting as this sample also exhibited trace crystalline NiO in pXRD (Fig. 3.1).

3.3.2. OER Performance of FeNiC. $(Fe_xNi_{1-x})_yC_z$ nanomaterials derived from PBAs are highly promising candidates for the OER, due to their high activity and promising electrochemical reaction kinetics. The alkaline OER properties of bimetallic FeNi nanocarbides with varying % Fe content towards OER are depicted in Fig. 3.3 and compared against monometallic FeC and NiC. One of the most useful ways to quantify OER electrocatalytic activity is the overpotential required to achieve a certain current density, and all the $(Fe_xNi_{1-x})_yC_z$ nanomaterials investigated in this work were compared at an ECSA-normalized activity from overpotentials extracted from the benchmarking standard current density of 10 mA cm^{-2} utilizing linear sweep voltammograms (LSVs) in alkaline OER conditions. The LSVs shown in Fig. 3.3a demonstrate that monometallic FeC did not achieve a current density of 10 mA cm^{-2}, and monometallic NiC had a delayed OER onset potential compared to samples with incorporated Fe. Nevertheless, it is important to highlight some unexpected differences in voltammetry for samples with incorporated Fe. While the $Fe_{0.25}Ni_{0.75}C$ sample exhibited an optimal rate of increased current density compared to other voltammograms presented, surpassing 80 mA cm^{-2} at 1.9 V, the onset of OER is comparable to that of the $Fe_{0.01}Ni_{0.99}C$ sample, despite the observed behavior of limiting current density. This limiting current density behavior was also observed in samples containing 5% Fe. Given that the rate of the OER reaction to the electrode surface can be influenced by mass transport,[123] overcoming the diffusion-limited current has been found to be achievable at higher rotation rates and an optimized catalyst mass loading.

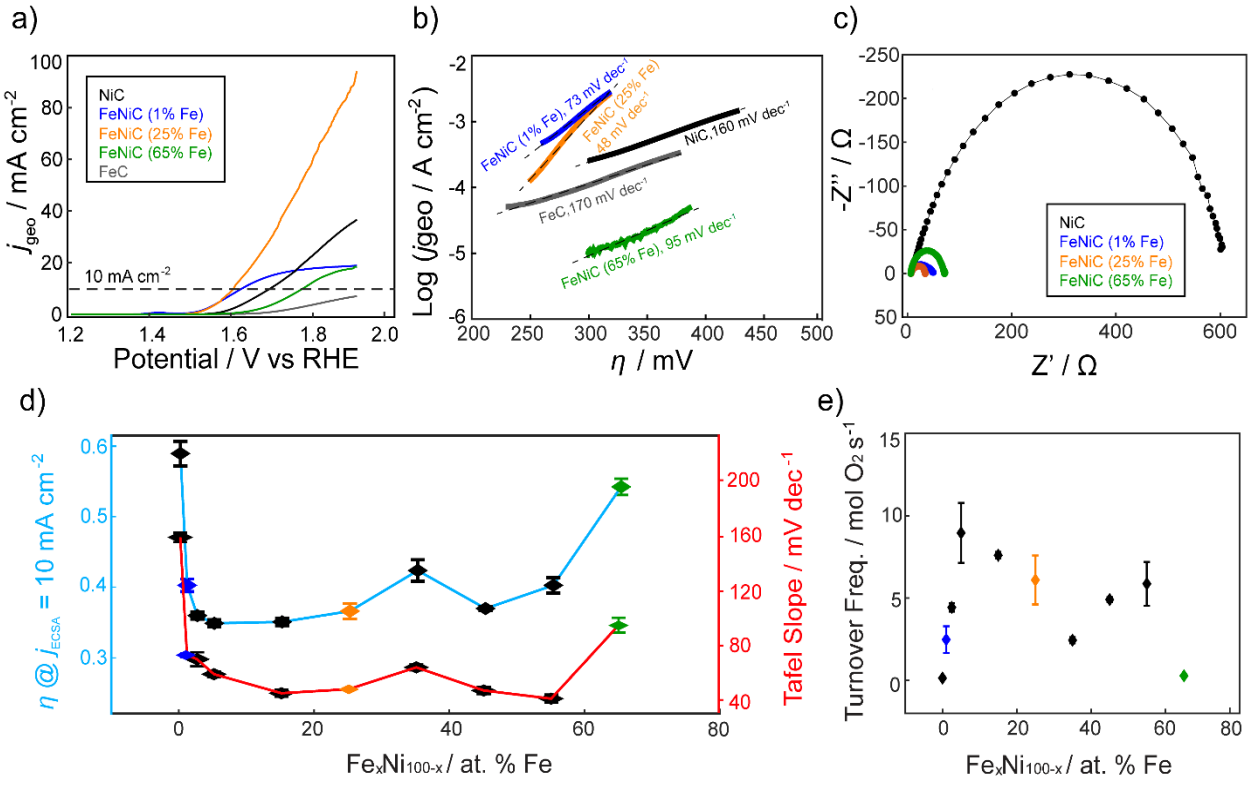

Figure 3.3. OER performance in 1.0 M KOH: a) LSVs of select $(Fe_xNi_{1-x})_yC_z$ nanomaterials with varying % Fe content, and b) the Tafel plots obtained from these LSVs. c) Nyquist plots (10^5 to 10^{-1} Hz) were performed for each sample. d) The overpotentials needed to attain 10 mA cm^{-2} (per ECSA) were acquired for each material (n = 3), denoted along the left y-axis (blue), while Tafel slopes extracted from the linear onset region of the LSVs are represented along the right y-axis (red). e) TOF values extracted at 1.6 V vs. RHE were also collected. All data were collected with a mass loading of 0.1 mg cm^{-2}, and error bars shown reflect the standard deviation of the mean for three measurements.

In order to assess the intrinsic activity of our FeNi nanocarbides as OER electrocatalysts, overpotential values from ECSA-normalized current densities of 10 mA cm^{-2} are depicted in Fig. 3.3d. The plot reveals that the incorporation of a small amount of Fe (1%) leads to an overpotential of 0.40 V, signifying a notable enhancement of 190 mV when compared to NiC (0.59 V). It is worth noting that the actual % Fe amount determined from XRF is closer to 0.3%, indicating that even a very small amount of Fe has a significant impact on OER activity (Table 3.1). It is evident from these results that intentional incorporation of low amounts of Fe results in more desirable

OER catalytic activity, which is also corroborated by literature that identifies the highly critical role of Fe in Ni- and Co-based catalysts.[54,118,121,124–126] Our best performing $(Fe_xNi_{1-x})_yC_z$ nanomaterials achieved a minima overpotential of 0.35 – 0.36 V (mass loading of 0.1 mg cm^{-2}) containing 2.5 – 25% Fe, which is competitive to FeNi oxide-based catalysts such as NiFeO (0.34 V),[100] NiFeOOH (0.32 V),[98] NiFe-LDH (0.32 V),[127] and non-oxide-based catalysts such as Ni_2P (0.35 V)[128] and Fe doped Ni_3S_2 (0.35 V).[129] To further quantify intrinsic activity, Fig. 3.3e showcases TOFs which denotes the O_2 molecules per active site at a potential of 1.6 V vs RHE, strategically chosen for its proximity to the onset OER potential. For the determination of TOF, we operate under the assumption that all catalytically active sites of Fe and Ni are uniformly active. The calculation remains insensitive to the precise surface composition due to the similar atomic volumes of Fe and Ni. The most remarkable TOF values which display high intrinsic activity, extracted at 1.6 V, were observed in the $(Fe_xNi_{1-x})_yC_z$ nanomaterials containing 5 and 15% Fe. These values were 7.6 and 9.0 O_2 s^{-1}, respectively, showcasing a notable improvement when compared to the monometallic NiC and $Fe_{0.65}Ni_{0.35}C$ samples, which exhibited TOF values of approximately 0.1 and 0.3 O_2 s^{-1}, respectively.

The Tafel plots in Figure 3.3b were obtained in the linear region close to the OER onset of the LSV curves where the reaction is solely charge-transfer controlled, as shown in Figure 3.3a. The Tafel slopes can be used to assess electrochemical kinetics, and we observed that the largest slope of 160 mV dec^{-1} for NiC, was reduced to 73 mV dec^{-1} for the sample containing 1% Fe (i.e. $Fe_{0.01}Ni_{0.99}C$). This large decrease in Tafel slope indicates a much faster electron transfer kinetics, and a more rapid rate of OER and the trends in Tafel slope closely correlated to OER activity trends. The lowest Tafel slopes achieved were for 25 % Fe (45 mV dec^{-1}) and 55% Fe (41 mV dec^{-1}), which correlates to a rapid, three electron transfer rate-determining step for OER in alkaline

conditions shown in Fig. 3.3d.[70] Remarkably, $Fe_{0.65}Ni_{0.35}C$ displayed a significantly lower Tafel slope, indicative of a two-electron transfer rate-determining step, contrasting with the one-electron transfer rate-determining step observed in NiC.[63] This suggests that while excess Fe may detrimentally impact OER activity, it can still influence catalyst kinetics.

To delve deeper into the dynamics of electrochemical reaction kinetics, EIS was conducted at a potential of 1.6 V vs. RHE. In Fig. 3.3c, the Nyquist plots of the catalysts are depicted. The semicircle diameter predominantly reflects the charge transfer resistance (R_{ct}) with a smaller diameter indicating more favorable kinetics for the OER. Compared to NiC, carbides containing even trace amounts of Fe (as low as 1% Fe) exhibited considerably smaller semicircle diameters, indicating accelerated charge-transfer kinetics upon the incorporation of Fe into the carbide catalyst. In line with the Tafel analysis, $Fe_{0.25}Ni_{0.75}C$ demonstrates the smallest semicircle diameter, suggesting the lowest R_{ct} when compared with monometallic NiC and nanocarbides containing 1% and 65% Fe. It's noteworthy that even $Fe_{0.65}Ni_{0.35}C$, which displayed lower catalytic activity than NiC, exhibited both a lower R_{ct} and Tafel slope when compared to NiC. This phenomenon could be ascribed to the presence of Fe.

3.3.3. OER Performance in FeNiCrC. Our previous section illustrates that catalytic degradation can result from rapid surface oxidation changes. A recent strategy to enhance performance in the catalysis field is to introduce Cr to Fe and Ni-based catalysts.[110,130,131] It is widely recognized that chromium plays a pivotal role in the corrosion resistance of stainless steel, reacting with oxygen to create a protective, passivating Cr_2O_3 film on the steel surface. Inspired by this principle, we integrated a comparable strategy into the design of our catalyst, aiming to withstand demanding oxidizing conditions. It is noteworthy that many commercially available

stainless steels typically contain approximately 10-20% chromium, and this was considered for the design of our trimetallic $Fe_{0.20}Ni_{0.70}Cr_{0.10}C$ electrocatalyst. pXRD characterization is shown in Fig. 3.4. The FeNiCrC matches the same Ni_3C phase as the majority of FeNi samples.

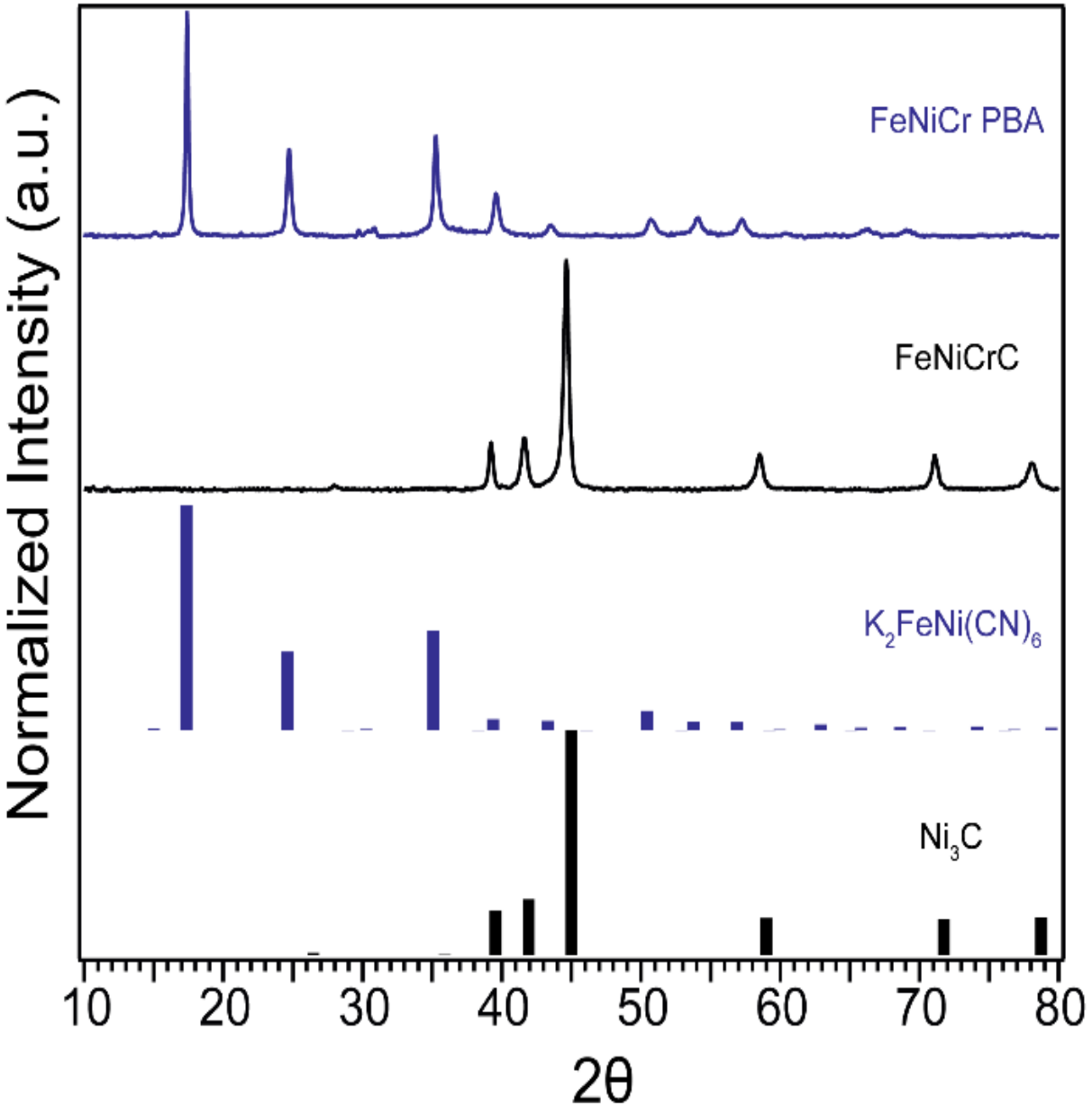

Figure 3.4. pXRD patterns of $Fe_{0.23}Ni_{0.70}Cr_{0.07}$ PBA precursor and $Fe_{0.23}Ni_{0.70}Cr_{0.07}$**C.** These materials are labeled by the actual metal composition obtained from XRF, rather than the theoretical ratios presented in the manuscript. Blue patterns reflect the $K_2FeNi(CN)_6$ and black patterns reflect the Ni_3C rhombohedral crystal structure (COD: 17005).

The long-term electrochemical stability assessment of $Fe_{0.20}Ni_{0.70}Cr_{0.10}C$ revealed a highly stable electrocatalyst for 1000 OER CV cycles in 1.0 M KOH with minimal change in overpotential, shown in Fig. 3.5a. The ex-situ Raman spectra before and after 10 OER CV cycles are shown for the $Fe_{0.20}Ni_{0.70}Cr_{0.10}C$ sample in Fig. 3.5b, with distinct peaks at 475, 561, and 668 cm^{-1}. The peak occurring at 561 cm^{-1} can be attributed to Cr-O bending modes, indicating that the chromium oxide layer formed.[132] The peak at 668 cm^{-1} can be ascribed to the $A1_g$ phonon mode of spinel Fe_3O_4,[110,133] and 475 cm^{-1} likely is attributed to vibrations for Ni-O.[128] These findings suggest that, despite the formation of surface metal oxides such as Fe_3O_4 and NiO, the catalyst's degradation was effectively mitigated in the presence of the chromium oxide layer. This points to the chromium oxide layer's ability to create a robust oxide surface layer, acting as a barrier that prevents O_2 from reacting with Fe and thereby averting further catalyst degradation.[134,135]

To further evaluate the activity of the $Fe_{0.20}Ni_{0.70}Cr_{0.10}C$ sample, a subset of our most promising $(Fe_xNi_{1-x})_yC_z$ nanomaterials and commercial oxide standards were prepared at an optimized mass loading of 0.3 mg cm^{-2} for comparison of overpotentials extracted at 10 mA cm^{-2}, as depicted in the bar graph in Fig. 3.5c. We found that the $Fe_{0.20}Ni_{0.70}Cr_{0.10}C$ sample achieved a competitive overpotential of 0.34 ± 0.01 V, and was comparable to the activity of $Fe_{0.25}Ni_{0.75}C$ (0.32 ± 0.01 V), however the sample containing Cr maintained robust stability in comparison. The overpotential achieved for our $Fe_{0.20}Ni_{0.70}Cr_{0.10}C$ sample (0.34 ± 0.003 V) is comparable against similar Cr containing OER catalyst materials in literature such as surface oxidized AISI 304 steel (0.25-0.34 V, extracted at 1.5 mA cm^{-2}),[130] and NiFeCr oxyhydroxide (0.30 V, 10 mA cm^{-2}).[110] Although LDH materials such as NiFeCr LDH (0.26 V, 10 mA cm^{-2}) tend to have more impressive overpotentials, LDHs in general are known to often suffer from structural degradation[102,103] In comparison to the surface oxidized AISI 304 steel overpotential (0.25-0.34 V) extracted at 1.5 mA

cm^{-2},[126] the $Fe_{0.20}Ni_{0.70}Cr_{0.10}C$ achieves a competitive overpotential value of 0.27 ± 0.003 V at the same current density.

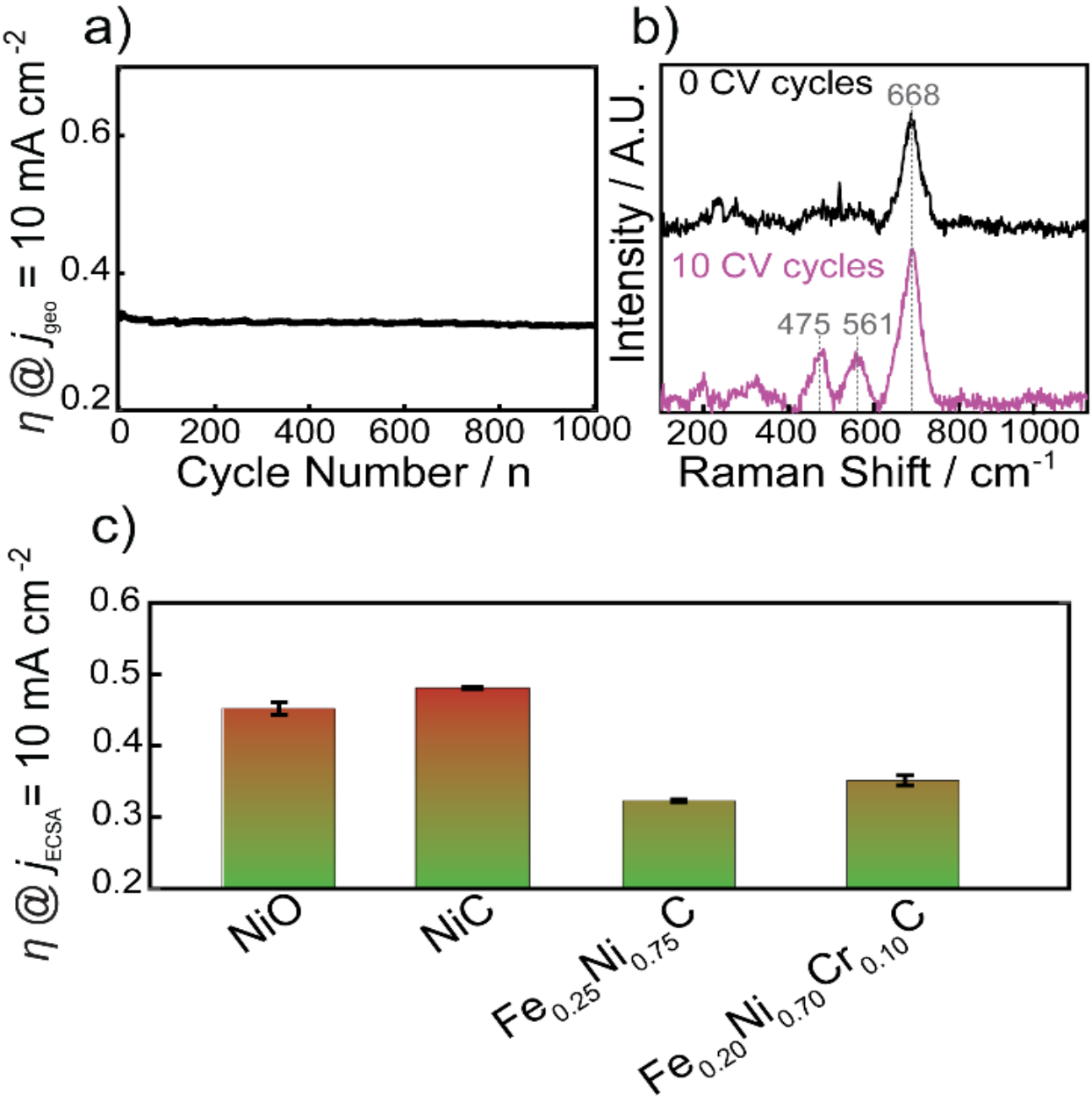

Figure 3.5. OER performance of $Fe_{0.20}Ni_{0.70}Cr_{0.10}C$ in 1.0 M KOH: a) Long-term electrochemical stability measurement of $Fe_{0.20}Ni_{0.70}Cr_{0.10}C$ in 1.0 M KOH for 1000 OER CV cycles, b) Raman spectra collected before (black) and after (magenta) 10 OER CV cycles, and c) bar graph of overpotentials extracted at 10 mA cm^{-2} of NiO, NiC, and $Fe_{0.25}Ni_{0.75}C$ compared to $Fe_{0.20}Ni_{0.70}Cr_{0.10}C$ at a mass loading of 0.3 mg cm^{-2} (n = 3).

3.3.4. Navigating Electrochemical Surface Oxide Reconstruction of Carbides with Fe Incorporation. While our earlier findings underscored the substantial influence of Fe integration during synthesis on tuning electrocatalytic activity and kinetics, it's crucial to emphasize the nuanced effects of Fe's capacity to enhance the initial OER activity, and influence how $(Fe_xNi_{1-x})_yC_z$ nanomaterials perform over time. The short-term electrochemical stability of selected $(Fe_xNi_{1-x})_yC_z$ nanomaterials was for 30 OER CV cycles in 1.0 M KOH (~ 1 h), measuring overpotential at a current density of 5 mA cm^{-2} in Fig. 3.6. The current density of 5 mA cm^{-2} was chosen due to certain samples that did not achieve 10 mA cm^{-2} after catalytic degradation. These select samples of varying % Fe content were of interest due to their differences in electrocatalytic activity and material composition. Significantly, in Fig. 3.6a, both the $Fe_{0.01}Ni_{0.99}C$ and $Fe_{0.25}Ni_{0.75}C$ samples exhibited notable activity loss, with an incremental rise in overpotential observed across the initial 28 OER CV cycles. Subsequently at the 29th CV cycle, a more pronounced rise in overpotential was observed for $Fe_{0.01}Ni_{0.99}C$, coinciding with rapid changes in voltammetric behavior for the 29th and 30th CV cycle without the presence of bubbles blocking the electrode surface. The impact of % Fe content on electrocatalytic OER stability is further elucidated in Fig. 3.6b, highlighting that $Fe_{0.01}Ni_{0.99}C$ and $Fe_{0.25}Ni_{0.75}C$ samples experienced an overpotential increase of approximately 200 mV and 100 mV, respectively. The robust stability of NiC aligns with our previous investigation,[109] while the introduction of Fe appears to instigate initial degradation in the OER catalyst, consistent with our findings on FeCo carbides.[23] Surprisingly, the stability of the $Fe_{0.65}Ni_{0.35}C$ sample defied expectations, as we anticipated Fe's contribution to further catalyst degradation based on the behavior observed in other Fe-containing samples. To delve deeper into this observed variance in catalyst degradation across samples with

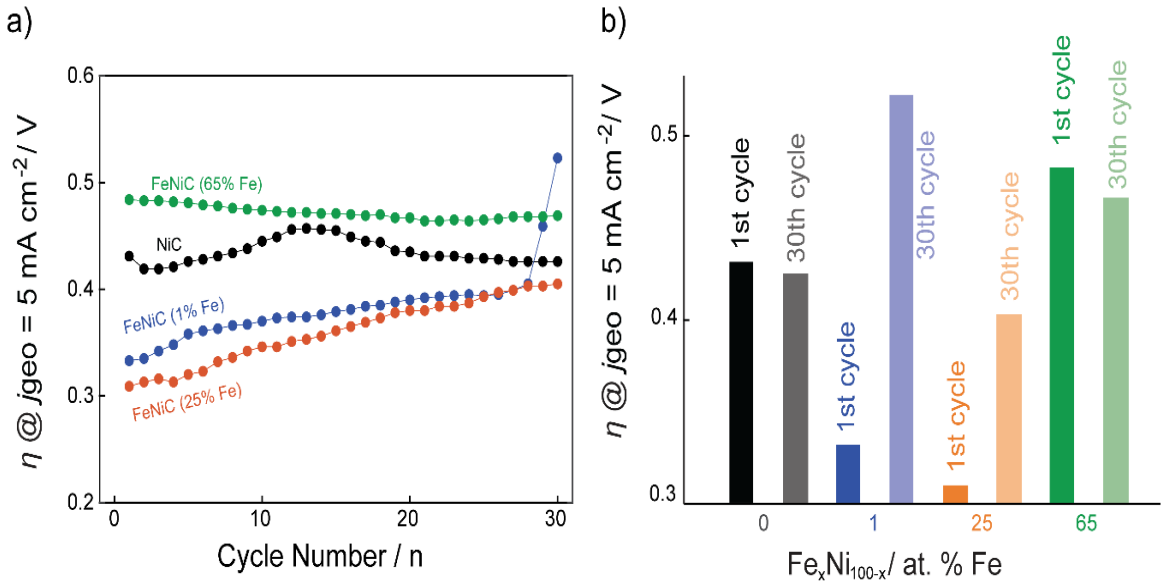

Figure 3.6. Short-term electrocatalytic OER stability of select $(Fe_xNi_{1-x})_yC_z$ nanomaterials with varying % Fe content with a) overpotentials extracted at a current density of 5 mA cm^{-2} for 30 OER CV cycles, and b) a bar chart representing the change in overpotential between the 1st and 30th CV cycle in 1.0 M KOH.

varying % Fe content, we conducted an analysis of material surface oxide composition during both chemical and electrochemical oxidation using Raman spectroscopy.

To understand the effects of surface oxide reconstruction in carbide catalysts, Raman spectroscopy was used to elucidate amorphous oxide features that cannot be detected by XRD. Select $(Fe_xNi_{1-x})_yC_z$ nanomaterials were drop casted onto gold-coated silicon wafers, and Raman spectra were collected before and after 24 h of submersion in 1.0 M KOH (Fig. 3.7a). Ex-situ Raman spectra collected before and after 30 OER CV cycles (~ 1 h) shown in Fig. 3.7b provided further insight into the electrochemical stability and surface oxide reconstruction. We note that the sharp, defined peak at 480 cm^{-1} observed in the majority of the Raman spectra is attributed to noise due to high energy cosmic rays. However, as Fe was incorporated into the $(Fe_xNi_{1-x})_yC_z$ samples, there was evidence of oxide formation after 24 h of chemical oxidation and ~1 h of electrochemical oxidation (30 OER CV cycles).

The broad peak feature from ~400 to ~700 cm^{-1} that is present in the spectrum of $Fe_{0.01}Ni_{0.99}C$ after 24 h of chemical and electrochemical oxidation corresponds to the typical bending vibrations for Ni-O at 540 cm^{-1},[136] further evidenced by the NiO reference standard shown. In particular, this broad feature often corresponds to the vibration peak that arises due to oxygen defect sites on the surface of an amorphous NiO particle.[111,137] $Fe_{0.25}Ni_{0.75}C$ was assigned to have oxide peak features that correspond to a mixture of Fe_3O_4 and NiO. $Fe_{0.65}Ni_{0.35}C$ previously revealed evidence of crystalline Ni oxide in the as-synthesized sample according to XRD (Fig. 3.1). Before and after exposure to chemical or electrochemical oxidation, the Raman spectra for $Fe_{0.65}Ni_{0.35}C$ exhibited a peak at 680 cm^{-1}, associated with the $A1_g$ phonon mode of spinel Fe_3O_4 [110,133] and also exhibited peaks from 200-300 cm^{-1} that correspond to Fe_2O_3,[22] indicating a mixed oxide where Fe^{2+} and Fe^{3+} could be present. However, after chemical and electrochemical oxidation, Fe_3O_4 was the prevalent species. Interestingly, $Fe_{0.65}Ni_{0.35}C$ also previously revealed evidence of crystalline Ni oxide in the as-synthesized sample according to XRD (Fig. 3.1), which means that $Fe_{0.65}Ni_{0.35}C$ has a mixture of crystalline Ni oxide and amorphous Fe oxide features.

Although monometallic NiC is one of the worst performing carbide catalysts reported in this work, it appears to be the most stable after electrochemical interrogation for 30 CV cycles and resists oxidation after 24 h in alkaline conditions (Fig. 3.7). Chemical and electrochemical oxidation appear to have the most significant effects on samples containing 1% and 25% Fe, which happen to show the most significant changes in surface oxide transformation (Fig. 3.7). The electrochemical oxidation of $Fe_{0.25}Ni_{0.75}C$ showed rapid changes within about 1 h (30 OER CV cycles), contrasting with the 24 h period observed for chemical oxidation. To discern the influence of chemical and electrochemical oxidation, we tested the $Fe_{0.25}Ni_{0.75}C$ sample at different chemical exposure time points. $Fe_{0.25}Ni_{0.75}C$ formed Fe_3O_4 in about 14 hours under alkaline conditions,

suggesting that the swift changes in electrochemical oxidation were not primarily due to chemical oxidation.

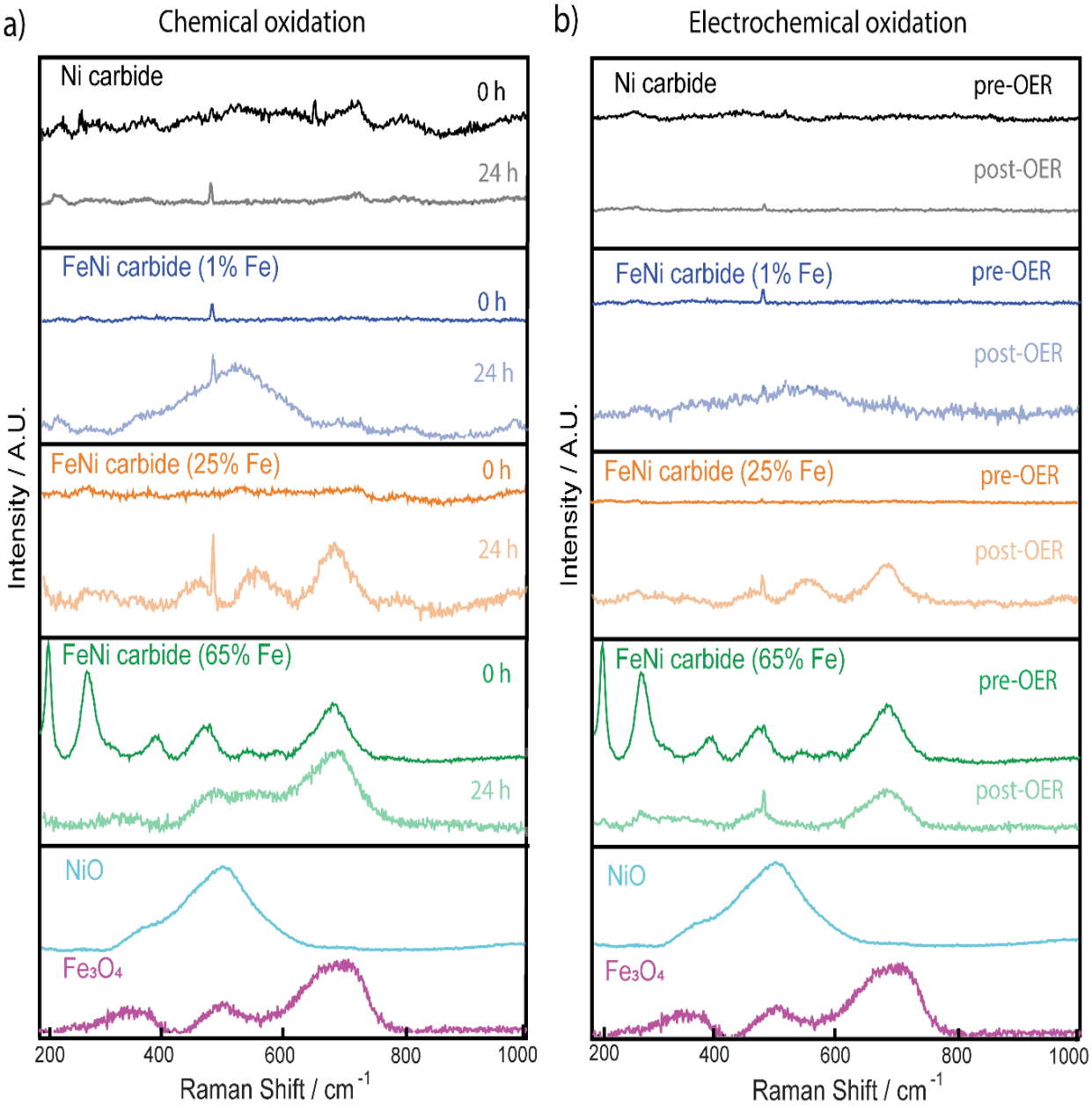

Figure 3.7. a) Raman spectra of select $(Fe_xNi_{1-x})_yC_z$ nanomaterial thin films with 0% Fe (black), 1% Fe (blue), 25% Fe (orange), and 65% Fe (green) on Au electrode surface for thin nanomaterial films before (light color) and thin films after alkaline aging for 24 h in 1.0 M KOH (dark color) and b) before and after 30 OER CV cycles. The samples were compared to Fe_3O_4 (magenta) and NiO (light blue) commercial standards.

This points to electrochemical oxidation mechanisms as the likely cause of the observed rapid changes in Fig. 3.7b, distinguishing them from the slower chemical oxidation process. Notably, $Fe_{0.65}Ni_{0.35}C$ already displayed evidence of Fe_3O_4 before and after chemical and electrochemical oxidation, therefore this likely indicates that the sample remained stable due to the surface oxide already being present in the sample.

Our investigation unveiled a correlation between the observed trends in material composition oxidation changes post-OER in Fig. 5 and the variations in short-term electrochemical stability illustrated in Fig. 3.6. Specifically, both NiC and $Fe_{0.65}Ni_{0.35}C$ demonstrated minimal deterioration in catalytic activity, and Raman spectroscopy indicated that the material composition before and after OER catalysis remained largely unchanged. In contrast, $Fe_{0.01}Ni_{0.99}C$ and $Fe_{0.25}Ni_{0.75}C$ samples exhibited significant deterioration in catalytic activity, with corresponding Raman spectra revealing evolved surface oxides. This result holds particular significance, given the general consensus that non-oxide-based catalysts, such as phosphides and carbides, are typically regarded as pre-catalysts, with the transformation to (oxy)hydroxide in electrochemical conditions deemed the "true" active catalyst.[29,58,71,138] While this generalization may hold merit, our findings highlight the importance of not overlooking the stability of surface oxides formed during OER electrocatalytic activity, while also considering that not all surface oxides are catalytically active for OER. For example, Kawashima et al. observed a significant deterioration in OER activity over time when testing a Ni_3N/Ni foam catalyst ascribed to the formation of a NiO/NiOOH shell.[139] It is also important to note that studies have also found that reduced electronic conductivity resulting from the emergence of the NiO/NiOOH shell, implicating that not all NiO/NiOOH species are OER active.[139,140] Therefore, our key focus in the next section is

to design a highly active FeNi-containing carbide catalyst that forms a degradation resistant and OER active oxide layer.

3.4 Conclusions

In summary, we have investigated the electrocatalytic OER performance of $(Fe_xNi_{1-x})_yC_z$ nanomaterials, and introduced a Cr-containing FeNi nanocarbide with promising long-term electrochemical stability. In particular, we identified the role of Fe for initially enhancing OER activity and kinetics and for contributing to catalyst degradation mechanisms. By investigating the effects of surface oxide reconstruction using Raman spectroscopy, we were able to elucidate that rapid surface oxide changes can cause catalyst degradation under oxidizing conditions, whereas catalysts that are able to resist harsh oxidation conditions remain relatively more stable. In addition, we found that NiC before and after OER interrogation remained electrochemically stable with no detectable oxide features in the Raman spectra, whereas $Fe_{0.01}Ni_{0.99}C$ with a small amount of Fe incorporation resulted in more rapid amorphous surface oxide formation and catalyst degradation. To engineer a catalyst resilient to corrosion and degradation, our study showcased the integration of chromium in the design of a trimetallic $Fe_{0.20}Ni_{0.70}Cr_{0.10}C$ catalyst as a promising strategy. This approach yielded a high-performance electrocatalysts with superior activity and stability towards the oxygen evolution reaction (OER), evidenced by an overpotential of 0.31 V at 10 mA cm^{-2} and a robust stability for 1000 OER CV cycles in the presence of a chromium oxide layer. These findings highlight the importance of tailored surface oxide compositions in catalyst design and pave the way for further exploration of trimetallic catalysts and their synergistic effects on electrocatalytic performance. Overall, this study contributes valuable insights towards the development of efficient and durable bi- and multimetallic carbide catalysts for renewable energy conversion and storage technologies.

CHAPTER 4

MODULATING CRYSTALLINE PHASE IN $FE_XCO_{1-X}C_Y$ VIA HALIDE-MEDIATED SYNTHESIS

Reprinted with permission from Bertini, I.A.; Lamichhane, B.; Bell, S.; Kattel, S.; Strouse, G.F. ACS Chemistry of Materials.

4.1 Abstract

The ability to control the compositional phase in first row transition metal bimetallic carbides, as well as systematically controlling the metal ratio, is complicated by the rich phase diagram, differences in metal reactivity, and differences in carbon solubility in the first-row metal carbides. Prussian Blue Analogues (PBAs) have been shown to act as a single source precursor for formation of nanocrystal metal carbides with maintenance of their metal. An investigation of crystal phase control in the ternary $(Fe_xCo_{1-x})_yC_z$ formed by PBA collapse has yet to be explored. In this study, we demonstrate the ability to tune phase (from most carbon rich to least) M_2C, M_5C_2, M_7C_3, M_3C, as well as the bimetallic alloy (M) in bimetallic FeCo nanocarbides through a strategy that pairs synthetic and DFT approaches to enable future targeted structure-function research on intriguing catalytic, therapeutic, and magnetic applications.

4.2 Introduction

Following from the scientific dogma of "form follows function", to obtain a desired property, the structure of a material dictates its potential uses. First row transition metal carbides possess rich phase diagrams,[141–145] where the structure and carbon content strongly influence the materials properties, reflecting changes in orbital interactions and subsequent band structure. In the catalytic literature, it is known chemical activity is dependent on phase (anatase vs. rutile TiO_2 for instance) or as observed in Fischer-Tropsch catalysis, the Hagg carbide (Fe_5C_2) is more catalytically active than other M_xC_y carbides.[141,144,146–152] Likewise, the presence of synergistic

effects in ternary systems (i.e FeCoP, FeCoO, FeCoC) has suggested ternary or higher entropy materials may be better catalysts if the structural phase of a material is controlled.[23,27,72,90,124,153–156] In ternary systems such as bimetallic carbides, the reaction phase space naturally becomes more complex, therefore the number of possible materials isolable increases.

Whether the goal is to prepare hardened materials, corrosion resistant, or improve catalytic activity, developing synthetic methods to isolate a specific compositional and structural phase from a reaction mixture is crucial.[20,152,157–159] When materials are grown via solid state methods, temperature and stoichiometry are employed to provide phase control; however, when grown as nanomaterials through solvent based methods, chemical control is strongly impacted by the thermodynamic and kinetic steps involved in nucleation and growth. As a result, being able to isolate a specific composition and structure is extremely difficult.[160–163]

A material system that exhibits a rich phase diagram, is known to have properties dependent on structure and composition[164], and is of immense interest in catalysis, as well as metallurgy, is the first row metal carbides.[143,165,166] The performance of the metal carbides is directly dependent on metal composition and crystallographic phase, particularly in the case of binary systems where synergistic effects have been hypothesized.[147,167–171] The bimetallic FeCoC ternary system has been identified as a promising material for catalytic, diagnostic imaging[172], data storage[173,174], and environmental remediation applications.[175] Although Fe and Co carbide materials are considered "ancient advance materials,"[20,158] there's been limited research on the use of synthetic parameters to prepare unique crystal phases.

Instead of focusing on the isolation of several different phases, most studies have investigated properties of mixed-phase or the one pure phase material isolable. Development of synthetic methods that allow careful control of the bimetallic composition in a specific

crystallographic phase is challenging for FeCoC as the phase diagram for FeC possesses a rich phase space. To date, monometallic carbides remain the only carbides whose structures have been thoroughly studied. The most common Fe carbide phases are Fe_3C and Fe_7C_3, while cobalt carbide prefers to crystallize in the Co_3C or Co_2C phase. Many other phases of iron carbides exist (FeC, Fe_2C, Fe_3C, Fe_3C_2, Fe_4C, Fe_5C_2, Fe_6C, Fe_7C_3, Fe_8C, $Fe_{20}C_9$, and $Fe_{23}C_{6)}$ that are said to be metastable phases.[152,176] The ternary Fe-Co-C phase diagram describe only the bimetallic alloy which packs in two crystal structures (FCC and BCC) and once the carbon wt% reaches 4%, the carbon crystallizes separately from the metal as graphitic carbon.[141,177] Despite the reported strategies for synthesizing Fe and Co carbide monometallic materials,[22,173,178,179] it is widely accepted that high temperature colloidal synthesis from chemical precursors provides the most control of nanomaterial phase, crystallinity, and size.[20] The formation of nanometal carbides from solvothermal decomposition of molecular precursors, such as $M(CO)_x$,[180,181] $M(CO_3)_x$,[182] carburization of MO_x,[183] and from Prussian Blue analogue[10,23,52,142] decomposition has been reported in the literature; however, the resultant materials exhibit mixed M_xC_y phase composition.

In monometallic nanocarbides, it has been reported that addition of halide salts lead to isolation of single phase Fe_2C, Fe_5C_2, Fe_7C_3, and Fe_3C and for cobalt Co_3C, and Co_2C, depending on the reaction conditions.[180–183] It is reasonable to assume that halide binding to the monomer or to the growing carbide nano-facet will be unique to each halide species and to the metal. Ma and co-workers[180] investigated synthetic control in the Hagg carbide (Fe_5C_2) using bromide ions, where it was observed that the addition of bromide ion allowed selective isolation of the Fe_5C_2 phase instead of Fe_3C (thermodynamically most stable). The use of chloride ions was reported by Carpenter and co-workers[4] to allow Fe_7C_3 and Fe_3C isolation,[1] while Gao and co-workers used chlorides to isolate Fe_2C, Fe_3C, and Fe_5C_2.[184] Both Ma and Carpenter expanded the use of halides

by demonstrating selective isolation of Co_2C instead of Co_3C.[185] The control of Fe_xC_y phase by addition of halide ions was attributed to bonding of the Fe to the halide through via Bader charge analysis.[184] While the role of halide salts on phase control is widely believed to reflect control of monomer activity, no comparative study of halide species have been performed, nor have bimetallic carbides been investigated, where phase control is more complex. Furthermore, halide mediated synthesis has not yet been translated to the ternary $(Fe_xCo_{1-x})_yC_z$ system.

Herein, we investigate the effect of halides on the isolation of pure phase bimetallic FeCo nanocarbides $(Fe_xCo_{1-x})_yC_z$ through the pairin g of experimental and computation- al strategies to further elucidate the mechanism of systematic synthetic control. The results of the study cleanly delineate regions of phase stability for Fe:Co metal ratios under selective halide concentrations. The impact of changing the halide salt, its concentration, and the metal ratio on conversion to a carbide phase was investigated. DFT calculations performed on the addition of carbon in the presence of the alkylamine at FeCo (110) facet allowed the competitive binding of the halide to the surface to be evaluated. The energetics from DFT provide a model where *C* diffusion in and out of the nano-carbide is controlled by surface stabilization. The observations in the nanocarbide synthesis via a thermal decomposition of a PBAs analogue provides a strategy to control of phase in a broader class of materials known as MX-ides (oxides, sulfides, selenides, phosphides, and nitrides). The ability to isolate bimetallic carbides of discrete -phases and potentially apply the strategy to multimetallic carbides, could provide a means for the catalytic community to test the hypothesis that catalytic performance is dependent on crystal structure and material composition for high-value multimetallic M-Xide families.

4.3. Experimental Methods

All commercially available reagents were used without further purification. Precursors for FeCo PBAs are $K_3Co(CN)_6$ and $K_3Fe(CN)_6$ (Sigma Aldrich, > 99%), KCl (Sigma Aldrich, 98%), $CoCl_2 \cdot 6H_2O$ (Thermo Fisher, > 99%), and $FeCl_2 \cdot 4H_2O$ (Thermo Fischer, > 99%). Solvents used for synthesis were ultrapure water (18.2 Ω/cm, Thermo Fisher Barnstead E-Pure Ultrapure filtration system), octadecylamine (Acros Organics, 90%), Acetone (VWR, ACS Grade), Toluene (VWR, ACS Grade).

4.3.1. General Synthesis of FeCo Prussian Blue Analog (PBA) Precursor. To produce the PBA precursors, two solutions are prepared and combined, creating the coordination polymer through a precipitation reaction. The stoichiometric ratios of the metals are controlled by adjusting the ratio of precursors in these solutions. In solution one, 5 mmol of KCl, x mmol $K_3Fe(CN)_6$ (x = 0, 0.1, 0.5, 0.9, 1), 1-x mmol $K_3Co(CN)_6$ (y = 1, 0.9, 0.5, 0.1, 0), 10 mL of ultrapure water, and a magnetic stir bar are added to a 100 mL round bottom flask. Solution two consists of 1 mmol of either $FeCl_2$ (> 50% Fe) or $CoCl_2$ (< 50% Fe) and 20 mL of ultrapure water are added to a 50 mL beaker. Solution two is then dropwise added to solution one at a rate of 5 mL/min and vigorously stirred. The subsequent reaction solution is left on the stirring for 1 hour to grow the PBA. The PBA are collected via centrifugation, washed with 30 mL of ultrapure water and dried in a furnace at 90°C for approximately 1.5 hrs, or until dry. The PBA precursors are characterized using pXRD, SEM, and XRF.

4.3.2. General Synthesis of Phase − Controlled $(Fe_xCo_{1-x})_yC_z$. In the typical synthesis, 200 mg of solid PBA, 0.1 to 3 mmol of tetrabutylammonium halide (TBAX, where X= F^-, Cl^-, Br^-, I^-), and 20 mL of octadecylamine (ODA) are added to a three-neck round bottom flask equipped with a condenser and heated to 330°C under inert air for 1 hour. The reaction is

subsequently quenched using toluene and the resultant nanocarbide is collected via centrifugation. The nanoparticles are washed with toluene (3x), acetone (1x), ultrapure water (3x), and again acetone (1x). The nanoparticles are dried in an oven at 90°C for 15 minutes. The nanoparticles are characterized using pXRD and XRF.

4.3.3. Materials Characterization. pXRD patterns of PBAs and PBA derived carbides were collected at room temperature on a Rigaku Miniflex powder diffractometer (Cu Kα source, λ = 1.54 Å, Supporting Fig. S3). The contributions of various crystalline phases were fitted and calculated as a percentage for each FexCo1−xCy, using the Halder – Wagner method as shown in Supporting Fig. S4. The elemental ratios in both PBA and nanocarbide were confirmed using XRF on a Panalytical Epsilon XRF analyzer (Cu Kα source, Supporting Fig. S2). Size and morphology of PBA precursors were investigated via SEM imaging (FEI Nova 400, 15 keV, Supporting Fig. S1). Size and morphology of the nanocarbides were estimated using ImageJ software (sample size = 10 particles) via TEM images, collected on a Tecnai Osiris TEM operating at 200 kV (Figure 2).

4.3.4. Computational Methods. We used spin-polarized density functional theory (DFT)[186] calculations within the Vienna *Ab initio* Simulation Package (VASP).[187,188] The generalized gradient approximation (GGA)[189] was used to account for the exchange correlations effect proposed by Perdew-Burke-Ernzerhof (PBE), and electron-ion interactions were described by the projected augmented plane wave (PAW)[190] potentials. Bulk Fe in body-centered cubic (bcc) models the mono-metallic (101) surface, and FeCo in the bcc structure is taken to model the bimetallic (110) surface. Both surfaces consist of 72 atoms in an A-B-A-B stacking pattern; the monometallic surface has 72 Fe atoms, and the bimetallic surface consists of 36 Fe and Co atoms. The Mono-metallic carbides observed in our experiment in hexagonal Fe_3C and orthorhombic

Co_2C are used to model the $Fe_3C(001)$ and $Co_2C(101)$ surfaces, respectively; $Fe_3C(001)$ surface consist of 48 Fe and 16 C atoms, while $Co_2C(101)$ surface consists of 40 Co and 20 C atoms. The bimetallic carbide $(FeCo)_3C(001)$ surface was constructed by replacing three Fe atoms with Co atoms in a hexagonal Fe_3C structure. It can have a Fe and Co-terminated surface; both terminated surfaces have 24 Co, Fe, and 16 C atoms. We used a supercell approach with a 3 × 3-unit cell (metallic and bimetallic surface) and 2×2-unit cell (mono-metallic barbide and bimetallic carbide) having four layers in a slab; the bottom two layers were fixed at the bulk position, and the top two layers were allowed to relax. Periodic interaction between the slab was minimized by a vacuum of 18 Å along the c-axis. We set an energy cut-off of 420 eV for total energy calculations, and a Brillion zone sampling was carried out using a Monkhorst-Pack[190] grid of 3×3×1 for the surface slab. A relaxed geometry was obtained when the force on each atom was less than 0.01 eV/Å and energy convergence of 10^{-5} eV**.**

4.3.5. Electrode Preparation. A catalyst slurry was prepared using 1mg of catalyst powder and 1mL of methanol. The slurry was sonicated until homogenized ~ 1 minute and then the suspension was dropcasted onto the carbon working electrode (5 mm x 4 mm) of a Pine Instruments carbon screen printed electrode (SPE). The mass loading onto the surface of the electrode is approximately 0.1 mg/cm^2. The electrodes were dried at room temperature for about 30 minutes before electrochemical measurements were performed.

4.3.6. Electrochemical Measurements. All electrochemical measurements were performed using a Pine Research 3 electrode screen printed electrode system, connected to a CH 660E potentiostat. The SPEs contain a carbon working and counter electrode as well as a Ag/AgCl reference electrode. For OER measurements, 1M KOH electrolyte was used and for HER, 1M

H_2SO_4 electrolyte was used. All potentials were converted to the reversible hydrogen electrode potential using equation 10.

(Eq. 10) $E_{vs.\ RHE} = E_{vs.\ Ag/AgCl} + 1.009\ V$

The potentials vs RHE were then used to calculate the overpotentials for OER using equation 11.

(Eq. 11) $\eta = E_{vs.\ RHE} - 1.23\ V$

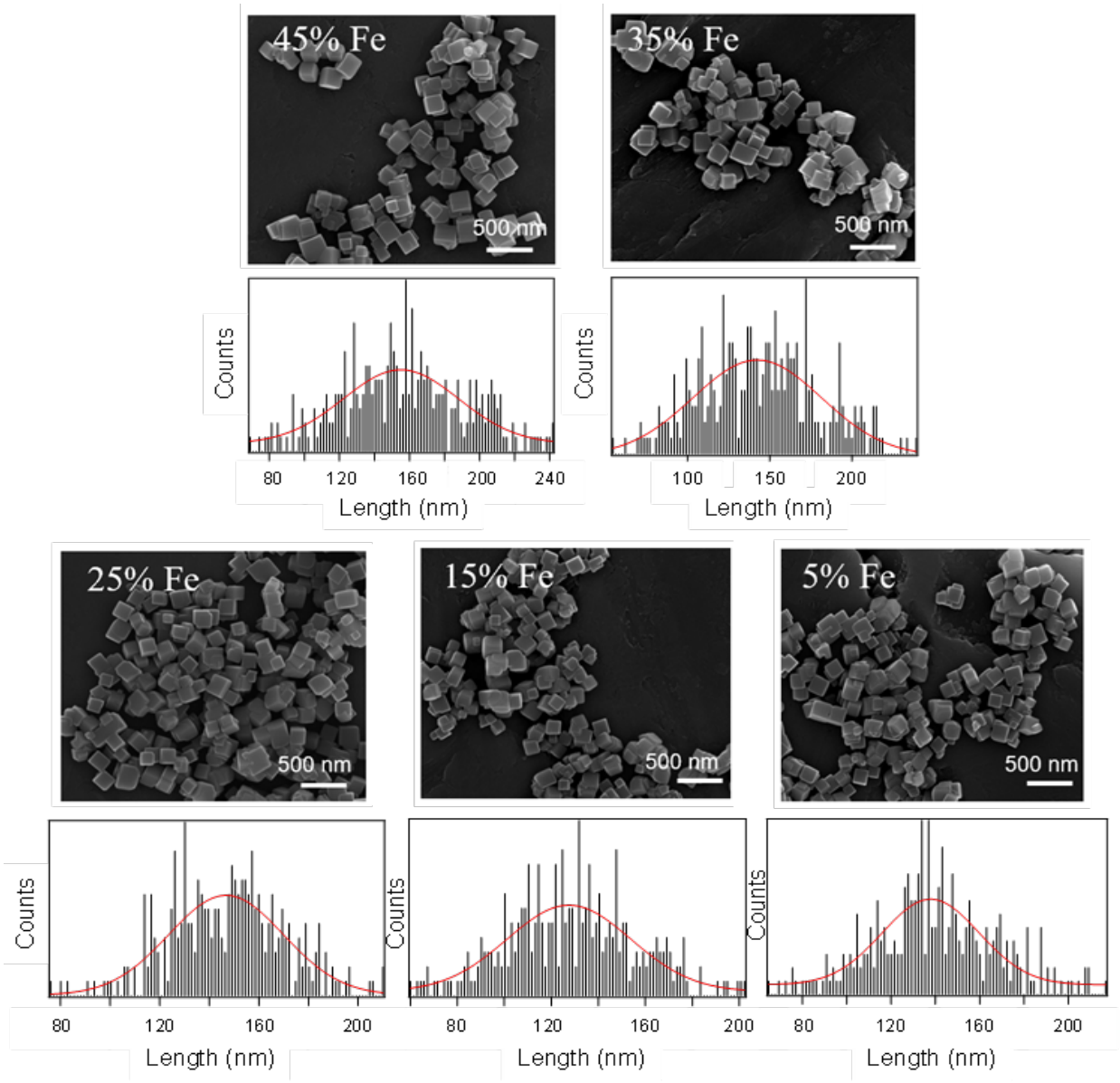

Figure 4.1: SEM imaged of select FeCo PBA precursors, sizes range from 50 to 150 nm depending on the ratio of Fe to Co. Histograms for size analysis are shown below.

4.4 Results and Discussion

4.4.1 Tuning $Fe_xCo_{1-x}C_y$ Phase via Synthetic Parameters. As shown schematically in Figure 4.2A, a set of high temperature solution collapse of Fe:Co PBAs were carried out in the presence of tetrabutyl ammonium halides (TBAX where X = F−, Cl−, Br−, I−). The reaction details are provided in APPENDIX B. The systematic evaluation of TBAX concentration at various Fe:Co

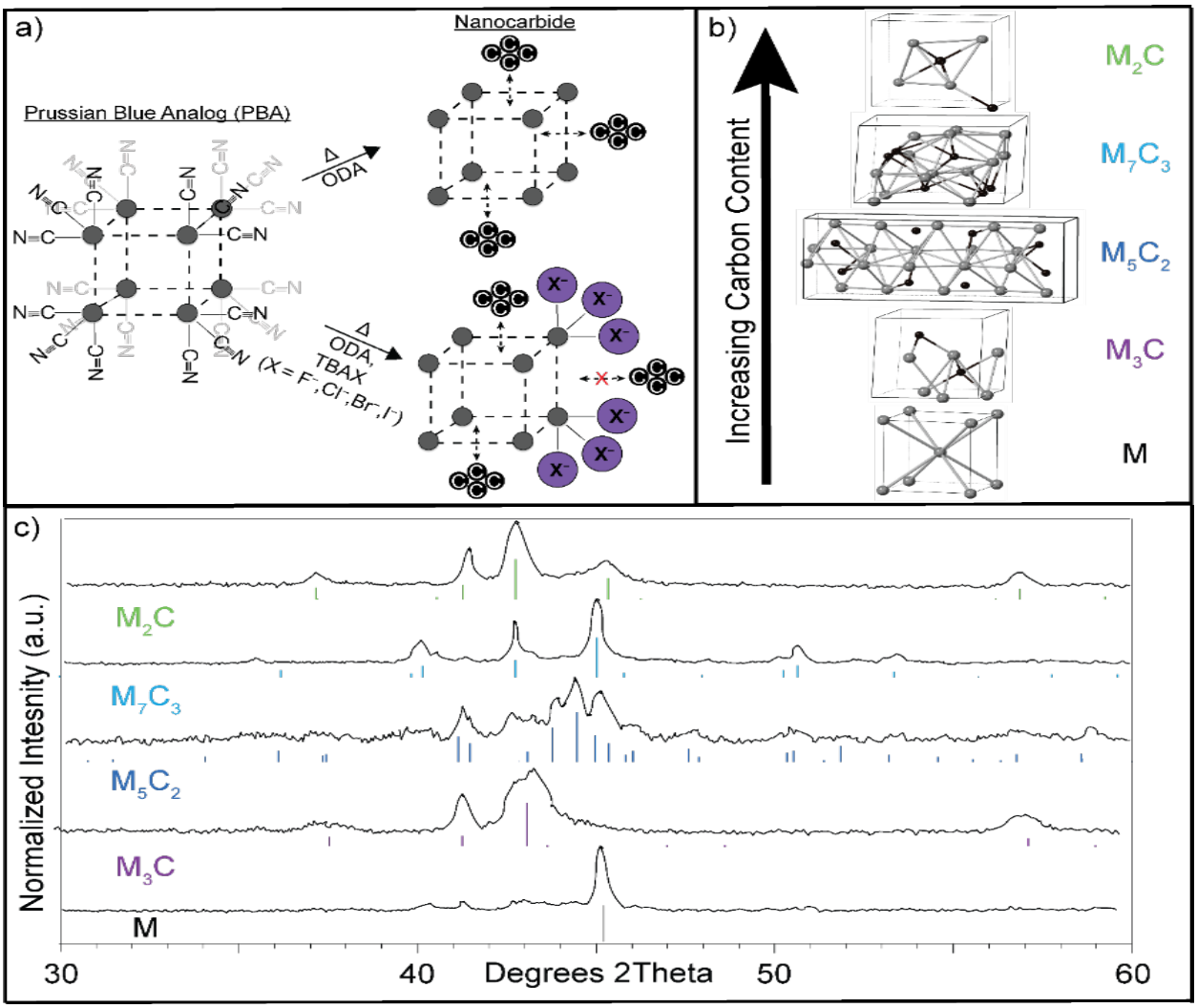

Figure 4.2. a) Schematic for the thermal conversion of mesocrystal Fe/Co PBA to nanocrystal M_xC_y in the presence of octadecylamine (ODA) and TBAX (X= F, Cl, Br, I). b) Thermodynamically stable M_xC_y phases for the $(Fe_xCo_{1-x})_yC_z$ system. c) Selected pXRD of isolated pure phase M_xC_y nanocrystals with reference patterns for phase assignment. Green represents M_2C phase (COD: 1528415), light blue represents M_7C_3 phase (ICSD: 76830), dark blue represents M_5C_2 phase (ICSD: 423885), purple represents M_3C phase (ICSD: 42542), and black represents the M FeCo metal alloy (ICSD:102381).

metal ratios on the phase isolation of the carbide and the change in metal ion ratio for the isolated carbide following thermal conversion of bimetallic Fe:Co PBAs provides insight into the ability to target composition and structure phase. All reactions were carried out for 1-h in boiling octadecylamine (ODA) under N2 to avoid oxide formation. The ratio of Fe to Co in the bimetallic PBAs were prepared by addition of controlled ratios of M(II) chloride to M(III) cyanometallate salts of Fe and Co to ensure Fe:Co composition, as previously described.[23] The PBA starting size is Fe:Co ratio dependent and ranged from 50 – 150 nm with a 20% size distribution (Figures 4.1 and 4.4). Isolation of the nanocarbide from the reaction is accomplished by centrifugation followed by magnetic separation from a toluene solution (XRF ratios for all resultant nanocarbides are reported in APPENDIX B).

In Figure 4.2B, the MxCy nanocarbide crystal phases for Fe and Co carbides that can form are shown. The isolated phases for each reaction condition are evaluated by the whole pattern fitting of the pXRD patterns available in APPENDIX A. In the data set, it is assumed that a pure phase is present if the fitting yields >95% of a single phase. For each reaction carried out, the isolated nanocarbide size is extracted from the pXRD data using Halder-Wagner pattern fitting, assuming a spherical particle.

Inspection of the results for each reaction in Tables 4.1 and 4.2, as well as APPENDIX B, reveals the reaction primarily produces mixed crystallographic phases. At certain combinations of TBAX and Fe:Co ratios, a single phase can be selectively isolated for the M_2C, M_7C_3, M_5C_2, M_3C, and M structural type.

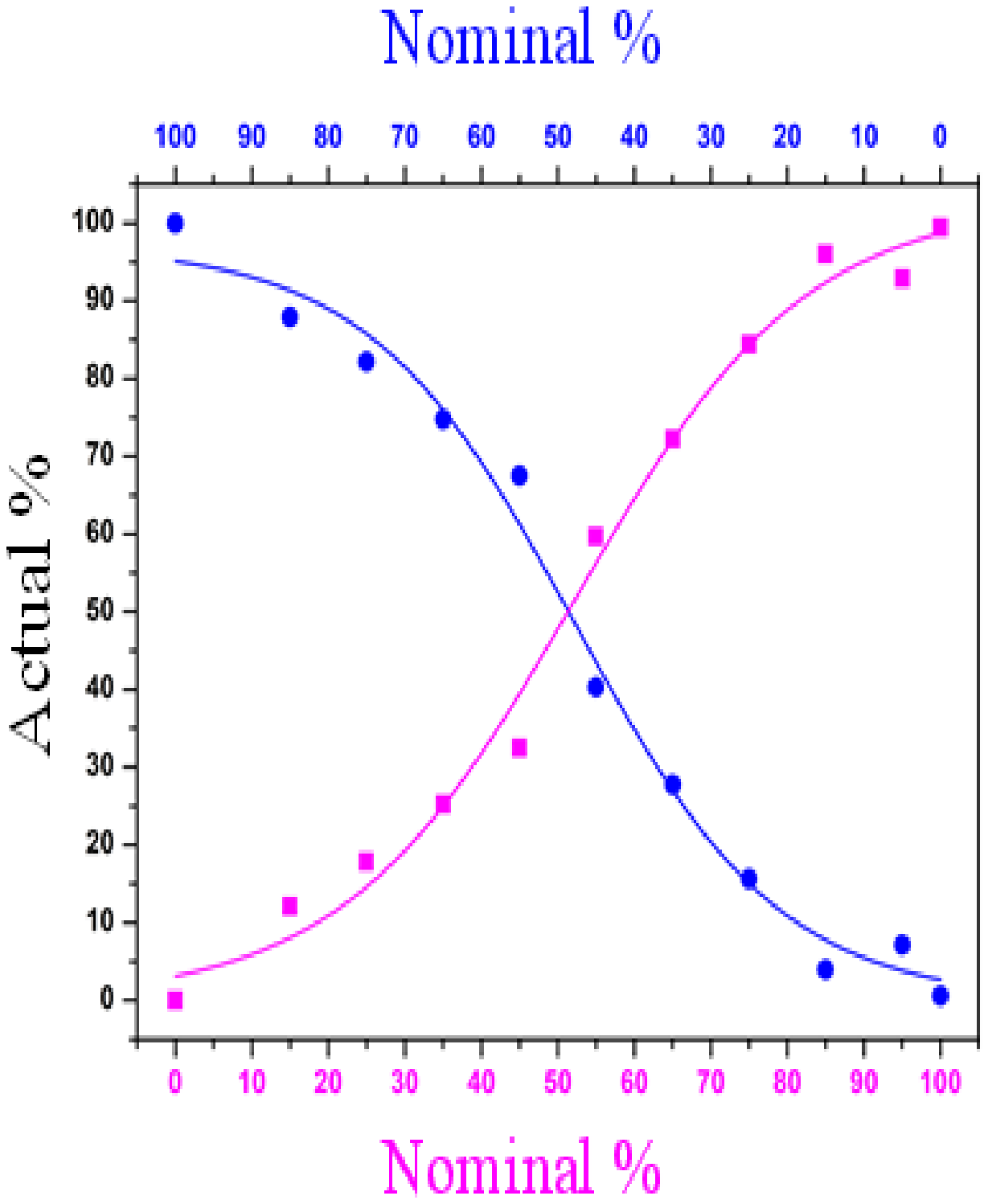

Figure 4.3: XRF elemental analysis of FeCo PBA with varying ratios of Fe:Co. Blue represents Fe % and pink represents Co %.

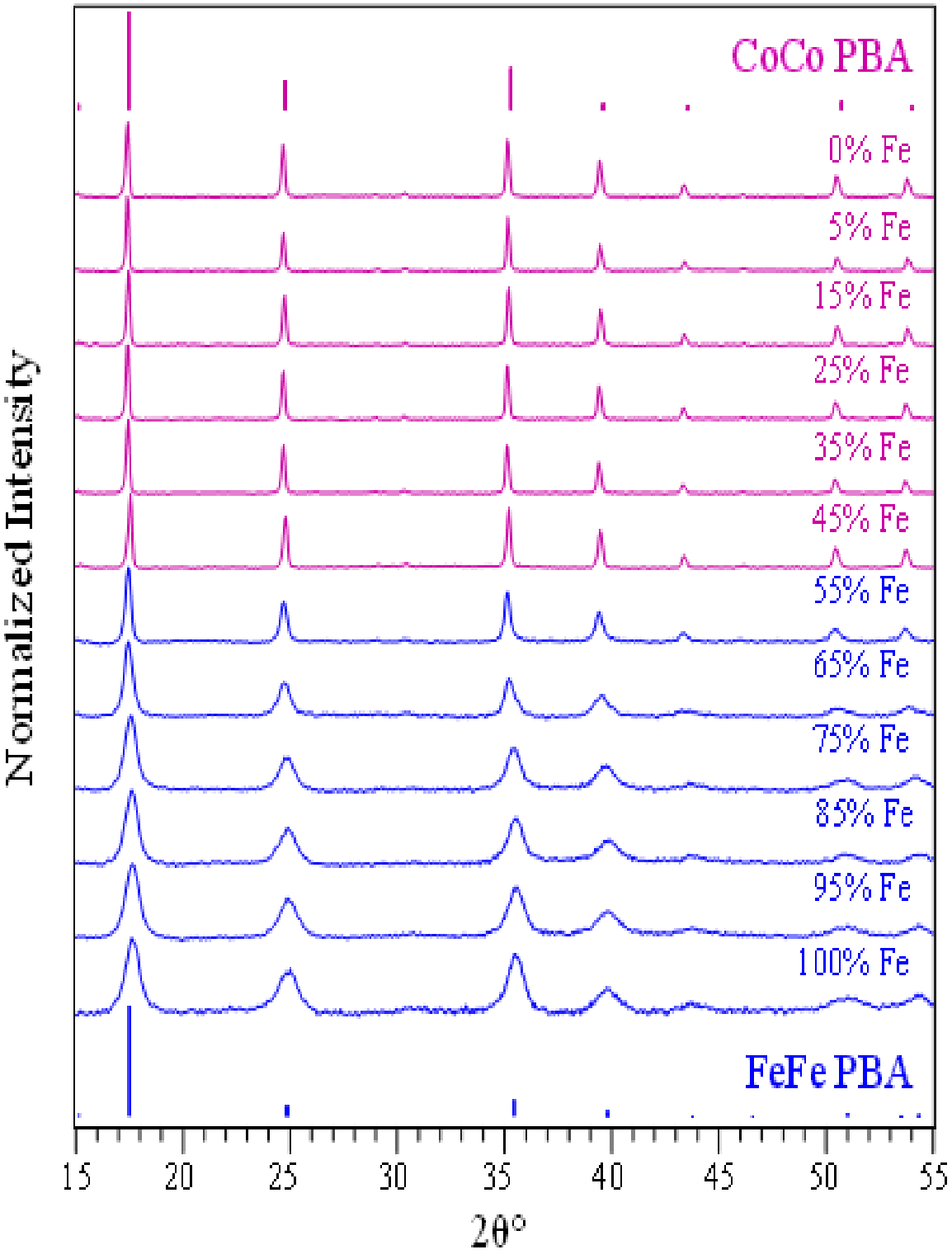

Figure 4.4: pXRD patterns of FeCo PBA precursors. The reference patterns for CoCo (ICSD: 45154 pink) and FeFe PBA (ICSD: 23102 blue) are shown as vertical bars.

Table 4.1. Synthetic parameters for the isolation of pure phase materials. Initial % Fe reflects the XRF ratio for the PBA precursor and the final % Fe reflects the XRF ratio for the carbide.

Isolated FeCoC Phase	Ref Card	TBAX	[TBAX] mmol	Time (hr)	Temp (°C)	% Fe Initial	% Fe Final
M_3C	ICSD:42542	TBAC	0.1	1	350	60	60
M_2C	ICSD:423885	TBAC	0.5	1	350	19	16
M_2C	COD:1528415	TBAC	1	1	350	19	10
M_2C	COD:1528415	TBAC	2	1	350	19	8
M_2C	COD:1528415	TBAC	2	1	350	35	13
M_7C_3	ICSD:76830	TBAC	3	1	350	80	72
M_2C	COD:1528415	TBAB	0.5	1	350	19	14
M_2C	COD:1528415	TBAB	1	1	350	19	7
M_2C	COD:1528415	TBAB	1	1	350	35	11
M_2C	COD:1528415	TBAB	2	1	350	19	5
M_2C	COD:1528415	TBAB	3	1	350	19	3
M	ICSD:102381	TBAB	3	1	350	35	3
M	ICSD:102381	TBAB	3	1	350	80	28
M_2C	COD:1528415	TBAI	0.5	1	350	19	10
M_2C	COD:1528415	TBAI	0.5	1	350	35	26
M	ICSD:102381	TBAI	3	1	350	19	4
M	ICSD:102381	TBAI	3	1	350	35	9
M	ICSD:102381	TBAI	3	1	350	60	11
M_5C_2	ICSD:423885	TBAI	3	1	350	80	35

Table 4.2. Resultant phases for the TBAX and TBAX concentration studies on the 60% Fe Fe_xCo_yC sample. Initial % Fe reflects the XRF ratio for the PBA precursor and the final % Fe reflects the XRF ratio for the carbide.

Isolated FeCoC Phase	Ref Card(s)	TBAX	[TBAX] mmol	Time (hr)	Temp (°C)	% Fe Initial	% Fe Final
M_2C,M_3C, M_5C_2	ICSD:423885, ICSD:42542, ICSD:423885	–	–	1	350	60	65
M_2C,M_5C_2	ICSD:423885, ICSD:423885	TBAF	0.5	1	350	60	58
M_2C,M_5C_2	ICSD:423885, ICSD:423885	TBAF	1	1	350	60	57
M_2C,M_5C_2	ICSD:423885, ICSD:423885	TBAF	2	1	350	60	58
M_2C, M_3C	ICSD:423885, ICSD:42542	TBAC	0.1	1	350	60	60
M_2C,M_3C, M_7C_3	ICSD:423885, ICSD:42542, ICSD:76830	TBAC	0.5	1	350	60	57
M_2C,M_3C, M_7C_3	ICSD:423885, ICSD:42542, ICSD:76830	TBAC	1	1	350	60	57
M_2C,M_3C, M_7C_3	ICSD:423885, ICSD:42542, ICSD:76830	TBAC	2	1	350	60	44
M_2C,M_3C, M_7C_3	ICSD:423885, ICSD:42542, ICSD:76830	TBAC	3	1	350	60	44
M_3C,M_5C_2	ICSD:42542, ICSD:423885	TBAB	0.5	1	350	60	55
M_2C,M_3C, M_5C_2	ICSD:423885, ICSD:42542, ICSD:423885	TBAB	1	1	350	60	46
M_2C,M_3C, M_5C_2	ICSD:423885, ICSD:42542, ICSD:423885	TBAB	2	1	350	60	21
M_2C,M_3C, M_5C_2	ICSD:423885, ICSD:42542, ICSD:423885	TBAB	3	1	350	60	6
M_2C,M_3C, M_5C_2	ICSD:423885, ICSD:42542, ICSD:423885	TBAI	0.5	1	350	60	56
M_2C,M_3C, M_5C_2	ICSD:423885, ICSD:42542, ICSD:423885	TBAI	1	1	350	60	45
M_5C_2, M	ICSD:423885, ICSD:102381	TBAI	2	1	350	60	24
M	ICSD:102381	TBAI	3	1	350	60	11

Representative pure phase pXRD patterns for the shown conditions are plotted Figure 4.2C. The plots in Figure 4.2C correspond to reaction conditions for 35% Fe sample with 1 mmol of TBAB for the M_2C orthorhombic phase (COD: 1528415), 80% Fe sample with 3 mmol TBAC to yield M_7C_3 phase (ICSD: 76830), 80% Fe sample with 3 mmol TBAI to yield the M_5C_2 phase (ICSD: 423885), 60% Fe sample with 0.1 mmol TBAC yields the M_3C phase (ICSD: 42542), and the cubic Fe_xCo_{1-x} metal alloy (M) (ICSD:102381) is for the 80% Fe sample with 3 mmol TBAB. The concentration of Fe in the PBA and carbide (initial and final), as well as all other synthetic parameters used to isolate pure phase materials are reported in Table 4.1, Table 4.2, APPENDIX B. Whole pattern fitting of the pXRD supports the assignment of pure phase in the isolated nanocrystals, but due to broadening of pXRD arising from the nanoscale dimensions, the phase purity and crystallinity of the nanocrystal is difficult to fully ascertain. In Figure 4.5, bright field TEM images on the carbide materials are presented. Figures 4.5a – d show low magnification images (magnification 40-150kx), with Figure 4.5e – h showing higher magnification (800k-1.2Mx), allowing fringe analysis. Figure 4.5i shows the particle and aggregate size analysis from the TEM. Electron diffraction for single nanocrystals is provided in Figure 4.6.

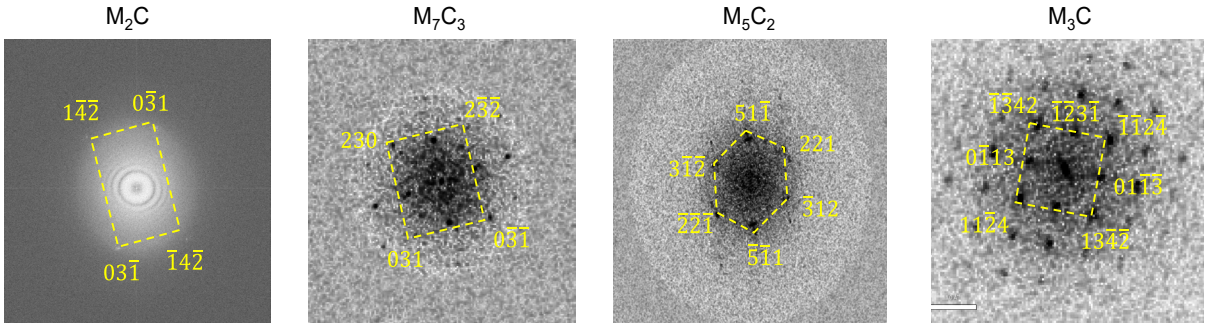

Figure 4.6: Electron diffraction images of all pure phase FeCo nanocarbides.

TEM imaging on M_5C_2 and M_7C_3 shows well defined faceted nanocrystals. It is worth noting that the M_7C_3 has smaller NPs (3 nm) observable at high magnification. The M_2C and M_3C

phases exhibit aggregates of nanocrystals. The M_2C sample appears to aggregate as spherical particles that have an average size of 240 nm in diameter composed of spherical particles with an average size of 18 nm (Figure 4.5e). The M_5C_2 sample aggregates as truncated rectangular crystals with an average width of 37 nm, comprised of smaller, somewhat rectangular particles with an average width of 7 nm (Figure 4.5f). The M_7C_3 aggregates into larger more crystalline rectangular crystals with an average length of 120 nm, which are composed of smaller spherical particles with

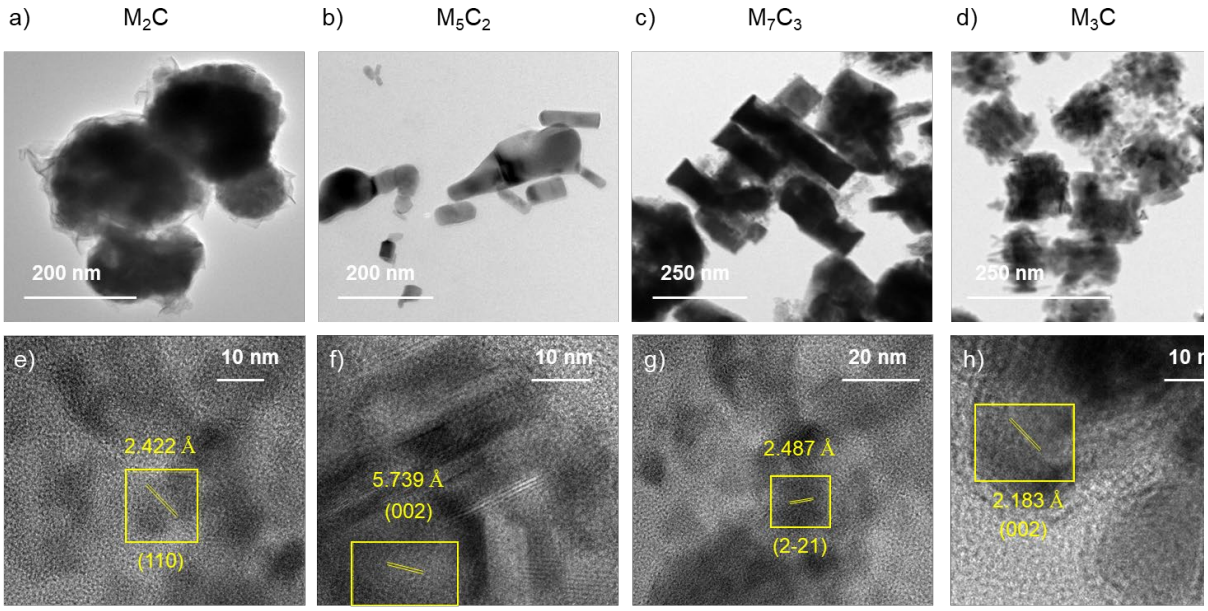

i) Nanocarbide Phase	M_2C	M_5C_2	M_7C_3	M_3C
Particle Size (nm)	18 +/- 8	7 +/- 2	2.9 +/- 0.6	16 +/- 4
Aggregate Size (nm)	240 +/- 108	37 +/- 20	120 +/- 81	108 +/- 34

Figure 4.5: a-d) Low magnification TEM images showing aggregate morphology of pure phase nanocarbides. e-f) High magnification TEM images of single particles of each carbide phase indexed to matching lattice fringes with measured d-spacing. i) Table of single particle size and aggregate size.

an average diameter of 3 nm (Figure 4.5g). The M_3C sample appears to aggregate as cubes that are comprised of spherical particles. The aggregates have an average width of 108 nm, and the spheres have an average diameter particle size of 16 nm (Figure 4.5h). Interestingly, the M_3C sample illustrates how the PBA's cubic sacrificial template has retained the mesoscale morphology yet is composed of smaller nanoscale carbides.

Fringe analysis on the high magnification data confirms that the assigned phase does not exhibit polycrystallinity within a nanocrystal. The M_2C phase sample was indexed based upon a d-spacing of 2.422Å correlating M_2C (110) lattice plane. Lattice fringe analysis reveals a d-spacing match of 5.739 Å to the (002) lattice plane of the M_5C_2 phase. Lattice fringe analysis reveals a d-spacing match of 2.487 Å, which correlates to the $(2\bar{2}1)$ lattice plane of the M_7C_3 phase. The M_3C material has a d-spacing match of 2.183 Å, corresponding to the (002) lattice plane of the M_3C phase. The fringe analysis assignments are confirmed by inspection of the electron diffraction patterns in Figure 4.6. The well-defined diffraction patterns arising from single particles are consistent with the observed faceting of the identified phases. The lack of amorphous rings or significantly different diffraction patterns supports the single-phase assumption from Figure 4.2.

Insight into the phase stability under the reaction conditions can be elucidated by replotting APPENDIX B in terms of a reaction phase space plot for each TBAX reaction condition (Figure 4.7). A cursory glance at the plot reveals reaction conditions lacking TBAX (Figure 4.7a), for Fe:Co ratios of < 60%, M_3C is the predominate species isolated from the reaction, while at > 60% M_5C_2 and M_7C_3 are the primary phases formed with loss of the M_2C and M_3C component. Addition of TBAX to the reaction leads to M_2C being the dominant component with M_3C being a minor phase for all halides and Fe:Co ratios below 60%. M_3C appears at >60% Fe:Co. At 80% Fe:Co in TBAI, the M_5C_2 phase is dominant, while in TBAC M_7C_3 is dominant. The results lead to the

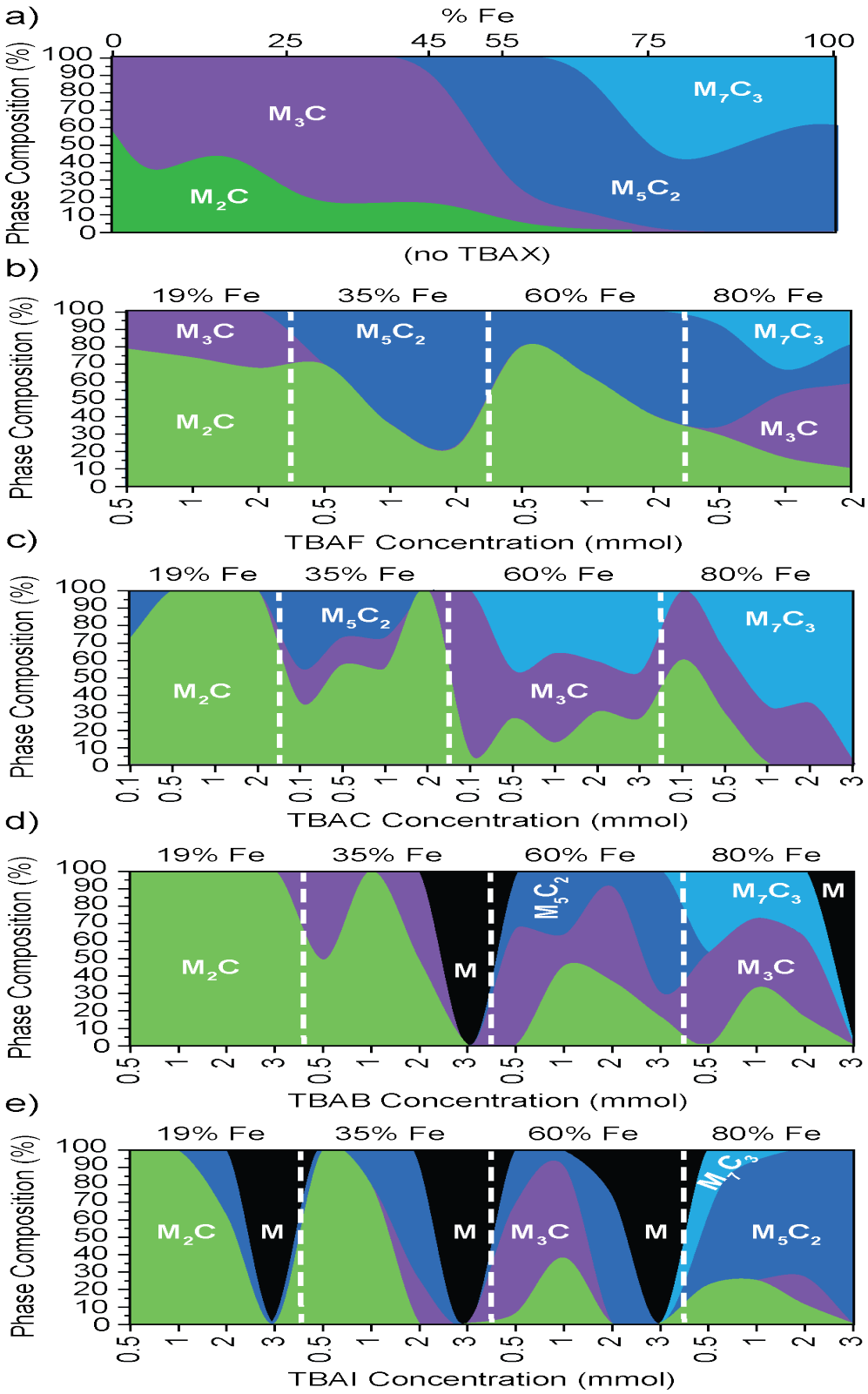

Figure 4.7. Phase diagrams produced from experimental Fe concentration, halide species, and halide concentration studies. A) phase composition as a function of TBAF and Fe concentration. B) phase composition as a function of TBAC and Fe concentration. C) phase composition as a function of TBAB and Fe concentration. D) phase composition as a function of TBAI and Fe concentration. Dotted white lines are placed between Fe concentration studies for clarity.

conclusion that M_2C, M_5C_2, and M_3C are competitive phases in the reaction space for binary metal carbides. The observation of mixed carbide phases with Fe_3C and Co_2C being reported as the predominant observed phase for Fe:Co binaries is consistent with the observations in Figure 4.7.[10,23,52,142]

Closer inspection of Figure 4.7 reveals stability regions can be identified in the reaction phase space that yield pure phases as reported in Table 4.2. The M alloy is observed at high concentrations of TBAB and TBAI. At 3 mmoles TBAF, metal fluoride contamination with metal carbides is observed, as shown in APPENDIX A. Single phase M_3C is isolated (> 95% of the composition) for 60% Fe with 0.5 mmol TBAC. The pure M_5C_2 phase isolated at 2 mmol TBAI for the 60% Fe sample. The pure phase M_7C_3 is observed to be isolable at high iron concentration with TBAC added. Pure phase M_2C can be isolated in TBAC and TBAB for 19% Fe at < 3 mmol TBAX. The result is consistent with reports on halide directing phase iron and cobalt monometallic carbides.[174,180–183]

The general trends for the reaction phase space as a function of TBAX and Fe:Co metal ratio shows that the halide is critical in directing the phases that form across the Fe:Co ratios. For all TBAX and TBAF reactions (Figure 4.7A and B), only mixed phase materials are isolated across all Fe:Co metal ratios. The phase composition varies with the Fe:Co ratio. The contribution of M_3C decreases with increasing iron content in the 0 TBAX reaction condition. Increasing iron content is observed to favor moderate amounts of carbon containing carbides, while higher cobalt leads to lower carbon content phases being formed. It is noteworthy that in the TBAF reaction, the M_3C phase appears in the mixed composition only at 80% iron and 19% iron, while for 0 TBAX the M_3C phase shows a decreasing contribution across as iron content increase, with no appearance of

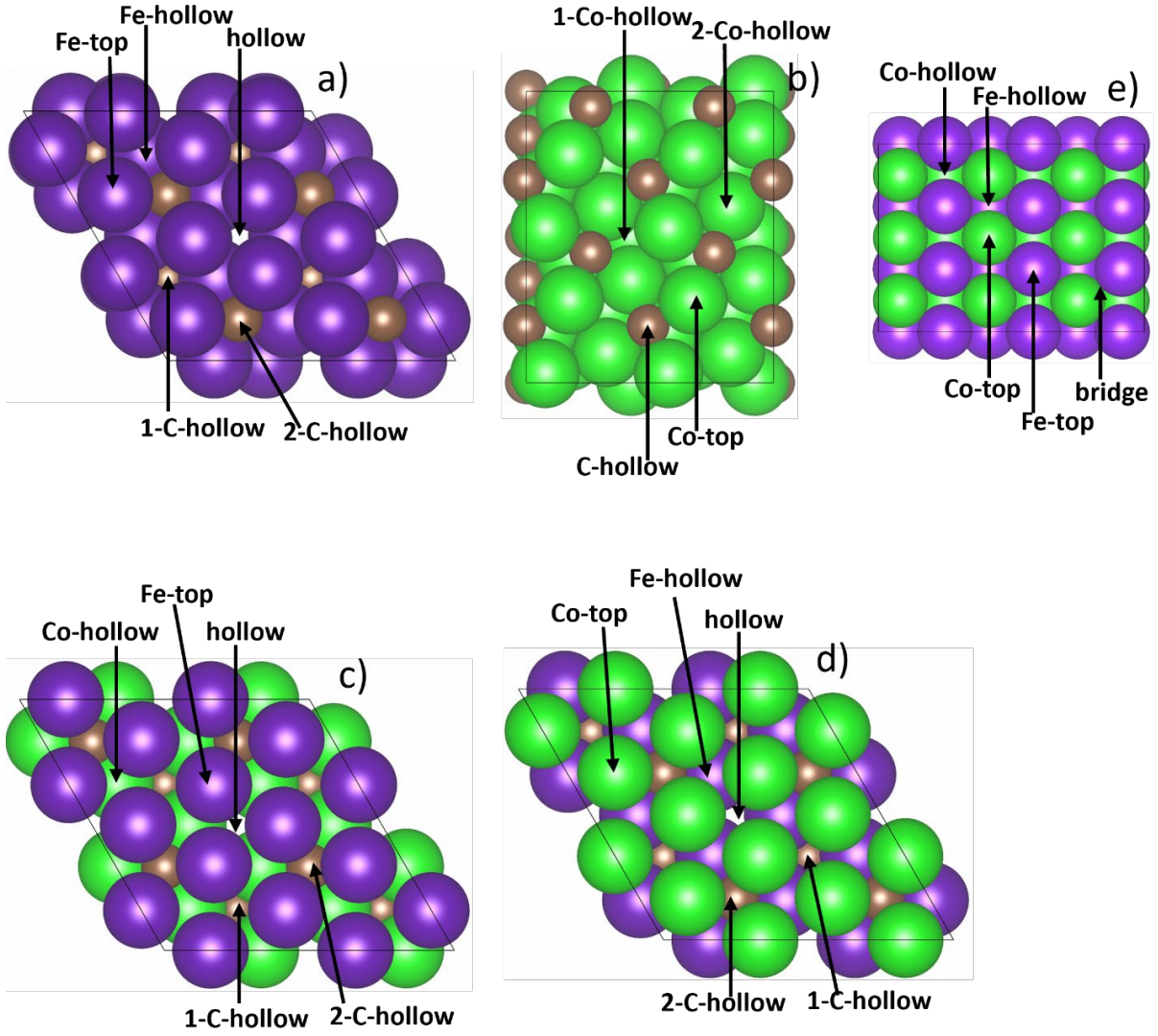

Figure 4.8: Top view of adsorption sites on mono-carbide and bimetallic carbide surfaces a) $Fe_3C(001)$ surface b) $Co_2C(101)$ surface c) Fe-terminated FeCoC(001) surface and d) Co-terminated FeCoC(001) surface.

the phase at 80% iron. For TBAB and TBAI (Figure 4.7 C and D), the trend continues with a steady shift to lower carbon content in the compositions as the amount of iron increases.

4.4.2. Theoretical Evidence of Halide Influence on Carbide Formation. Metal nanocarbides can form by diffusion of carbon into (folding in) and out of (ejection of) a preformed nuclei. Earlier studies on the thermal decomposition reaction that converts PBA to the metal carbide suggest that the carbon is formed by the decomposition of the cyanide linker (CN) to form

NCN- and C as products, diffusion of the NCN- out of the decomposing PBA (nucleating metal carbide), and growth of the metal carbide by cyclic decomposition of the cyanide.[10] Growth of metal carbides from a nanometal has been shown to occur through carbon folding into the metal alloy by thermal decomposition of solvents, ligands, or other organic species in solution.[20,158] Thus, during carbide formation and subsequent thermal processing, it is possible that carbon diffusion represents an equilibrium problem. To understand the carbide formation at various metal contents, the stability of the carbon (C) as an adatom to the surface of a metal and a carbide must be evaluated. Additionally, this equilibrium process of C diffusion is anticipated to be impacted by the binding of the halide (X = F-, Cl-, Br-, and I-) anion and, therefore, must also be taken into consideration.

In earlier reported DFT calculations on carbide formation from a metal through C diffusion into the metal, it was observed that the binding energy (BE) of the C in the presence of chloride was impacted.[184] It was reported that Cl and C have competitive BEs; however, the impact of the X series on the BEs and subsequent carbide phase was not reported. Building upon the earlier reports and to evaluate all possible C diffusion equilibrium and understand the TBAX relationship on phase isolation, first-principles density functional theory (DFT) calculations were performed to compute the BEs of X vs. C atoms on the $Fe_3C(001)$, $Co_2C(101)$, Fe-terminated $(FeCo)_3C(001)$, Co-terminated $(FeCo)_3C(001)$, and FeCo bimetallic(110) surfaces.

The 1st X/C/NH3 binding affinity at the five available sites in each slab model is shown in APPENDIX B and Figure 4.8. For the Fe_3C surface, the identifiable sites are Fe top, Fe-hollow, hollow, 1-C-hollow, and 2-C-hollow (Figure 4.8a). For the Co_2C, the sites are Co top, Co-hollow, hollow, 1-C-hollow, and 2-C-hollow (Figure 4.8b). The Fe terminated $(FeCo)_3C$ has sites Fe top, Co-hollow, hollow, 1-C-hollow, and 2-C-hollow (Figure 4.8c); while the possible sites on Co

terminated $(FeCo)_3C$ are Co-top, Fe-hollow, hollow, 1-C-hollow, and 2-C-hollow (Figure 4.8d). On FeCo (110), the available sites are Fe-hollow, Co-hollow, Co-top, and Fe-top(Figure 4.8e).

Comparing the impact on C BE in the presence and absence of X provides insight into the stability of the carbide phase, indirectly reflecting the energetics of C diffusion. The BEs for the second absorption of the X, C, and the alkylamine (modeled as NH_3) are shown in Figure 4.9g. Figure 4.9a-f shows the energetically most stable sites for the second adsorption of the C or X on

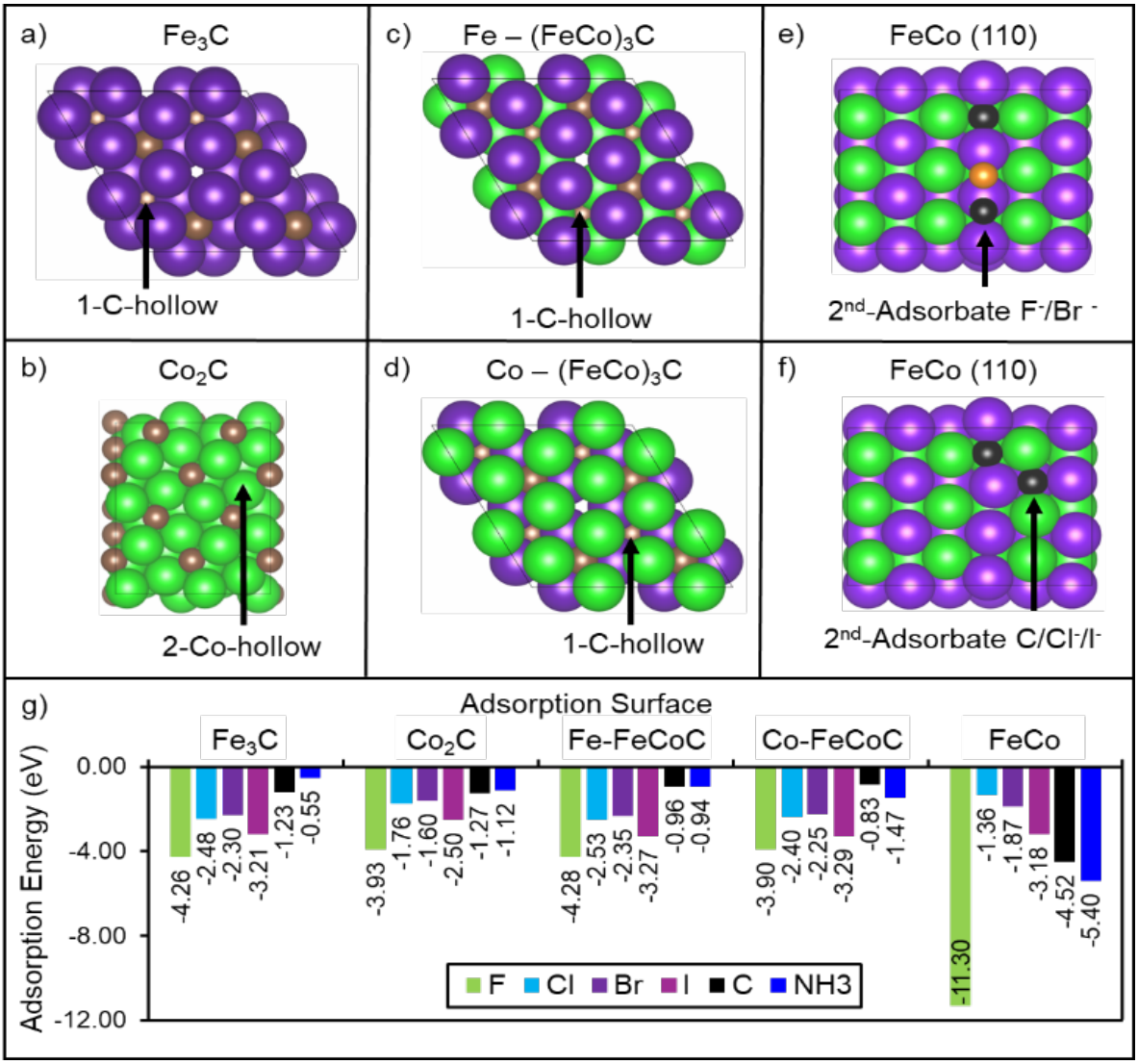

Figure 4.9 Top view of 2nd adsorption sites on binary and ternary carbide, and metal alloy surfaces. a) $Fe_3C(001)$ surface b) $Co_2C(101)$ surface c) Fe-terminated FeCoC(001) surface and d) Co-terminated FeCoC(001) surface e) FeCo (110) F and Br 2nd adsorption site, f) C, Cl, I 2nd adsorption site, and g) plot of 2nd adsorption energies

the pre-adsorbed C surfaces. The reference energy of C is obtained from the energy of the C atom in the graphite bulk phase. The reference energy of the halide anions (X) is calculated as ½ the total energy of the diatomic X_2 in the molecular state. The data is provided in Figure 4.9 and in the APPENDIX B. BE calculations using the reference energy of X obtained from X optimized in an atomic state are also performed, and the results are included in APPENDIX B for the bimetallic FeCo(110) surface. The data shows that changing the reference state of X changes the absolute values of BEs but not the trends.

From the BE calculations, the most stable site for C adsorption on the Fe_3C (001) surface is the 1-C-hollow site, with DFT calculated energies for the 2nd adsorption (in C pre-adsorbed Fe_3C(001) surface) of F, Cl, Br, and I as -4.26 eV, 2.48 eV, -2.30 eV, and -3.21 eV respectively. The most stable site for C adsorption on the Co_2C (101) surface is the 2-Co-hollow, with DFT computed energies for the 2nd adsorption of F, Cl, Br, and I as -3.93 eV, -1.76 eV, -1.60 eV, -2.50 eV. The most stable site for C binding on the Fe-terminated $(FeCo)_3C$ (001) surface is hollow, with DFT calculated 2nd adsorption energy for F, Cl, Br, I of -4.28 eV, -2.53 eV, -2.35 eV, and -3.27 eV. The most stable site for the Co-terminated $(FeCo)_3C$ (001) surface is also the hollow with 2nd adsorption energies for F, Cl, Br, and I of -3.90 eV, -2.40 eV, -2.25 eV, -3.29 eV. On the FeCo (110) surface, there are 2 stable sites for second F/Br and Cl/I adsorption, and these sites are at the 1-Co-hollow and 1-Fe-hollow, respectively. The DFT computed binding energies for second F-, Cl-, Br-, I- adsorption on C pre-adsorbed FeCo (110) surface are -11.30 eV, -1.36 eV, -1.87 eV, and -3.18 eV. The opposite calculations of halide pre-adsorbed surfaces with a halide or carbon 2nd adsorption are shown in APPENDIX B.

Since the reactions are carried out in octadecylamine, and the RNH_2 group is the surface passivation layer, the impact of RNH_2 on X/C binding at the FeCo (110) face needs to also be

considered. The details of the calculations are available in APPENDIX B. The alkylamine (RNH_2) is modeled as the ammonia molecule (NH_3) to mimic the passivating ligand. Our DFT results show that on the carbide phases, the BE of NH_3 and C are nearly identical, although the NH_3 is less stable on Fe_3C. On the metal alloy, NH_3 is the second most stable, which can be rationalized by the Lewis basicity of the amine interacting with the acidic metal sites. In addition, the NH_3 is less stable on an iron carbide phase relative to the cobalt carbide phase. This observation supports our experimental data from Figure 4.7 where the major phase isolated amongst all Fe percentages was the M_2C (Co_2C phase type). The observation suggests reactions carried out in alkylamines may restrict carbon diffusion into the preformed metal carbide from PBA collapse, and potentially the lowering of the barrier for carbide formation, as reported earlier.[163]

In the DFT models computed of pre-adsorbed C, the trend from greatest to least stable absorbate follows F- > I- > Cl- > Br-. The order of stability reflects contributions from electronegativity and softness of the X. This trend seen in both binary and ternary carbides is important as it supports our experimental results of tuning carbide phase accessibility based on X species, where the energies of each X entity are different but close in magnitude. Calculations on the metal carbide and metal alloy confirm that binding the X to the surface when a C atom is pre-adsorbed is more favorable than adding an additional C atom. In addition, the DFT results support our earlier conclusion that RNH_2 passivation lowers the thermodynamic barrier for carbide formation.[10] This implies that the presence of the X in the metal carbide may reduce the probability of carbon diffusion into the metal carbide through C folding. The diffusion of carbon out of the material would likewise be expected to be impacted, in the presence of a bound X, as the energy of binding is higher (less negative) for C on the carbide surface regardless of the carbide phase. By comparison, the metal alloy favors C diffusion into the alloy relative to the halides except for

F. The DFT results, in general, suggest that X-mediated synthesis promotes the formation of metal-rich carbide phases, which agrees with experimental results in Figure 4.7. In Figure 4.7, the carbon content increases with decreasing halide size for a given iron to cobalt metal ratio. While the halide competes with the alkylamine for binding at the surface of the growing nanocarbide, the halide is more favorable based on DFT modeling. This suggests that the alkylamine passivating ligand is most likely not involved in phase control. Since the DFT predicts the C adsorption at the surface is nearly the same energy as the RNH_2, the DFT supports the earlier conclusion that RNH_2 is critical for the formation of the carbide in a PBA decomposition reaction.[163,191]

4.4.3. Carbide Isolation and Stability. The experimentally observed phases and the DFT modeling predict that carbon diffusion is impacted by the presence of the halide, whether this is due to changes in metal activity, carbide formation energies, or changes in surface adsorption of C is less clear. It is well known that TBAX thermally decomposes to generate halide ions that can form alkyl halides through SN2 reactions.[192,193] By analogy, it is believed thermal decomposition of the TBAX leads to halide release at < 150°C and subsequent halide attack on PBA lattice vacancies where water termination of metal sites exists. As a result, the formation of the nanocarbide from the PBA is anticipated to be modified by the polarizability of the halide species. To evaluate the role of the halide in the conversion to form the nanocarbide, scanning differential thermal analysis (SDT) on the 19% Fe samples at 1 mmol TBAX is shown in Figure 4.10, and the temperature for carbide and alloy formation presented in Table 4.4. The TBAF shows water loss at 100°C consistent with TBAF being hygroscopic. This leads to a water loss feature at 117°C in TBAF, but no water loss feature for TBAC, TBAB, and TBAI. In Figure 4.10, the TBAF SDT

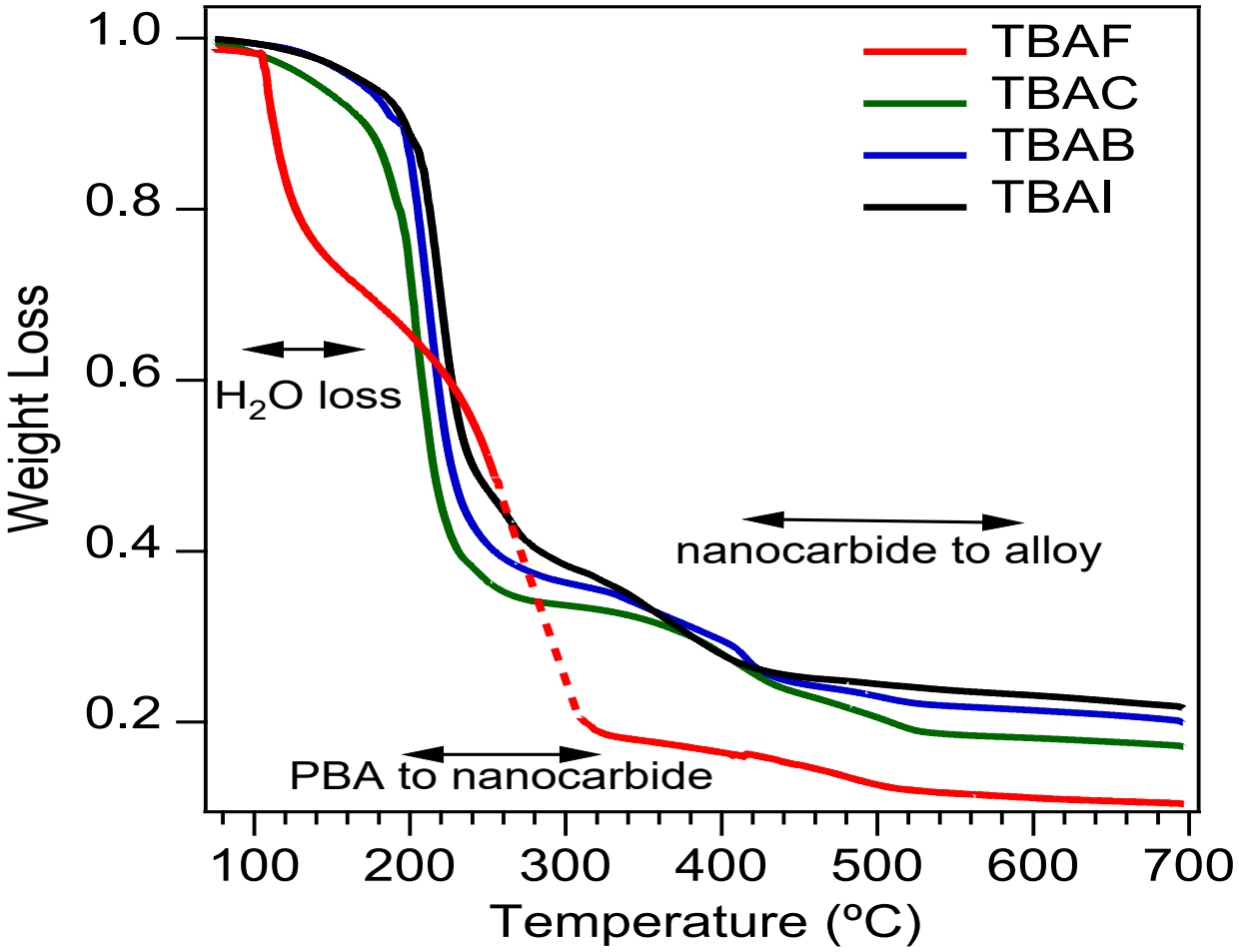

Figure 4.10. Scanning differential thermal analysis (SDT) studies on 19% Fe ($Fe_{0.19}Co_{0.81}C$) with 1 mmol of TBAX to the reaction. The water loss, PBA to nanocarbide, and nanocarbide to alloy regions are identified. The interpolated curve for TBAF is shown as a red dashed line.

shows signal loss due to an instrumental error. As previously reported in the absence of TBAX, water loss from the PBA and subsequent PBA reconstruction occurs at < 300°C, the loss of NCN leads to carbide formation above 300°C, and the alloy is isolated at temperatures exceeding 500°C.[163] In the presence of TBAX, the SDT data reveals no defined water loss event and the PBA to carbide transition occurs at lower temperature (235°C, TBAI → 275°C, TBAF) and the nanocarbide is thermally stable up to 505°C, TBAF → 515°C, TBAI. The SDT data shows that the presence of TBAX has no defined water loss event, as previously observed in the absence of

Table 4.3. TBAX dependent temperatures for PBA to nanocarbide and nanocarbide to alloy formation.

Sample	PBA → Carbide	Carbide → Alloy
19% No TBAX	285°C	570°C
19% 1 TBAF	275°C	505°C
19% 1 TBAC	260°C	510°C
19% 1 TBAB	250°C	515°C
19% 1 TBAI	235°C	510°C

TBAX,[10] which suggests replacement of the water in the PBA vacancies by the TBAX or halide ion occurs upon mixing. The transition to the alloy also shows a decrease in temperature relative to no TBAX and is largely constant across the TBAX series. Although beyond the scope of the study, the data implies the nanocarbide is anticipated to be stable up to ~500°C for catalytic applications, while the alloy could be used for high temperature catalysis. In the SDT, the conversion to the nanocarbide shifts to a lower temperature for the halide series as a function of halide polarizability (TBAF → TBAI). The dependence on polarizability is consistent with hard-soft acid base theory, and the DFT formation energy predictions in Figure 4.9. For the no TBAX condition, the observed SDT transitions corroborate the speculation that the presence of the TBAX halide lowers the energy barrier for carbide formation.

In Figure 4.11a, the accessible compositions for a given halide additive are plotted. The halide type, concentration, and ratio of Fe:Co dictate the phase that is isolated. The fact that the lowest energy carbide is M_5C_2, but the most isolated phase from the PBA thermal collapse is M_2C, suggests that the reaction is kinetically controlled, and the addition of halides manipulates the precursor activity to provide phase control over carbides formation. Figure 4.11b shows the relative energies of the starting material (FeCo PBA), FeCo carbide, and FeCo alloy. The results

from Figure 4.11a lead to modification of our earlier reaction mechanism hypothesis.[10] The model in Figure 4.11b now shows where the impact of halide in the barrier height for carbide phase provides the kinetic control over the isolable carbide phase. The kinetic barrier likely reflects carbon diffusion during nucleation of the carbide phase as the PBA decomposes. In Figure 4.11c, the energies of the carbide phases are illustrated as compared to the precursor and alloy materials. The relative energies of the carbide phases are very close, which supports our experimental findings that specific experimental conditions (halide species, halide, and metal concentrations) are vital in the isolation of a target carbide phase.

Reflecting the rich carbide phase diagram for metal carbides, it is important to evaluate carbide thermal stability. The stability of the nanocarbide can be evaluated by conducting annealing experiments on the carbide in octadecylamine at 350°C with 2 mmol TBAC, reveal no change in phase for a sample aliquot measured at 1 and 24 h for the 19%, 35%, 60% and 80% Fe

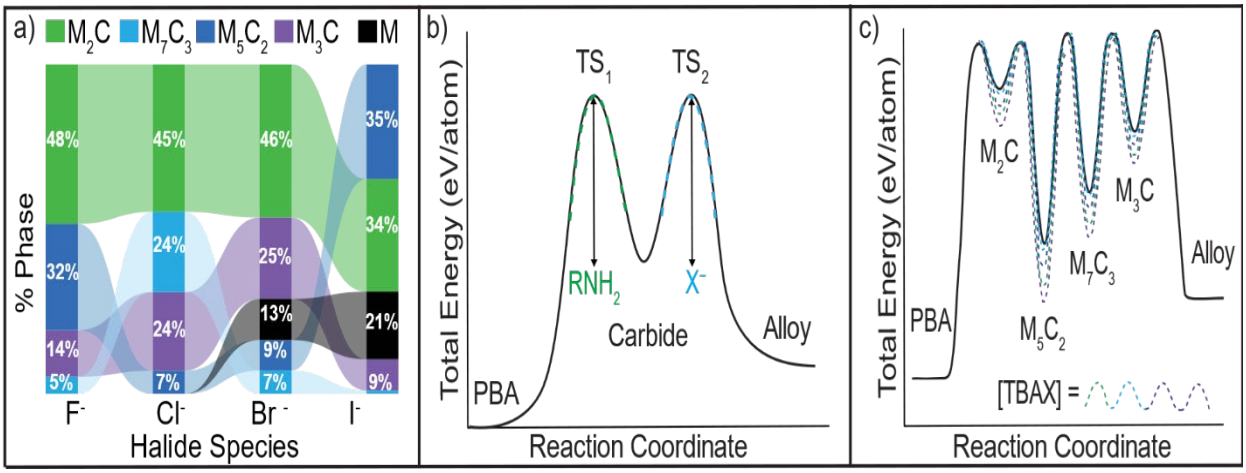

Figure 4.11. a) a ribbon plot depicting carbide phase dependence on halide species. B) A reaction coordinate diagram describing the decomposition of PBA to carbide and metal alloy. The green dotted line represents the carbide formation thermodynamic barrier that is dependent on the presence of RNH_2 and the light blue dotted line represents the alloy formation thermodynamic barrier which is dependent on the presence of X^-. An inset showing the relative energies for each unique carbide phase is shown below. The colored dotted lines represent modulation of the thermodynamic barrier by varying halide species (TBAX) and halide concentrations ([TBAX]).

samples, as shown in Figure 4.12. The annealing study confirms the isolated carbide phase from the decomposition of PBA in alkylamine is halide and metal ratio dependent and the isolated carbide is stable under reaction conditions. The observed stability of the nanocarbide implies carbon diffusion into and out of the material is at equilibrium.

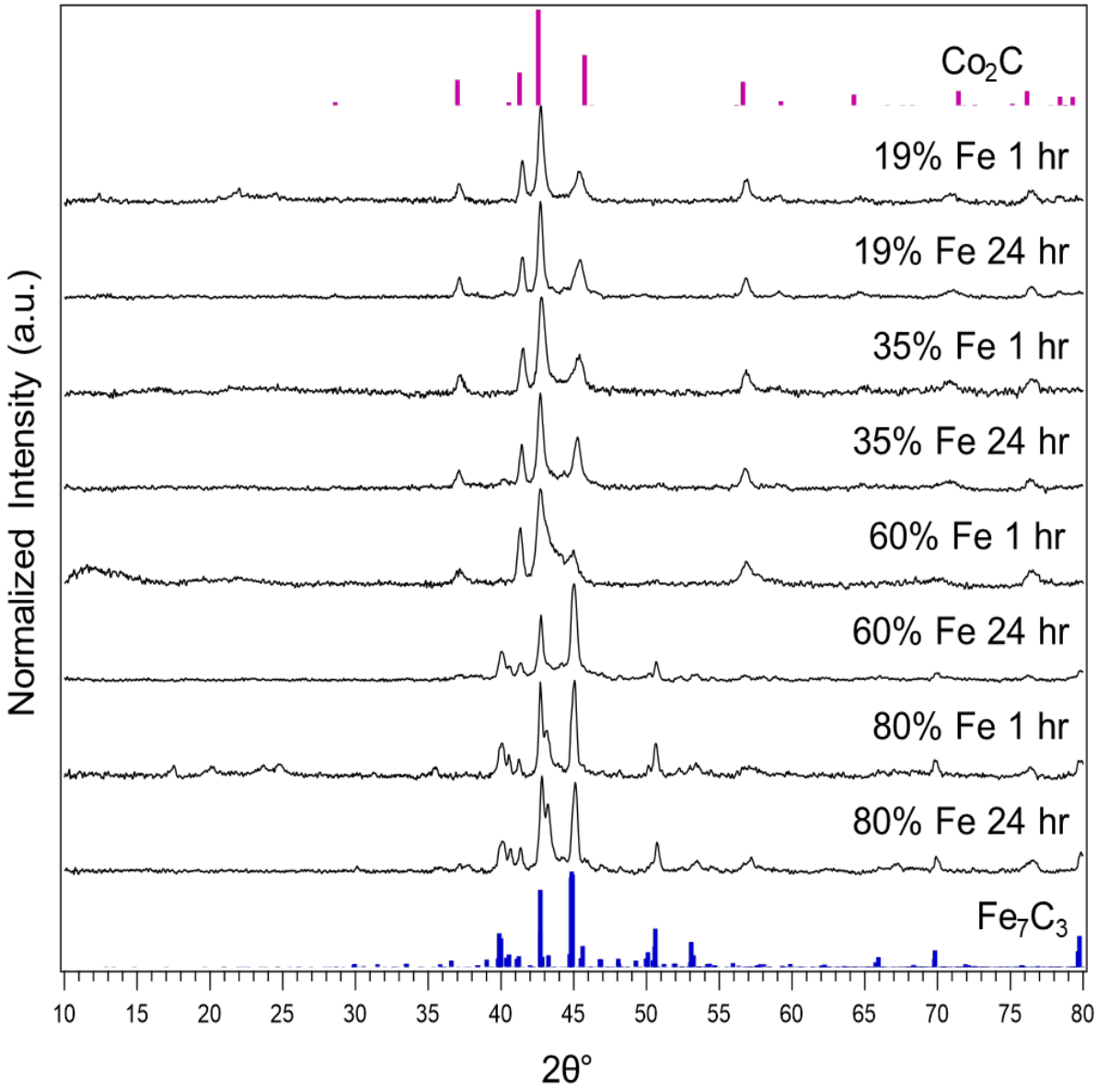

Figure 4.12. Time dependent pXRD measurements of select ratios under 1 hr and 24 hr reaction times with the addition of 2 mmol TBAC. Pink bars represent the Co_2C reference pattern, and blue bars represent the Fe_7C_3 reference pattern.

4.4.4. Electrocatalytic Activity. It has been demonstrated that in metal carbides, the metal species and metal ratio can influence the observed overpotential for HER and OER electrocatalytic activity.[23,52,72,194] The phase of the carbide has also been hypothesized to influence catalytic activity for metal carbides.[195,196] In Figure 4.13, linear sweep voltammograms and overpotential at

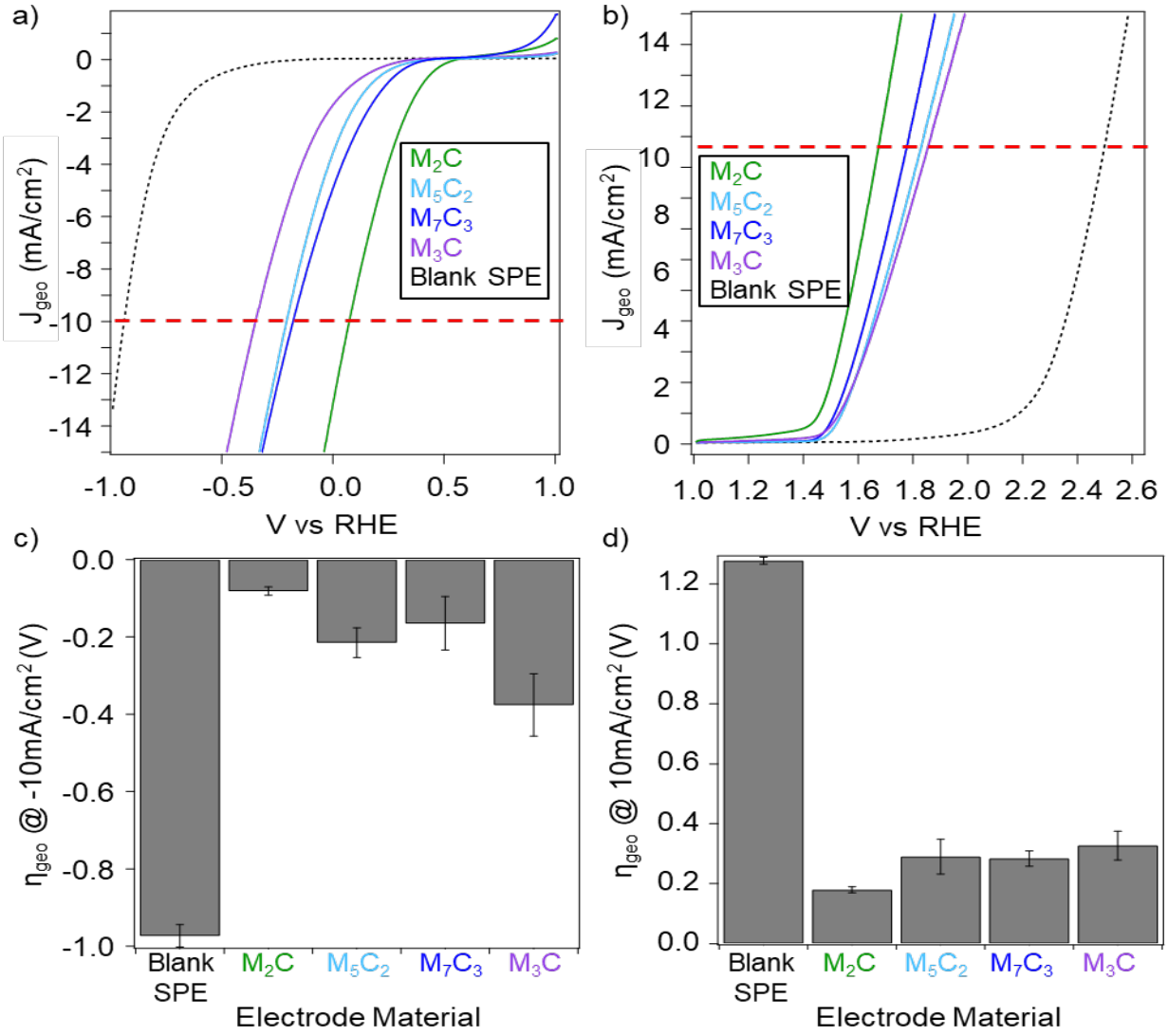

Figure 4.13. Linear sweep voltammograms to evaluate electrocatalytic performance in HER a) and OER b) for each pure phase FeCo nanocarbide. The red dotted line represents the standard current densities required to be considered a catalyst. c) and d) are bar charts comparing the HER and OER overpotentials for each sample. Purple represents M_2C, dark blue represents M_7C_3, light blue represents M_5C_2, green represents M_2C, black represents the blank electrode.

10mA/cm^2 are shown for the phase pure nanocarbides presented in Figure 4.2 (M_2C: 11% Fe, M_7C_3: 28% Fe, M_5C_2: 35% Fe, M_3C: 60% Fe). The linear sweep voltammograms were measured under alkaline conditions for OER and acidic conditions for HER on samples drop cast from methanol onto a carbon screen printed electrode. The lowest observed overpotential for OER and HER is for the M_2C phase, with an increase in overpotential occurring as total metal content in the carbide increases. Inspection of the OER and HER overpotentials for the carbide phase studies in Table 4.4 reveals that the materials would be appropriate for application as an effective electrocatalyst for solar water splitting,[40] since the combined overpotentials is less than 0.45 V. Further studies to interrogate the potential of nanocarbides for solar water splitting are underway.

We have reported that increasing iron content leads to a lower decrease in overpotential for < 20% iron and an increase in overpotential at higher iron percentages in mixed phase Fe/Co carbides.[23] For the reported data, it is important to note that in addition to changes in metal to carbon content in the phase, the Fe to Co ratio is changing with a higher Fe ratio corresponding to a higher metal content in the nanocarbide. The observation of a lower overpotential for lower metal content carbides in Figure 4.13 explains the observation in the earlier manuscript, implying phase purity is important in lowering overpotential in addition to metal concentration. The data clearly

Table 4.4 Phase dependent HER, OER, and combined overpotential measured by linear sweep voltammetry.

Phase	% Fe	η_{HER} (V)	η_{OER} (V)	$\Delta\eta$ (V) $\eta_{OER} - \eta_{HER}$
M_2C	11	-0.082	0.180	0.262
M_7C_3	28	-0.165	0.284	0.449
M_5C_2	35	-0.215	0.290	0.505
M_3C	60	-0.376	0.327	0.703

indicates that to fully evaluate electrocatalytic activities both phase and metal ratio must be evaluated simultaneously.

4.5. Conclusions

It is known that in thermal collapse mechanisms, ligand additives can control not only the rate of reaction but also the phase of the isolated material.[197] In the case of PBA decomposition of bimetallic PBA mesocrystal precursors, the addition of halides is vital to the systematic control of metal carbide. The developed synthetic approach provides a means to selectively isolate targeted, single phase ternary $(Fe_xCo_{1-x})_yC_z$ materials by judicious choice of the halide additive and its concentration to control carbon adsorption and carbide growth. The study supports the hypothesis that halides facilitate the isolation of a targeted carbide in the thermal decomposition reaction following the initial PBA to carbide step. The role of halides in controlling growth appears to be reflective of the carbon diffusion equilibrium into and out of the isolated carbide. Theoretical modelling supports the experimental conclusion that addition of halides to a PBA thermal decomposition reaction impacts the growth behavior and carbon incorporation into the isolable nanocarbides. The observed experimental dependence of the halide on the carbide phase, coupled to DFT modelling supports a mechanism wherein co-coordination of RNH2 and the halide impacts the thermodynamic stability of the carbon. The DFT observations support a two-step mechanism where carbon rich carbides form as PBA collapses, followed by carbon diffusion out of the material, leading to metal rich phases. From the DFT BEs, the lower carbon stability in the Fe-terminated carbide would suggest a higher metal to carbon material would be stabilized with increasing iron content. The effect on the carbide phase with increasing iron was reported for mixed phase Fe-Co carbides previously.[23] The isolated nanocarbides are thermally stable under the reaction conditions, and over a wide temperature range after isolation as shown by SDT

measurements. The DFT modelling supports that the control reflects regulating the flow of carbon in and out of the materials.

Our experimental results coupled with theory provide a guide to enable future researchers to make pure phase ternary carbides for catalytic studies, and potential for formation of phase control to the broader MX-ide family (O, P, N, S, Se, Te) which have been heavily studied in OER and HER electrocatalytic reactions.[17,23,195,198–205,25–27,30,52,55,124,194] The phase pure carbides exhibit electrocatalytic activity that is phase dependent and could be used in solar catalysis based on the HER/OER overpotentials. Regardless of the future applications, the coupling of theoretical modelling in the prediction of reaction outcome is a power tool that enables a rapid advancement of materials. Further studies are underway investigating the catalytic and magnetic properties of the ternary $(Fe_xCo_{1-x})_yC_z$ range as well as expanding this work to related materials.

CHAPTER 5

FROM MONOMETALLIC TO PENTAMETALLIC: SYNTHESIS OF PBA-DERIVED MEDIUM AND HIGH ENTROPY NANOCARBIDES FOR THE OXYGEN EVOLUTION REACTION (OER)

5.1 Introduction

Nanoparticulate high entropy materials (HEMs) are of increasing interest for applications in catalysis due to their high surface area to volume ratio as compared to bulk counterparts as well as the synergistic "cocktail effect" that has been observed in enhancing catalytic activity and selectivity. [206–209] The quest for novel materials with superior mechanical, thermal, and electrical properties have created significant interest in the synthesis, characterization, and applications of high entropy carbides. Furthermore, investigations into these properties have revealed the exceptional performance of high entropy carbides in harsh environments, like high temperature, high pressure, and corrosive applications. HEMs are defined as solid solutions which contain five or more elements each contributing to an overall high configurational entropy that allows for increased stabilization of the otherwise metastable crystal. These materials are thermodynamically favored (- ΔG) as the elements occupy equivalent crystal lattice sites giving rise to a large entropic term (-$T\Delta S$) that can overcome any enthalpic contributions (ΔH) in the overall thermodynamic formation of the nanocrystal.[160] High entropy carbides (HECs) therefore are carbon interstitial alloys which contain four or more metals. Carbide nanomaterials are generally said to be metastable kinetic phases as high temperature often disfavors the formation of nanomaterials.[164] Recently there have been efforts to produce colloidal nano-HEMs, however the control of elemental composition is highly dependent on uniform addition, availability, and reactivity of the

injected precursor solutions which pose a huge challenge in the ability to tune metal stoichiometries of resultant nanomaterials.[160] One of the key challenges that remains is achieving precise control over the composition, size, and morphology of nanoparticles to tune their properties for specific applications. Furthermore, understanding the fundamental mechanisms governing the synthesis, phase transformation, and property enhancement of high entropy carbides is essential for advancing the field. Additionally, exploring new synthesis routes, developing scalable fabrication methods, and elucidating structure-property relationships will pave the way for further advancements in high entropy carbide nanomaterials. Recently, synthetic techniques such as mechanical alloying (ball-milling), arc melting, solvothermal synthesis, chemical vapor deposition, and template-assisted methods have been employed in an attempt to control the size, morphology, and composition of resultant nanomaterials. One solution to this issue is to implement a single source precursor method that allows for the control of all metal compositions simultaneously. Prussian blue analogues (PBAs) are a unique class of coordination polymers that allow for such stoichiometric control. Previously our group has shown the ability to control metal stoichiometries in our resultant nanocarbide materials in bimetallic and trimetallic systems through the use of PBAs as single source precursors.[23,163]

Herein we expand our use of PBAs as single source precursors from monometallic all the way to pentametallic materials for the production of high entropy carbide materials containing up to five metals enabling us to tune the metal ratio of the HEC. Additionally, these materials are tested for activity as catalysts in electrochemical water splitting reaction (OER and HER).

5.2. Experimental Methods

All commercially available reagents were used without further purification. Precursors for all PBAs were $K_3Cr(CN)_6$ (made in house), $K_3Mn(CN)_6$ (made in house), $K_3Fe(CN)_6$ (Sigma

Aldrich, >99%), $K_3Co(CN)_6$ (Sigma Aldrich, >99%), $K_2Ni(CN)_4$ (Alfa Aesar, >99%), KCl (Sigma Aldrich, 98%), $CrCl_3 \cdot 6H_2O$ (Sigma Aldrich, 98%), $MnCl_2 \cdot 4H_2O$ (Sigma Aldrich, 98%), $FeCl_2 \cdot 4H_2O$ (Thermo Fisher, >99%). $CoCl_2 \cdot 6H_2O$ (Thermo Fisher, >99%), and $NiCl_2 \cdot 6H_2O$ (Thermo Fisher, >99%). Solvents used for synthesis were ultrapure water (18.2 Ω cm^{-1} at 25.0 °C, Thermo Scientific Barnstead E-Pure ultrapure water purification system), octadecylamine (ODA) (Thermo Fisher, 90%), acetone (VWR, ACS Grade) and toluene (VWR, ACS Grade).

5.2.1. General Synthesis of Prussian Blue Analogue Precursors. All PBA precursors (from monometallic to pentametallic) are synthesized through a known precipitation method adapted from Hardy et al. Succinctly, two solutions are prepared, a 5mM solution of all cyanometallate salts in equimolar ratios which sum to 1 mmol, as well as a 10mM solution of all metal chloride salts in equimolar ratios which sum to 1 mmol with an additional 5 mmol KCl used as a chelating agent for the PBA formation. For monometallic solution one has 1 mmol cyanometallate salt and solution two has 1 mmol of metal chloride salt and 5 mmol of KCl, for bimetallic there are 0.5 mmol of each cyanometallate salt in solution 1 and 0.5 mmol of metal chloride salts with the added 5 mmol KCl. The same method is used for trimetallic, tetrametallic, and pentametallic PBAs. One solutions are prepared, solution 2 is slowly added to solution 1 and the resultant reaction mixture is stirred at room temperature for at least 2 hours to ensure PBA formation. The reaction mixture is centrifuged, the PBA is collected and then washed thrice with ultrapure H_2O. The PBAs are dried at 120 °C for approximately 30 minutes or until completely dry. The PBAs are characterized by pXRD, SEM, EDX, XRF, SDT, and FT-IR.

5.2.2. General Synthesis of Nanocarbides. All nanocarbides (from monometallic to pentametallic) are synthesized through a high temperature organic synthesis method. In summary, 200mg of the PBA precursor and 17.24g (20mL) of octadecylamine are added to a three-neck

round bottom flask equipped with a condenser. Under inert atmosphere the reaction mixture is heated to 350°C (BP of octadecylamine) for an hour and subsequently quenched with toluene. The resultant reaction mixture is centrifuged (hot ~ 150°C), the pellet is then washed thrice with toluene, once with acetone, thrice with ultrapure H_2O, and once more with acetone. The resultant nanocarbides are dried @ 100°C for approximately 15 minutes or until dry. The nanocarbides are characterized by pXRD, XRF, SDT, and TEM. They are also electrochemically tested using linear sweep voltammetry (LSV).

5.2.3. Materials Characterization. pXRD patterns of PBAs and PBA derived nanocarbides were collected at room temperature on a Rigaku Miniflex powder diffractometer (Cu Kα source, λ = 1.54 Å). Elemental ratios in both PBA and nanocarbides were confirmed using XRF on a Panalytical Epsilon XRF analyzer (Cu Kα source). Size, morphology, and elemental disribution of PBA precursors were investigated *using* SEM imaging on a Jeoul (15 keV,) equipped with an energy dispersive x-ray spectrometer (EDX). Size, size dispersity, and morphology of the PBAs and nanocarbides were estimated using ImageJ software (sample size = 100 particles) *using SEM and* TEM images (collected on a Tecnai Osiris TEM, 200 kV). Scanning differential calorimetry was used to interrogate the thermal stability of PBA and nanocarbide materials, collected on a TA instruments Q600 ramp rate 10°C/min up to 700°C.

5.2.4. Electrode Preparation. A catalyst slurry was prepared using 1mg of catalyst powder and 1mL of methanol. The slurry was sonicated until homogenized ~ 1 minute and then the suspension was dropcasted onto the carbon working electrode (5 mm x 4 mm) of a Pine instruments screen printed electrode (SPE). The mass loading onto the surface of the electrode is approximately 0.2 mg/cm^2. The electrodes were dried at room temperature for about 30 minutes before electrochemical measurements were performed.

5.2.5. Electrochemical Measurements. All electrochemical measurements were performed using a Pine research 3 electrode screen printed electrode system, connected to a CH 660E potentiostat. The SPEs contain a carbon working and counter electrode as well as a Ag/AgCl reference electrode. For OER measurements, 1M KOH electrolyte was used and for HER, 1M H_2SO_4 electrolyte was used. All potentials were converted to the reversible hydrogen electrode potential using the equation 11.

$$E_{vs.\ RHE} = E_{vs.\ Ag/AgCl} + 1.009\ V \quad \text{(Eq. 11)}$$

The potentials vs RHE were then used to calculate the overpotentials for OER using equation 10.

$$\eta = E_{vs.\ RHE} - 1.23\ V \quad \text{(Eq. 10)}$$

Tafel slopes were calculated from the linear kinetic region from the plot of log(j) vs η.

5.3. Results and Discussion

5.3.1. PBAs as Sacrificial Single Source Precursors. Previous work in the Strouse group at FSU has shown that Prussian blue analogues can be implemented as single source precursors for

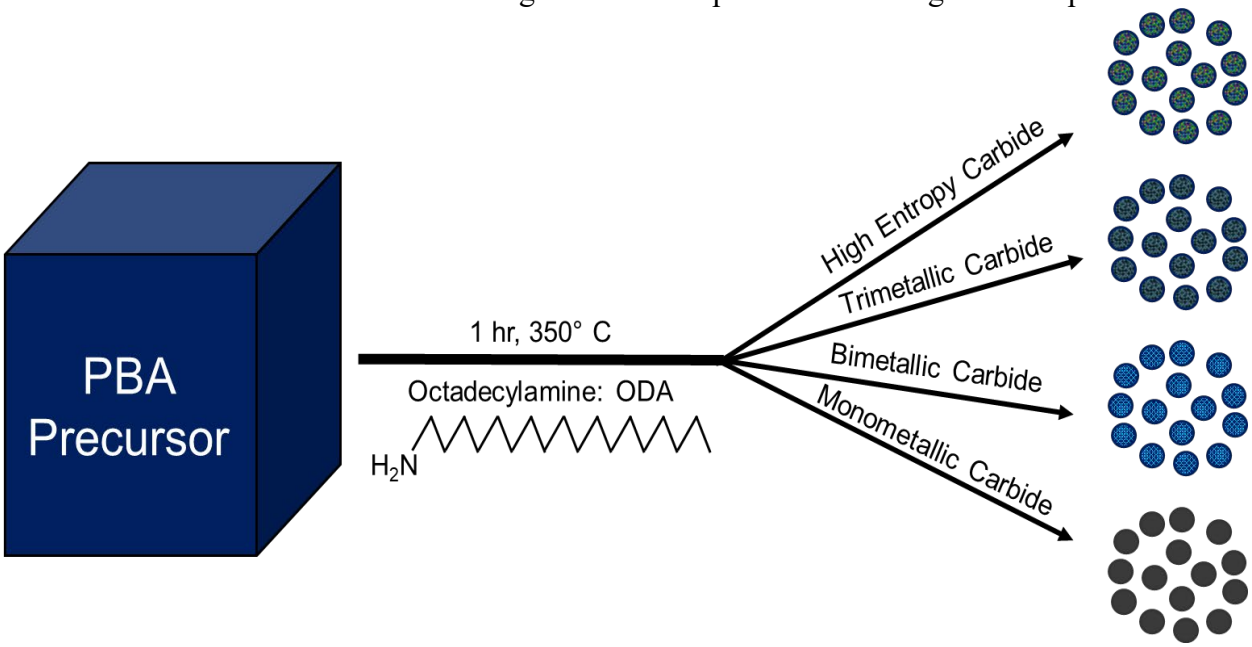

Scheme 1. Prussian Blue Analogues as functional single source precursor for the synthesis of high entropy carbides with controlled metal ratios.

Table 5.1. XRF confirmed elemental compositions for PBA precursors and PBA-derived nanocarbides.

Metal	Target %	Actual % (PBA)	Actual % (Carbide)
Monometallic			
Ni	100	100	99
Bimetallic			
Fe	50	38	38
Ni	50	62	62
Trimetallic			
Fe	33	32	30
Co	33	38	36
Ni	33	30	34
Tetrametallic			
Cr	25	13	7
Fe	25	30	27
Co	25	28	32
Ni	25	29	34
Pentametallic			
Cr	20	13	12
Mn	20	16	17
Fe	20	24	24
Co	20	27	27
Ni	20	20	21

the formation of monometallic and bimetallic nanocarbide materials.[10,23,52,142] Additionally, it was found that the metal ratio of multi-metallic systems can be systematically tuned based on the composition of the PBA precursor[23]. In this work, we translate our synthesis to a multitude of nanocarbide materials showing that PBAs are an efficient, scalable, and rational single source precursor solution for the production of nanocarbides with controlled compositions from one metal to five metal systems. Scheme 1 illustrates the top-down synthetic pathway where PBAs are used as a sacrificial template to produce the resultant nanocarbide materials. For the formation of the carbide, the solvent and temperature of reaction are crucial. In earlier studies, we found that the reaction must be done at the boiling point of the solvent to obtain higher quality nanomaterials,

using this method can produce nanomaterials on the gram scale, and that the size of the resultant material is proportional to the PBA precursor size.[10,52,191] Therefore all materials in this study were synthesized by decomposing PBA precursor in boiling octadecylamine for one hour.

5.3.2. Elemental Composition Verification of PBA and PBA – Derived Nanocarbides. The elemental composition of PBA precursors and PBA-derived nanocarbides were verified using XRF and SEM/EDS characterizations. The XRF values in table 5.1 show the ratio of metals in starting PBA materials is majorly maintained in the resultant nanocarbide. A complete list of XRF values for all nanocarbides produced with differing compositions from monometallic to pentametallic is shown in appendix c. Appendix C also includes XRF data from experiments in controlling the metal ratios in bimetallic to pentametallic systems. The elemental compositions were verified using SEM/EDX where XRF alone indicates the elemental make up in the sample as a whole but does not provide information on the distribution of the elements in the material. Figure 5.1 shows the SEM/EDX elemental mapping results for bimetallic to pentametallic PBA (5.1 a − d), and bimetallic to pentametallic nanocarbide (5.1 e − h). Each color corresponds with a metal; blue is Cr Kα, red is Mn Kα, green is Fe Kα, orange is Co Kα, and purple is Ni Kα. For a material to be considered a high entropy material, the elemental composition must be nearly one to one, contain randomly distributed elements (solid solution), and comprise at least 5 unique elements. As illustrated in 5.1, there is a random and proportional distribution of the elements in both PBA precursors and PBA-derived nanocarbides. To ensure there was a random and proportional distribution of metals in these samples, higher magnification images were collected and support the findings of the lower magnification results shown in figure 5.2. It is important to demonstrate the elemental proportions on a single particle for these materials to be categorized as high entropy.

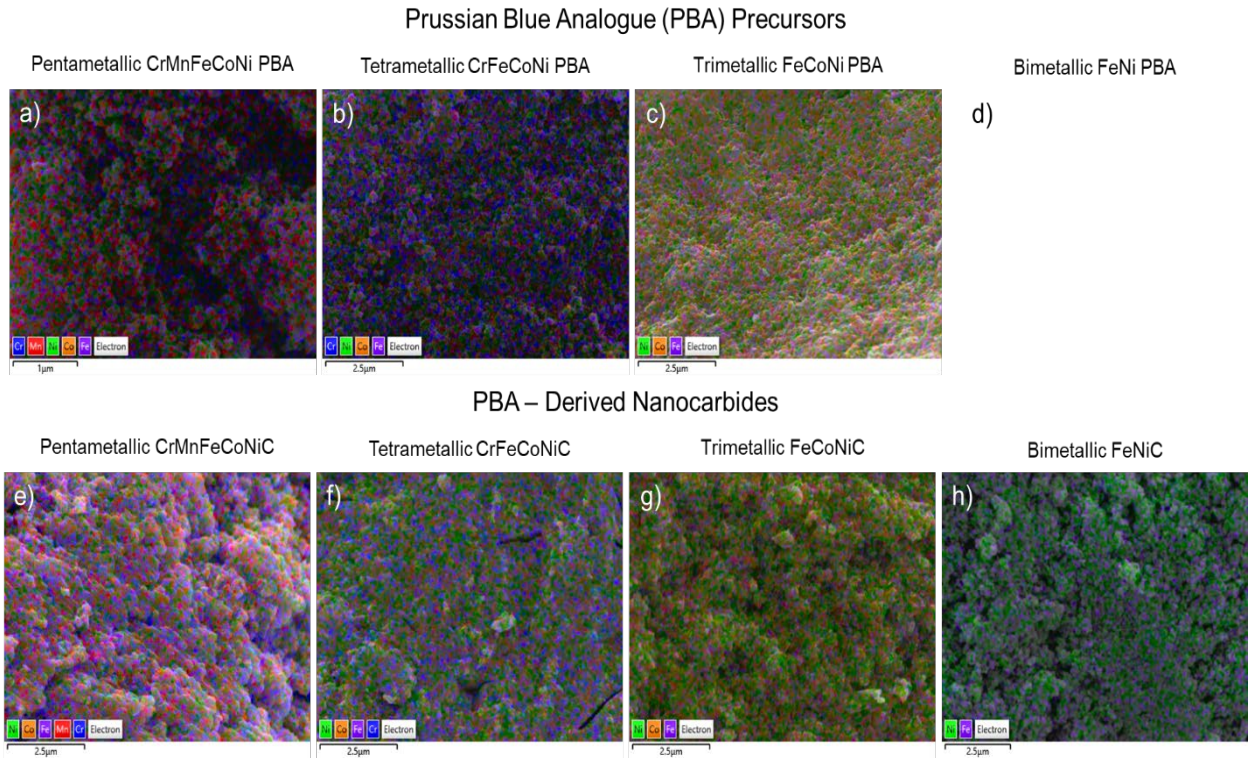

Figure 5.1. SEM/EDS mapping elemental compositions on select as synthesized PBA precursors and PBA-derived nanocarbides. Blue represents chromium, red represents manganese, purple represents iron, orange represents cobalt, and green represents nickel.

5.3.3. Morphology, Size, and Lattice Fringe Analysis of PBA – Derived Nanocarbides.

Once elemental composition was confirmed, TEM images of the selected set of nanocarbides were executed shown in figure 5.3. Interestingly, the morphology of the nanocarbides does not change with different metal compositions. The range of morphologies seen in these materials are ____ to spheres. The pentametallic CrMnFeCoNiC nanocarbides (figure 5.3 a) show a spherical structure with an average size of 17 nm. The tetrametallic CrFeCoNiC nanocarbides (figure 5.3 b) show a spherical structure with an average size of 16nm. The trimetallic FeCoNiC nanocarbides (figure 5.3 c) show a spherical structure with an average size of 11nm. The bimetallic FeNiC nanocarbides (figure 5.3 d) show a rod like structure with an average size of 55 +/- 15 nm. The monometallic Ni_3C nanocarbides (figure 5.3 e) show a hexagonal platelet like structure with an average size of

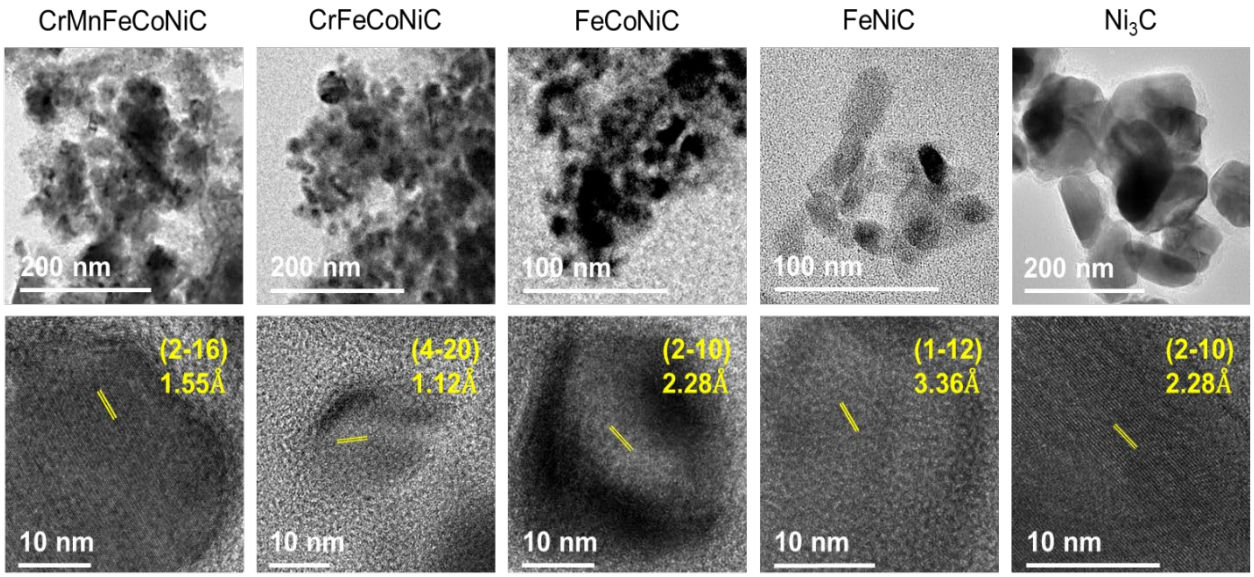

Figure 5.2. TEM images of monometallic to pentametallic PBA-derived nanocarbides. a-e images are lower magnification to highlight morphological features whereas f-j are higher magnification images displaying lattice fringes within single particles.

86 +/- 26 nm. Interestingly, the nanocarbides decrease in size from monometallic to trimetallic and then slightly increase in size as the 4th and 5th metals are incorporated. Higher magnification images were gathered for lattice fringe analysis of the individual particles. Figure 5.3f shows the lattice fringes seen in the pentametallic nanocarbide, the fringe pattern was indexed to the d-spacing of 1.55Å which matches the (2-16) lattice plane for the Ni_3C crystal structure. Figure 5.3 g shows the lattice fringes seen in the tetrametallic nanocarbide, the fringe pattern was analyzed and matches the (4-20) lattice plane for the Ni_3C crystal structure. Figure 5.3 h shows the lattice fringes seen in the trimetallic nanocarbide, the fringe pattern was analyzed and matches the (2-10) lattice plane for the Ni_3C crystal structure. Figure 5.3 i shows the lattice fringes seen in the bimetallic nanocarbide, the fringe pattern was analyzed and matches the (1-12) lattice plane for the Ni_3C

Table 5.2. TEM measured nanocarbide particle size.

Sample	CrMnFeCoNiC	CrFeCoNiC	FeCoNiC	FeNiC	Ni_3C
Particle Size	17 +/- 5 nm	16 +/- 3 nm	11+/- 2 nm	55 +/- 15 nm	86 +/- 26 nm

crystal structure. Figure 5.3 j shows the lattice fringes seen in the monometallic nanocarbide, the fringe pattern was analyzed and matches the (2-10) lattice plane for the Ni_3C crystal structure.

5.3.4. Structural Characterization of PBA and PBA – Derived Nanocarbides. The crystal structure of the PBA precursors (Figure 5.4a) and nanocarbides (Figure 5.4b) were investigated using pXRD analysis. All PBAs, except the Ni PBA, match well to the cubic Fm3m PBA structure type (ICSD: 89398) with a small shift (< 1°) of all reflections toward a higher 2θ indicative of a small lattice distortion as the crystal accommodates smaller elements into its coordination sites. The monometallic Ni PBA matches the tetrahedrally coordinated Prussian

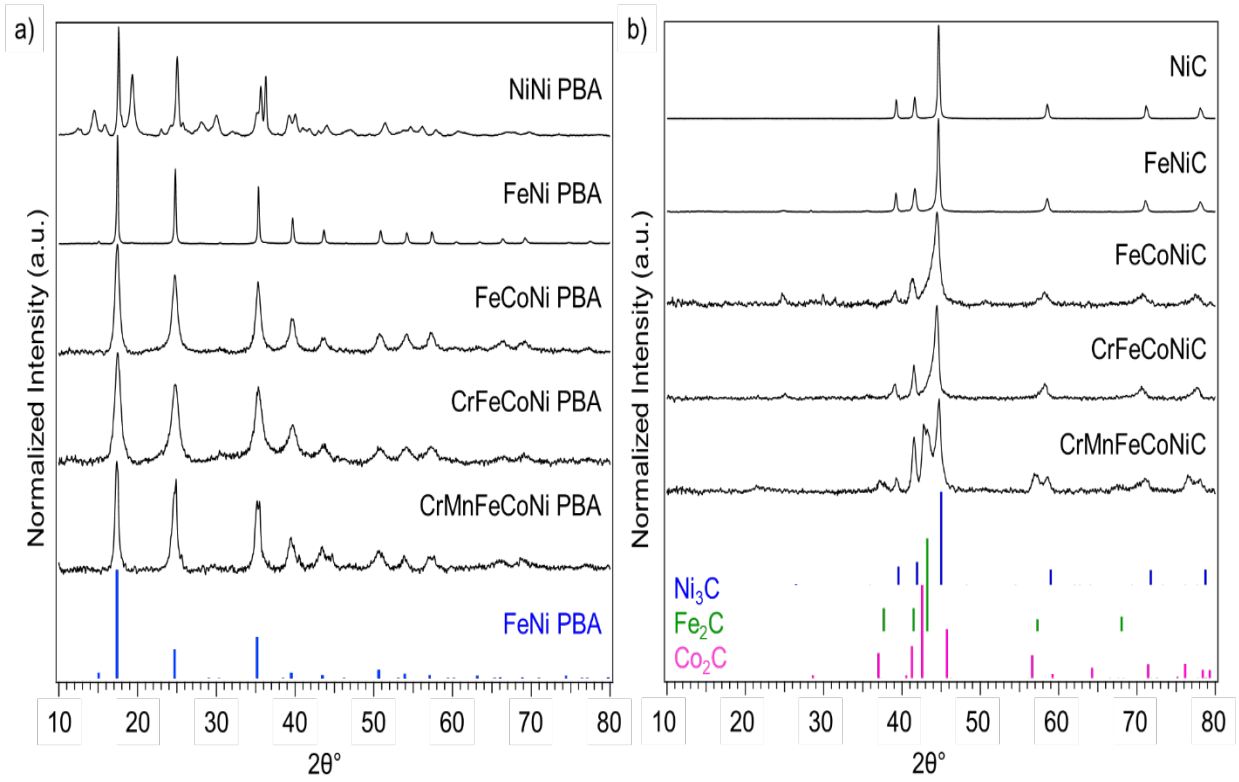

Figure 5.3. pXRD of monometallic to pentametallic a) PBA precursors and b) PBA-derived nanocarbides. Reference patterns are shown below. For a) a representative pattern of $FeNi(CN)_6$ was chosen as it is the most common structure type for PBA, and b) blue card represents the Ni_3C phase (ICSD: 17005) , green card represents Fe_2C phase (ICSD: 42542), and pink reflections represent Co_2C phase (COD: 1528415).

Blue Analogue structure (ICSD:28668) as Ni^{2+} prefers to coordinate in a tetrahedral confirmation over octahedral to satisfy its octet. In figure 5.4b there is one major phase, Ni_3C (ICSD: 17005), that is preferred by the majority of nanocarbides. In our other studies we've seen composition dependent phase evolutions in bimetallic FeCo and FeNi systems, where the metal ratio is critical in the separation of single phase materials. [23] Notably as the entropy of the system increases, more metals are added, there is an addition of phase complexity rather than the typical "cocktail effect" seen in literature where the increased entropy leads to a single more stable phase.[162,210] This could be due to the fact that carbides are intrinsically metastable (kinetic) phases, therefore the resultant phase is dependent on a multitude of factors, not just composition alone.[cite FeCo halide] A library of all iterations of nanocarbides produced from differing compositions of PBA are available in Appendix D.

5.3.5. Electrochemical Water Splitting Activities for PBA – Derived Nanocarbides. Carbides are materials of interest in many fields from biomedical to heterogenous catalysis for their diverse range of intriguing properties.[20,150,158,211–213] Our previous work has shown PBA−derived nanocarbides as promising electrocatalysts for the OER and HER.[23,52] A series of monometallic to pentametallic PBA−derived nanocarbides were tested for catalytic activity in the HER and OER shown in Figure 5.5. Figure 5.5a and b are the linear sweep voltammograms resultant for each material as well as a blank electrode. The LSVs were run in triplicate on a three-electrode carbon screen printed electrode purchased from pine research in 1M H_2SO_4 electrolyte for HER measurements and 1M KOH for OER measurements with a catalyst mass loading of 0.1 mg/cm^2. No further optimization of the analytical method was performed. Surprisingly, the material that performed the best for the HER was monometallic Co_2C. Although a trend correlating composition to increasing entropy was hypothesized, the results show no real trend for the HER.

The performance from best to worst HER electrocatalyst is Co_2C > Fe_3C > FeCoNiC > CrFeCoNiC > CrMnFeCoNiC > FeNiC > Ni_3C with overpotentials of −0.220 V, −0.482 V, −0.559 V, −0.580 V, −0.650 V, −0.672 V, and −0.681 V vs. RHE respectively. Interestingly, the best performing HER catalyst was also the best performing OER catalyst, Co_2C which produced an overpotential of 0.543 V. The order for best to worst OER catalyst is Co_2C > FeNiC > FeCoNiC > CrFeCoNiC > CrMnFeCoNiC > Fe_3C > Ni_3C with overpotentials of 0.543 V, 0.578 V, 0.718 V, 0.742 V, 0.829 V, 1.066 V, and 1.276 V respectively. There is a general trend of decreasing catalytic activity with increasing entropic contribution from bimetallic to pentametallic carbides. Although this trend is exactly the opposite from what we expected, we believe that the phase of the material is playing a critical role in the activity of the catalysts. In our previous work we saw that the M_2C (Co_2C) structure outperformed any other carbide structure in the FeCo system and the M_3C phase performed the worst. Unfortunately, the Ni_3C (M_3C) phase was the predominant phase formed in this study, however, further studies are underway to tune the phase of these high entropy materials in order to obtain better performing catalysts. With potential phase contributions, unoptimized metal ratio, and unoptimized electrochemical measurements it was not surprising that these catalysts were not the next best OER or HER electrocatalyst. Nonetheless, this study trailblazes the path for future studies optimizing the performance of these materials.

Table 5.3. OER and HER overpotentials vs RHE.

Electrocatalyst	OER (η vs RHE)	HER (η vs RHE)
Fe_3C	1.066	-0.482
Co_2C	0.543	-0.22
Ni_3C	1.276	-0.681
FeNiC	0.578	-0.672
FeCoNiC	0.718	-0.559
CrFeCoNiC	0.742	-0.58
CrMnFeCoNiC	0.829	-0.65

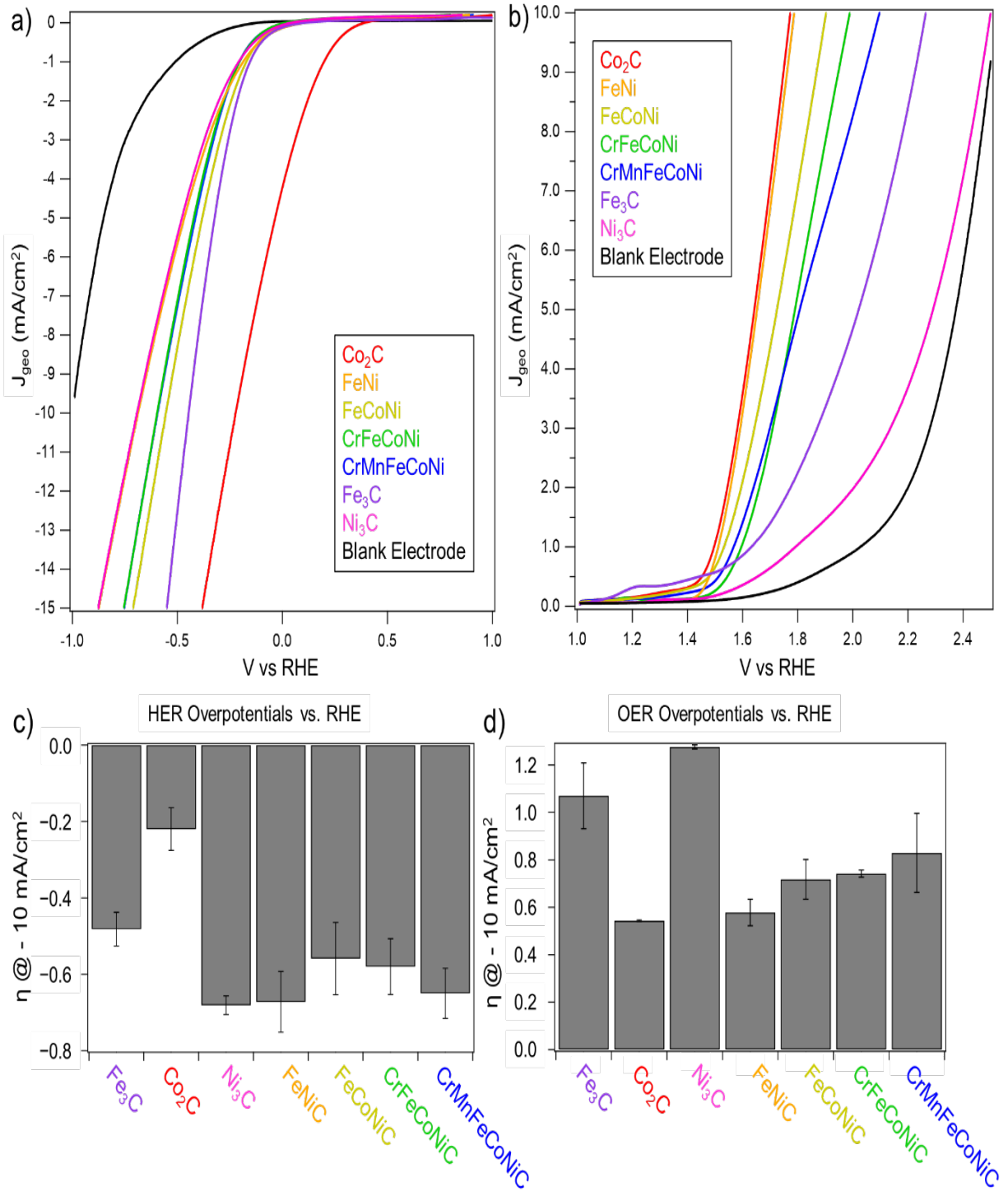

Figure 5.4. Linear sweep voltammograms to evaluate electrocatalytic performance in HER (a and OER (b for monometallic to pentametallic nanocarbides. c) and d) are bar charts comparing the overpotentials for each sample. Purple represents Fe_3C, red represents Co_2C, pink represents Ni_3C, orange represents FeNiC, gold represents FeCoNiC, green represents CrFeCoNiC, and blue represents CrMnFeCoNiC.

5.4. Conclusions

In conclusion, high entropy carbide nanomaterials hold tremendous potential for revolutionizing materials science and engineering. In this study we have shown that Prussian Blue Analogues can be implemented to form solid solution nanocarbide materials from monometallic to pentametallic (high entropy) systems. The PBA serves as a single-source sacrificial precursor that controls the composition of the resultant nanocarbide. Unlike what has been seen in the literature, these materials seem to become more structurally complex as entropy is increased, yet they maintain their metal compositions as solid solutions. The best performing OER and HER catalyst in this study was the Co_2C nanocarbide by generating overpotentials of 0.543 V and −0.220 V respectively. Although these materials are not outperforming state of the art materials, recent advancements have demonstrated nanocarbides exceptional catalytic properties and significant opportunities remain for further exploration and development.[21,23,52,53,71,198,214,215] By focusing on synthetic control of composition, phase, size, and morphology, researchers can unlock new capabilities and propel the field of high entropy carbide nanomaterials towards transformative innovations.

CHAPTER 6

FROM MONOMETALLIC TO PENTAMETALLIC: SYNTHESIS OF PBA-DERIVED MEDIUM AND HIGH ENTROPY NANOMX-IDES FOR THE OXYGEN EVOLUTION REACTION

6.1 Introduction

The rapid advancement of renewable energy technologies and the persistent demand for efficient, sustainable chemical processes have necessitated the development of novel materials with exceptional catalytic properties. High-entropy materials (HEMs), characterized by their unique multi-element compositions resulting in remarkable physical and chemical properties, have received significant attention in recent years.[162,208,216–220] Among these, high-entropy phosphides, oxides, sulfides, and carbides derived from Prussian blue analogues (PBAs) have emerged as promising candidates due to their tunable compositions, scalability, and ability to be implemented as a single source precursors.[54,204,221–226] The traditional catalytic materials, while effective, often suffer from limitations such as high cost, limited availability, and suboptimal stability under operational conditions. Noble metals like platinum, iridium, and ruthenium, for instance, are excellent catalysts for reactions like the oxygen evolution reaction (OER) and hydrogen evolution reaction (HER) but are neither cost-effective nor sustainable for large-scale deployment.[17,36,37,227,228] Therefore, the motivation behind this research is to explore and develop new classes of PBA – derived HEMs that can offer comparable or superior catalytic performance while being economically viable and sustainable.

Prussian blue analogues, with their well-defined frameworks and versatile chemistry, serve as ideal precursors for the synthesis of high-entropy phosphides, oxides, sulfides, and carbides. The ability to incorporate multiple metal cations into the Prussian blue framework and

subsequently convert these into various high-entropy phases provides a unique approach to designing materials with tailored properties. This research aims to leverage the inherent flexibility of PBAs to create HEMs with enhanced catalytic activity, stability, and cost-effectiveness.[54,222,223]

Recent advancements have demonstrated the potential of HEMs in various catalytic applications. High-entropy oxides, for example, have shown remarkable performance in OER due to their stable multi-cationic structures, which promote enhanced catalytic activity and stability.[208,222,229,230] High-entropy carbides and phosphides have also been explored for their excellent electrical conductivity and catalytic efficiency, making them suitable for applications in HER and OER.[218,231–233] However, there remains a significant gap in understanding the full potential of high-entropy sulfides and the synergistic effects of multiple anionic species in these complex materials.

To date, research has predominantly focused on single-phase HEMs, and the exploration of mixed-phase high-entropy materials derived from PBAs remains in its infancy. Additionally, while the synthesis of high-entropy oxides have been extensively studied, there is limited knowledge regarding the controlled synthesis of high-entropy carbides, phosphides, and sulfides from PBAs.[162,208,216,222,229] Addressing these gaps is crucial for fully harnessing the potential of these materials and developing a comprehensive understanding of their structure-property relationships.

The primary objective of this research is to synthesize and characterize high-entropy phosphides, oxides, sulfides, and carbides derived from Prussian blue analogues, and to evaluate their catalytic performance in key reactions such as OER and HER. By systematically varying the composition and synthesis conditions, we aim to elucidate the fundamental principles governing the catalytic behavior of these materials and identify the optimal compositions for specific

applications. Furthermore, this research seeks to address the scalability and practical applicability of high-entropy materials. By utilizing PBAs as precursors, we aim to develop synthesis protocols that are not only effective but also scalable and economically feasible for large-scale production. The insights gained from this study will provide a solid foundation for the future design and development of high-entropy materials with tailored properties for a wide range of catalytic applications. Herein, monometallic to pentametallic MX-ides (X= C, O, P, S) are synthesized using PBAs as a single source precursor and subsequently characterized using pXRD and XRF.

6.2 Experimental Methods

All commercially available reagents were used without further purification. Precursors for all PBAs were $K_3Cr(CN)_6$ (made in house), $K_3Mn(CN)_6$ (made in house), $K_3Fe(CN)_6$ (Sigma Aldrich, >99%), $K_3Co(CN)_6$ (Sigma Aldrich, >99%), $K_2Ni(CN)_4$ (Alfa Aesar, >99%), KCl (Sigma Aldrich, 98%), $CrCl_3 \cdot 6H_2O$ (Sigma Aldrich, 98%), $MnCl_2 \cdot 4H_2O$ (Sigma Aldrich, 98%), $FeCl_2 \cdot 4H_2O$ (Thermo Fisher, >99%). $CoCl_2 \cdot 6H_2O$ (Thermo Fisher, >99%), and $NiCl_2 \cdot 6H_2O$ (Thermo Fisher, >99%). Solvents used for synthesis were ultrapure water (18.2 Ω cm^{-1} at 25.0 °C, Thermo Scientific Barnstead E-Pure ultrapure water purification system), octadecylamine (ODA) (Thermo Fisher, 90%), dodecanethiol (DDT) (Thermo Fisher, >99%), trioctylphosphine (TOP) (Thermo Fisher, >99%), acetone ((VWR, ACS Grade) and toluene (VWR, ACS Grade).

6.2.1. General Synthesis of Prussian Blue Analogue Precursors. All PBA precursors (from monometallic to pentametallic) are synthesized through a known precipitation method adapted from Hardy et al. Succinctly, two solutions are prepared, a 5mM solution of all cyanometallate salts in equimolar ratios which sum to 1 mmol, as well as a 10mM solution of all metal chloride salts in equimolar ratios which sum to 1 mmol with an additional 5 mmol KCl used as a chelating agent for the PBA formation. For monometallic solution one has 1 mmol

cyanometallate salt and solution two has 1 mmol of metal chloride salt and 5 mmol of KCl, for bimetallic there are 0.5 mmol of each cyanometallate salt in solution 1 and 0.5 mmol of metal chloride salts with the added 5 mmol KCl. The same method is used for trimetallic, tetrametallic, and pentametallic PBAs. One solutions are prepared, solution 2 is slowly added to solution 1 and the resultant reaction mixture is stirred at room temperature for at least 2 hours to ensure PBA formation. The reaction mixture is centrifuged, the PBA is collected and then washed thrice with ultrapure H_2O. The PBAs are dried at 120 °C for approximately 30 minutes or until completely dry. The PBAs are characterized by pXRD, SEM, EDX, XRF, SDT, and FT-IR.

6.2.2. General Synthesis of Nanocarbides. All nanocarbides (from monometallic to pentametallic) are synthesized through a high temperature organic synthesis method. In summary, 200mg of the PBA precursor and 17.24g (20mL) of octadecylamine are added to a three-neck round bottom flask equipped with a condenser. Under inert atmosphere the reaction mixture is heated to 350°C (BP of octadecylamine) for an hour and subsequently quenched with toluene. The resultant reaction mixture is centrifuged (hot ~ 150°C), the pellet is then washed thrice with toluene, once with acetone, thrice with ultrapure H_2O, and once more with acetone. The resultant nanocarbides are dried @ 100°C for approximately 15 minutes or until dry. The nanocarbides are characterized by pXRD, XRF, SDT, and TEM. They are also electrochemically tested using linear sweep voltammetry (LSV).

6.2.3. General Synthesis of Nano-oxides. All nano-oxides (from monometallic to pentametallic) are synthesized through a solid-state decomposition reaction. Briefly, 200mg of the PBA precursor is loaded into a quartz boat and then into a tube furnace, open to air on both sides. The tube furnace is closed and heated up to 350°C for 10 minutes and subsequently cooled to room

temperature. The nano-oxides are characterized by pXRD, XRF, SDT, and TEM. They are also electrochemically tested using linear sweep voltammetry (LSV).

6.2.4. General Synthesis of Nanosulfides. All nanosulfides (from monometallic to pentametallic) are synthesized through a high temperature organic synthesis method. In summary, 200mg of the PBA precursor and 20mL of dodecanethiol are added to a three-neck round bottom flask equipped with a condenser. Under inert atmosphere the reaction mixture is heated to 270°C (BP of dodecanethiol) for an hour and subsequently quenched with toluene. The resultant reaction mixture is centrifuged, the pellet is then washed thrice with toluene, once with acetone, thrice with ultrapure H_2O, and once more with acetone. The resultant nanosulfides are dried @ 100°C for approximately 15 minutes or until dry. The nanosulfides are characterized by pXRD, XRF, SDT, and TEM. They are also electrochemically tested using linear sweep voltammetry (LSV).

6.2.5. General Synthesis of Nanophosphides. All nanophosphides (from monometallic to pentametallic) are synthesized through a high temperature organic synthesis method. In summary, 200mg of the PBA precursor and 20mL of trioctylphosphine are added to a three-neck round bottom flask equipped with a condenser. Under inert atmosphere the reaction mixture is heated to 270°C (BP of trioctylphosphine) for an hour and subsequently quenched with toluene. The resultant reaction mixture is centrifuged, the pellet is then washed thrice with toluene, once with acetone, thrice with ultrapure H_2O, and once more with acetone. The resultant nanophosphides are dried @ 100°C for approximately 15 minutes or until dry. The nanophosphides are characterized by pXRD, XRF, SDT, and TEM. They are also electrochemically tested using linear sweep voltammetry (LSV).

6.2.6. Materials Characterization. pXRD patterns of PBAs and PBA derived nanomaterials were collected at room temperature on a Rigaku Miniflex powder diffractometer

(Cu Kα source, λ = 1.54 Å). Elemental ratios in both PBA and nanomaterials were confirmed using XRF on a Panalytical Epsilon XRF analyzer (Cu Kα source). Size, morphology, and elemental disribution of PBA precursors were investigated *using* SEM imaging on a Jeoul (15 keV,) equipped with an energy dispersive x-ray spectrometer (EDX). Size, size dispersity, and morphology of the PBAs and nanomaterials were estimated using ImageJ software (sample size = 100 particles) *using SEM and* TEM images (collected on a Tecnai Osiris TEM, 200 kV). Scanning differential calorimetry was used to interrogate the thermal stability of PBA and nanocarbide materials, collected on a TA instruments Q600 ramp rate 10°C/min up to 700°C.

6.2.7. Electrode Preparation. A catalyst slurry was prepared using 1mg of catalyst powder and 1mL of methanol. The slurry was sonicated until homogenized ~ 1 minute and then the suspension was dropcasted onto the carbon working electrode (5 mm x 4 mm) of a Pine instruments screen printed electrode (SPE). The mass loading onto the surface of the electrode is approximately 0.2 mg/cm^2. The electrodes were dried at room temperature for about 30 minutes before electrochemical measurements were performed.

6.2.8. Electrochemical Measurements. All electrochemical measurements were performed using a Pine research 3 electrode screen printed electrode system, connected to a CH 660E potentiostat. The SPEs contain a carbon working and counter electrode as well as a Ag/AgCl reference electrode. For OER measurements, 1M KOH electrolyte was used and for HER, 1M H_2SO_4 electrolyte was used. All potentials were converted to the reversible hydrogen electrode potential using the equation 11.

The potentials vs RHE were then used to calculate the overpotentials for OER using equation 10.

6.3 Results and Discussion

6.3.1. Monometallic PBA – Derived M-Xides. Several monometallic MX-ides were synthesized using our PBA thermal decomposition method. The motivation behind synthesizing these monometallic materials is to gain insight on pure phase compositions that can be used as a building block for fitting more complex systems. Figure 6.1. shows the pXRD results of cobalt PBA − derived sulfide which matches the Co_9S_8 crystal phase. The reference pattern from the crystallography open database for the Co_9S_8 crystal phase is shown below as blue bars. The XRF results from this sample show less than 1% impurities. The sulfide was synthesized by boiling the Co PBA in dodecanethiol for an hour. The pXRD results for the synthesized cobalt and nickel PBA – derived monometallic phosphides are shown in Figure 6.2. The cobalt PBA – derived phosphide matches the CoP crystal phase and the nickel PBA – derived phosphide matched to the Ni_2P crystal phase. The XRF results also indicate less than 1% impurities for both materials. The

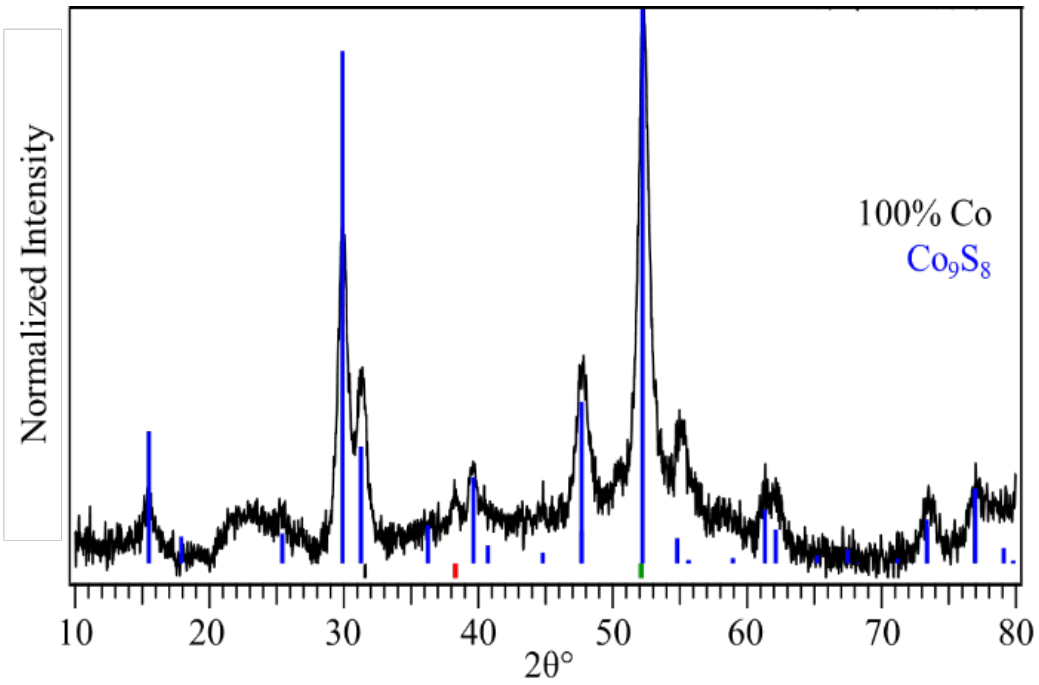

Figure 6.1. pXRD of PBA – derived monometallic sulfide: Co_9S_8. Reference pattern shown in blue (COD:1011005)

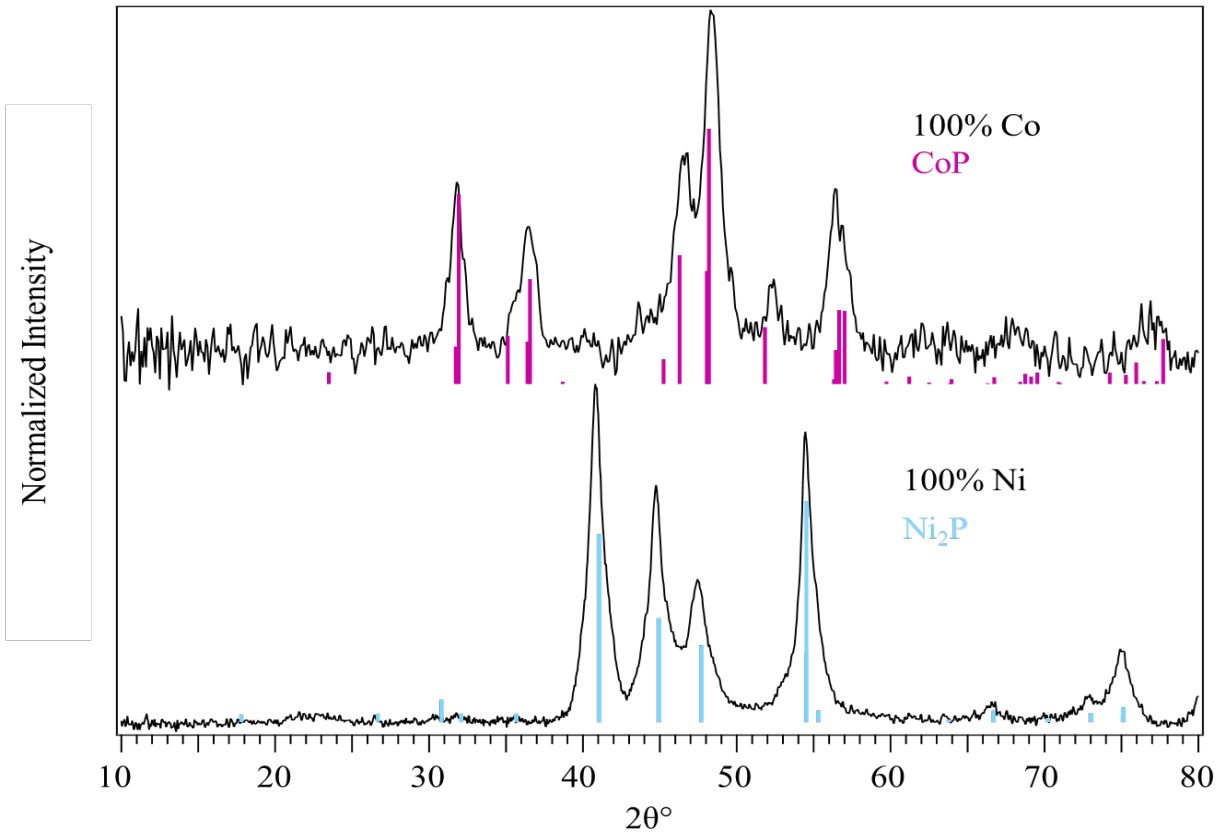

Figure 6.2. pXRD of PBA – derived monometallic phosphides: CoP and Ni_2P. Reference pattern for CoP in pink (COD: 9008928) and Ni_2P shown in light blue (ICSD: 646102).

phosphides were synthesized by boiling each PBA in trioctylphosphine for an hour. The pXRD results for the PBA – derived monometallic oxides are shown in Figure 6.3. The iron variant produced the Fe_3O_4 crystal phase, the cobalt variant produced the Co_3O_4 crystal phase, and the nickel variant produced the NiO_2 crystal phase. The iron and cobalt were both pure phase materials, however the nickel variant has an impurity phase of the $FeNi_3$ alloy. The oxides were synthesized via a solid-state route by heating each PBA to 350°C, held at temperature for 10 minutes, and cooling back to room temperature. We believe the isolation of the $FeNi_3$ impurity is due to the lack of solvent present in this method. Our previous work has shown that solvent influences the

thermodynamic barrier for the formation of alloy.[163] The XRF values also show less than 1% impurities in the oxide materials.

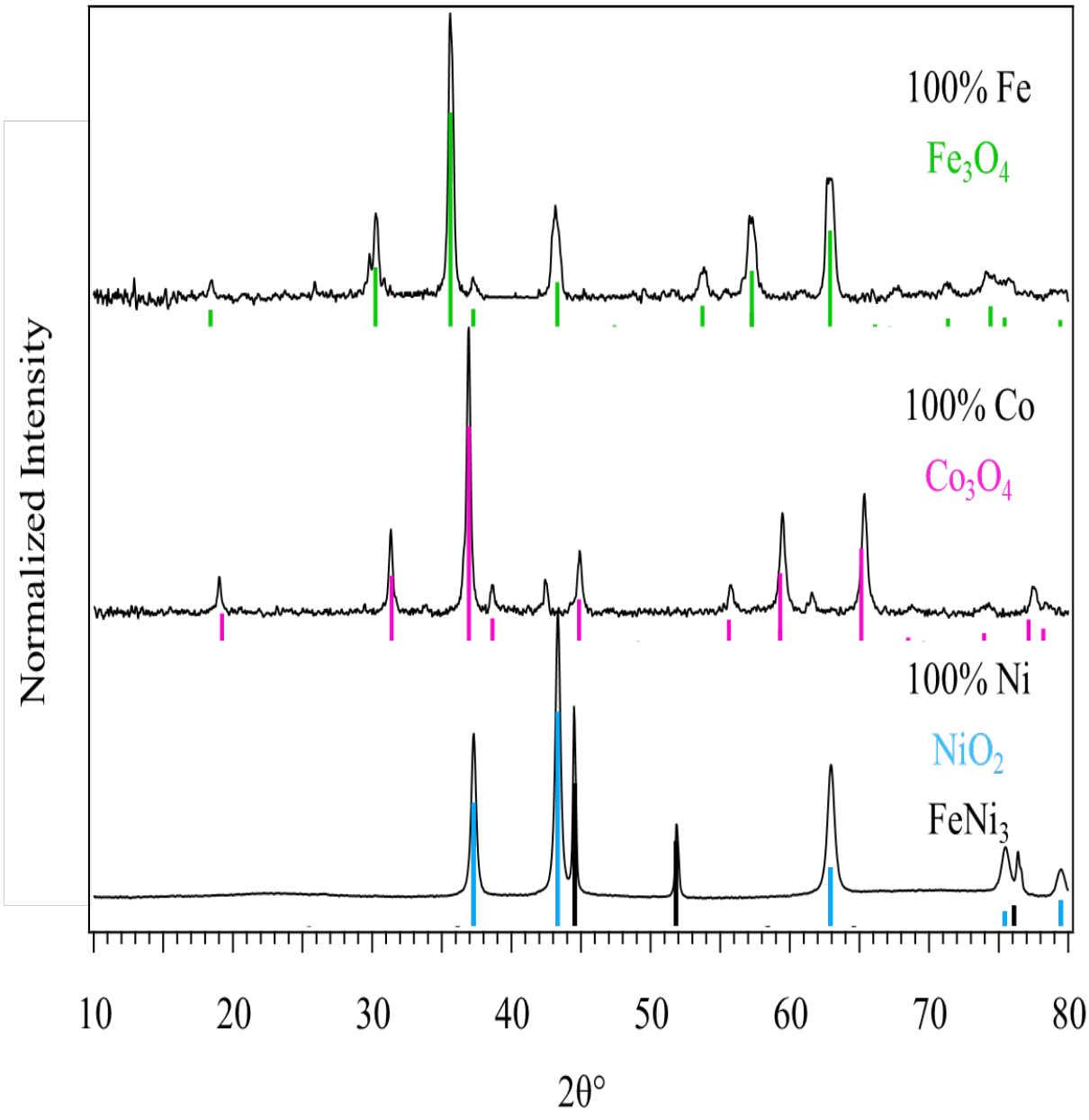

Figure 6.3. pXRD of PBA – derived monometallic oxides, Fe_3O_4, Co_3O_4, NiO_2. Reference pattern for Fe_3O_4 in green (ICSD: 75627) Co_3O_4 in pink (ICSD: 24210) and NiO_2 shown in light be (COD: 1522025).

6.3.2. Bimetallic PBA – Derived M-Xides. Several bimetallic MX-ides were synthesized using our PBA thermal decomposition method. The motivation behind synthesizing these bimetallic materials was to gain insight on the dependence of phase on metal compositions. The materials were synthesized in the same manner as the monometallic materials. The pXRD of

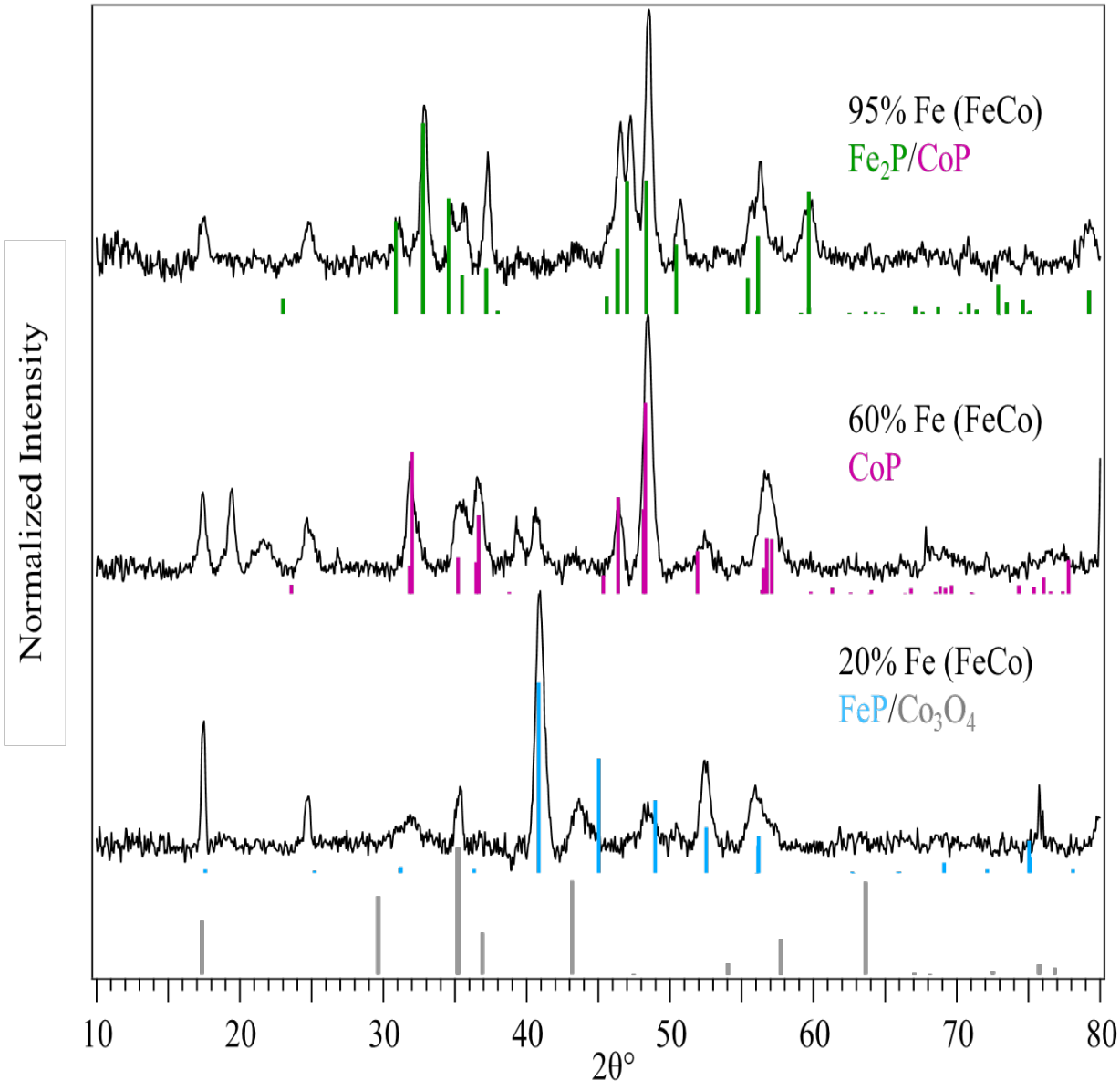

Figure 6.4. pXRD of PBA – derived FeCo bimetallic phosphides containing 95%, 60% and 20% Fe. Reference pattern for FeP in light blue (ICSD: 94379), Fe_2P in green (COD: 1008826), CoP in pink (COD: 9008928), and Co_3O_4 in grey (ICSD: 24210).

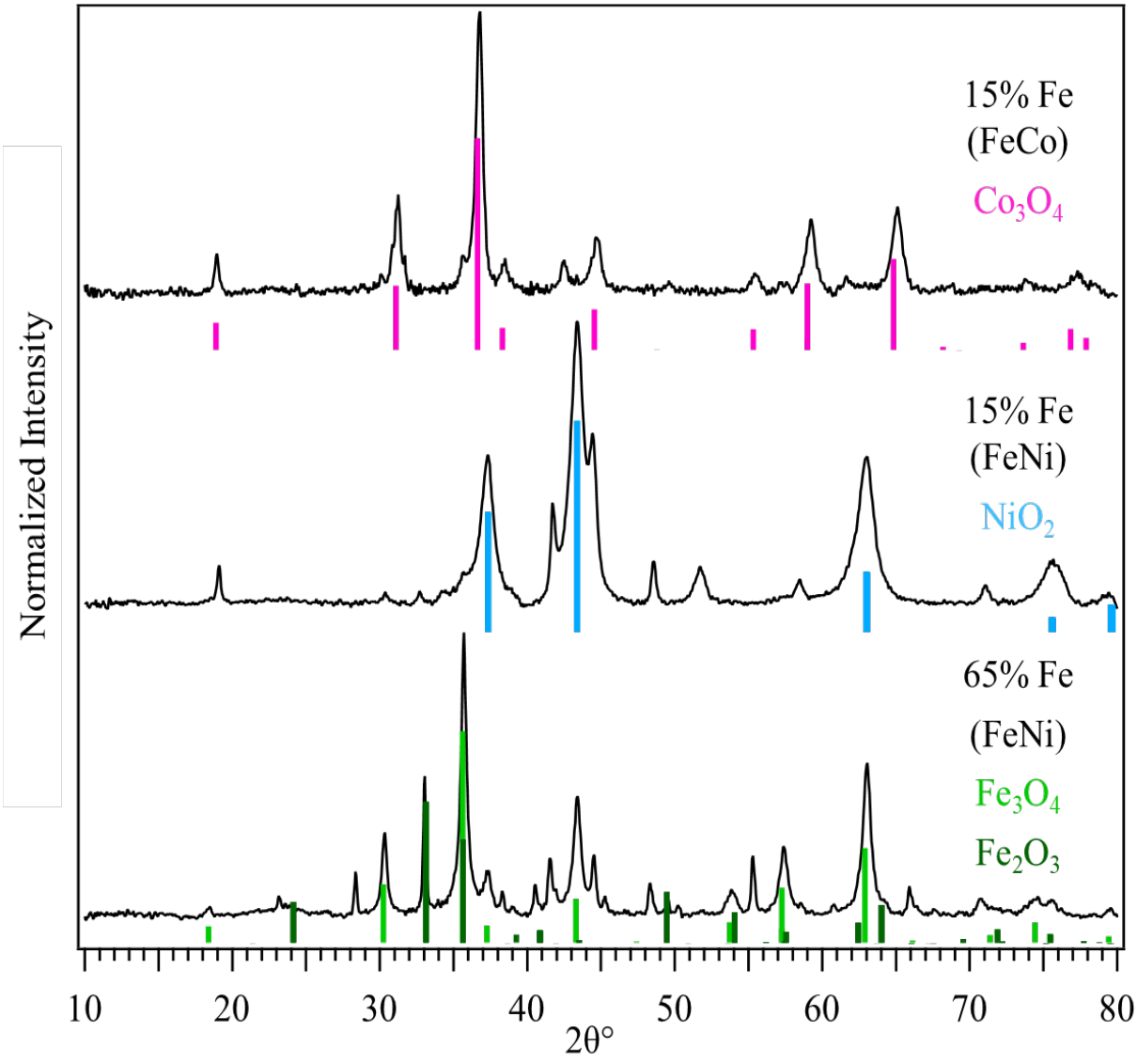

Figure 6.5. pXRD of PBA – derived FeCo and FeNi bimetallic oxides, Fe_3O_4, Co_3O_4, NiO_2. Reference pattern for Fe_2O_3 in dark green (ICSD: 15840), Fe_3O_4 in light green (ICSD: 75627) Co_3O_4 in pink (ICSD: 24210) and NiO_2 shown in light be (COD: 1522025).

bimetallic FeCo and FeNi phosphides are shown in Figure 6.4. The results show that 95% Fe FeCo produces a mixture of iron and cobalt phosphide phases with the major phase being Fe_2P and minor phase CoP. When the amount of Fe decreases to 60% the only phosphide phase isolated is CoP, however this sample is contaminated with a minor amount of Co_3O_4. Notably, as the amount of Fe is further decreased, a new FeP phase is isolated rather than the maintenance of the CoP phase.

There was an oxide impurity in this sample as well. Which is not surprising based on literature reports of phosphides being prone to oxidation under ambient conditions.[30,126,234–237] The XRF results show the maintenance of metal ratios from PBA to phosphide, similar to carbide results. This suggests that PBA is a practical precursor for the synthesis of ratio controlled phosphides, which also agrees with results in literature.[156] Figure 6.5. shows the pXRD results for the 15% Fe FeCo, 15 % Fe FeNi and 65% Fe FeNi PBA – derived oxides. The 15% Fe FeCo oxide matches the Co_3O_4 phase, the 15% Fe FeNi primarily matches the NiO_2 phase and thet 65% Fe FeNi has a mixed oxide composition of Fe_3O_4 and Fe_2O_3.

6.3.3. Pentametallic PBA – Derived M-Xides. Pentametallic materials were synthesized as previously stated. Figure 6.6 shows the pXRD results of each pentametallic material synthesized. The pentametallic carbide (CrMnFeCoNiC) reveals a mixed carbide containing the $Fe_{2.4}C$ and the Ni_3C structure types. The pentametallic oxide (CrMnFeCoNiO) produced a mixed oxide containing both MnO_2 and Co_3O_4 structure types. The pentametallic phosphide (CrMnFeCoNiP) produced a mixed phosphide containing both FeP and CoP structure types. The pentametallic sulfide (CrMnFeCoNiS) produced a pure phase sulfide matching the Co_3S_4 structure type. The pentametallic alloy produced an alloy matching the Fe face centered cubic structure type, however there was a large impurity of MnO in this sample. The oxide impurity was unsurprising as Mn based materials tend to oxidize easily under ambient conditions, and many metal alloys are not air stable as well.[15,30,161,198]

6.4 Conclusions and Future Work

In this work PBAs were implemented as single source precursors for the production of monometallic, bimetallic, and pentametallic nanomaterials. It was found that the metal ratio was maintained from the PBA to the PBA – derived materials, an important attribute for the future use

in various applications like catalysis and magnetism. Pure phase materials were created from the monometallic PBAs and in the pentametallic sulfide. Majorly mixed phase materials were produced in more complex systems. The work done in chapter 4 poses as a potential avenue to

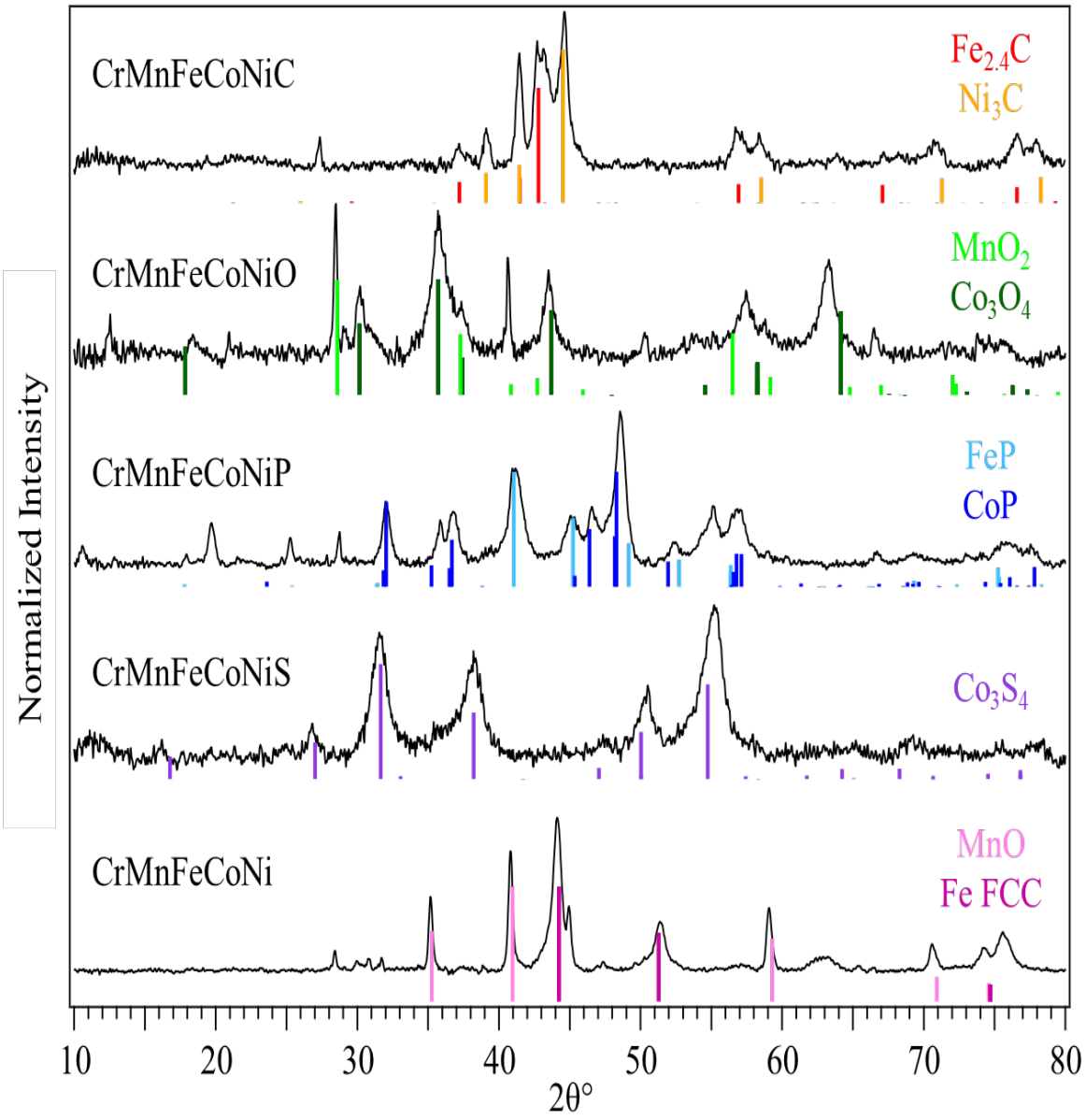

Figure 6.6. pXRD of PBA – derived CrMnFeCoNi pentametallic high entropy materials, CrMnFeCoNiC, CrMnFeCoNiO, CrMnFeCoNiP, CrMnFeCoNiS, and CrMnFeCoNi alloy. Reference pattern for $Fe_{2.4}C$ in red (COD: 1545252), Ni_3C in orange (ICSD: 17005), MnO_2 in light green (COD:1514232), Co_3O_4 in dark green (ICSD: 24210), FeP in light blue (ICSD: 94379), CoP in dark blue (COD: 9008928), Co_3S_4 in purple (COD:1011005), MnO in light pink (COD: 9006660), Fe FCC (ICSD: 44862).

control phase compositions in these more complex systems. The current materials should be further characterized using SEM or TEM/EDS for elemental mapping. The materials that possess impurities should be resynthesized or separated from impurities to ensure accurate characterizations. The synthesis of PBA materials needs to be optimized in the future to effectively control size, shape, and phase compositions. However, there are known routes to achieve these goals in the literature, as well as in this thesis. [238–241] Other future work includes testing PBA – derived materials in targeted applications like catalysis and magnetism.

CHAPTER 7

SUMMARY AND OUTLOOK

This thesis serves to pioneer the design of new advanced materials that are cost effective, globally accessible, sustainable, and scalable. In this work a library of new materials has been synthesized, characterized, and tested for application in the OER and HER. In accordance with the structure – property dogma, there is a specific focus on controlling complex material characteristics like crystal phase composition and elemental composition to produce next generation materials. Insight on reactivity, structure, material transformations, and catalytic properties have been revealed from the monometallic building blocks to the high entropy pentametallic materials studied in this work. This work uncovered a potentially universal approach to isolate pure phase carbide materials, a solution that has been researched for several decades now.[141,149,184,212,242–246] The versatility of PBA – derived synthesis was explored by implementing this technique on several ceramic type materials (oxide, phosphide, carbide, and sulfides).

Future studies that further expand this field include optimization studies on reaction conditions to create size, shape, and morphologically controlled materials, expanding metallic ratio studies to optimize OER and HER performance, optimizing OER/HER testing protocols, expanding synthesis to other first and second row transition metals, translation of the halide - mediated phase control to other ceramic type systems, and testing PBA – derived carbide materials for other applications in catalysis and magnetism based on the properties of the monometallic iron, chromium, and cobalt carbide systems.[20,134,157,158,174,176]

APPENDIX A: PXRD POWDER MATCHING FOR ALL AS – SYNTHESIZED FECO NANOCARBIDES

Appendix A contains the complete pXRD data for all as synthesized $Fe_xCo_{1-x}C_y$ nanocarbides. Synthetic parameters tested were concentration of Fe, halide species, and halide concentrations. Four different concentrations (19%, 35%, 60%,80% Fe) of Fe were tested. Four halide species were tested (TBAF, TBAC, TBAB, TBAI). Four to five halide concentrations were tested ranging from 0.1 mmol per reaction to 3 mmol per reaction. Appendix A is to be used in reference for chapter 4.

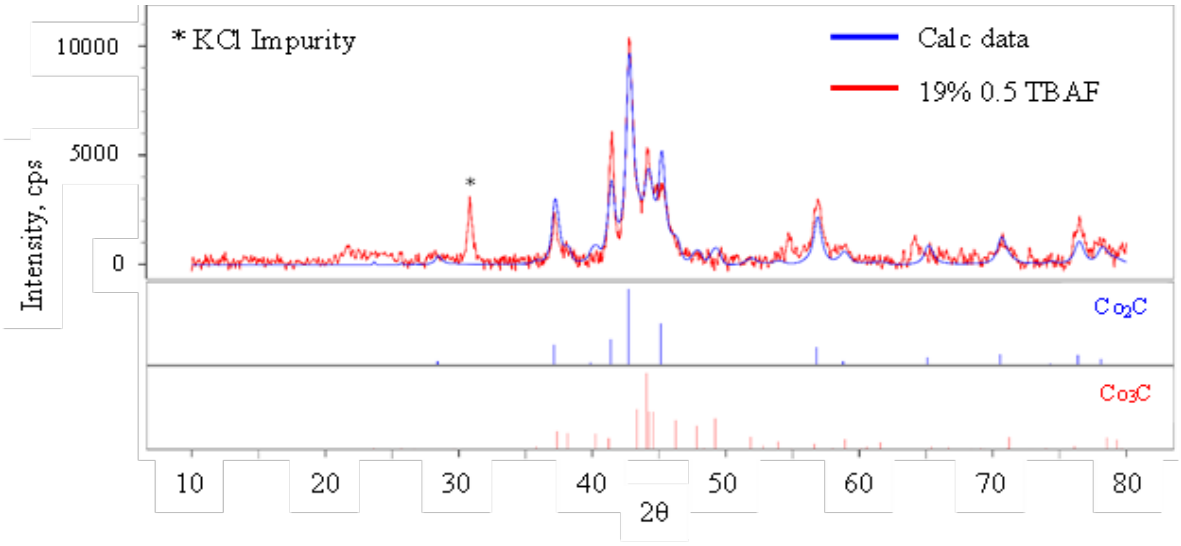
* KCl Impurity
Calc data
19% 0.5 TBAF
Intensity, cps
10000
5000
0
Co2C
Co3C
10
20
30
40
50
60
70
80
2θ

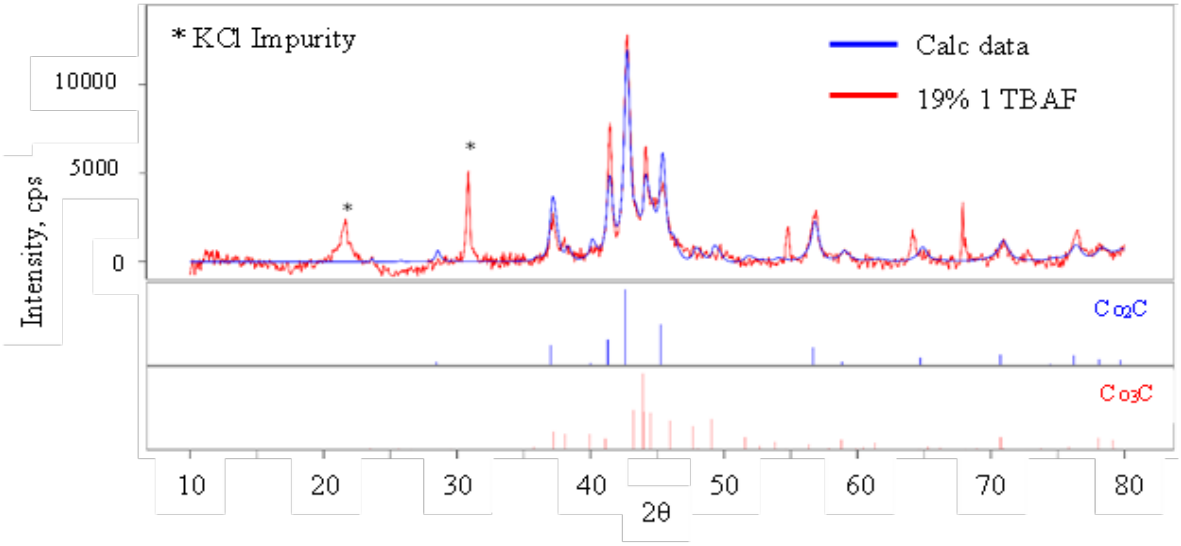
* KCl Impurity
Calc data
19% 1 TBAF
Intensity, cps
10000
5000
0
Co2C
Co3C
10
20
30
40
50
60
70
80
2θ

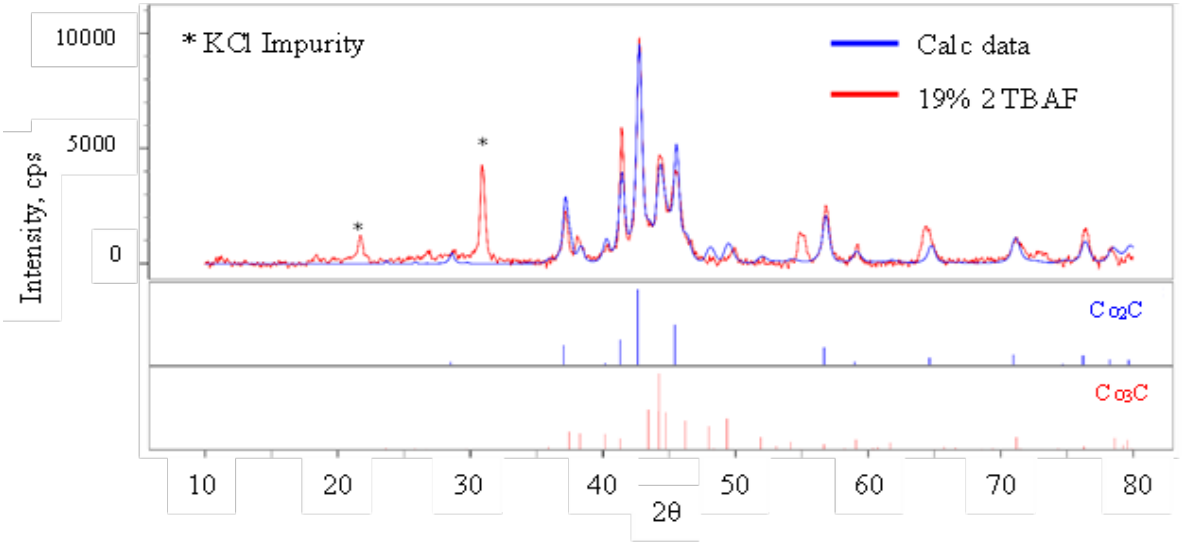
* KCl Impurity
Calc data
19% 2 TBAF
Intensity, cps
10000
5000
0
Co2C
Co3C
10
20
30
40
50
60
70
80
2θ

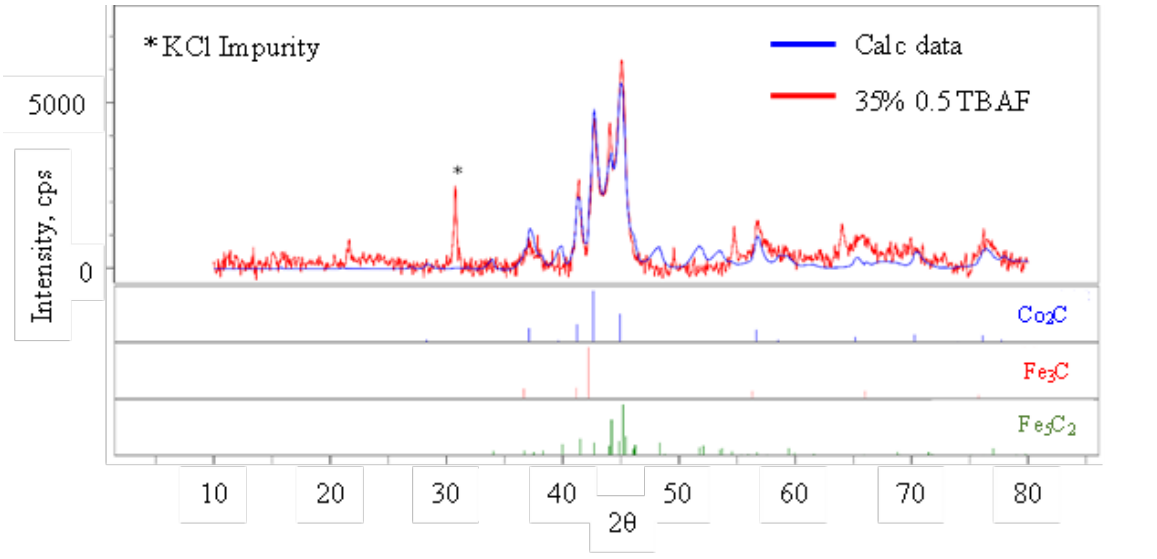
* KCl Impurity
Calc data
35% 0.5 TBAF
5000
0
Intensity, cps
Co2C
Fe3C
Fe5C2
10
20
30
40
50
60
70
80
2θ

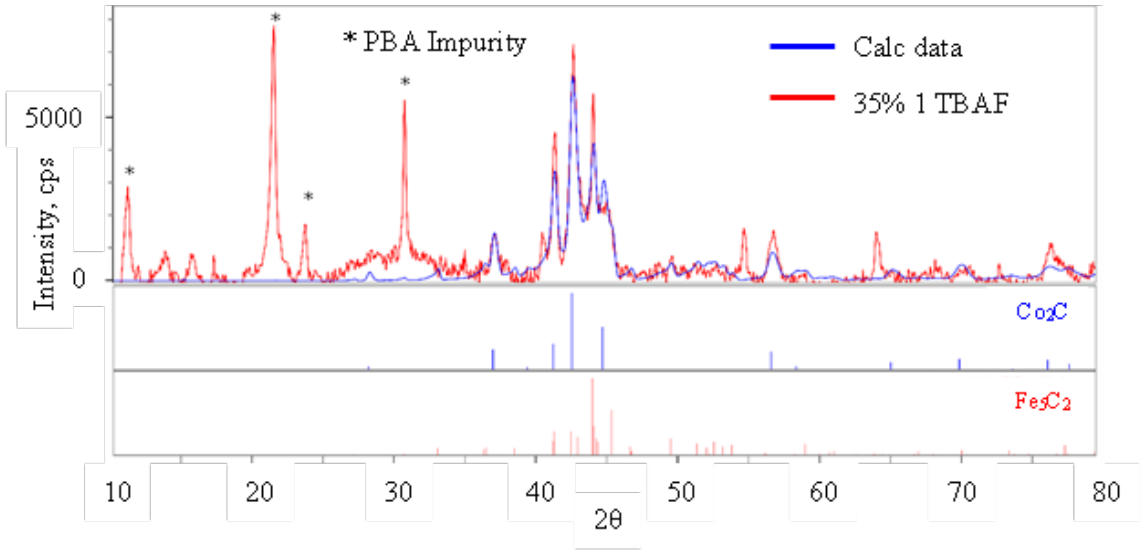
* PBA Impurity
Calc data
35% 1 TBAF
5000
0
Intensity, cps
Co2C
Fe5C2
10
20
30
40
50
60
70
80
2θ

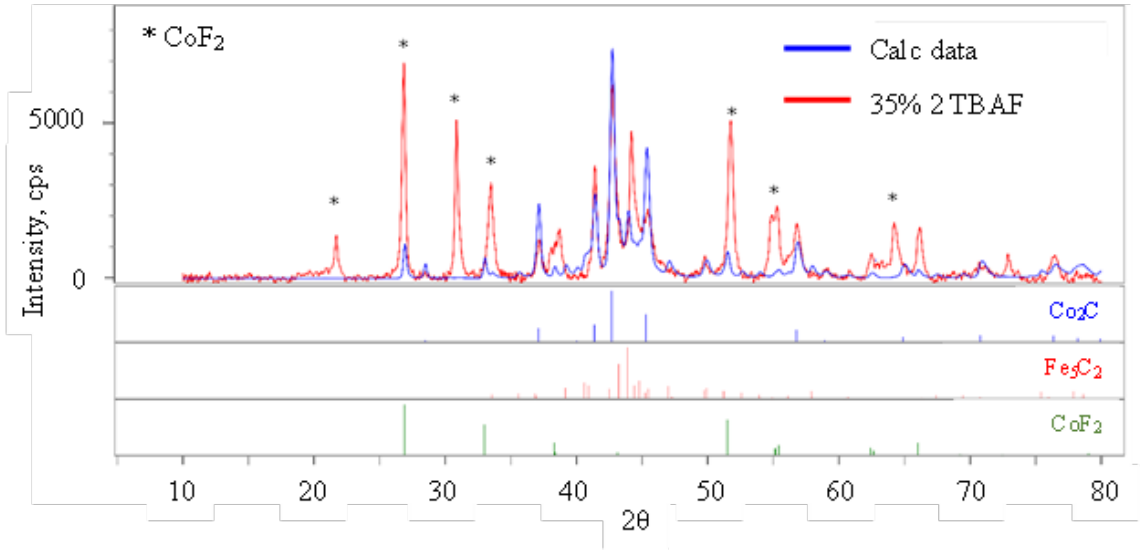
* CoF2
Calc data
35% 2 TBAF
5000
0
Intensity, cps
Co2C
Fe5C2
CoF2
10
20
30
40
50
60
70
80
2θ

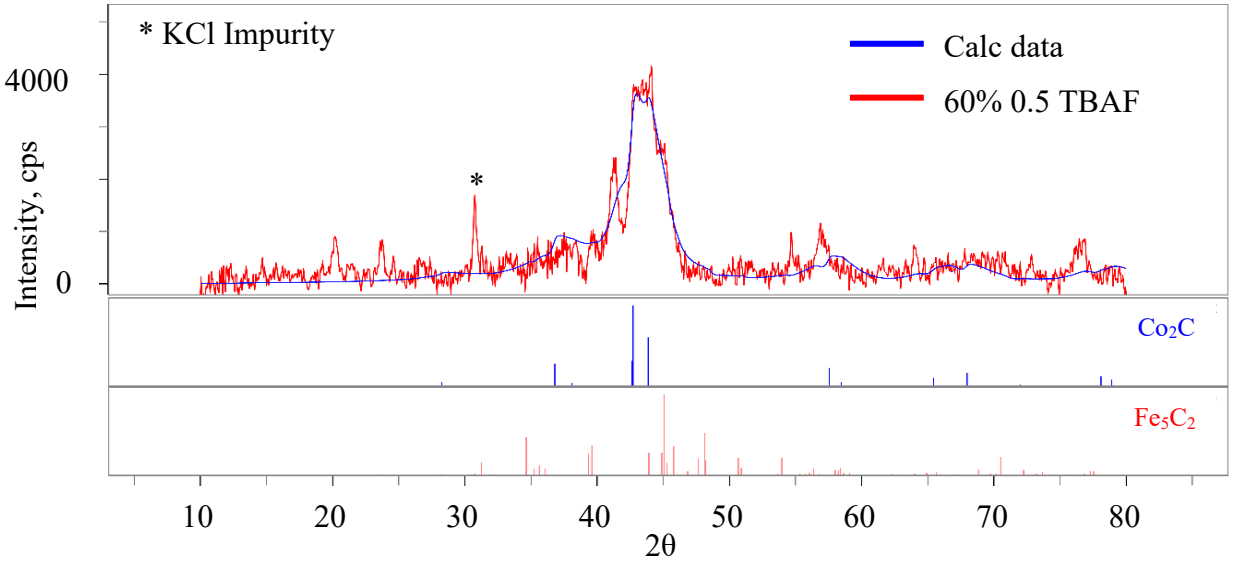
* KCl Impurity
Calc data
60% 0.5 TBAF
4000
0
Intensity, cps
Co2C
Fe5C2
10
20
30
40
50
60
70
80
2θ

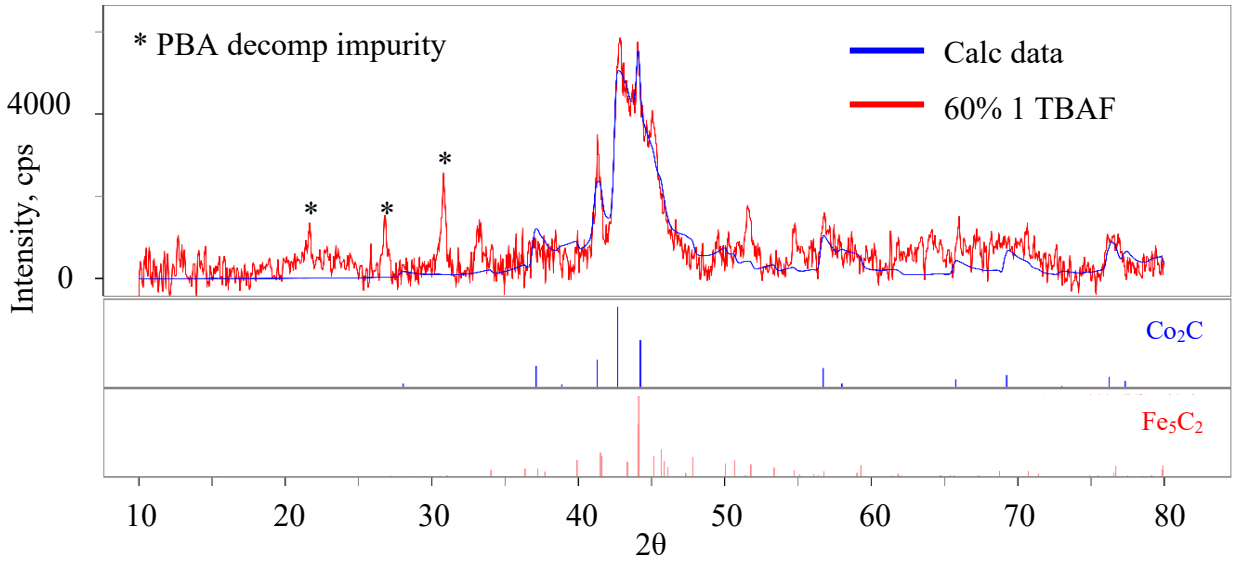
* PBA decomp impurity
Calc data
60% 1 TBAF
4000
0
Intensity, cps
Co2C
Fe5C2
10
20
30
40
50
60
70
80
2θ

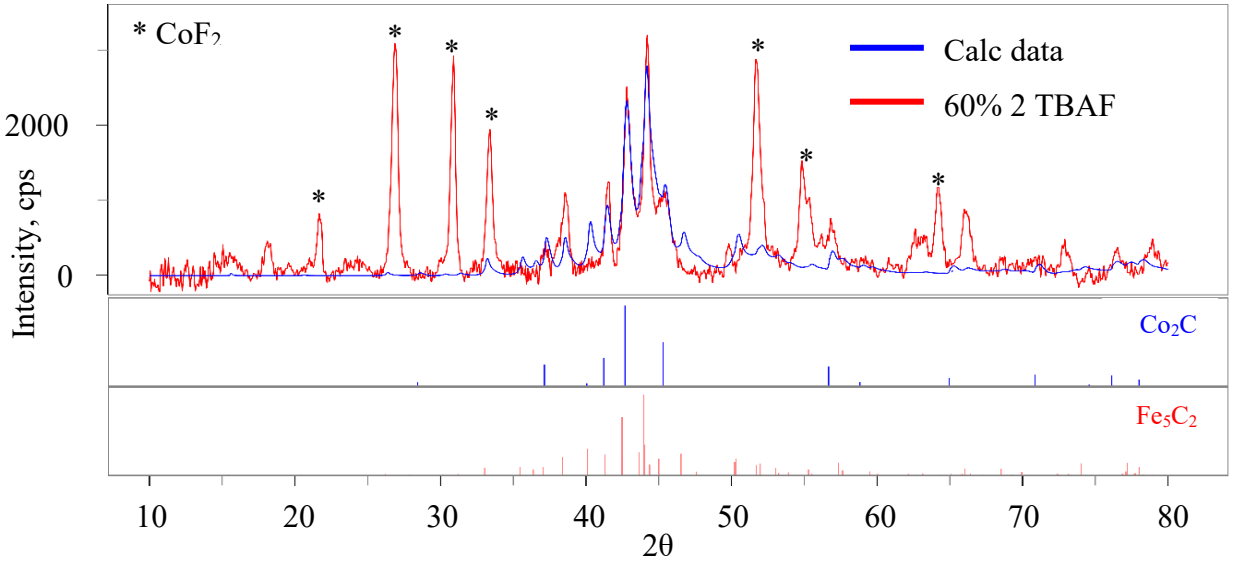
* CoF2
Calc data
60% 2 TBAF
2000
0
Intensity, cps
Co2C
Fe5C2
10
20
30
40
50
60
70
80
2θ

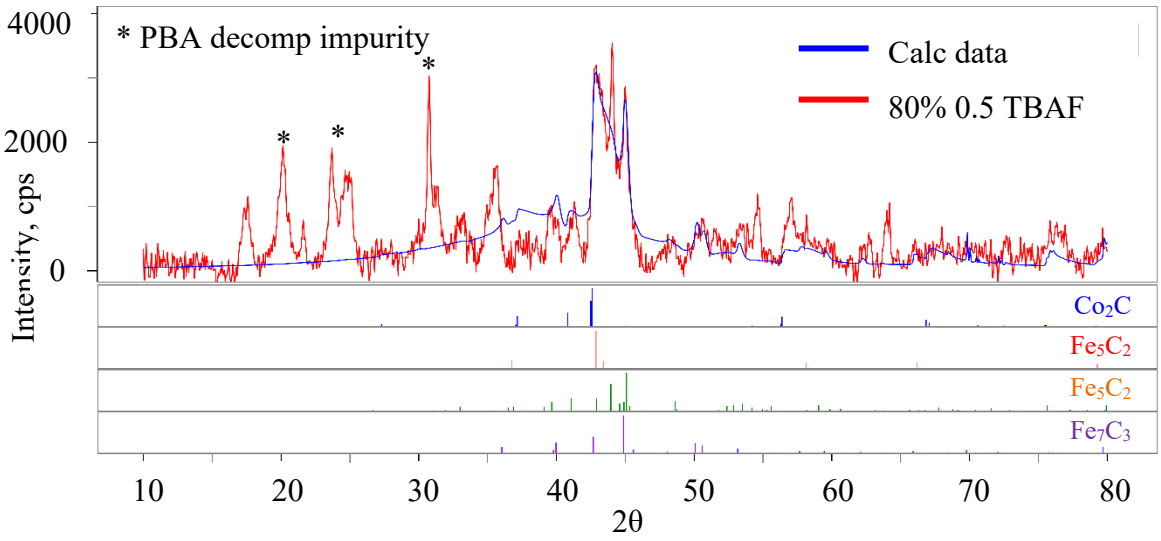
* PBA decomp impurity
Calc data
80% 0.5 TBAF
Intensity, cps
4000
2000
0
Co2C
Fe5C2
Fe5C2
Fe7C3
10
20
30
40
50
60
70
80
2θ

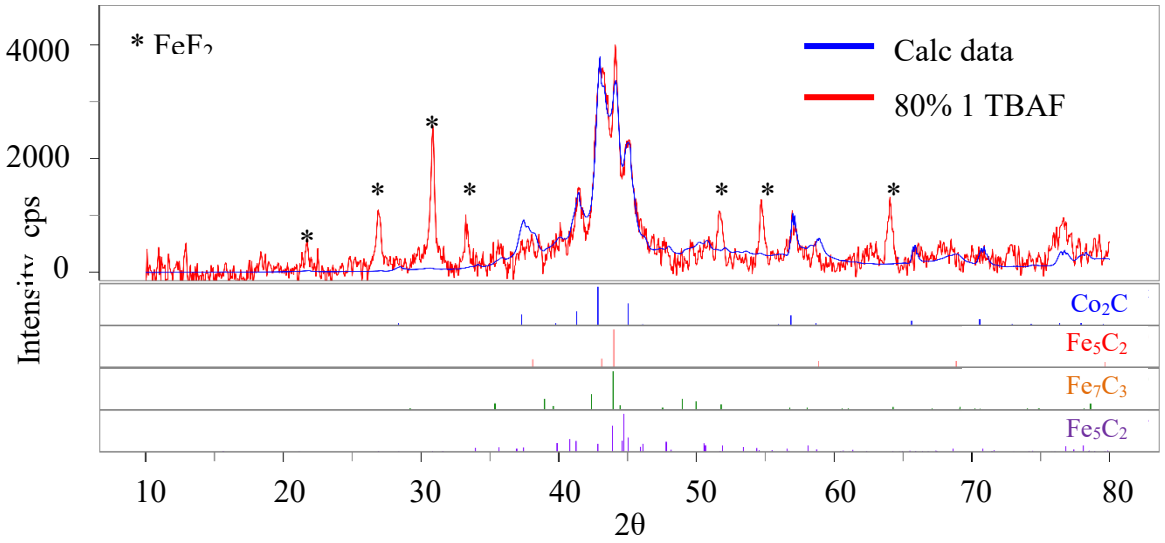
* FeF2
Calc data
80% 1 TBAF
Intensity, cps
4000
2000
0
Co2C
Fe5C2
Fe7C3
Fe5C2
10
20
30
40
50
60
70
80
2θ

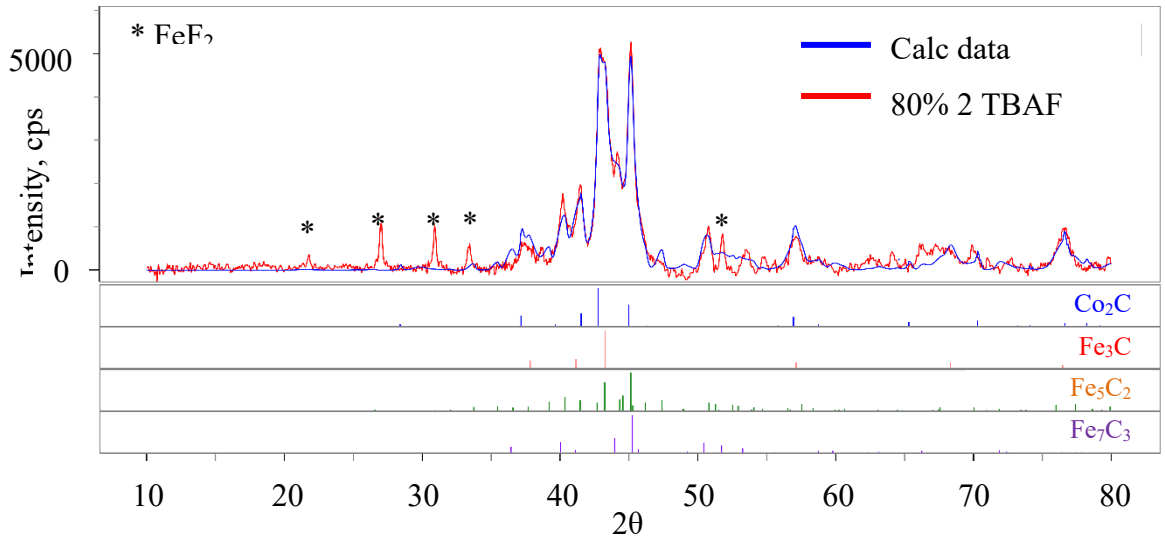
* FeF2
Calc data
80% 2 TBAF
Intensity, cps
5000
0
Co2C
Fe3C
Fe5C2
Fe7C3
10
20
30
40
50
60
70
80
2θ

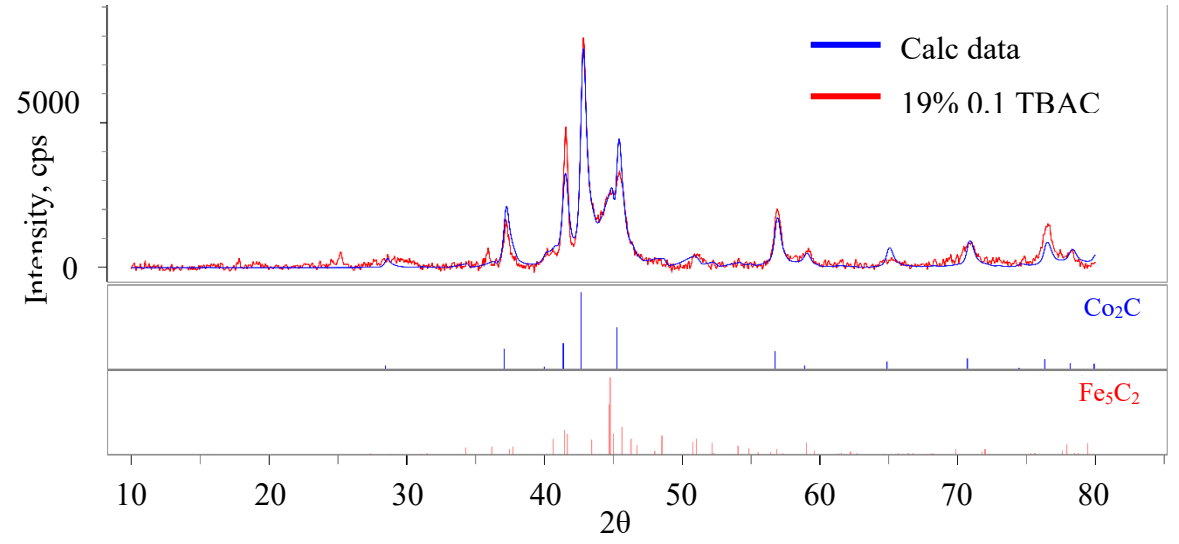
Calc data
19% 0.1 TBAC
5000
0
Intensity, cps
Co2C
Fe5C2
10
20
30
40
50
60
70
80
2θ

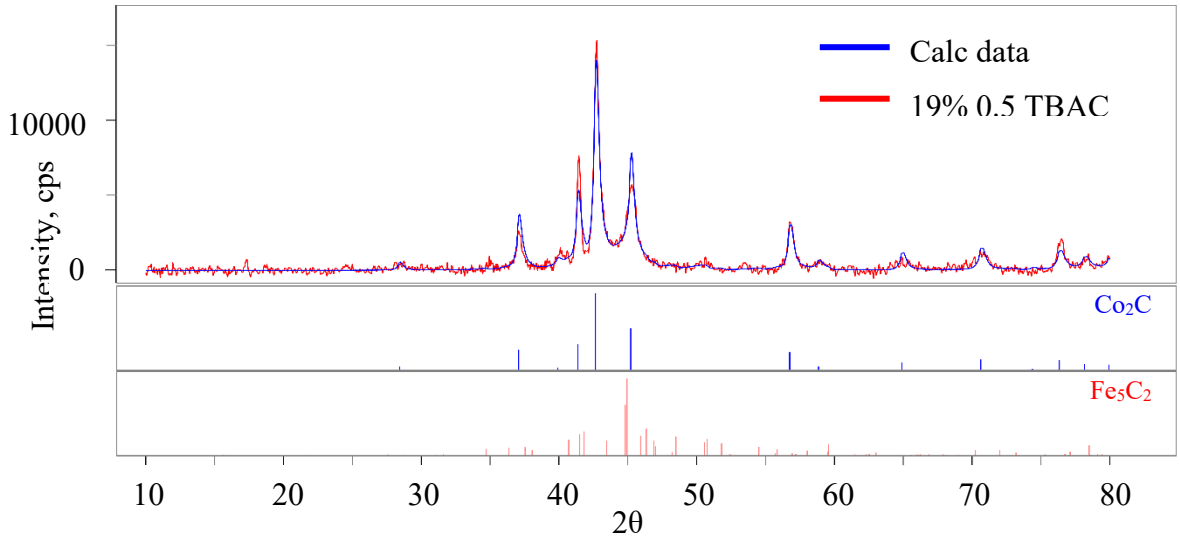
Calc data
19% 0.5 TBAC
10000
0
Intensity, cps
Co2C
Fe5C2
10
20
30
40
50
60
70
80
2θ

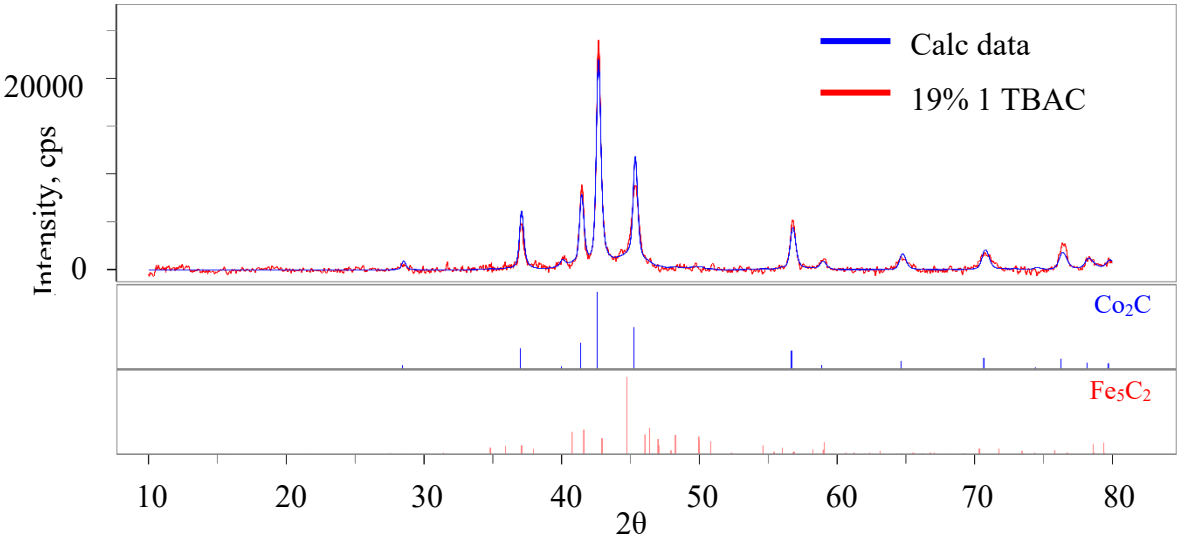
Calc data
19% 1 TBAC
20000
0
Intensity, cps
Co2C
Fe5C2
10
20
30
40
50
60
70
80
2θ

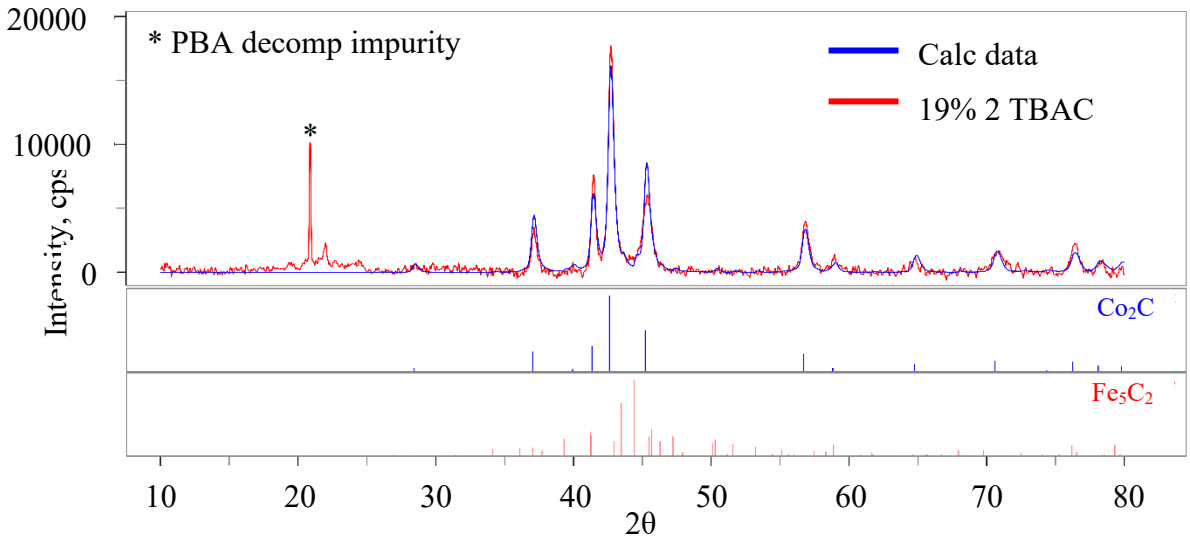
20000
10000
0
Intensity, cps
* PBA decomp impurity
*
Calc data
19% 2 TBAC
Co2C
Fe5C2
10
20
30
40
50
60
70
80
2θ

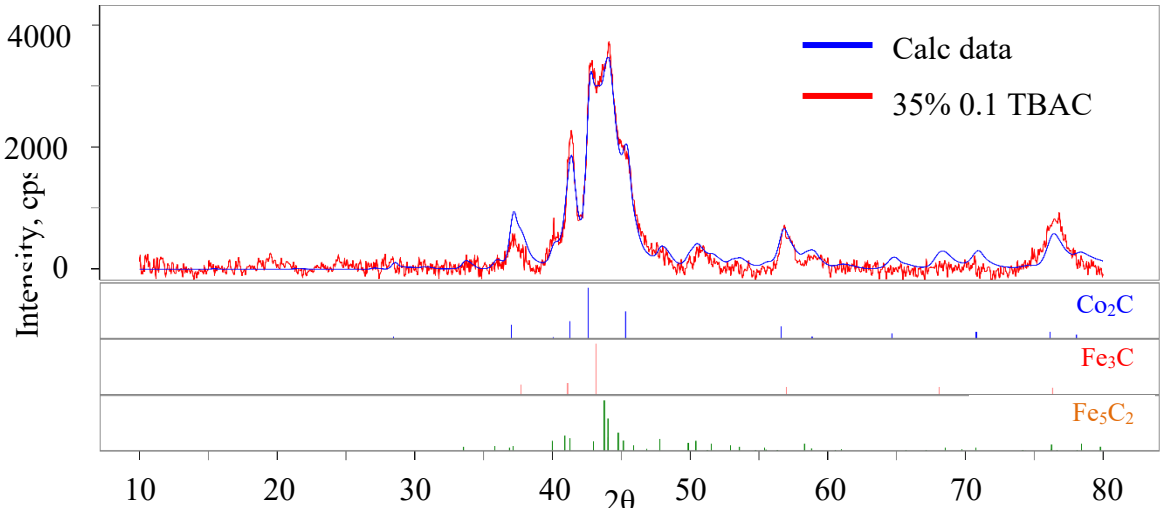
4000
2000
0
Intensity, cps
Calc data
35% 0.1 TBAC
Co2C
Fe3C
Fe5C2
10
20
30
40
50
60
70
80
2θ

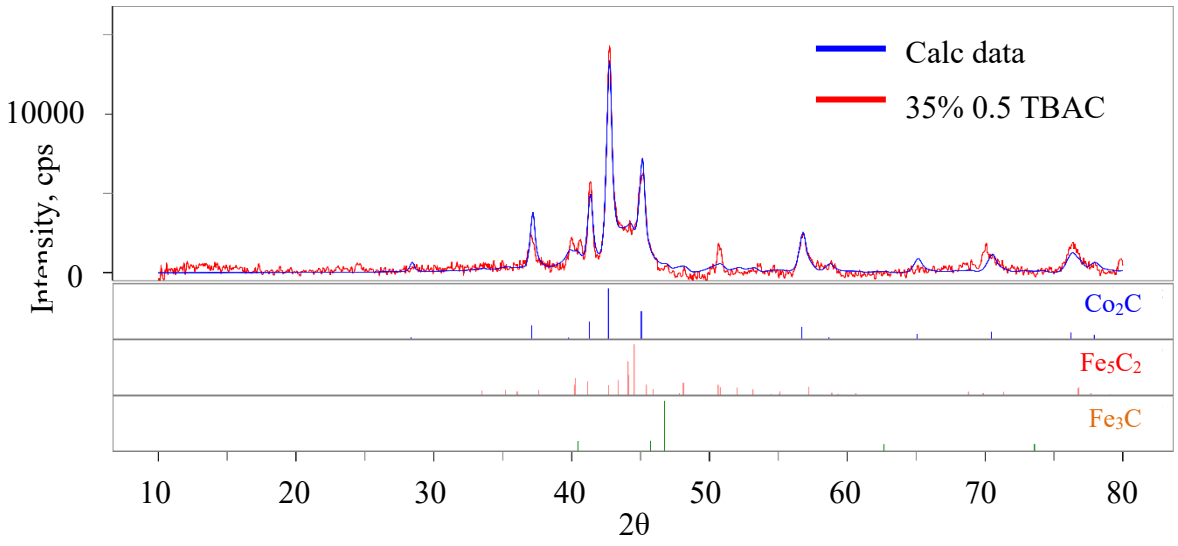
10000
0
Intensity, cps
Calc data
35% 0.5 TBAC
Co2C
Fe5C2
Fe3C
10
20
30
40
50
60
70
80
2θ

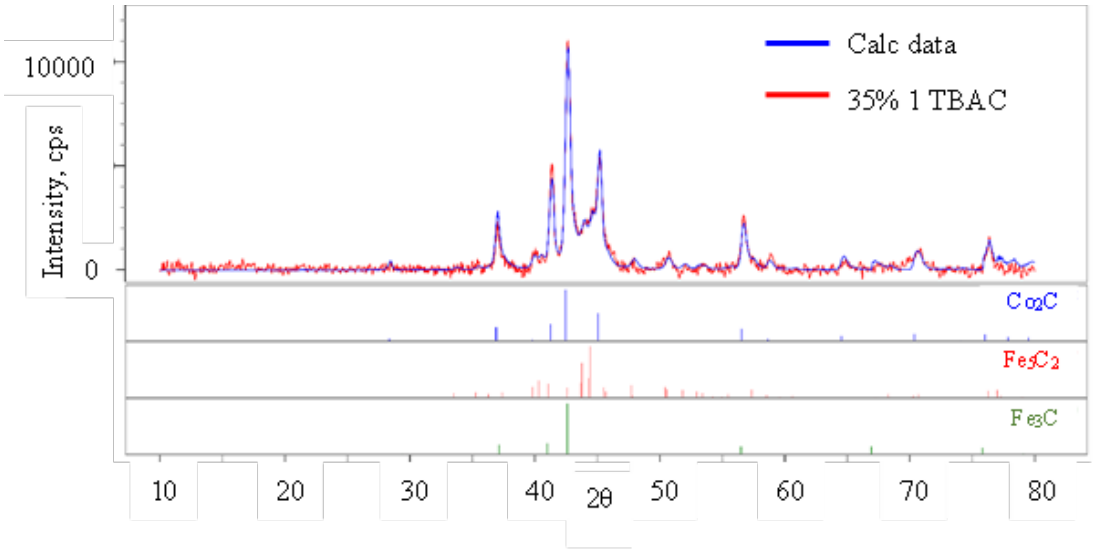
Calc data
35% 1 TBAC
10000
Intensity, cps
0
Co2C
Fe5C2
Fe3C
10
20
30
40
2θ
50
60
70
80

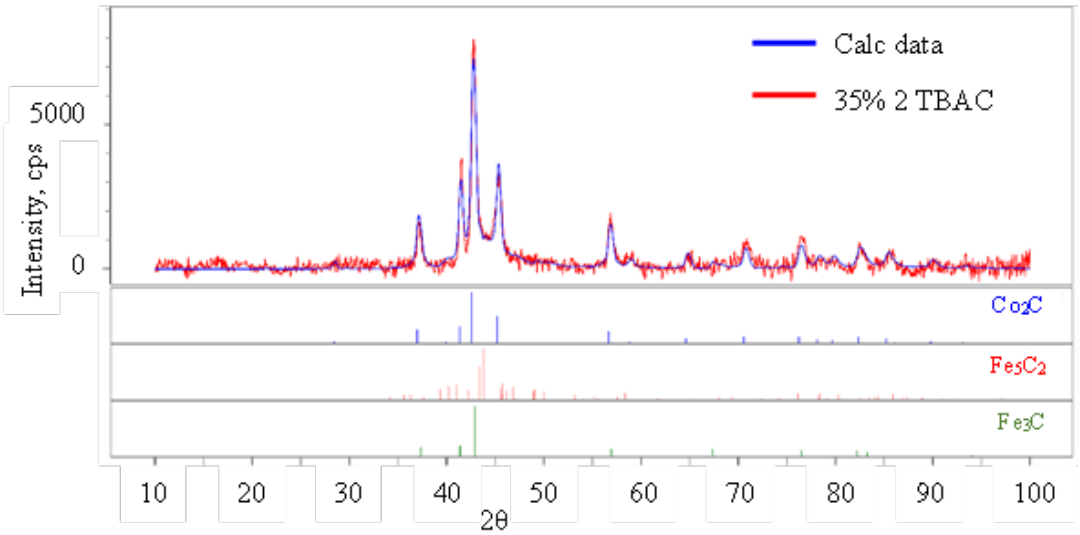
Calc data
35% 2 TBAC
5000
Intensity, cps
0
Co2C
Fe5C2
Fe3C
10
20
30
40
50
60
70
80
90
100
2θ

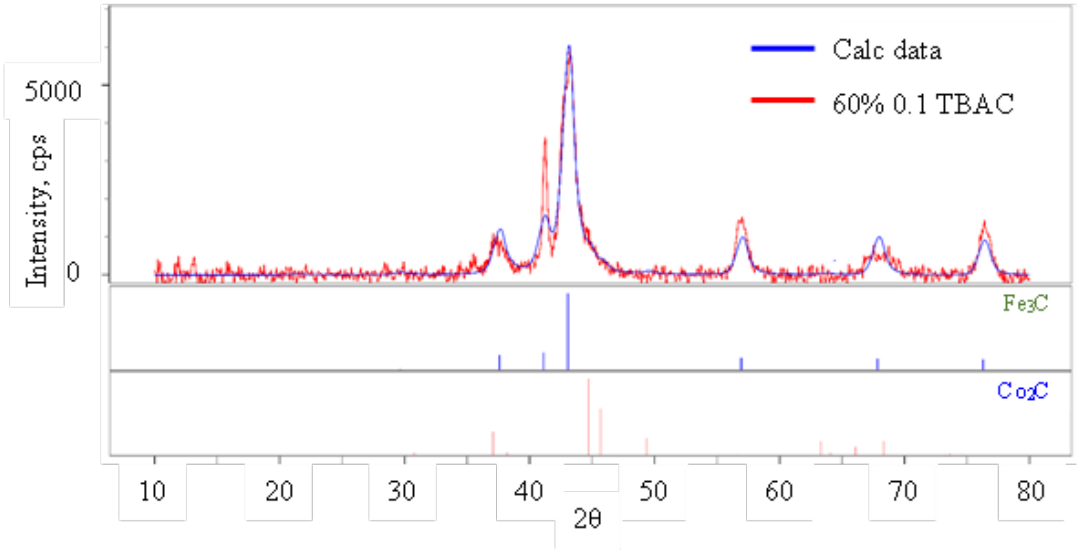
Calc data
60% 0.1 TBAC
5000
Intensity, cps
0
Fe3C
Co2C
10
20
30
40
2θ
50
60
70
80

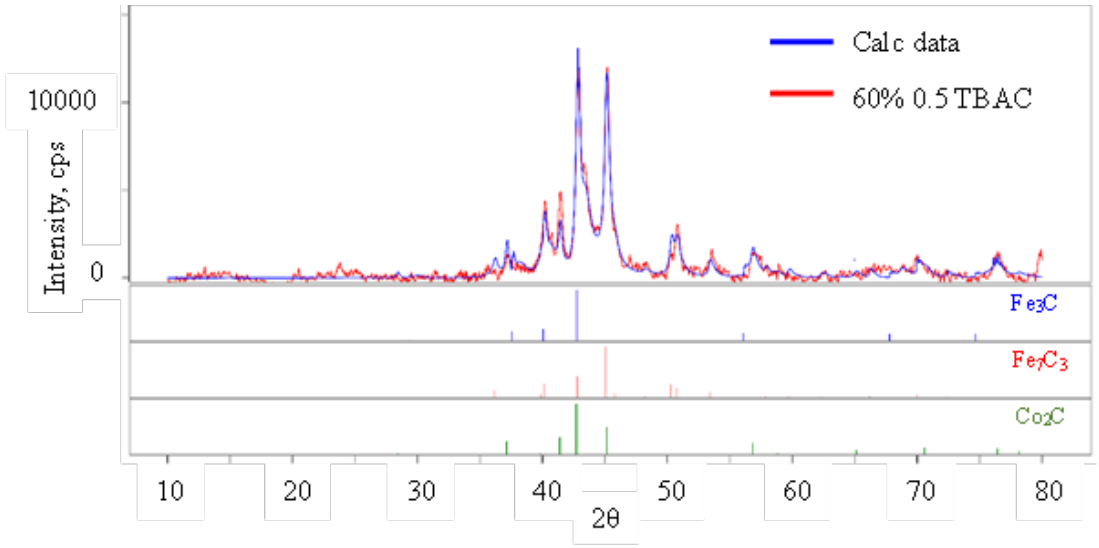
Calc data
60% 0.5 TBAC
10000
Intensity, cps
0
Fe3C
Fe7C3
Co2C
10
20
30
40
50
60
70
80
2θ

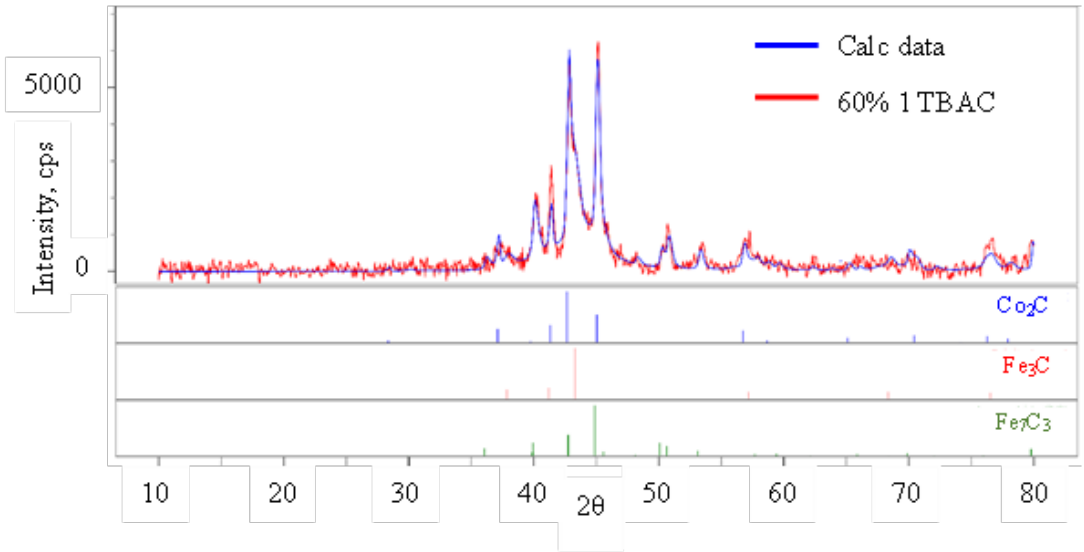
Calc data
60% 1 TBAC
5000
Intensity, cps
0
Co2C
Fe3C
Fe7C3
10
20
30
40
50
60
70
80
2θ

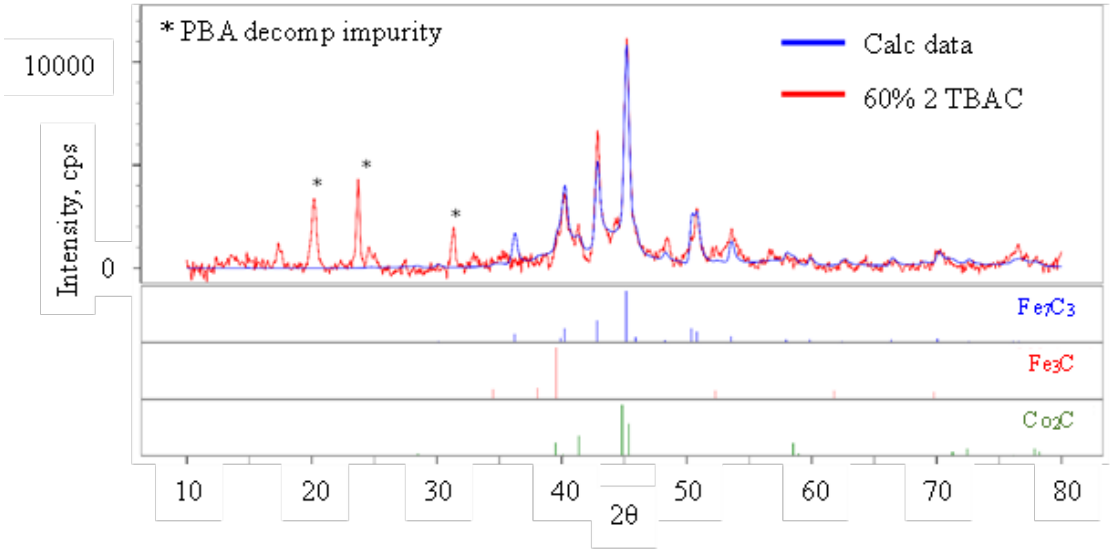
* PBA decomp impurity
Calc data
60% 2 TBAC
10000
Intensity, cps
0
Fe7C3
Fe3C
Co2C
10
20
30
40
50
60
70
80
2θ

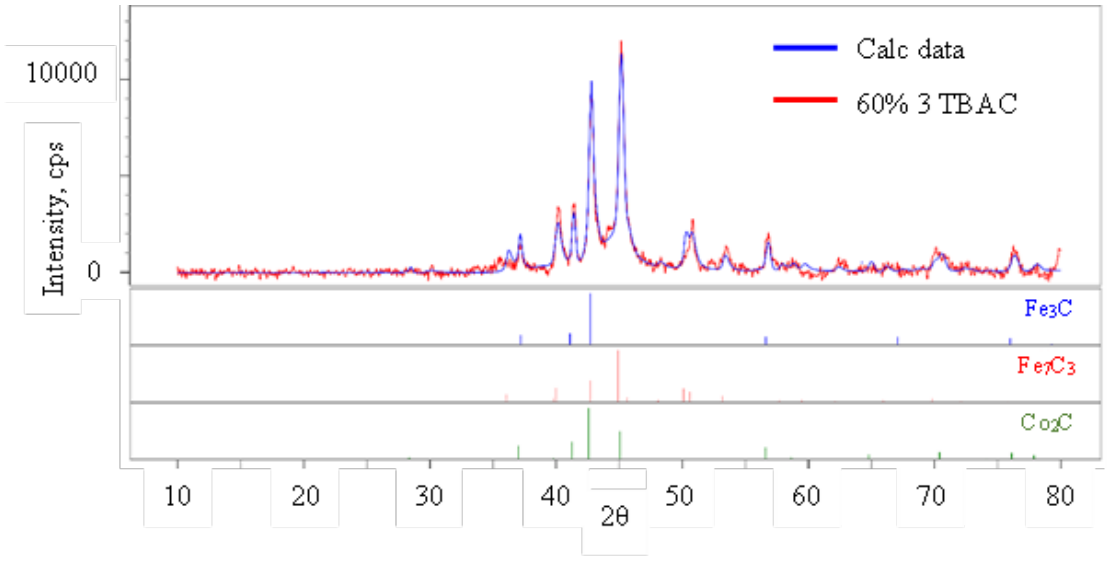
Calc data
60% 3 TBAC
10000
Intensity, cps
0
Fe3C
Fe7C3
Co2C
10
20
30
40
50
60
70
80
2θ

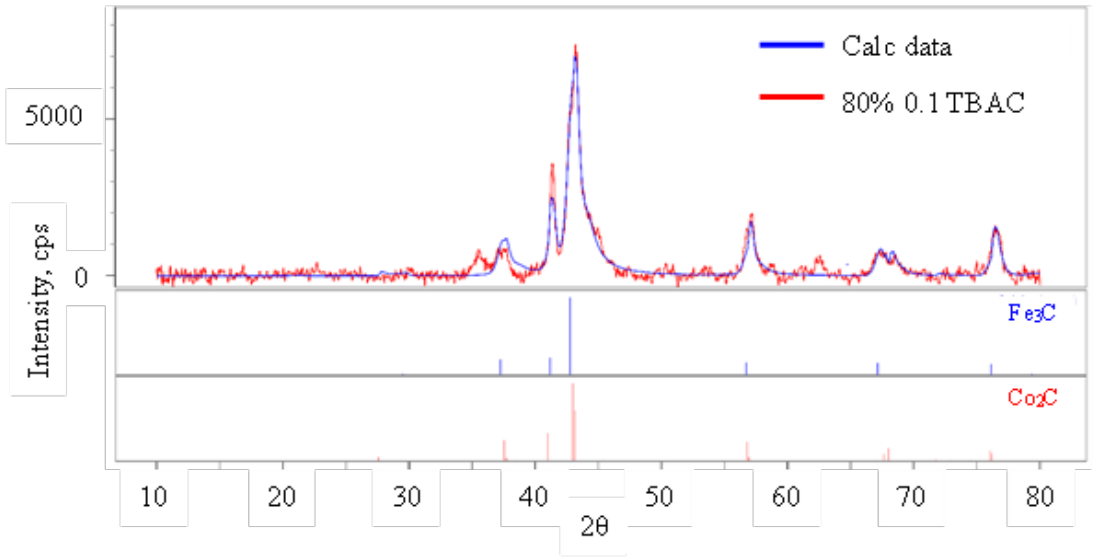
Calc data
80% 0.1 TBAC
5000
Intensity, cps
0
Fe3C
Co2C
10
20
30
40
50
60
70
80
2θ

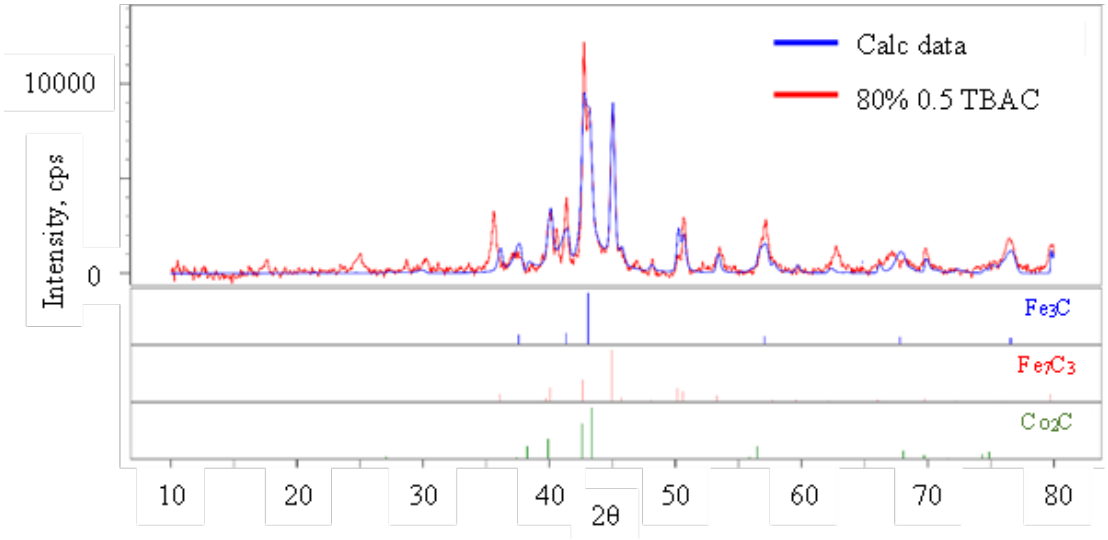
Calc data
80% 0.5 TBAC
10000
Intensity, cps
0
Fe3C
Fe7C3
Co2C
10
20
30
40
50
60
70
80
2θ

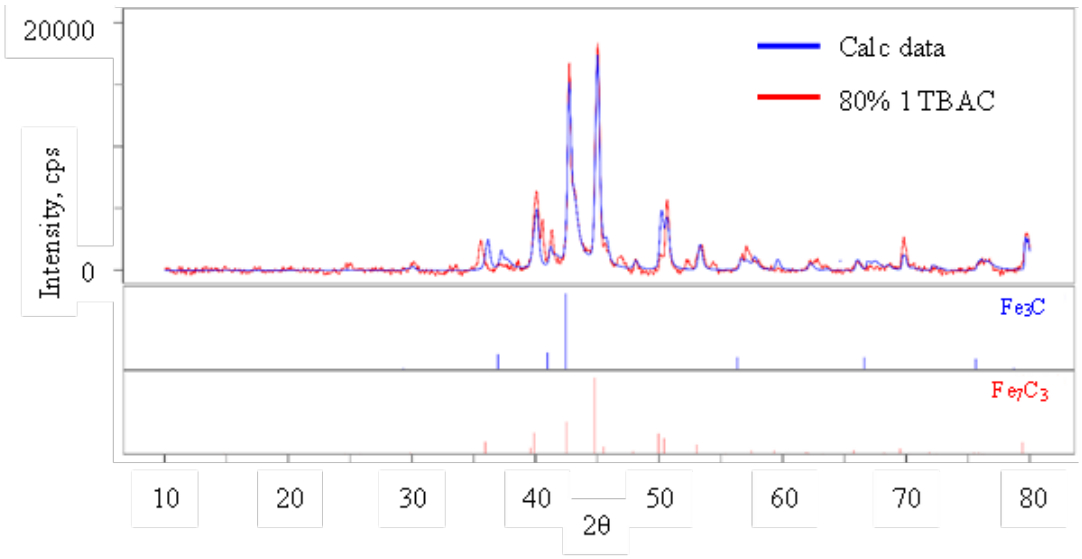
20000
Intensity, cps
0
Calc data
80% 1 TBAC
Fe3C
Fe7C3
10
20
30
40
50
60
70
80
2θ

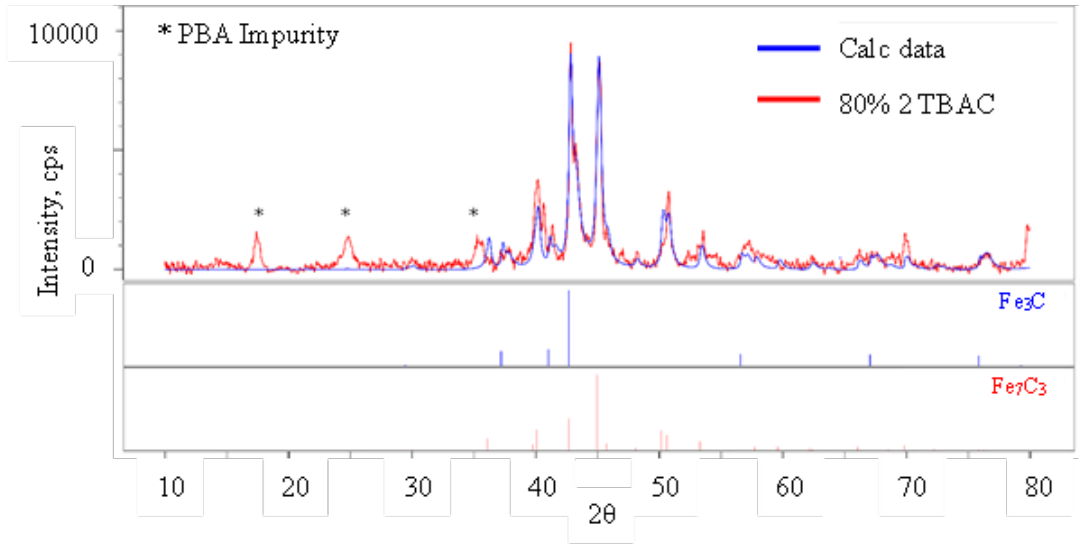
10000
* PBA Impurity
Intensity, cps
0
Calc data
80% 2 TBAC
*
*
*
Fe3C
Fe7C3
10
20
30
40
50
60
70
80
2θ

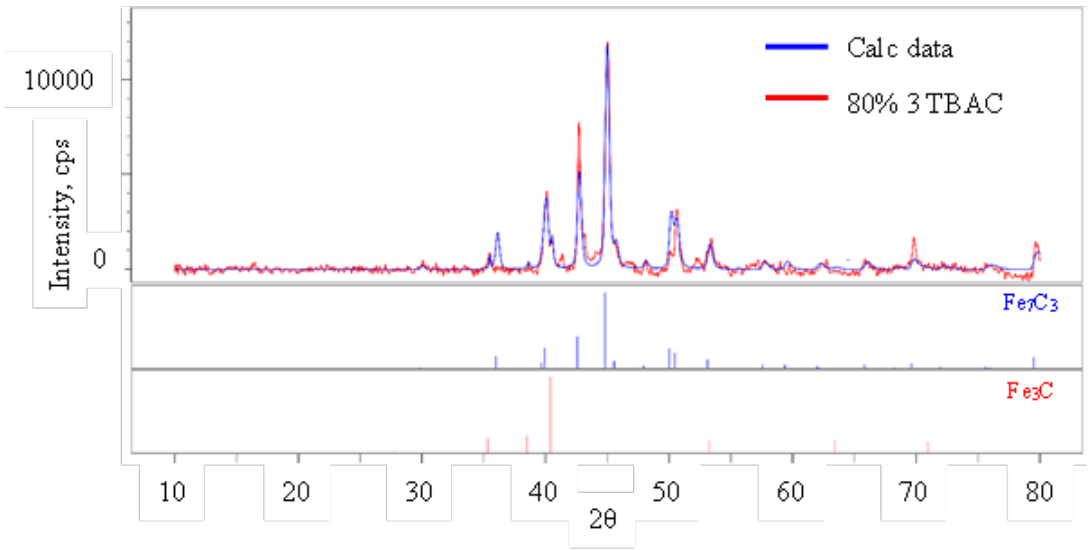
10000
Intensity, cps
0
Calc data
80% 3 TBAC
Fe7C3
Fe3C
10
20
30
40
50
60
70
80
2θ

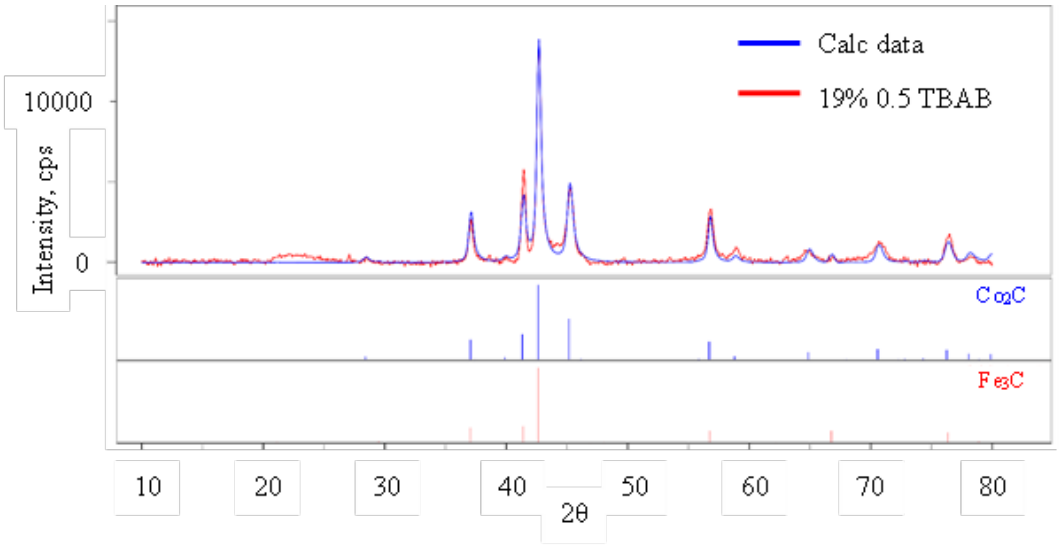
Calc data
19% 0.5 TBAB
10000
Intensity, cps
0
Co2C
Fe3C
10
20
30
40
50
60
70
80
2θ

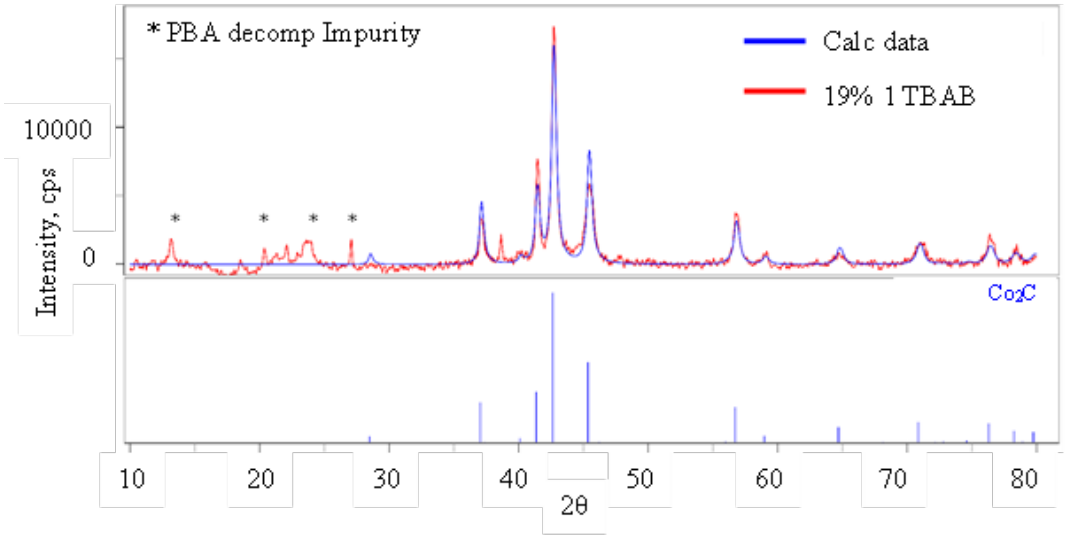
* PBA decomp Impurity
Calc data
19% 1 TBAB
10000
Intensity, cps
0
Co2C
10
20
30
40
50
60
70
80
2θ

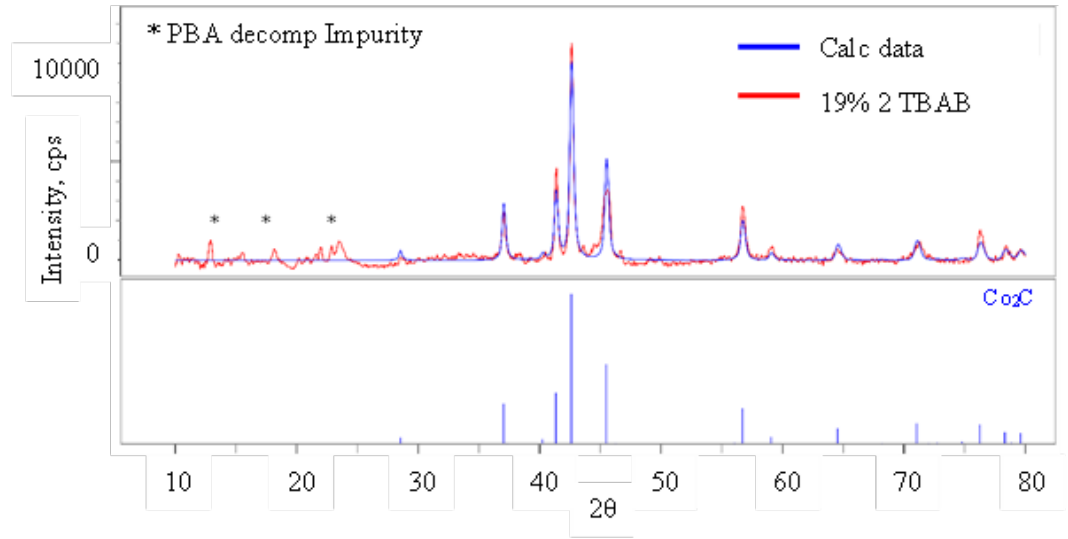
* PBA decomp Impurity
Calc data
19% 2 TBAB
10000
Intensity, cps
0
Co2C
10
20
30
40
50
60
70
80
2θ

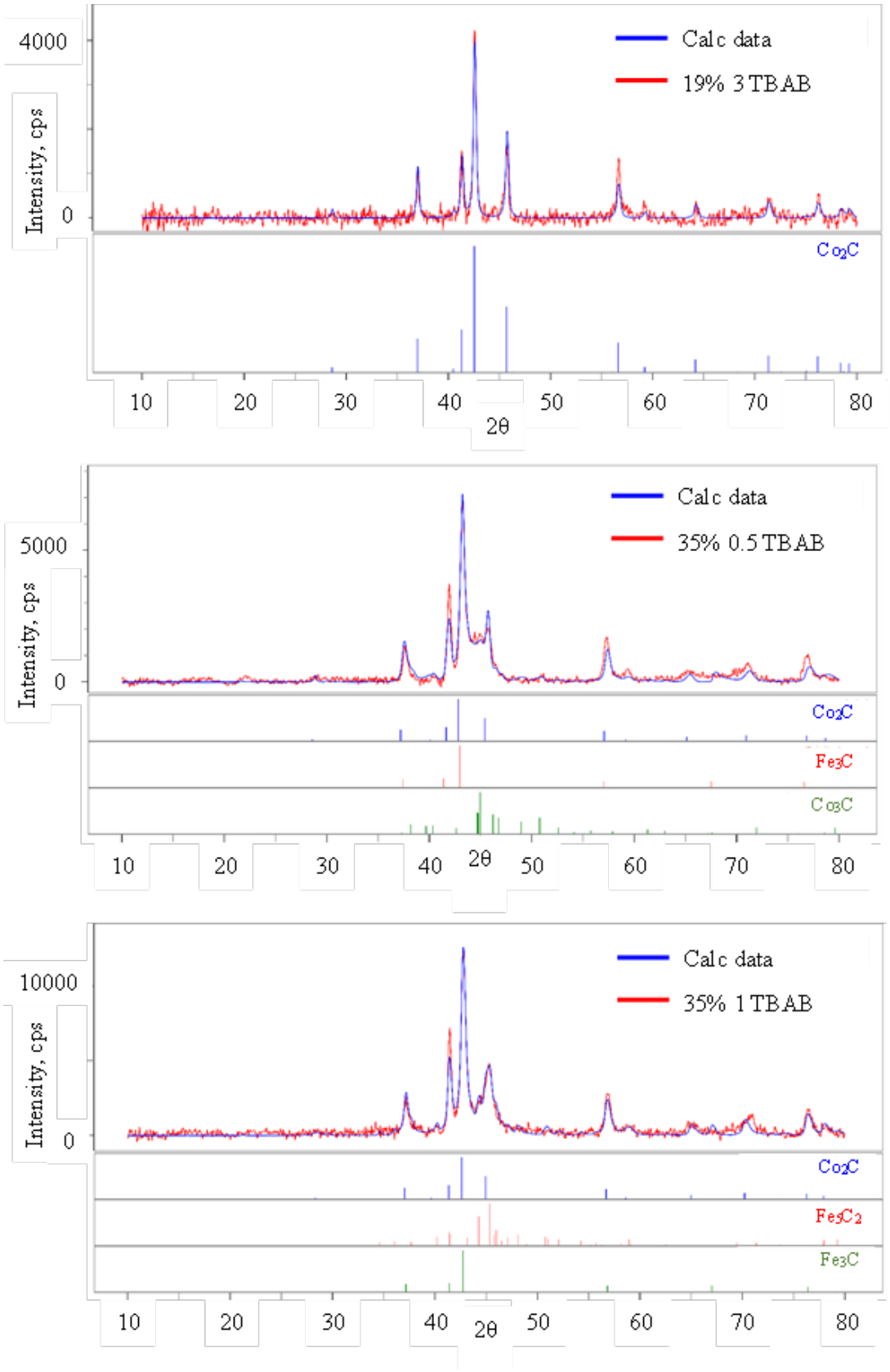
4000
Intensity, cps
0
Calc data
19% 3TBAB
Co2C
10
20
30
40
2θ
50
60
70
80
5000
Intensity, cps
0
Calc data
35% 0.5TBAB
Co2C
Fe3C
Co3C
10
20
30
40
2θ
50
60
70
80
10000
Intensity, cps
0
Calc data
35% 1TBAB
Co2C
Fe5C2
Fe3C
10
20
30
40
2θ
50
60
70
80

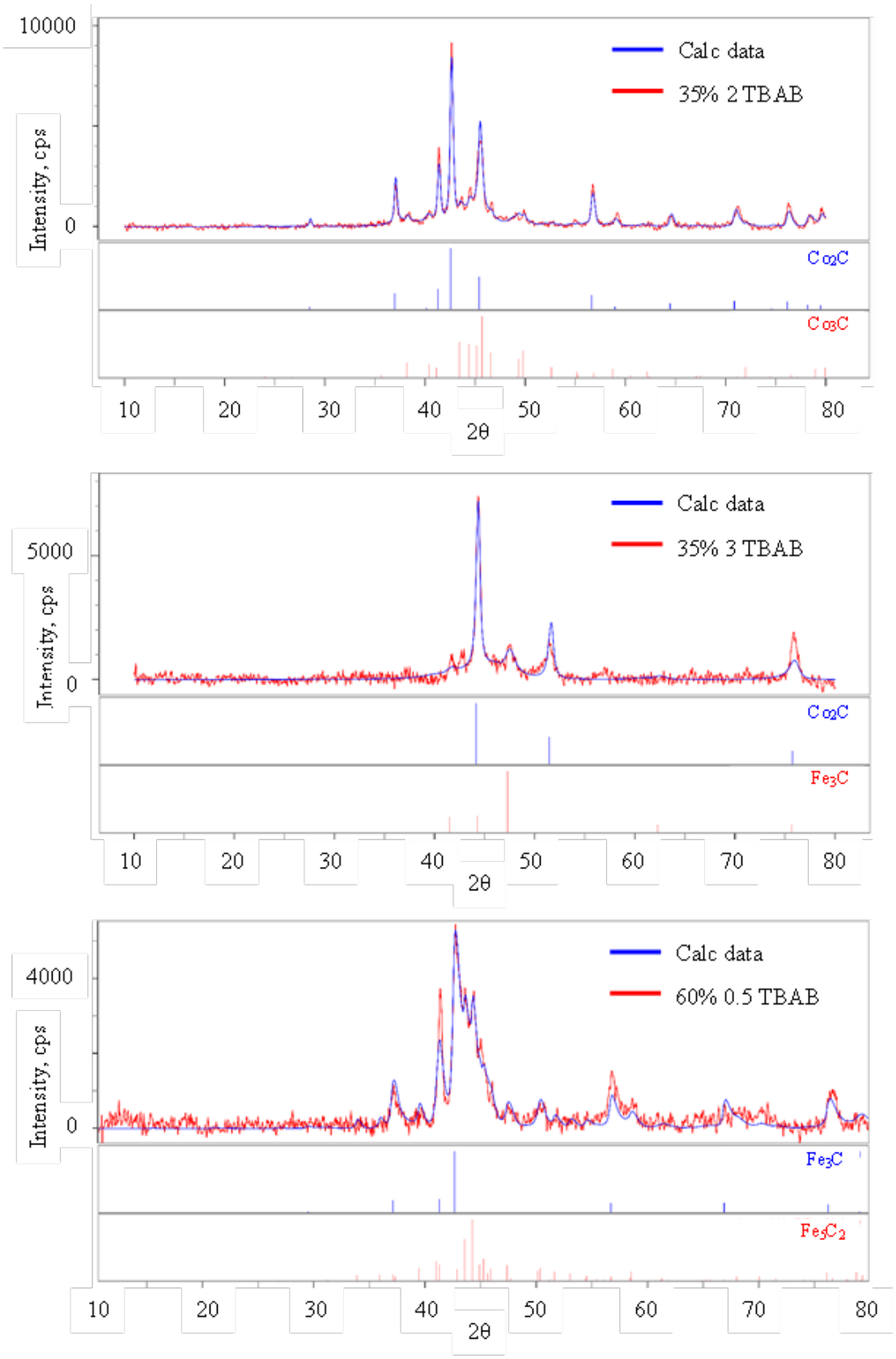
10000
Intensity, cps
0
Calc data
35% 2 TBAB
Co2C
Co3C
10
20
30
40
50
60
70
80
2θ
5000
Intensity, cps
0
Calc data
35% 3 TBAB
Co2C
Fe3C
10
20
30
40
50
60
70
80
2θ
4000
Intensity, cps
0
Calc data
60% 0.5 TBAB
Fe3C
Fe5C2
10
20
30
40
50
60
70
80
2θ

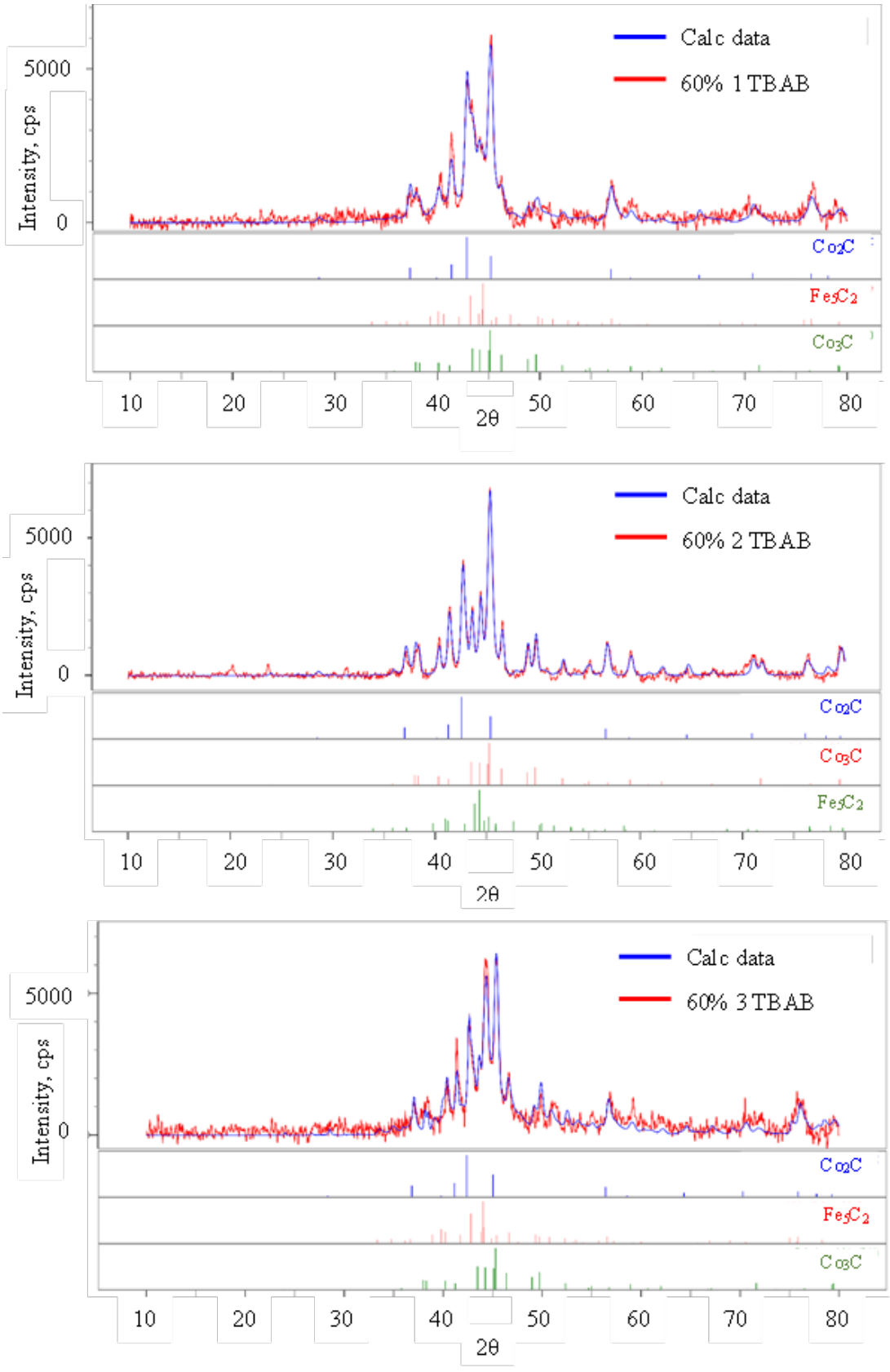
Calc data
60% 1 TBAB
5000
Intensity, cps
0
Co2C
Fe5C2
Co3C
10
20
30
40
50
60
70
80
2θ
Calc data
60% 2 TBAB
5000
Intensity, cps
0
Co2C
Co3C
Fe5C2
10
20
30
40
50
60
70
80
2θ
Calc data
60% 3 TBAB
5000
Intensity, cps
0
Co2C
Fe5C2
Co3C
10
20
30
40
50
60
70
80
2θ

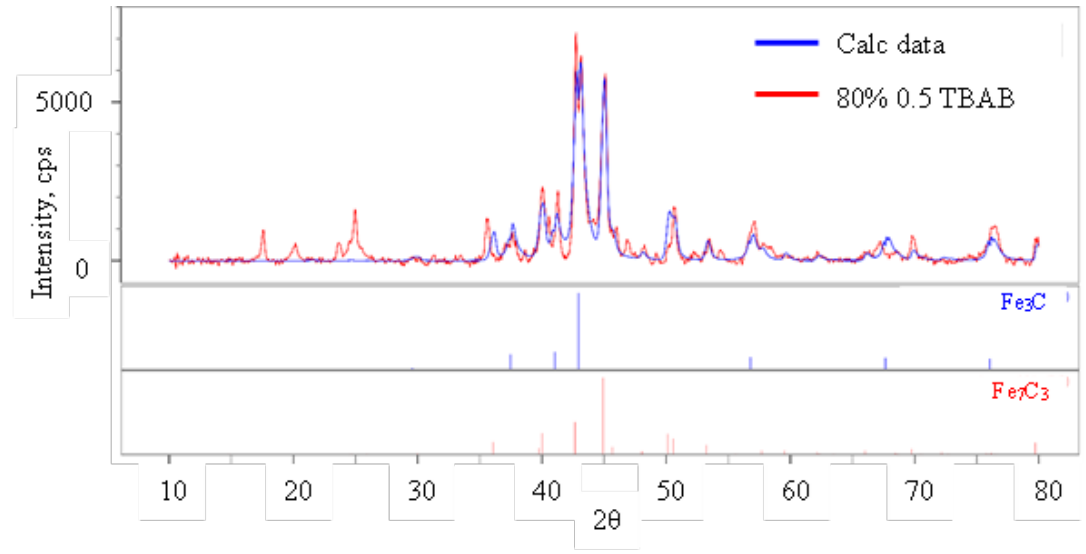
Calc data
80% 0.5 TBAB
5000
0
Intensity, cps
Fe3C
Fe7C3
10
20
30
40
50
60
70
80
2θ

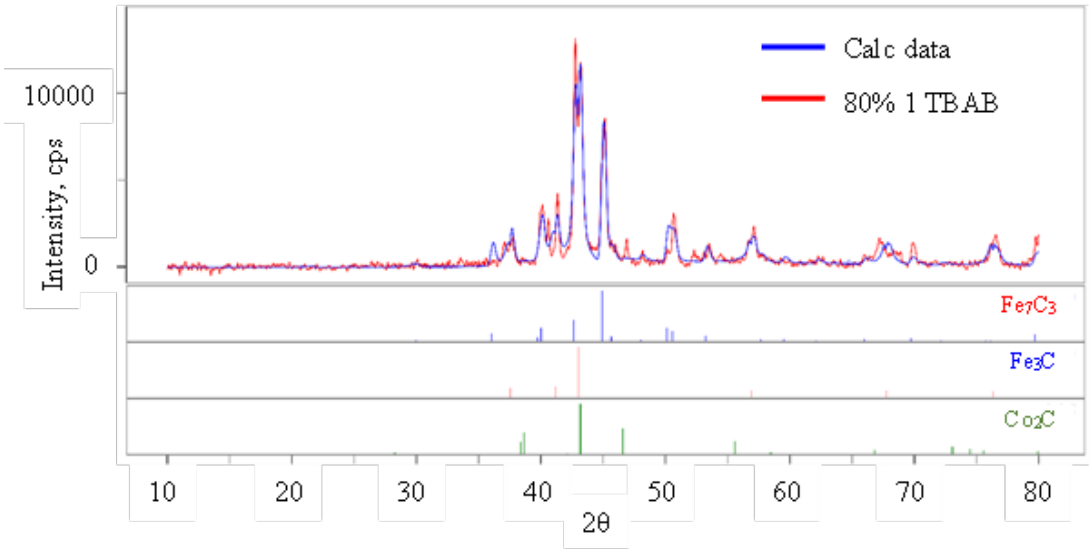
Calc data
80% 1 TBAB
10000
0
Intensity, cps
Fe7C3
Fe3C
Co2C
10
20
30
40
50
60
70
80
2θ

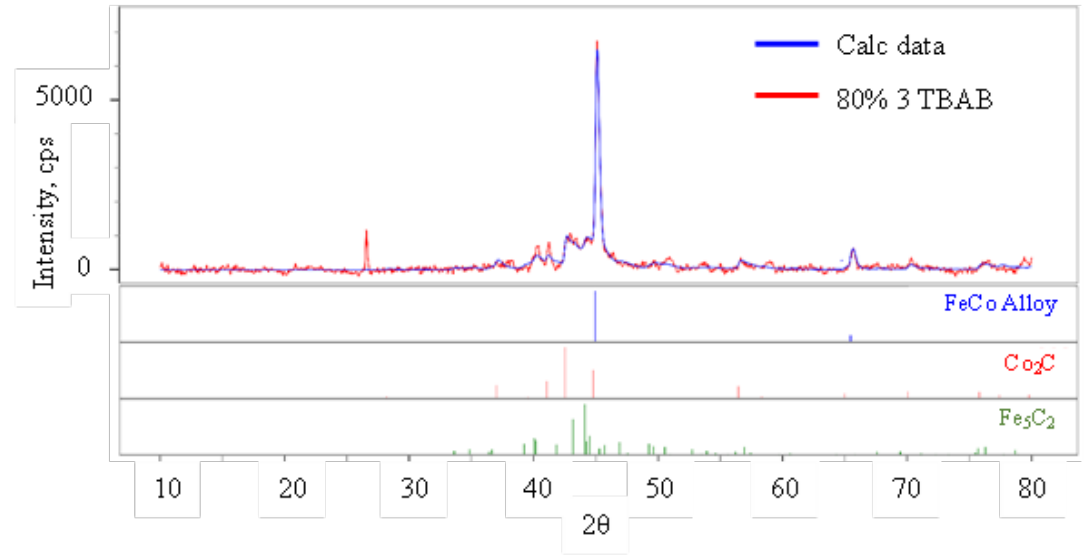
Calc data
80% 3 TBAB
5000
0
Intensity, cps
FeCo Alloy
Co2C
Fe5C2
10
20
30
40
50
60
70
80
2θ

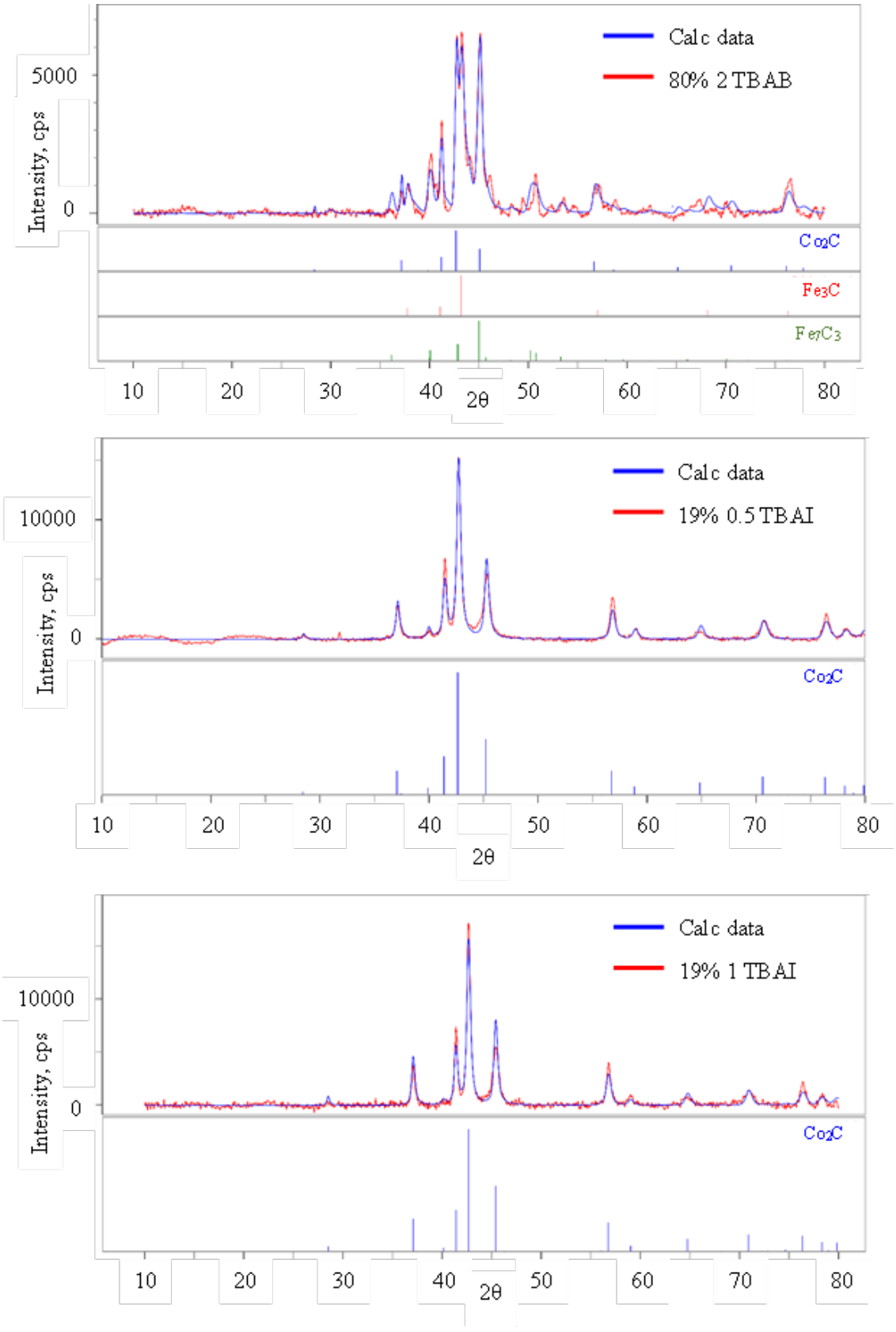
Calc data
80% 2 TBAB
5000
0
Intensity, cps
Co2C
Fe3C
Fe7C3
10
20
30
40
2θ
50
60
70
80
Calc data
19% 0.5 TBAI
10000
0
Intensity, cps
Co2C
10
20
30
40
2θ
50
60
70
80
Calc data
19% 1 TBAI
10000
0
Intensity, cps
Co2C
10
20
30
40
2θ
50
60
70
80

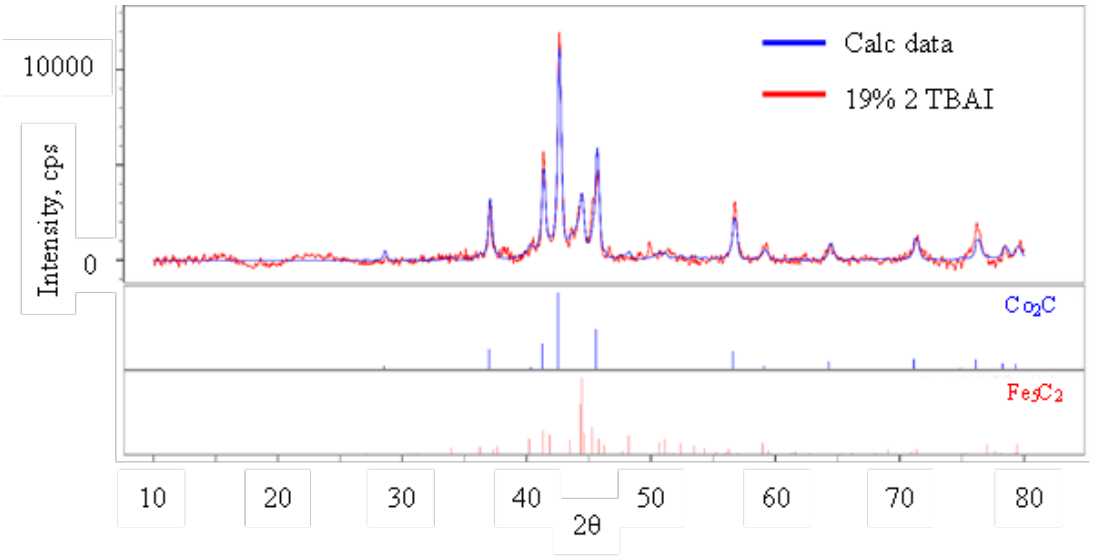
Calc data
19% 2 TBAI
Co2C
Fe5C2
Intensity, cps
10000
0
10
20
30
40
50
60
70
80
2θ

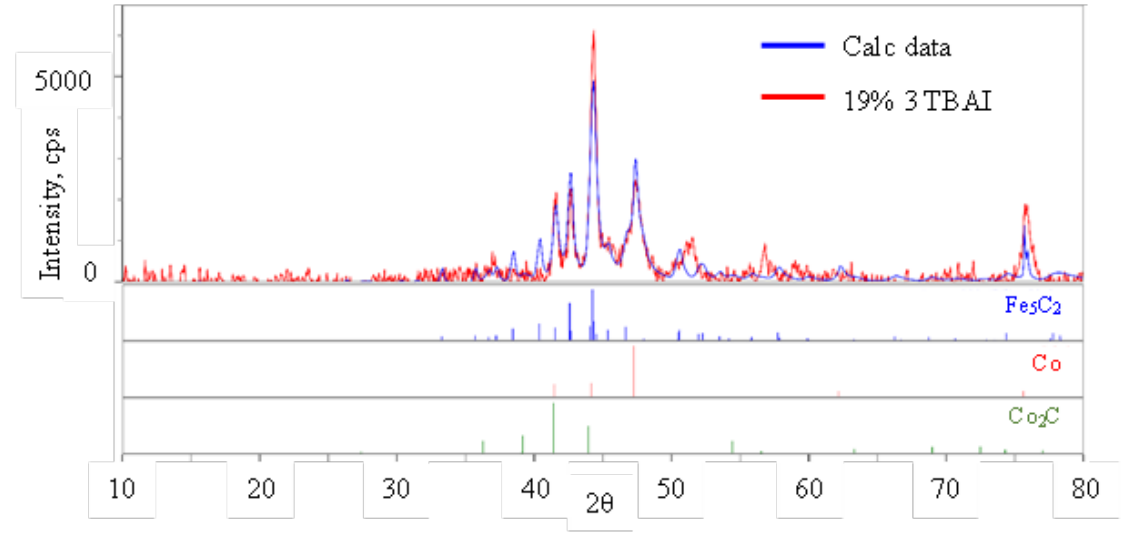
Calc data
19% 3 TBAI
Fe5C2
Co
Co2C
Intensity, cps
5000
0
10
20
30
40
50
60
70
80
2θ

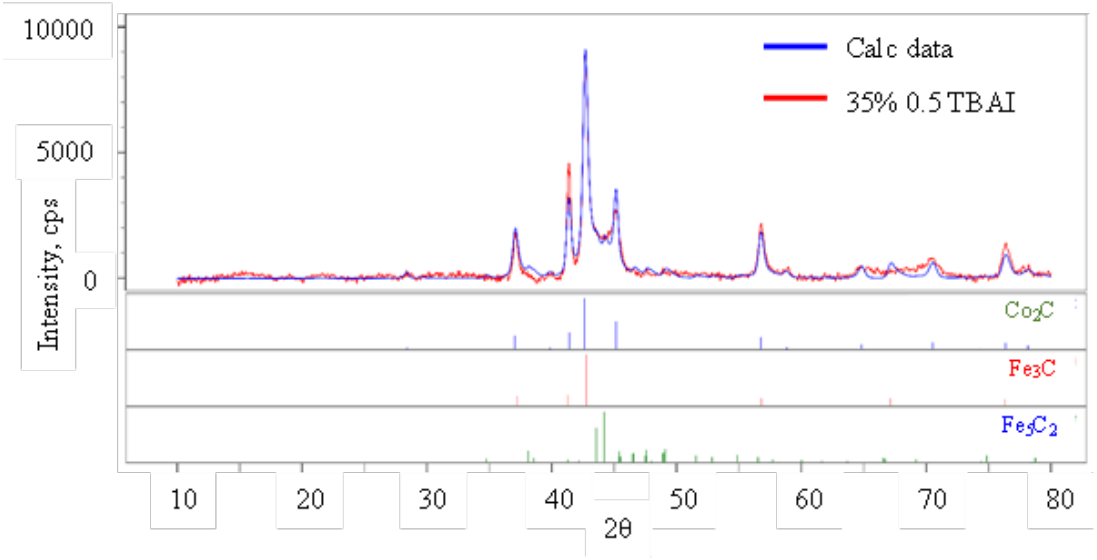
Calc data
35% 0.5 TBAI
Co2C
Fe3C
Fe5C2
Intensity, cps
10000
5000
0
10
20
30
40
50
60
70
80
2θ

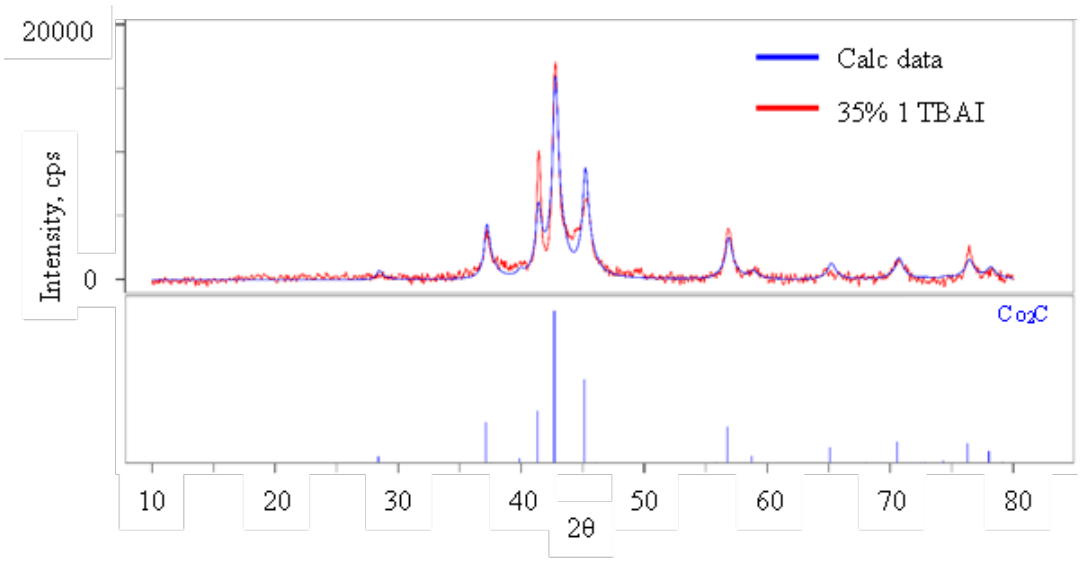
20000
Intensity, cps
0
Calc data
35% 1 TBAI
Co2C
10
20
30
40
50
60
70
80
2θ

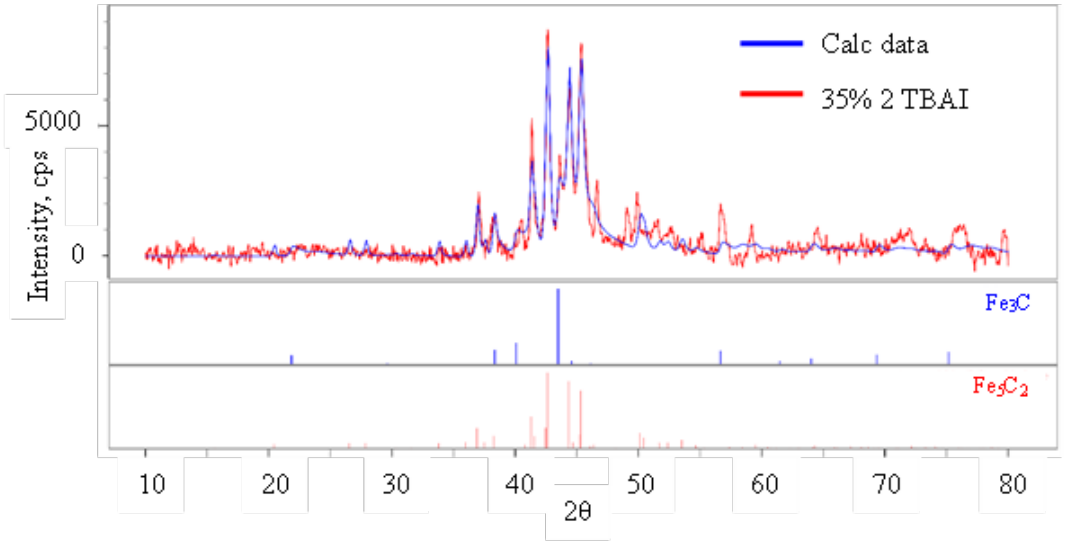
5000
Intensity, cps
0
Calc data
35% 2 TBAI
Fe3C
Fe5C2
10
20
30
40
50
60
70
80
2θ

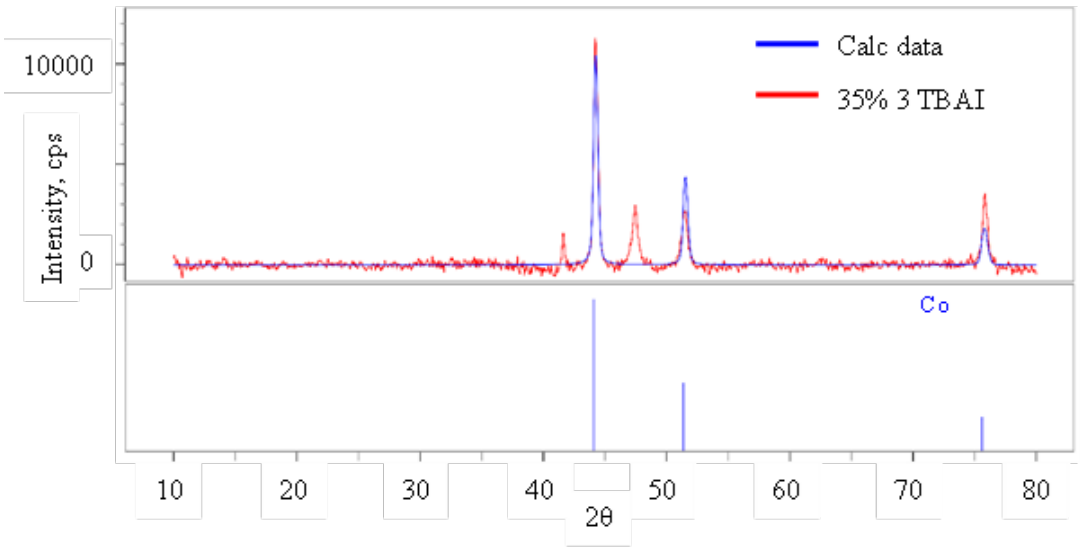
10000
Intensity, cps
0
Calc data
35% 3 TBAI
Co
10
20
30
40
50
60
70
80
2θ

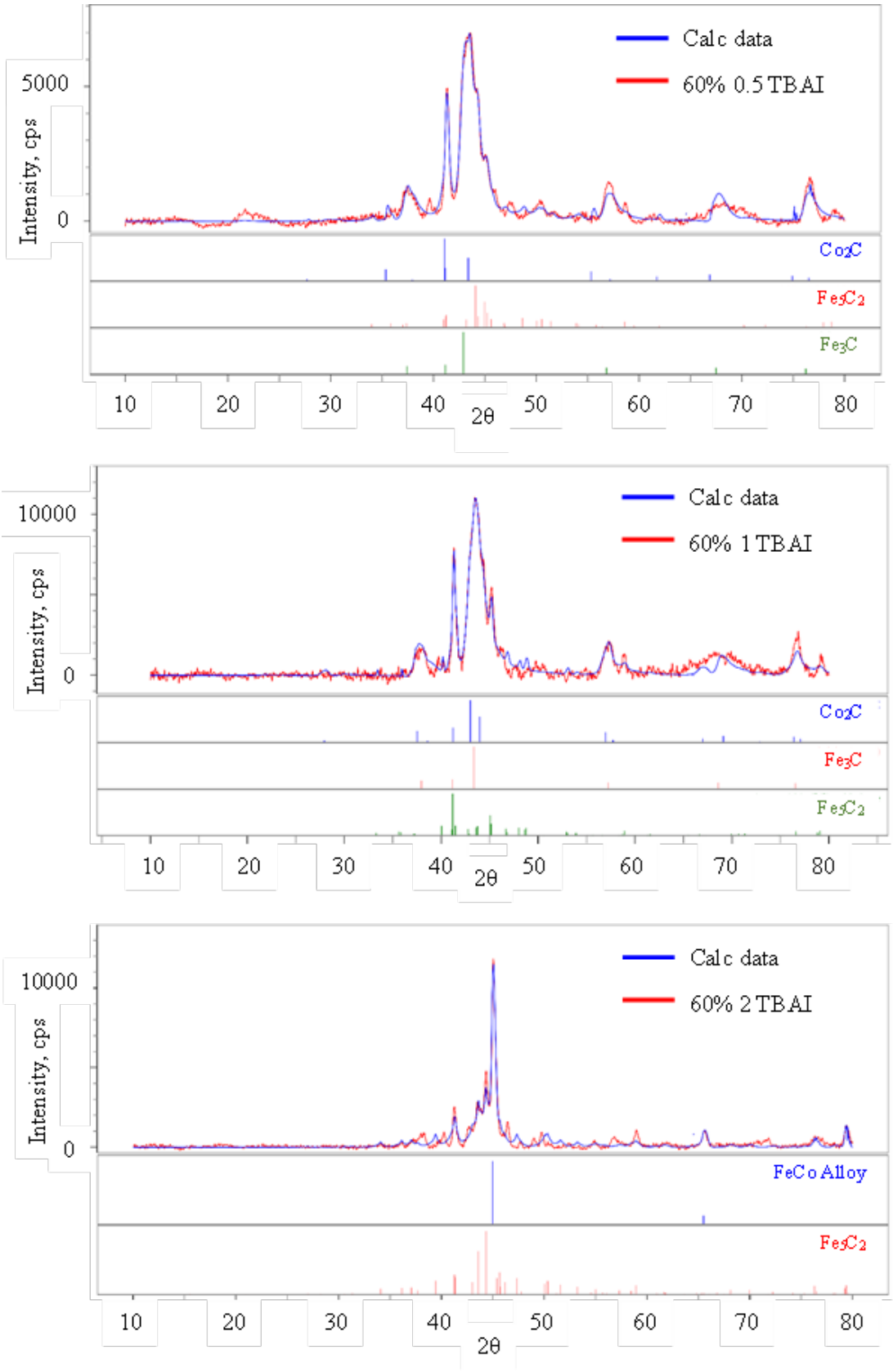
Calc data
60% 0.5 TBAI
5000
0
Intensity, cps
Co2C
Fe5C2
Fe3C
10
20
30
40
2θ
50
60
70
80
Calc data
60% 1 TBAI
10000
0
Intensity, cps
Co2C
Fe3C
Fe5C2
10
20
30
40
2θ
50
60
70
80
Calc data
60% 2 TBAI
10000
0
Intensity, cps
FeCo Alloy
Fe5C2
10
20
30
40
2θ
50
60
70
80

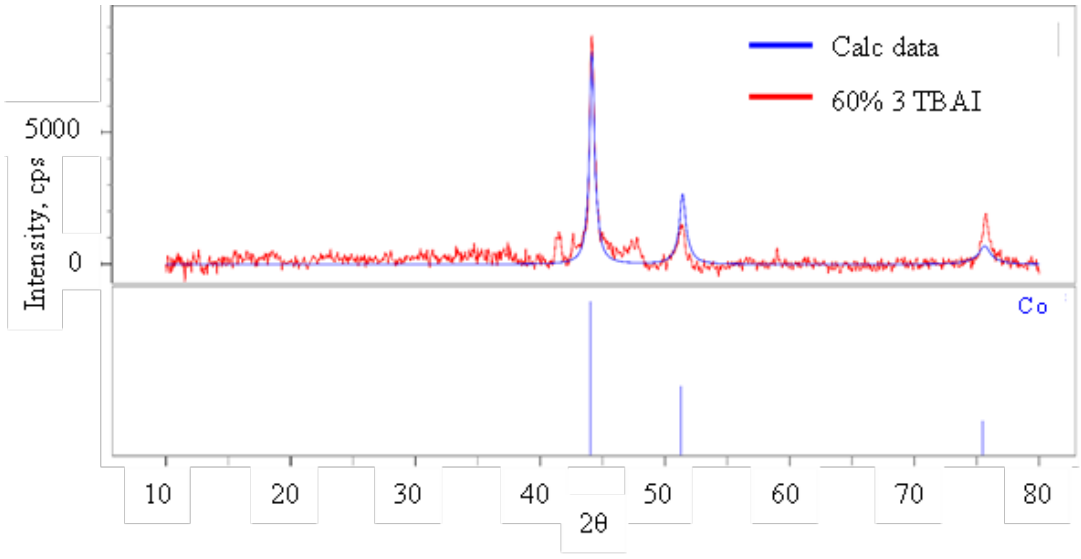
Calc data
60% 3 TBAI
5000
0
Intensity, cps
Co
10
20
30
40
50
60
70
80
2θ

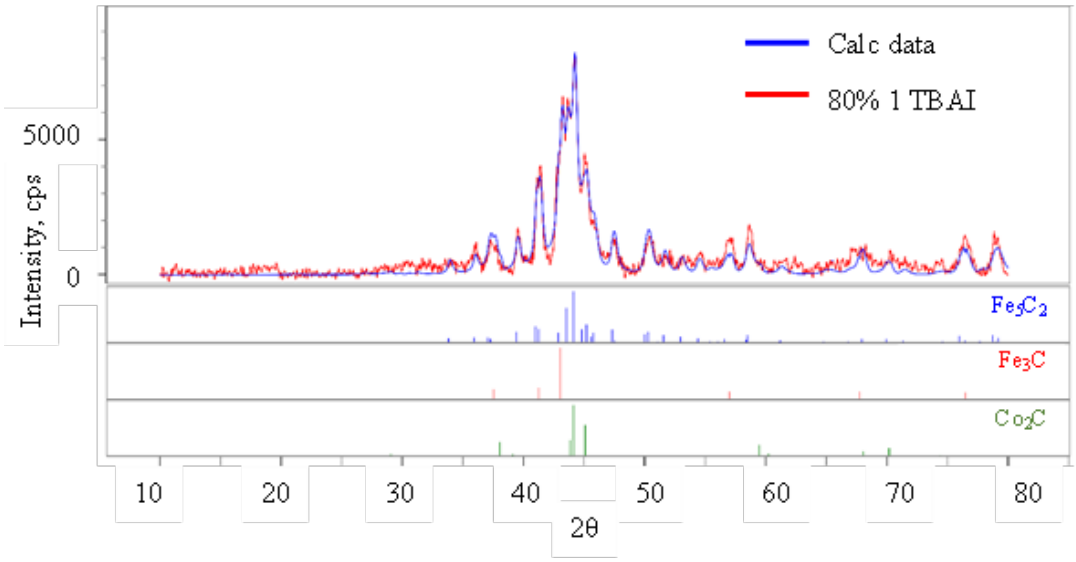
Calc data
80% 1 TBAI
5000
0
Intensity, cps
Fe5C2
Fe3C
Co2C
10
20
30
40
50
60
70
80
2θ

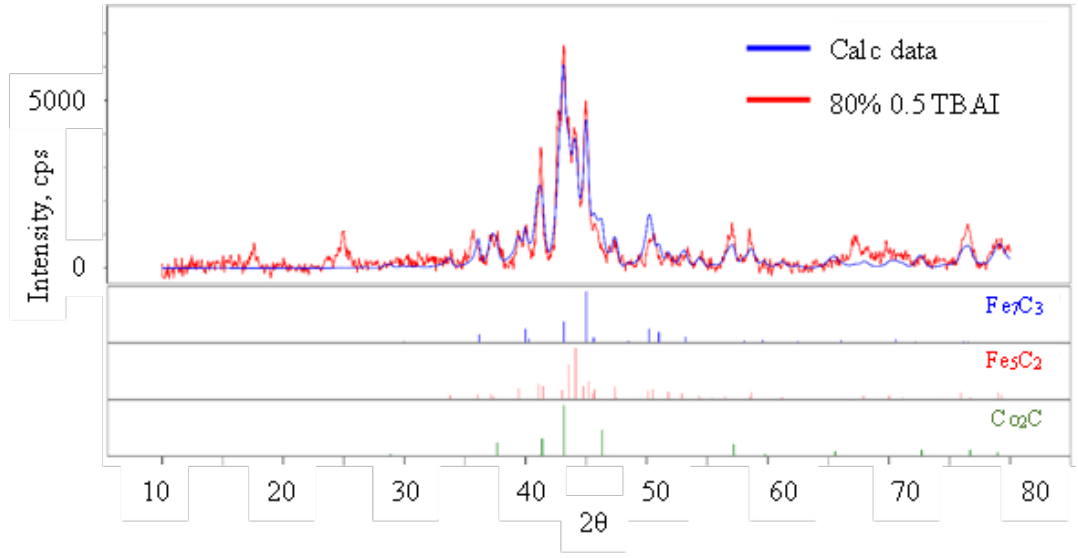
Calc data
80% 0.5 TBAI
5000
0
Intensity, cps
Fe7C3
Fe5C2
Co2C
10
20
30
40
50
60
70
80
2θ

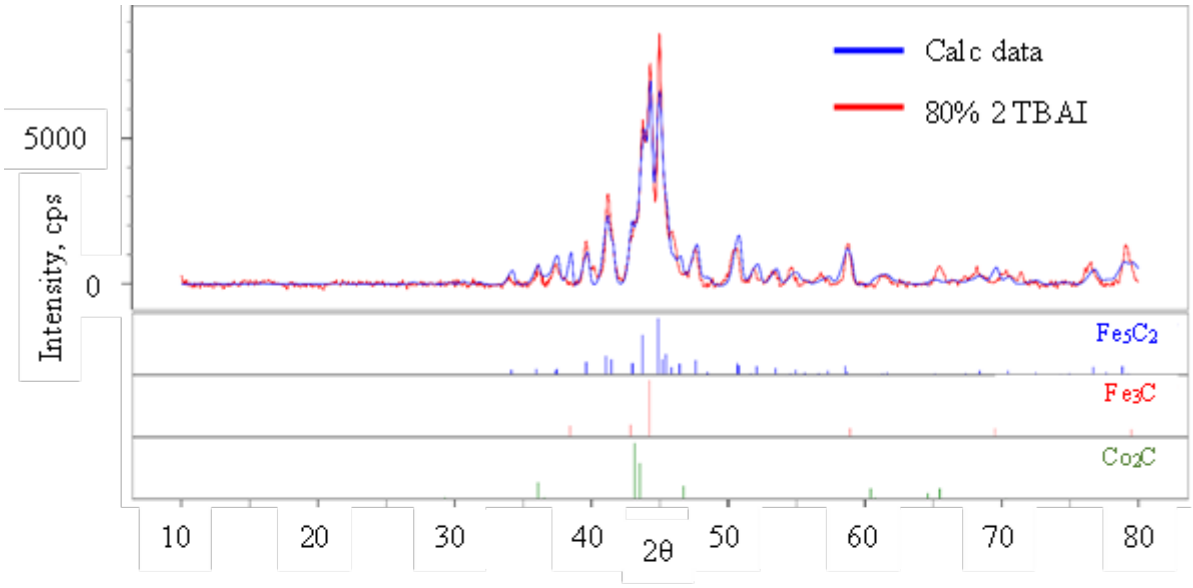
Calc data
80% 2 TBAI
5000
0
Intensity, cps
Fe5C2
Fe3C
Co2C
10
20
30
40
50
60
70
80
2θ

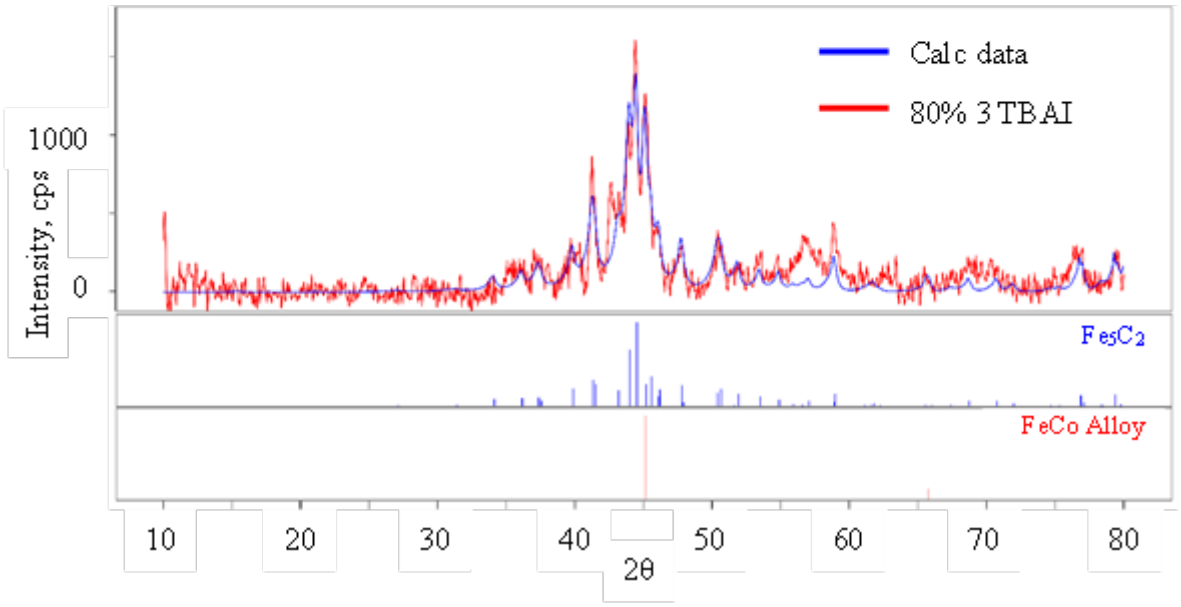
Calc data
80% 3 TBAI
1000
0
Intensity, cps
Fe5C2
FeCo Alloy
10
20
30
40
50
60
70
80
2θ

APPENDIX B: TABLE OF COMPLETE SYNTHETIC RANGE FOR FECO HALIDE – MEDIATED PHASE CONTROL

Reference for chapter 4. Complete experimental results for reactions run with varying halide species, metal ratio, and halide concentrations. Supporting tables for computational calculations.

Table B1. Experimental results for TBAF mediated FeCoC Studies.

TBAX	[TBAX] mmol	Temp	Time	% Fe Initial	% Fe Final	FeCoC Phase	Ref. card
-	0	350 °C	1 h	19	19	M_2C, M_3C	COD:1528415 ICSD:42542
				35	35	M_2C, M_3C	COD:1528415 ICSD:42542
				60	65	M_2C, M_3C M_5C_2	COD:1528415 ICSD:42542 ICSD:423885
				80	80	M_5C_2 M_7C_3	ICSD:423885 ICSD:76830
TBAF	0.5	350 °C	1 h	19	18	M_2C M_3C	COD:1528415 ICSD:42542
				35	33	M_2C M_3C M_5C_2	COD:1528415 ICSD:42542 ICSD:423885
				60	58	M_2C M_5C_2	COD:1528415 ICSD:423885
				80	80	M_2C M_5C_2 M_7C_3	COD:1528415 ICSD:423885 ICSD:76830
	1	350 °C	1 h	19	17	M_2C M_3C	COD:1528415 ICSD:42542
				35	33	M_2C M_5C_2	COD:1528415 ICSD:423885
				60	57	M_2C M_5C_2	COD:1528415 ICSD:423885
				80	80	M_2C, M_3C M_5C_2, M_7C_3	COD:1528415 ICSD:42542, 423885, 76830
	2	350 °C	1 h	19	11	M_2C M_3C	COD:1528415 ICSD:42542
				35	33	M_2C M_5C_2	COD:1528415 ICSD:423885b
				60	58	M_2C M_5C_2	COD:1528415 ICSD:423885
				80	79	M_2C, M_3C M_5C_2 M_7C_3	COD:1528415 ICSD:42542 423885, 76830

Table B2. Experimental results for TBAC mediated FeCoC Studies.

TBAX	[TBAX] mmol	Temp	Time	% Fe Initial	% Fe Final	FeCoC Phase	Ref. card
TBAC	0.1	350 °C	1 h	19	17	M_2C M_5C_2	COD:1528415 ICSD:423885
				35	33	M_2C M_3C M_5C_2	COD:1528415 ICSD:42542 ICSD:423885
				60	60	M_3C	ICSD:42542
				80	80	M_2C M_3C	COD:1528415 ICSD:42542
	0.5	350 °C	1 hr	19	16	M_2C	COD:1528415
				35	34	M_2C M_3C M_5C_2	COD:1528415 ICSD:42542 ICSD:423885
				60	57	M_2C M_3C M_7C_3	COD:1528415 ICSD:42542 ICSD:76830
				80	80	M_2C M_3C M_7C_3 M	COD:1528415 ICSD:42542 ICSD:76830
	1	350 °C	1 hr	19	10	M_2C	COD:1528415
				35	29	M_2C M_3C M_5C_2	COD:1528415 ICSD:42542 ICSD:423885
				60	57	M_2C M_3C M_7C_3	COD:1528415 ICSD:42542 ICSD:76830
				80	80	M_3C M_7C_3	ICSD:42542 ICSD:76830
	2	350 °C	1 hr	19	8	M_2C	COD:1528415
				35	13	M_2C	COD:1528415
				60	44	M_2C M_3C M_7C_3	COD:1528415 ICSD:42542 ICSD:76830
				80	72	M_3C M_7C_3	ICSD:42542 ICSD:76830
	3	350 °C	1 hr	60	44	M_2C M_3C M_7C_3	COD:1528415 ICSD:42542 ICSD:76830
				80	72	M_7C_3	ICSD:76830

Table B3. Experimental results for TBAB mediated FeCoC Studies.

TBAX	[TBAX] mmol	Temp	Time	% Fe Initial	% Fe Final	FeCoC Phase	Ref. card
TBAB	0.5	350 °C	1 hr	19	14	M_2C	COD:1528415
				35	30	M_2C M_3C	COD:1528415 ICSD:42542
				60	55	M_3C M_5C_2	ICSD:42542 ICSD:423885
				80	80	M_3C M_5C_2 M_7C_3	ICSD:42542 ICSD:423885 ICSD:76830
	1	350 °C	1 hr	19	7	M_2C	COD:1528415
				35	11	M_2C M_3C	COD:1528415 ICSD:42542
				60	46	M_2C M_3C M_5C_2	COD:1528415 ICSD:42542 ICSD:423885
				80	79	M_2C M_3C M_7C_3 M	COD:1528415 ICSD:42542 ICSD:76830
	2	350 °C	1 hr	19	3	M_2C	COD:1528415
				35	5	M_2C M_3C	COD:1528415 ICSD:42542
				60	21	M_2C M_3C M_5C_2	COD:1528415 ICSD:42542 ICSD:423885
				80	60	M_2C M_3C M_5C_2	COD:1528415 ICSD:42542 ICSD:423885
	3	350 °C	1 hr	19	--	M_2C	COD:1528415
				35	3	M	ICSD:102381
				60	6	M_2C M_3C M_5C_2	COD:1528415 ICSD:42542 ICSD:423885
				80	28	M	ICSD:102381

Table B4. Experimental results for TBAI mediated FeCoC Studies.

TBAX	[TBAX] mmol	Temp	Time	% Fe	% Fe	FeCoC	Ref. card
TBAI	0.5	350 °C	1 hr	19	10	M_2C	COD:1528415
				35	26	M_2C	COD:1528415
				60	56	M_2C M_3C M_5C_2	COD:1528415 ICSD:42542 ICSD:423885
				80	80	M_2C M_5C_2 M_7C_3	COD:1528415 ICSD:423885 ICSD:76830
	1	350 °C	1 hr	19	5	M_2C	COD:1528415
				35	14	M_2C	COD:1528415
				60	45	M_2C M_3C M_5C_2	COD:1528415 ICSD:42542 ICSD:423885
				80	78	M_2C M_5C_2	COD:1528415 ICSD:423885
	2	350 °C	1 hr	19	3	M_2C M_5C_2	COD:1528415 ICSD:423885
				35	7	M_3C M_5C_2	ICSD:76830 ICSD:423885
				60	24	M_5C_2 M	ICSD:423885 ICSD:102381
				80	59	M_2C M_3C M_5C_2	COD:1528415 ICSD:42542 ICSD:423885
	3	350 °C	1 hr	19	4	M	ICSD:102381
				35	9	M	ICSD:102381
				60	11	M	ICSD:102381
				80	35	M_5C_2	ICSD:423885

Table B5: Comparison of adsorption energies obtained using different reference states for X and C atoms on FeCo(110) surface. ; the second column represents BEs calculated using the reference state of X atom as ½ the energy of X molecule and energy of C atom from the graphite phase. The last column represents previously reported BEs. The lowest energies are highlighted in blue.

Element	Most Stable Site	BE (eV) (changing reference state)	BE (eV)(previously reported BE)
NH_3	Fe-hollow	-0.02	-0.02
NH_3	Co-hollow	Move to top	Move to top
NH_3	Fe-top	2.49	2.49
NH_3	Co-top	-1.93	-4.21
NH_3	bridge	Move to hollow	Move to hollow
C	Fe-hollow	Unstable	Unstable
C	Co-hollow	-4.13	-11.50
C	Fe-top	1.34	-6.30
C	Co-top	Unstable	Unstable
C	bridge	Move to hollow	Move to hollow
F	Fe-hollow	-3.81	-4.51
F	Co-hollow	-1.70	-2.41
F	Fe-top	Unstable	Unstable
F	Co-top	Unstable	Unstable
F	bridge	Move to hollow	Move to hollow
Cl	Fe-hollow	Unstable	Unstable
Cl	Co-hollow	-10.40	-11.89
Cl	Fe-top	-4.11	-5.60
Cl	Co-top	-6.87	-8.36
Cl	bridge	Move to hollow	Move to hollow
Br	Fe-hollow	-2.02	-3.25
Br	Co-hollow	-4.96	-6.20
Br	Fe-top	Unstable	Unstable
Br	Co-top	1.96	-0.72
Br	bridge	Move to hollow	Move to hollow
I	Fe-hollow	Unstable	Unstable
I	Co-hollow	-10.38	-10.38
I	Fe-top	-2.00	-2.00
I	Co-top	-5.30	-5.30
I	bridge	Move to hollow	Move to hollow

Table B6: Binding energies (BE) for thermodynamically most stable configuration for first C/X adsorption on $Fe_3C(001)$ surface.

Most favorable site	Adsorbate	Binding energy (eV)
1-C-hollow	C	-1.33
1-C-hollow	F	-4.61
1-C-hollow	Cl	-2.84
hollow	Br	-2.60
1-C-hollow	I	-3.56

Table B7: Binding energies for lowest energy configuration for first C/X adsorption on $Co_2C(101)$ surface.

Most favorable site	adsorbate	Binding energy (eV)
2-Co-hollow	C	0.29
1-Co-hollow	F	-3.42
1-Co-hollow	Cl	-1.79
1-Co-hollow	Br	-1.63
1-Co-hollow	I	-2.54

Table B8: Binding energies for lowest energy configuration for first C/X adsorption on Fe-terminated FeCoC(001) surface.

Most favorable site	adsorbate	Binding energy (eV)
hollow	C	-1.12
1-C-hollow	F	-4.47
1-C-hollow	Cl	-2.75
1-C-hollow	Br	-2.59
1-C-hollow	I	-3.52

Table B9: Binding energies for lowest energy configuration for first C/X adsorption on Co-terminated FeCoC(001) surface.

Most favorable site	adsorbate	Binding energy (eV)
hollow	C	-0.95
1-C-hollow	F	-4.12
1-C-hollow	Cl	-2.65
1-C-hollow	Br	-2.51
1-C-hollow	I	-3.47

Table B10: Binding energies for C on C pre-adsorbed, C on X-pre adsorbed, and X on C pre-adsorbed $Fe_3C(001)$ surface.

Most favorable site	1st adsorbate	2nd adsorbate	2nd adsorbate BE (eV)
hollow	C	C	-1.23
hollow	F	C	-1.01
hollow	Cl	C	-0.99
1-C-hollow	Br	C	-1.02
hollow	I	C	-0.98
hollow	C	F	-4.26
hollow	C	Cl	-2.48
hollow	C	Br	-2.30
hollow	C	I	-3.21
top	C	NH_3	-0.55

Table B11: Binding energies of C on C/X/NH_3 pre-adsorbed, X on C pre-adsorbed, and NH_3 on C pre-adsorbed FeCo(110) surface. Here, the second column represents BEs calculated using the reference states of the X atom as ½ the energy of the X molecule and the energy of the C atom from the graphite phase. The last column represents previously reported BEs. The lowest energies are highlighted in blue. The binding energies are lower for all carbon 1st adsorbate variants than carbon as 2nd adsorbate.

Most-favorable site	Pre-adsorbed species	2nd adsorbate	2nd adsorbate BE (eV)	2nd adsorbate BE (eV)
1-Fe-hollow	C	C	-4.52	-11.89
1-Co-hollow	F	C	-2.22	-9.59
1-Co-hollow	Cl	C	3.95	-3.42
1-Co-hollow	Br	C	-1.97	-9.34
1-Fe-hollow	I	C	5.12	-2.25
1-Co-hollow	NH_3	C	-1.93	-7.02
1-Co-hollow	C	F	-11.30	-12.00
1-Fe-hollow	C	Cl	-1.36	-2.85
1-Co-hollow	C	Br	-1.87	-3.11
1-Fe-hollow	C	I	-3.18	-3.18
1-Co-hollow	C	NH_3	-5.40	-5.40

Table B12: Binding energies for C on C pre-adsorbed, C on X-preadsorbed, X on C pre-adsorbed, and NH_3 on C pre-adsorbed $Co_2C(101)$ surface.

Most favorable site	1st adsorbate	2nd adsorbate	2nd adsorbate BE (eV)
1-Co-hollow	C	C	-1.27
Co-top	F	C	-0.22
1-Co-hollow	Cl	C	0.51
1-Co-hollow	Br	C	0.74
Co-top	I	C	1.67
hollow	C	F	-3.93
hollow	C	Cl	-1.76
hollow	C	Br	-1.60
hollow	C	I	-2.50
top	C	NH_3	-1.12

Table B13: Binding energies for C on C pre-adsorbed, C on X-preadsorbed, and X on C pre-adsorbed Fe-terminated FeCoC(001) surface.

Most favorable site	1st adsorbate	2nd adsorbate	2nd adsorbate BE (eV)
1-C-hollow	C	C	-0.96
hollow	F	C	-0.93
hollow	Cl	C	-0.89
hollow	Br	C	-0.88
hollow	I	C	-0.86
1-C-hollow	C	F	-4.28
1-C-hollow	C	Cl	-2.53
1-C-hollow	C	Br	-2.35
1-C-hollow	C	I	-3.27
top	C	NH_3	-0.93

Table B14: Binding energies for C on C pre-adsorbed, C on X-preadsorbed, and X on C pre-adsorbed Co-terminated FeCoC(001) surface.

Most favorable site	1st adsorbate	2nd adsorbate	2nd adsorbate BE (eV)
1-C-hollow	C	C	-0.83
hollow	F	C	-0.74
hollow	Cl	C	-0.71
hollow	Br	C	-0.71
hollow	I	C	-0.68
1-C-hollow	C	F	-3.90
1-C-hollow	C	Cl	-2.40
1-C-hollow	C	Br	-2.25
1-C-hollow	C	I	-3.29
top	C	NH_3	-1.47

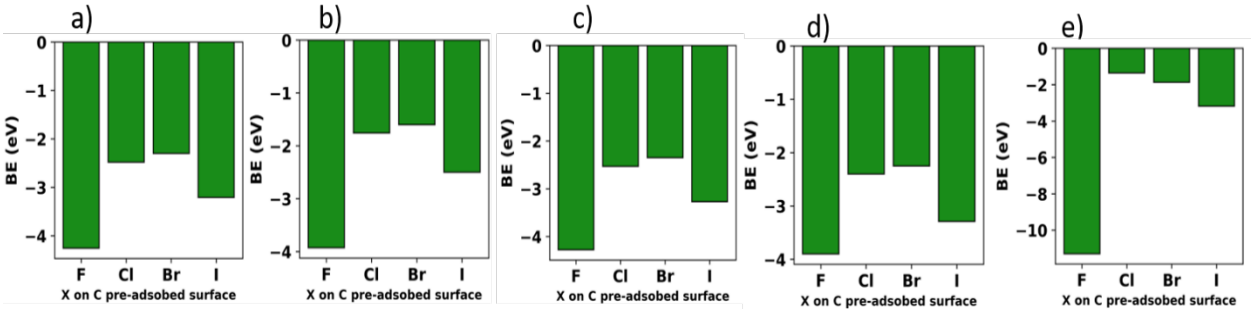

Figure B1: X BEs on C pre-adsobed surfaces: a) $Fe_3C(001)$ b) $Co_2C(101)$ c) Fe-terminated FeCoC(001) d) Co-terminated FeCoC(001), and e) bimetallic FeCo(110).

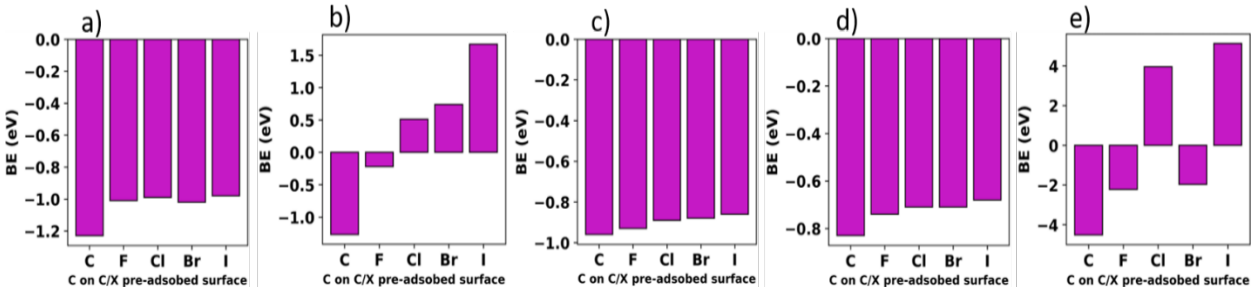

Figure B2: C BEs on C/X pre-adsobed surfaces: a) $Fe_3C(001)$ b) $Co_2C(101)$ c) Fe-terminated FeCoC(001) d) Co-terminated FeCoC(001), and e) bimetallic FeCo(110).

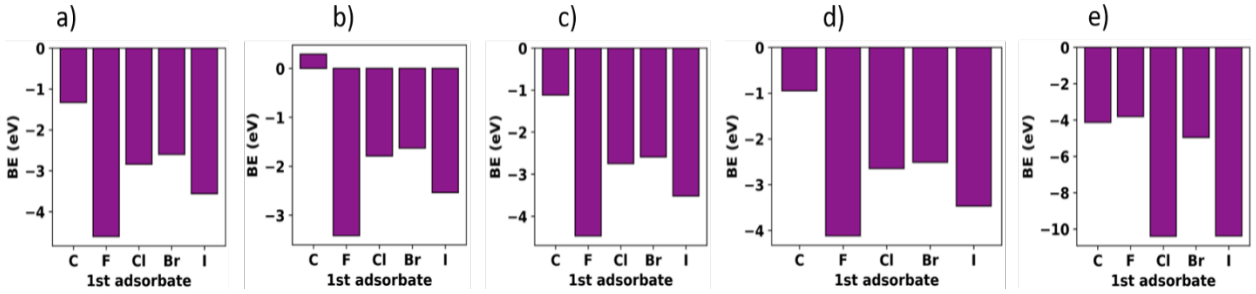

Figure B3: The first adsorbate BEs trend on: a) $Fe_3C(001)$ b) $Co_2C(101)$ c) Fe-terminated FeCoC(001) d) Co-terminated FeCoC(001), and e) bimetallic FeCo(110) surfaces.

APPENDIX C: XRF VALUES FOR ALL PBA AND CARBIDES FROM MONOMETALLIC TO PENTAMETALLIC

Appendix C includes all XRF data for monometallic to pentametallic PBA and PBA – derived carbides.

Table C1: XRF for monometallic PBA and PBA – Derived carbides

Metal	Target %	Actual % (PBA)	Actual % (Carbide)
Monometallic			
Cr	100	98	96
Mn	100	99	99
Fe	100	99	98
Co	100	100	99
Ni	100	100	99

Table C2: XRF for bimetallic PBA and PBA – Derived carbides

Metal	Target %	Actual % (PBA)	Actual % (Carbide)
Bimetallic			
Cr	50	18	18
Mn	50	82	82
Cr	50	5	5
Mn	50	95	95
Cr	50	24	24
Fe	50	76	76
Cr	50	13	14
Fe	50	87	86
Cr	50	27	27
Co	50	73	73
Cr	50	11	18
Co	50	89	82
Cr	50	30	30
Ni	50	70	70
Cr	50	33	42
Ni	50	67	58
Mn	50	42	41
Cr	50	58	59
Mn	50	26	26
Fe	50	74	74
Mn	50	39	40
Co	50	61	60

Table C2 Continued.

Metal	Target %	Actual % (PBA)	Actual % (Carbide)
Bimetallic			
Cr	50	18	18
Mn	50	82	82
Cr	50	5	5
Mn	50	95	95
Cr	50	24	24
Fe	50	76	76
Cr	50	13	14
Fe	50	87	86
Cr	50	27	27
Co	50	73	73
Cr	50	11	18
Co	50	89	82
Cr	50	30	30
Ni	50	70	70
Cr	50	33	42
Ni	50	67	58
Mn	50	42	41
Cr	50	58	59
Mn	50	26	26
Fe	50	74	74
Mn	50	39	40
Co	50	61	60
Mn	50	99	99
Ni	50	1	1
Fe	50	80	3
Cr	50	20	97
Fe	50	51	49
Mn	50	49	51
Fe	50	38	38
Co	50	62	62
Fe	50	38	38
Ni	50	62	62

Table C2 Continued.

Metal	Target %	Actual % (PBA)	Actual % (Carbide)
Bimetallic			
Co	50	NR	
Cr	50		
Co	50	49	49
Mn	50	51	51
Co	50	55	55
Fe	50	45	45
Co	50	47	47
Ni	50	53	53
Ni	50	2	3
Cr	50	98	97
Ni	50	54	54
Mn	50	46	46
Ni	50	53	53
Fe	50	47	47
Ni	50	57	57
Co	50	43	43

Table C3: XRF for trimetallic PBA and PBA – Derived carbides

Metal	Target %	Actual % (PBA)	Actual % (Carbide)
Trimetallic			
Cr	33	10	4
Fe	33	49	46
Co	33	41	50
Cr	33	20	15
Fe	33	37	38
Ni	33	43	47
Cr	33	16	12
Co	33	39	42
Ni	33	45	46
Mn	33	25	26
Fe	33	41	41
Co	33	34	33
Mn	33	22	25
Fe	33	53	48
Ni	33	25	27
Mn	33	25	30
Co	33	40	44
Ni	33	35	26

Table C3 Continued

Metal	Target %	Actual % (PBA)	Actual % (Carbide)
Trimetallic			
Fe	33	32	30
Co	33	38	36
Ni	33	30	34
Cr	33	17	19
Mn	33	28	28
Fe	33	55	54
Cr	33	20	18
Mn	33	30	37
Co	33	50	55
Cr	33	25	36
Mn	33	25	29
Ni	33	50	35

Table C4: XRF for tetrametallic PBA and PBA – Derived carbides

Metal	Target %	Actual % (PBA)	Actual % (Carbide)
Tetrametallic			
Cr	25	13	7
Fe	25	30	27
Co	25	28	32
Ni	25	29	34
Mn	25	27	28
Fe	25	25	26
Co	25	31	32
Ni	25	17	15
Cr	25	17	17
Mn	25	22	22
Co	25	35	36
Ni	25	26	25
Cr	25	18	18
Mn	25	20	21
Fe	25	32	33
Ni	25	30	28
Cr	25	13	11
Mn	25	22	21
Fe	25	31	32
Co	25	34	36

Table C5: XRF for Pentametallic PBA and PBA – Derived carbides

Metal	Target %	Actual % (PBA)	Actual % (Carbide)
Tetrametallic			
Cr	40	26	24
Mn	40	39	32
Fe	6.67	19	22
Co	6.67	11	13
Ni	6.67	5	9
Cr	30	22	22
Mn	30	27	27
Fe	13.33	18	18
Co	13.33	17	17
Ni	13.33	13	13
Cr	20	13	12
Mn	20	16	17
Fe	20	24	24
Co	20	27	27
Ni	20	21	39

APPENDIX D: PXRD FOR ALL PBA AND CARBIDES FROM MONOMETALLIC TO PENTAMETALLIC

Appendix D includes all pXRD data for monometallic to pentametallic PBA and PBA – derived carbides.

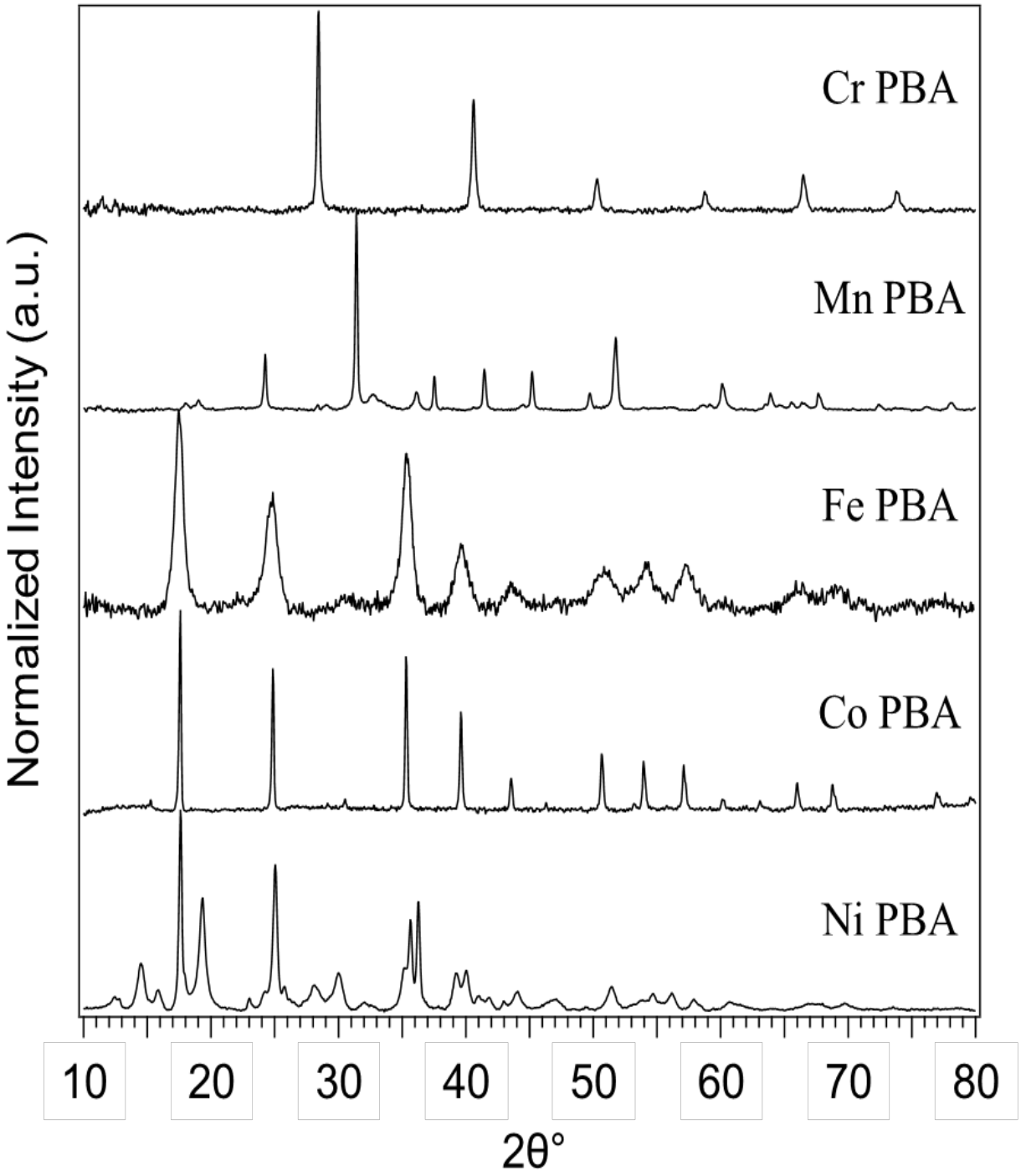

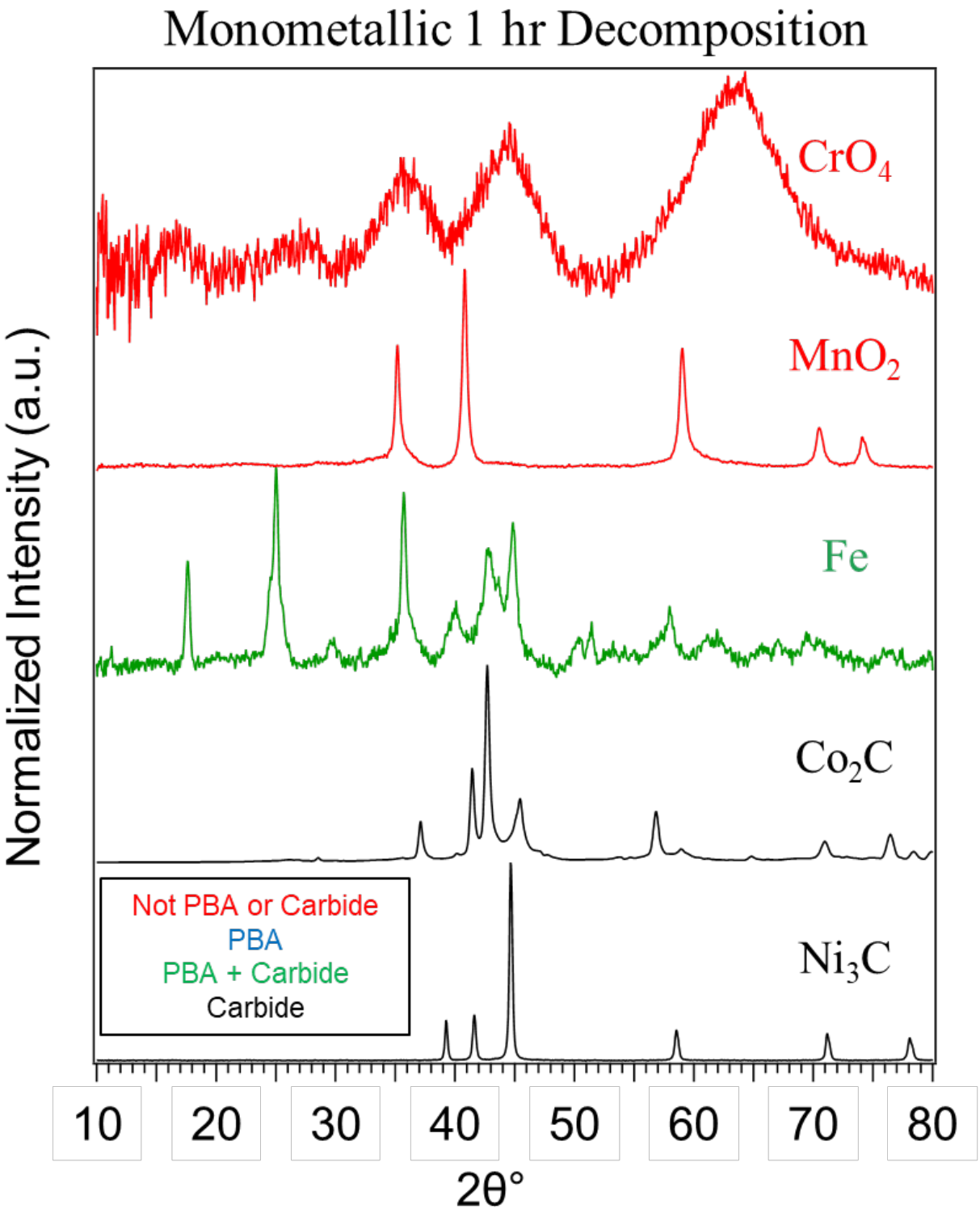
Monometallic 1 hr Decomposition
Normalized Intensity (a.u.)
CrO_4
MnO_2
Fe
Co_2C
Ni_3C
Not PBA or Carbide
PBA
PBA + Carbide
Carbide
10
20
30
40
50
60
70
80
2θ°

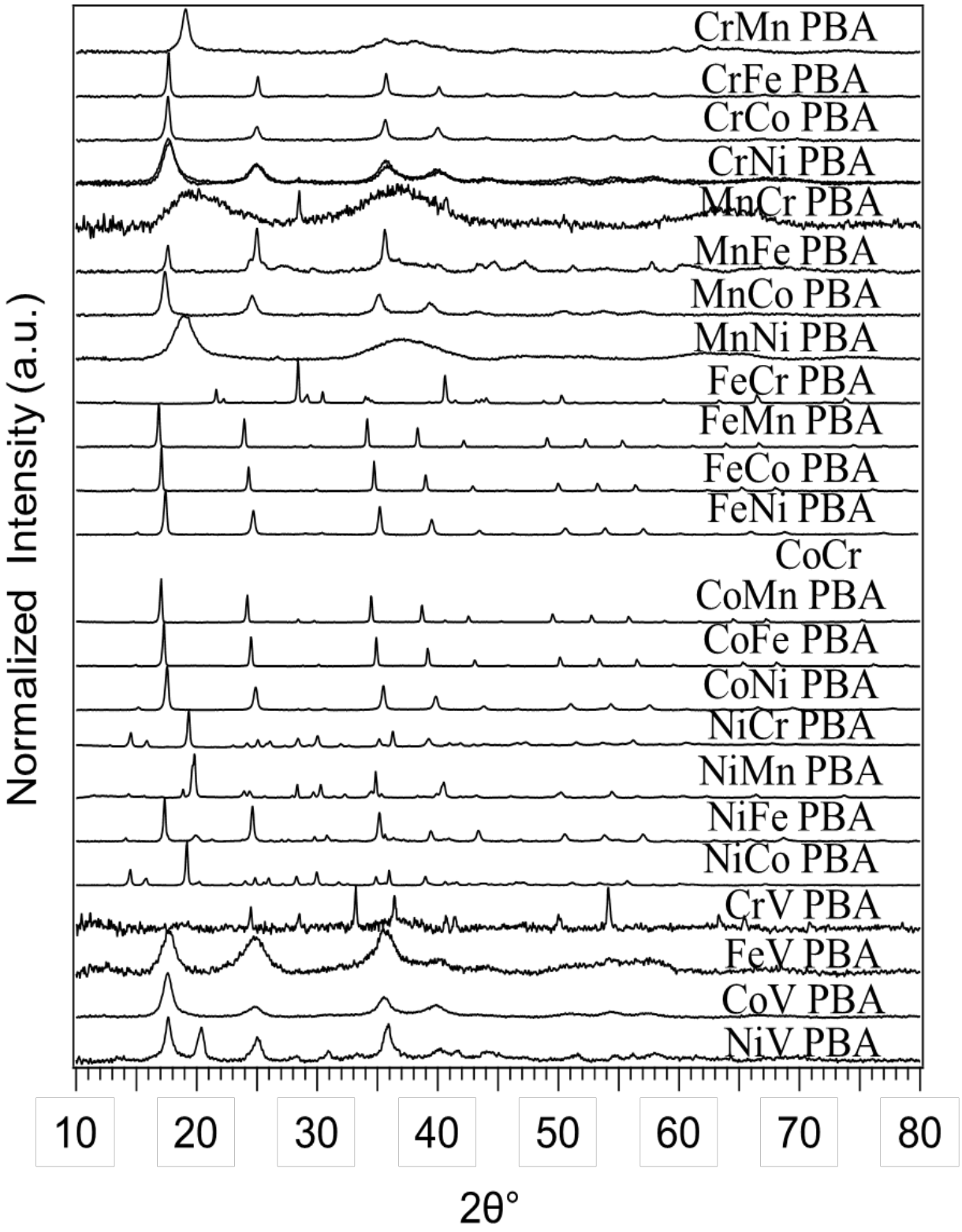
CrMn PBA
CrFe PBA
CrCo PBA
CrNi PBA
MnCr PBA
MnFe PBA
MnCo PBA
MnNi PBA
FeCr PBA
FeMn PBA
FeCo PBA
FeNi PBA
CoCr
CoMn PBA
CoFe PBA
CoNi PBA
NiCr PBA
NiMn PBA
NiFe PBA
NiCo PBA
CrV PBA
FeV PBA
CoV PBA
NiV PBA
Normalized Intensity (a.u.)
10
20
30
40
50
60
70
80
2θ°

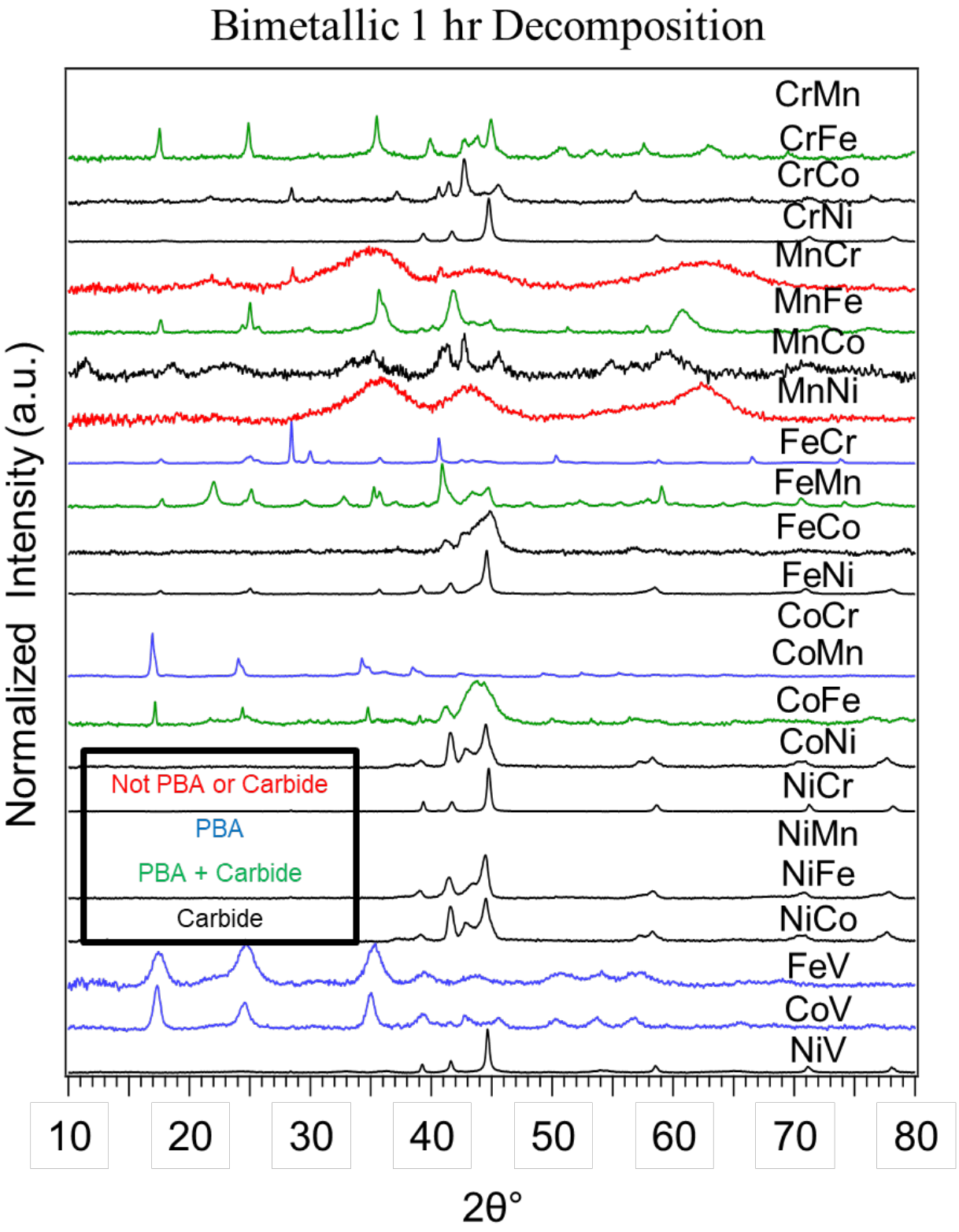
Bimetallic 1 hr Decomposition
Normalized Intensity (a.u.)
CrMn
CrFe
CrCo
CrNi
MnCr
MnFe
MnCo
MnNi
FeCr
FeMn
FeCo
FeNi
CoCr
CoMn
CoFe
CoNi
NiCr
NiMn
NiFe
NiCo
FeV
CoV
NiV
Not PBA or Carbide
PBA
PBA + Carbide
Carbide
10
20
30
40
50
60
70
80
2θ°

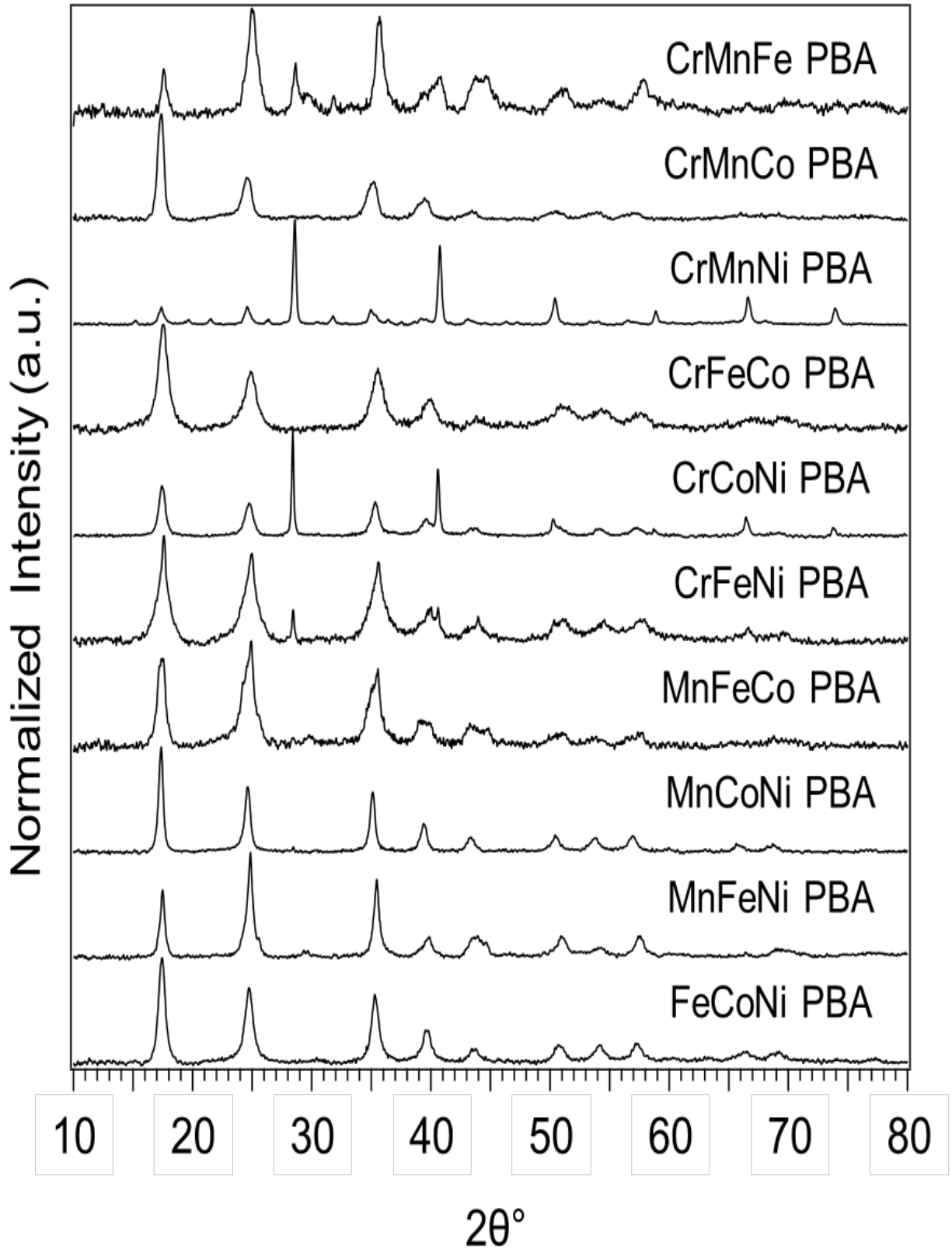
CrMnFe PBA
CrMnCo PBA
CrMnNi PBA
CrFeCo PBA
CrCoNi PBA
CrFeNi PBA
MnFeCo PBA
MnCoNi PBA
MnFeNi PBA
FeCoNi PBA
Normalized Intensity (a.u.)
10
20
30
40
50
60
70
80
2θ°

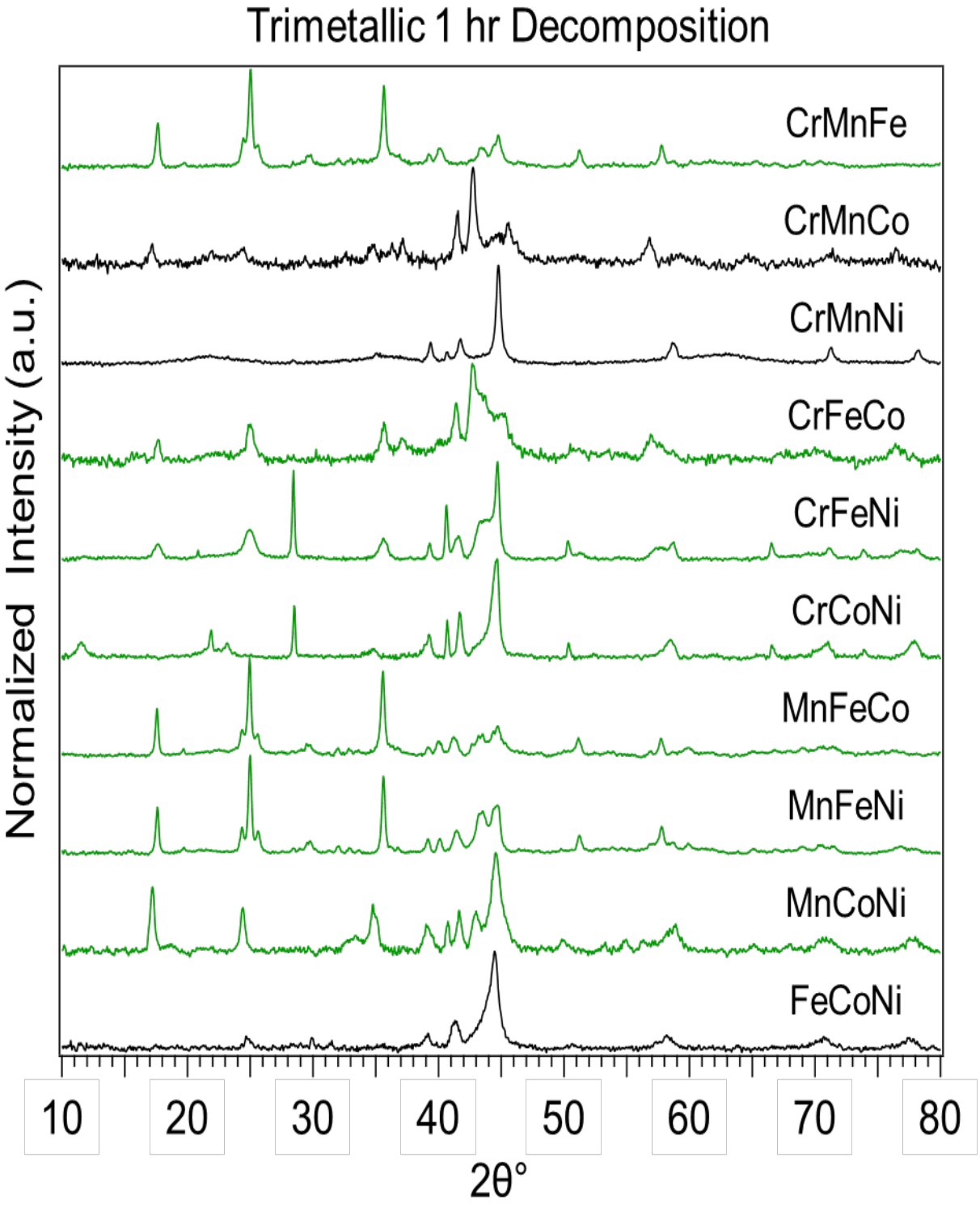
Trimetallic 1 hr Decomposition
Normalized Intensity (a.u.)
CrMnFe
CrMnCo
CrMnNi
CrFeCo
CrFeNi
CrCoNi
MnFeCo
MnFeNi
MnCoNi
FeCoNi
10
20
30
40
50
60
70
80
2θ°

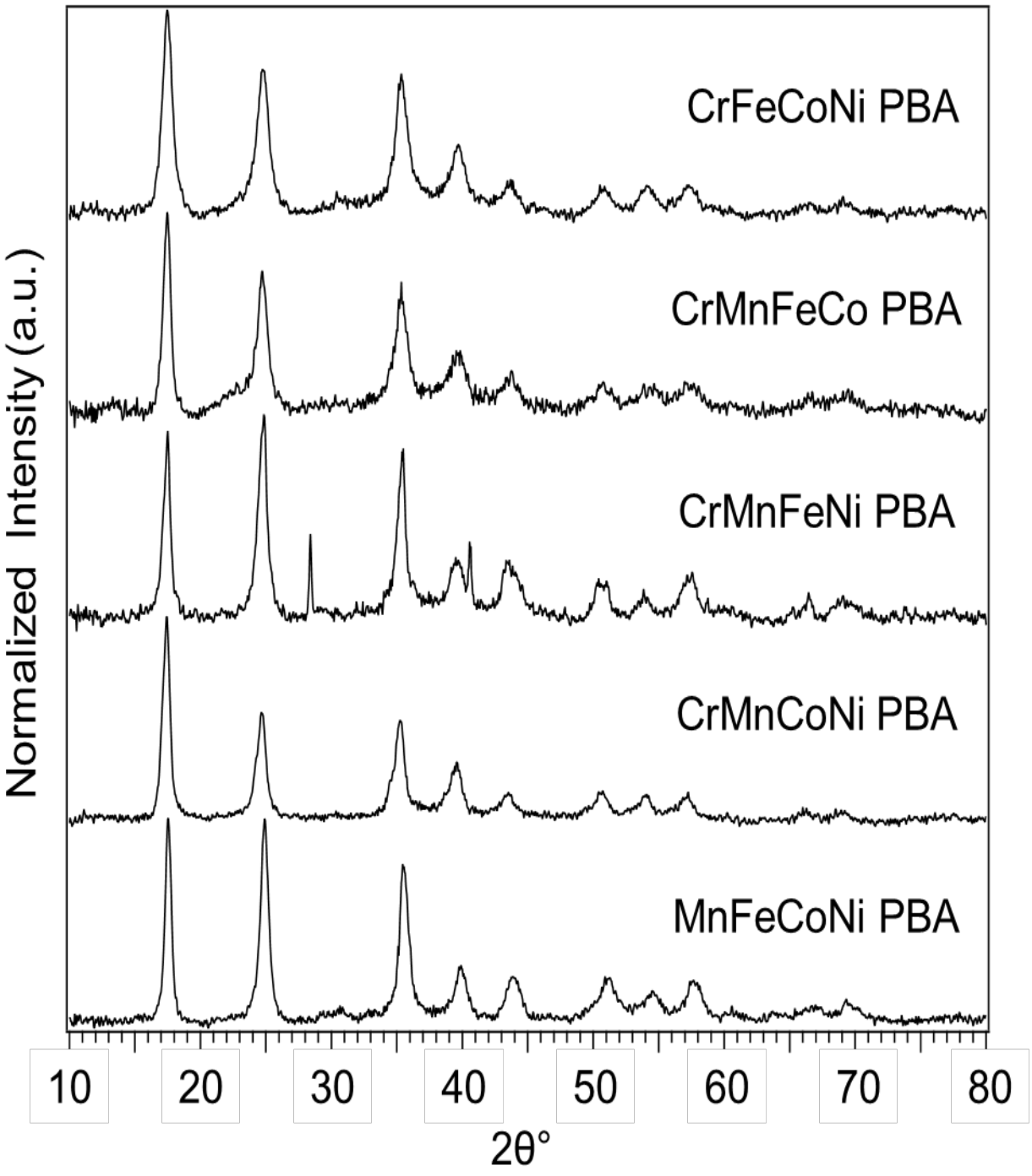
CrFeCoNi PBA
CrMnFeCo PBA
CrMnFeNi PBA
CrMnCoNi PBA
MnFeCoNi PBA
Normalized Intensity (a.u.)
10
20
30
40
50
60
70
80
2θ°

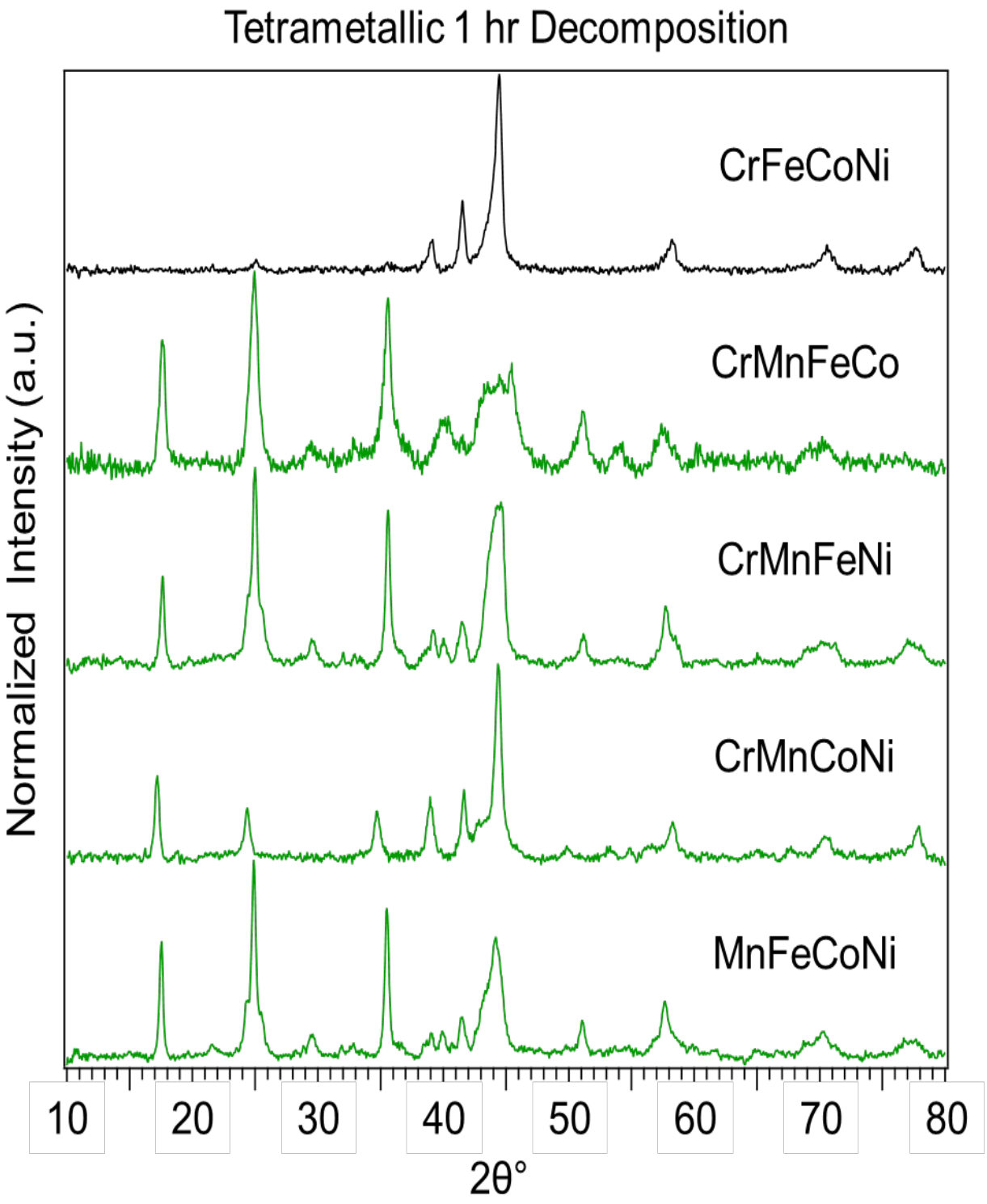
Tetrametallic 1 hr Decomposition
CrFeCoNi
CrMnFeCo
CrMnFeNi
CrMnCoNi
MnFeCoNi
Normalized Intensity (a.u.)
10
20
30
40
50
60
70
80
2θ°

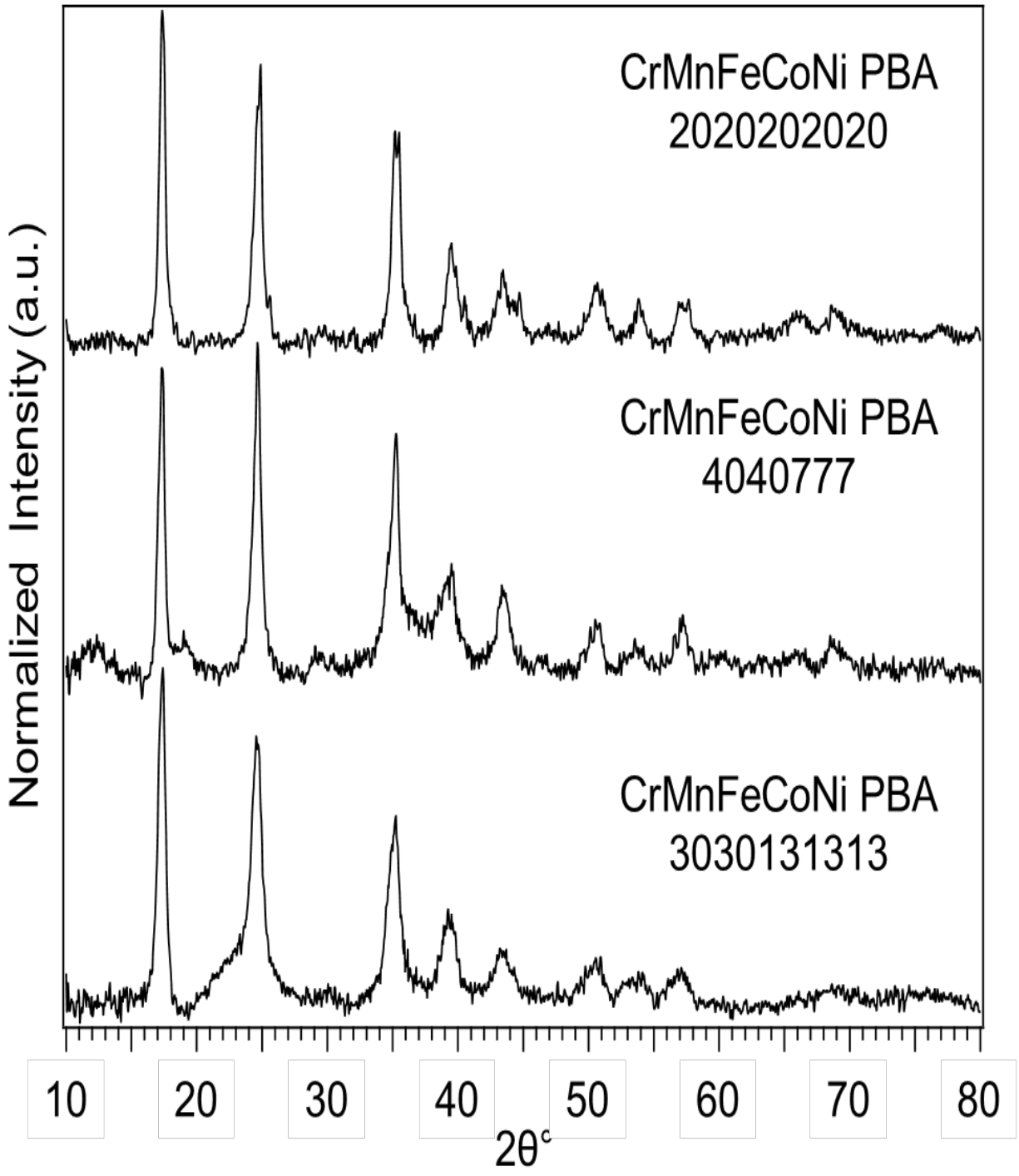
CrMnFeCoNi PBA
2020202020
CrMnFeCoNi PBA
4040777
CrMnFeCoNi PBA
3030131313
Normalized Intensity (a.u.)
10
20
30
40
50
60
70
80
2θ°

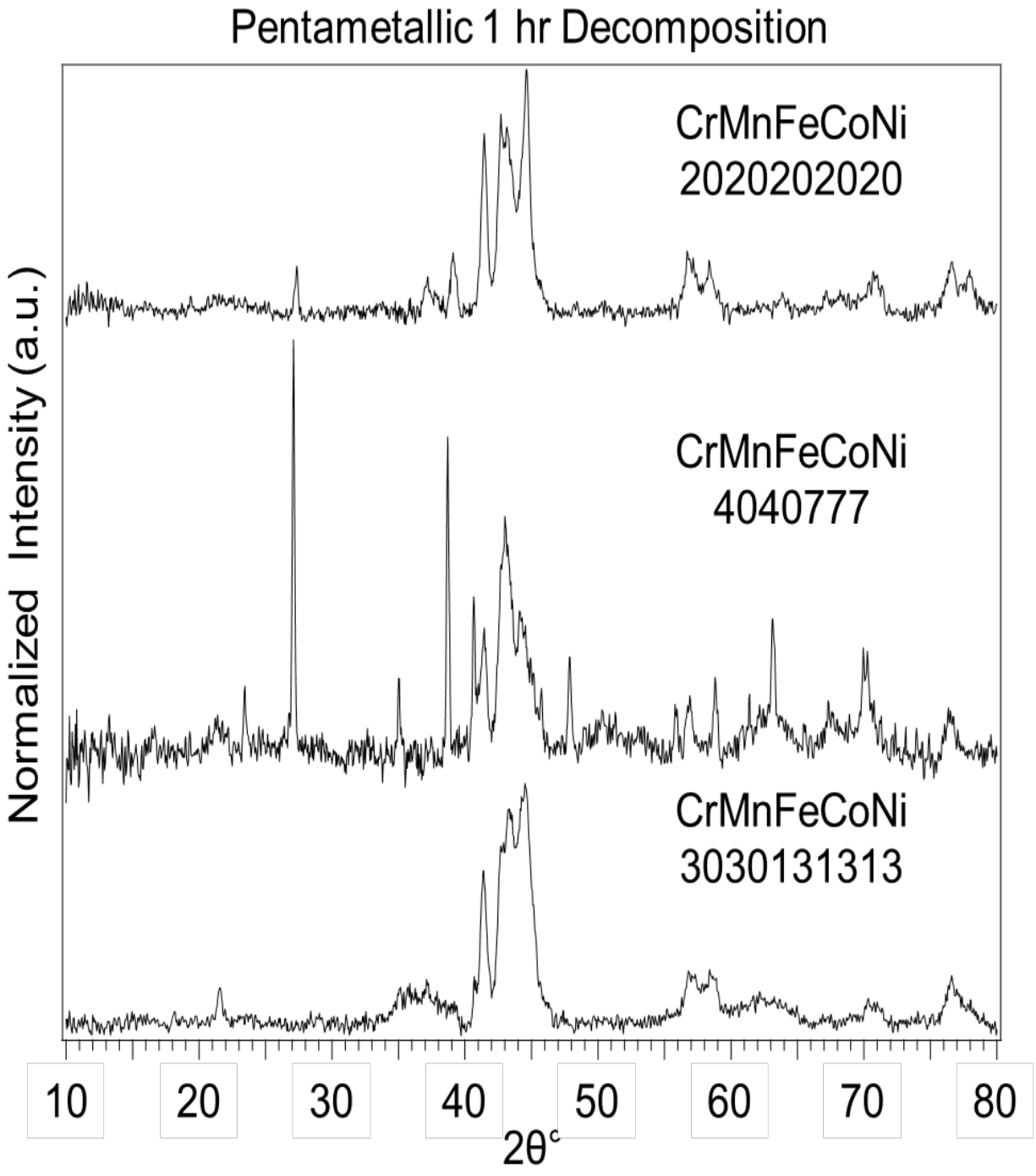
Pentametallic 1 hr Decomposition
CrMnFeCoNi
2020202020
CrMnFeCoNi
4040777
CrMnFeCoNi
3030131313
Normalized Intensity (a.u.)
10
20
30
40
50
60
70
80
2θ°

REFERENCES

(1) Bayda, S.; Adeel, M.; Tuccinardi, T.; Cordani, M.; Rizzolio, F.; Baeza, A. Molecules The History of Nanoscience and Nanotechnology: From Chemical-Physical Applications to Nanomedicine. *Molecules* **2020**, *25*, 112. https://doi.org/10.3390/molecules25010112.

(2) Thanh, N. T. K.; Maclean, N.; Mahiddine, S. Mechanisms of Nucleation and Growth of Nanoparticles in Solution. **2014**. https://doi.org/10.1021/cr400544s.

(3) Lamer, V. K.; Dinegar, R. H. Theory, Production and Mechanism of Formation of Monodispersed Hydrosols.

(4) Vreeland, E. C.; Watt, J.; Schober, G. B.; Hance, B. G.; Austin, M. J.; Price, A. D.; Fellows, B. D.; Monson, T. C.; Hudak, N. S.; Maldonado-Camargo, L.; Bohorquez, A. C.; Rinaldi, C.; Huber, D. L.; Crayton Pruitt, ⊥ J. Enhanced Nanoparticle Size Control by Extending LaMer's Mechanism. **2015**. https://doi.org/10.1021/acs.chemmater.5b02510.

(5) Watzky, M. A.; Finke, R. G. Transition Metal Nanocluster Formation Kinetic and Mechanistic Studies. A New Mechanism When Hydrogen Is the Reductant: Slow, Continuous Nucleation and Fast Autocatalytic Surface Growth. **1997**.

(6) Avrami, M. View Online Export Citation CrossMark Kinetics of Phase Change. I General Theory . *J. Chem. Phys* **1939**, *7*, 1103–1112. https://doi.org/10.1063/1.1750380.

(7) Avrami, M. View Online Export Citation CrossMark Kinetics of Phase Change. II Transformation-Time Relations for Random Distribution of Nuclei . *J. Chem. Phys* **1940**, *8*, 212–224. https://doi.org/10.1063/1.1750631.

(8) Avrami, M. View Online Export Citation CrossMark Granulation, Phase Change, and Microstructure Kinetics of Phase Change. III . *J. Chem. Phys* **1941**, *9*, 177–184. https://doi.org/10.1063/1.1750872.

(9) Mekuye, B.; Abera, B. Nanomaterials: An Overview of Synthesis, Classification, Characterization, and Applications. **2023**. https://doi.org/10.1002/nano.202300038.

(10) Hardy, D. A.; Nguyen, E. T.; Parrish, S. E.; Schriber, E. A.; Schlicker, L.; Gili, A.; Kamutzki, F.; Hohman, J. N.; Strouse, G. F. Prussian Blue Iron−Cobalt Mesocrystals as a Template for the Growth of Fe/Co Carbide (Cementite) and Fe/Co Nanocrystals. **2019**. https://doi.org/10.1021/acs.chemmater.9b02957.

(11) Wan, C.; Leonard, B. M. Iron-Doped Molybdenum Carbide Catalyst with High Activity and Stability for the Hydrogen Evolution Reaction. *Chem. Mater.* **2015**, *27* (12), 4281–4288. https://doi.org/10.1021/ACS.CHEMMATER.5B00621/SUPPL_FILE/CM5B00621_SI_001.PDF.

(12) Xie, X.; Du, L.; Yan, L.; Park, S.; Qiu, Y.; Sokolowski, J.; Wang, W.; Shao, Y.; Xie, X.;

Yan, L.; Park, S.; Qiu, Y.; Sokolowski, J.; Wang, W.; Shao, Y.; Du, L. Oxygen Evolution Reaction in Alkaline Environment: Material Challenges and Solutions. *Adv. Funct. Mater.* **2022**, *32* (21), 2110036. https://doi.org/10.1002/ADFM.202110036.

(13) Geiger, S.; Kasian, O.; Mingers, A. M.; Nicley, S. S.; Haenen, K.; Mayrhofer, K. J. J.; Cherevko, S. Catalyst Stability Benchmarking for the Oxygen Evolution Reaction: The Importance of Backing Electrode Material and Dissolution in Accelerated Aging Studies. *ChemSusChem* **2017**, *10* (21), 4140–4143. https://doi.org/10.1002/CSSC.201701523.

(14) Novák, P.; Bellezze, T.; Cabibbo, M.; Gamsjäger, E.; Wiessner, M.; Rajnovic, D.; Jaworska, L.; Hanus, P.; Shishkin, A.; Goel, G.; Goel, S. Solutions of Critical Raw Materials Issues Regarding Iron-Based Alloys. *Mater. 2021, Vol. 14, Page 899* **2021**, *14* (4), 899. https://doi.org/10.3390/MA14040899.

(15) Feng, C.; Faheem, M. B.; Fu, J.; Xiao, Y.; Li, C.; Li, Y. Fe-Based Electrocatalysts for Oxygen Evolution Reaction: Progress and Perspectives. *ACS Catal.* **2020**, *10* (7), 4019–4047. https://doi.org/10.1021/ACSCATAL.9B05445/ASSET/IMAGES/LARGE/CS9B05445_0018.JPEG.

(16) Bossel, U.; Eliasson, B. Energy Hydrogen Economy.

(17) Danilovic, N.; Subbaraman, R.; Chang, K.-C.; Hyoung Chang, S.; J. Kang, Y.; Snyder, J.; P. Paulikas, A.; Strmcnik, D.; Kim, Y.-T.; Myers, D.; R. Stamenkovic, V.; M. Markovic, N. Activity–Stability Trends for the Oxygen Evolution Reaction on Monometallic Oxides in Acidic Environments. *J. Phys. Chem. Lett.* **2014**, *5* (14), 2474–2478. https://doi.org/10.1021/jz501061n.

(18) Xu, J.; Li, J.; Xiong, D.; Zhang, B.; Liu, Y.; Wu, K. H.; Amorim, I.; Li, W.; Liu, L. Trends in Activity for the Oxygen Evolution Reaction on Transition Metal (M = Fe, Co, Ni) Phosphide Pre-Catalysts. *Chem. Sci.* **2018**, *9* (14), 3470–3476. https://doi.org/10.1039/C7SC05033J.

(19) Li, S.; Ren, P.; Yang, C.; Liu, X.; Yin, Z.; Li, W.; Yang, H.; Li, J.; Wang, X.; Wang, Y.; Cao, R.; Lin, L.; Yao, S.; Wen, X.; Ma, D. Fe5C2 Nanoparticles as Low-Cost HER Electrocatalyst: The Importance of Co Substitution. *Sci. Bull.* **2018**, *63* (20), 1358–1363. https://doi.org/10.1016/J.SCIB.2018.09.016.

(20) Wang, X.; Zhu, K.; Ju, Y.; Li, Y.; Li, W.; Xu, J.; Hou, Y. Iron Carbides: Magic Materials with Magnetic and Catalytic Properties. https://doi.org/10.1016/j.jmmm.2019.165432.

(21) Wang, Y.; Wu, Q.; Zhang, B.; Tian, L.; Li, K.; Zhang, X. Recent Advances in Transition Metal Carbide Electrocatalysts for Oxygen Evolution Reaction. *Catalysts* **2020**, *10* (10), 1–30. https://doi.org/10.3390/catal10101164.

(22) Starchikov, S. S.; Zayakhanov, V. A.; Lyubutin, I. S.; Vasiliev, A. L.; Lyubutina, M. V.; Chumakov, N. K.; Funtov, K. O.; Kulikova, L. F.; Agafonov, V. N.; Davydov, V. A.

Evolution of the Phase Composition, Crystal Structure and Magnetic Properties of Core@shell Nanoparticles Obtained during Conversion of Ferrocene at High Pressure and High Temperature. *Appl. Surf. Sci.* **2023**, *615*, 156269. https://doi.org/10.1016/J.APSUSC.2022.156269.

(23) Ritz, A. J.; Bertini, I. A.; Nguyen, E. T.; Strouse, G. F.; Lazenby, R. A. Electrocatalytic Activity and Surface Oxide Reconstruction of Bimetallic Iron-Cobalt Nanocarbide Electrocatalysts for the Oxygen Evolution Reaction †. **2023**. https://doi.org/10.1039/d3ra07003d.

(24) Spanos, I.; Justus Masa, ·; Zeradjanin, A.; Schlögl, · Robert. The Effect of Iron Impurities on Transition Metal Catalysts for the Oxygen Evolution Reaction in Alkaline Environment: Activity Mediators or Active Sites? *Catal. Letters* **2021**, *151*, 1843–1856. https://doi.org/10.1007/s10562-020-03478-4.

(25) Ding, X.; Li, W.; Kuang, H.; Qu, M.; Cui, M.; Zhao, C.; Qi, D. C.; Oropeza, F. E.; Zhang, K. H. L. An Fe Stabilized Metallic Phase of NiS2 for the Highly Efficient Oxygen Evolution Reaction. *Nanoscale* **2019**, *11* (48), 23217–23225. https://doi.org/10.1039/C9NR07832K.

(26) Lin, C.; Wang, P.; Jin, H.; Zhao, J.; Chen, D.; Liu, S.; Zhang, C.; Mu, S. An Iron-Doped Cobalt Phosphide Nano-Electrocatalyst Derived from a Metal–Organic Framework for Efficient Water Splitting. *Dalt. Trans.* **2019**, *48* (44), 16555–16561. https://doi.org/10.1039/C9DT03619A.

(27) Zhang, G.; Yuan, J.; Liu, Y.; Lu, W.; Fu, N.; Li, W.; Huang, H. Boosting the Oxygen Evolution Reaction in Non-Precious Catalysts by Structural and Electronic Engineering. *J. Mater. Chem. A* **2018**, *6* (22), 10253–10263. https://doi.org/10.1039/C8TA02542H.

(28) Yang, C.; Zhao, B.; Gao, R.; Yao, S.; Zhai, P.; Li, S.; Yu, J.; Hou, Y.; Ma, D. Construction of Synergistic Fe5C2/Co Heterostructured Nanoparticles as an Enhanced Low Temperature Fischer-Tropsch Synthesis Catalyst. *ACS Catal.* **2017**, *7* (9), 5661–5667. https://doi.org/10.1021/ACSCATAL.7B01142/ASSET/IMAGES/LARGE/CS-2017-011425_0005.JPEG.

(29) Wygant, B. R.; Kawashima, K.; Mullins, C. B. Catalyst or Precatalyst? The Effect of Oxidation on Transition Metal Carbide, Pnictide, and Chalcogenide Oxygen Evolution Catalysts. *ACS Energy Lett.* **2018**, *3* (12), 2956–2966. https://doi.org/10.1021/acsenergylett.8b01774.

(30) Luo, R.; Qian, Z.; Xing, L.; Du, C.; Yin, G.; Zhao, S.; Du, L. Re-Looking into the Active Moieties of Metal X-Ides (X- = Phosph-, Sulf-, Nitr-, and Carb-) Toward Oxygen Evolution Reaction. *Adv. Funct. Mater.* **2021**, *31* (37), 2102918. https://doi.org/10.1002/ADFM.202102918.

(31) Jeon, Y.; Choi, K.; Im, S. Dual-Source Method: A Facile Method to Obtain Orthogonal Monolithic Bimetallic (Fe/Co) Prussian Blue Analog. *Bull. Korean Chem. Soc.* **2015**, *36*

(12), 2966–2969. https://doi.org/10.1002/bkcs.10600.

(32) Li, R.; Zhou, D.; Luo, J.; Xu, W.; Li, J.; Li, S.; Cheng, P.; Yuan, D. The Urchin-like Sphere Arrays Co3O4 as a Bifunctional Catalyst for Hydrogen Evolution Reaction and Oxygen Evolution Reaction. *J. Power Sources* **2017**, *341*, 250–256. https://doi.org/10.1016/J.JPOWSOUR.2016.10.096.

(33) Roger, I.; Shipman, M. A.; Symes, M. D. Earth-Abundant Catalysts for Electrochemical and Photoelectrochemical Water Splitting. *Nat. Rev. Chem. 2017 11* **2017**, *1* (1), 1–13. https://doi.org/10.1038/s41570-016-0003.

(34) Maeda, K.; Domen, K. Photocatalytic Water Splitting: Recent Progress and Future Challenges. *J. Phys. Chem. Lett.* **2010**, *1* (18), 2655–2661. https://doi.org/10.1021/JZ1007966/ASSET/IMAGES/LARGE/JZ-2010-007966_0006.JPEG.

(35) Deng, H.; Zhang, C.; Xie, Y.; Tumlin, T.; Giri, L.; Karna, S. P.; Lin, J. This Article Is Licensed under a Creative Commons Attribution-NonCommercial 3.0 Unported Licence. **2016**. https://doi.org/10.1039/c5ta09322h.

(36) Audichon, T.; Napporn, T. W.; Canaff, C.; Morais, C.; Comminges, C.; Kokoh, K. B. IrO 2 Coated on RuO 2 as Efficient and Stable Electroactive Nanocatalysts for Electrochemical Water Splitting. **2016**. https://doi.org/10.1021/acs.jpcc.5b11868.

(37) Lee, Y.; Suntivich, J.; J. May, K.; E. Perry, E.; Shao-Horn, Y. Synthesis and Activities of Rutile IrO2 and RuO2 Nanoparticles for Oxygen Evolution in Acid and Alkaline Solutions. *J. Phys. Chem. Lett.* **2012**, *3* (3), 399–404. https://doi.org/10.1021/jz2016507.

(38) Cao, L.; Luo, Q.; Chen, J.; Wang, L.; Lin, Y.; Wang, H.; Liu, X.; Shen, X.; Zhang, W.; Liu, W.; Qi, Z.; Jiang, Z.; Yang, J.; Yao, T. Dynamic Oxygen Adsorption on Single-Atomic Ruthenium Catalyst with High Performance for Acidic Oxygen Evolution Reaction. *Nat. Commun. 2019 101* **2019**, *10* (1), 1–9. https://doi.org/10.1038/s41467-019-12886-z.

(39) Jung, S.; Mccrory, C. C. L.; Ferrer, I. M.; Peters, J. C.; Jaramillo, T. F. Benchmarking Nanoparticulate Metal Oxide Electrocatalysts for the Alkaline Water Oxidation Reaction †. **2016**. https://doi.org/10.1039/c5ta07586f.

(40) C. L. McCrory, C.; Jung, S.; C. Peters, J.; F. Jaramillo, T. Benchmarking Heterogeneous Electrocatalysts for the Oxygen Evolution Reaction. *J. Am. Chem. Soc.* **2013**, *135* (45), 16977–16987. https://doi.org/10.1021/ja407115p.

(41) Myekhlai, M.; Benedetti, T. M.; Gloag, L.; Gonçales, V. R.; Cheong, S.; Chen, H. S.; Gooding, J. J.; Tilley, R. D. Increasing the Formation of Active Sites on Highly Crystalline Co Branched Nanoparticles for Improved Oxygen Evolution Reaction Electrocatalysis. *ChemCatChem* **2020**, *12* (11), 3126–3131. https://doi.org/10.1002/CCTC.202000224.

(42) Saddeler, S.; Hagemann, U.; Schulz, S. Effect of the Size and Shape on the Electrocatalytic Activity of Co3O4Nanoparticles in the Oxygen Evolution Reaction. *Inorg. Chem.* **2020**, *59* (14), 10013–10024. https://doi.org/10.1021/ACS.INORGCHEM.0C01180/ASSET/IMAGES/LARGE/IC0C01180_0012.JPEG.

(43) Yang, C.; Zhao, R.; Xiang, H.; Wu, J.; Zhong, W.; Li, W.; Zhang, Q.; Yang, N.; Li, X. Ni-Activated Transition Metal Carbides for Efficient Hydrogen Evolution in Acidic and Alkaline Solutions. *Adv. Energy Mater.* **2020**, *10* (37), 2002260. https://doi.org/10.1002/AENM.202002260.

(44) Cheng, Y. W.; Dai, J. H.; Zhang, Y. M.; Song, Y. Two-Dimensional, Ordered, Double Transition Metal Carbides (MXenes): A New Family of Promising Catalysts for the Hydrogen Evolution Reaction. *J. Phys. Chem. C* **2018**, *122* (49), 28113–28122. https://doi.org/10.1021/ACS.JPCC.8B08914/ASSET/IMAGES/LARGE/JP-2018-08914Y_0008.JPEG.

(45) Tang, Y. J.; Liu, C. H.; Huang, W.; Wang, X. L.; Dong, L. Z.; Li, S. L.; Lan, Y. Q. Bimetallic Carbides-Based Nanocomposite as Superior Electrocatalyst for Oxygen Evolution Reaction. *ACS Appl. Mater. Interfaces* **2017**, *9* (20), 16977–16985. https://doi.org/10.1021/ACSAMI.7B01096/ASSET/IMAGES/LARGE/AM-2017-01096M_0004.JPEG.

(46) Kim, J.-H.; Kawashima, K.; R. Wygant, B.; Mabayoje, O.; Liu, Y.; H. Wang, J.; Buddie Mullins, C. Transformation of a Cobalt Carbide (Co3C) Oxygen Evolution Precatalyst. *ACS Appl. Energy Mater.* **2018**, *1* (10), 5145–5150. https://doi.org/10.1021/acsaem.8b01336.

(47) Masa, J.; Weide, P.; Peeters, D.; Sinev, I.; Xia, W.; Sun, Z.; Somsen, C.; Muhler, M.; Schuhmann, W. Amorphous Cobalt Boride (Co 2 B) as a Highly Effi Cient Nonprecious Catalyst for Electrochemical Water Splitting: Oxygen and Hydrogen Evolution. **2016**. https://doi.org/10.1002/aenm.201502313.

(48) Xiao, Y.; Hwang, J.-Y.; Sun, Y.-K. Transition Metal Carbide-Based Materials: Synthesis and Applications in Electrochemical Energy Storage. **2016**. https://doi.org/10.1039/c6ta03832h.

(49) Yu, X.; Zhang, M.; Yuan, W.; Shi, G. A High-Performance Three-Dimensional Ni-Fe Layered Double Hydroxide/Graphene Electrode for Water Oxidation †. **2015**. https://doi.org/10.1039/c5ta01034a.

(50) Mehdi, M.; An, B.-S.; Kim, H.; Lee, S.; Lee, C.; Seo, M.; Noh, M. W.; Cho, W.-C.; Kim, C.-H.; Choi, C. H.; Kim, B.-H.; Kim, M.; Cho, H.-S.; Mehdi, M.; Lee, S.; Lee, C.; Seo, M.; Kim, M.; Cho, H.-S. Rational Design of a Stable Fe-Rich Ni-Fe Layered Double Hydroxide for the Industrially Relevant Dynamic Operation of Alkaline Water Electrolyzers. **2023**. https://doi.org/10.1002/aenm.202204403.

(51) Seredych, M.; Shuck, C. E.; Pinto, D.; Alhabeb, M.; Precetti, E.; Deysher, G.; Anasori, B.; Kurra, N.; Gogotsi, Y. High-Temperature Behavior and Surface Chemistry of Carbide MXenes Studied by Thermal Analysis. *Chem. Mater.* **2019**, *31* (9), 3324–3332. https://doi.org/10.1021/ACS.CHEMMATER.9B00397/ASSET/IMAGES/LARGE/CM-2019-003978_0003.JPEG.

(52) Nguyen, E. T.; Bertini, I. A.; Ritz, A. J.; Lazenby, R. A.; Mao, K.; Mcbride, J. R.; Mattia, A. V; Kuszynski, J. E.; Wenzel, S. F.; Bennett, S. D.; Strouse, G. F. A Single Source, Scalable Route for Direct Isolation of Earth-Abundant Nanometal Carbide Water-Splitting Electrocatalysts. *Inorg. Chem* **2024**, *2022*, 61. https://doi.org/10.1021/acs.inorgchem.2c01713.

(53) Feng, M.; Huang, J.; Peng, Y.; Huang, C.; Yue, X.; Huang, S. Tuning Electronic Structures of Transition Metal Carbides to Boost Oxygen Evolution Reactions in Acidic Medium. *ACS Nano* **2022**, *16* (9), 13834–13844. https://doi.org/10.1021/ACSNANO.2C02099/ASSET/IMAGES/MEDIUM/NN2C02099_M001.GIF.

(54) Chuang, C. H.; Hsiao, L. Y.; Yeh, M. H.; Wang, Y. C.; Chang, S. C.; Tsai, L. D.; Ho, K. C. Prussian Blue Analogue-Derived Metal Oxides as Electrocatalysts for Oxygen Evolution Reaction: Tailoring the Molar Ratio of Cobalt to Iron. *ACS Appl. Energy Mater.* **2020**, *3* (12), 11752–11762. https://doi.org/10.1021/ACSAEM.0C01903/ASSET/IMAGES/LARGE/AE0C01903_0008.JPEG.

(55) Friebel, D.; W. Louie, M.; Bajdich, M.; E. Sanwald, K.; Cai, Y.; M. Wise, A.; Cheng, M.-J.; Sokaras, D.; Weng, T.-C.; Alonso-Mori, R.; C. Davis, R.; R. Bargar, J.; K. Nørskov, J.; Nilsson, A.; T. Bell, A. Identification of Highly Active Fe Sites in (Ni,Fe)OOH for Electrocatalytic Water Splitting. *J. Am. Chem. Soc.* **2015**, *137* (3), 1305–1313. https://doi.org/10.1021/ja511559d.

(56) Sun, W.; Liu, J. Y.; Gong, X. Q.; Zaman, W. Q.; Cao, L. M.; Yang, J. OER Activity Manipulated by IrO6 Coordination Geometry: An Insight from Pyrochlore Iridates. *Sci. Reports 2016 61* **2016**, *6* (1), 1–10. https://doi.org/10.1038/srep38429.

(57) Escalera-López, D.; Czioska, S.; Geppert, J.; Boubnov, A.; Röse, P.; Saraç, E.; Krewer, U.; Grunwaldt, J.-D.; Cherevko, S. Phase-and Surface Composition-Dependent Electrochemical Stability of Ir-Ru Nanoparticles during Oxygen Evolution Reaction. **2021**. https://doi.org/10.1021/acscatal.1c01682.

(58) Sivanantham, A.; Ganesan, P.; Vinu, A.; Shanmugam, S. Surface Activation and Reconstruction of Non-Oxide-Based Catalysts through in Situ Electrochemical Tuning for Oxygen Evolution Reactions in Alkaline Media. *ACS Catal.* **2020**, *10* (1), 463–493. https://doi.org/10.1021/ACSCATAL.9B04216/ASSET/IMAGES/LARGE/CS9B04216_0024.JPEG.

(59) Xu, J.; Sousa, J. P. S.; Mordvinova, N. E.; Costa, J. D.; Petrovykh, D. Y.; Kovnir, K.;

Lebedev, O. I.; Kolen'Ko, Y. V. Al-Induced in Situ Formation of Highly Active Nanostructured Water-Oxidation Electrocatalyst Based on Ni-Phosphide. *ACS Catal.* **2018**, *8* (3), 2595–2600. https://doi.org/10.1021/ACSCATAL.7B03817/ASSET/IMAGES/LARGE/CS-2017-038179_0005.JPEG.

(60) Sankar, S.; Sugawara, Y.; Assa Aravindh, S.; Jose, R.; Tamaki, T.; Anilkumar, G. M.; Yamaguchi, T. Tuning Palladium Nickel Phosphide toward Efficient Oxygen Evolution Performance. *ACS Appl. Energy Mater.* **2020**, *3* (1), 879–888. https://doi.org/10.1021/ACSAEM.9B01996/ASSET/IMAGES/LARGE/AE9B01996_0005.JPEG.

(61) Li, S.; Peng, S.; Huang, L.; Cui, X.; Al-Enizi, A. M.; Zheng, G. Carbon-Coated Co3+-Rich Cobalt Selenide Derived from ZIF-67 for Efficient Electrochemical Water Oxidation. *ACS Appl. Mater. Interfaces* **2016**, *8* (32), 20534–20539. https://doi.org/10.1021/ACSAMI.6B07986/ASSET/IMAGES/LARGE/AM-2016-07986Y_0005.JPEG.

(62) Pell, W. G.; Zolfaghari, A.; Conway, B. E. Capacitance of the Double-Layer at Polycrystalline Pt Electrodes Bearing a Surface-Oxide Film. *J. Electroanal. Chem.* **2002**, *532* (1–2), 13–23. https://doi.org/10.1016/S0022-0728(02)00676-9.

(63) Lukaszewski, M.; Soszko, M.; Czerwiński, A. Electrochemical Methods of Real Surface Area Determination of Noble Metal Electrodes – an Overview. *Int. J. Electrochem. Sci.* **2016**, *11* (6), 4442–4469. https://doi.org/10.20964/2016.06.71.

(64) Walter, M. G.; Warren, E. L.; McKone, J. R.; Boettcher, S. W.; Mi, Q.; Santori, E. A.; Lewis, N. S. Solar Water Splitting Cells. *Chem. Rev.* **2010**, *110* (11), 6446–6473. https://doi.org/10.1021/CR1002326/ASSET/IMAGES/LARGE/CR-2010-002326_0024.JPEG.

(65) Yu, L.; Sun, S.; Li, H.; Xu, Z. J. Effects of Catalyst Mass Loading on Electrocatalytic Activity: An Example of Oxygen Evolution Reaction. *Fundam. Res.* **2021**, *1* (4), 448–452. https://doi.org/10.1016/J.FMRE.2021.06.006.

(66) Linnemann, J.; Kanokkanchana, K.; Tschulik, K. Design Strategies for Electrocatalysts from an Electrochemist's Perspective. *ACS Catal.* **2021**, *11* (9), 5318–5346. https://doi.org/10.1021/ACSCATAL.0C04118/ASSET/IMAGES/LARGE/CS0C04118_0016.JPEG.

(67) Lai, Y.; Chi, Y.; Jia -, X.; Liang, Q.; Brocks, G.; Bieberle-Hütter, A. Oxygen Evolution Reaction (OER) Mechanism under Alkaline and Acidic Conditions. *J. Phys. Energy* **2021**, *3* (2), 026001. https://doi.org/10.1088/2515-7655/ABDC85.

(68) Alobaid, A.; Wang, C.; Adomaitis, R. A. Mechanism and Kinetics of HER and OER on NiFe LDH Films in an Alkaline Electrolyte. *J. Electrochem. Soc.* **2018**, *165* (15), J3395–J3404. https://doi.org/10.1149/2.0481815JES/XML.

(69) Wei Seh, Z.; Kibsgaard, J.; Dickens, C. F.; Chorkendorff, I.; Nørskov, J. K.; Jaramillo, T. F. REVIEW SUMMARY Combining Theory and Experiment in Electrocatalysis: Insights into Materials Design. https://doi.org/10.1126/science.aad4998.

(70) Anantharaj, S.; R Ede, ab S.; Karthick, ab K.; Sam Sankar, ab S.; Sangeetha, ab K.; E Karthik, ab P.; Kundu, S. Precision and Correctness in the Evaluation of Electrocatalytic Water Splitting: Revisiting Activity Parameters with a Critical Assessment. | *Energy Environ. Sci* **2018**, *11*, 744. https://doi.org/10.1039/c7ee03457a.

(71) Kim, J. H.; Kawashima, K.; Wygant, B. R.; Mabayoje, O.; Liu, Y.; Wang, J. H.; Mullins, C. B. Transformation of a Cobalt Carbide (Co3C) Oxygen Evolution Precatalyst. *ACS Appl. Energy Mater.* **2018**, *1* (10), 5145–5150. https://doi.org/10.1021/ACSAEM.8B01336/ASSET/IMAGES/LARGE/AE-2018-01336M_0005.JPEG.

(72) Mendoza-Garcia, A.; Su, D.; Sun, S. Sea Urchin-like Cobalt-Iron Phosphide as an Active Catalyst for Oxygen Evolution Reaction. *Nanoscale* **2016**, *8* (6), 3244–3247. https://doi.org/10.1039/c5nr08763e.

(73) Burke, M. S.; Kast, M. G.; Trotochaud, L.; Smith, A. M.; Boettcher, S. W. Cobalt−Iron (Oxy)Hydroxide Oxygen Evolution Electrocatalysts: The Role of Structure and Composition on Activity, Stability, and Mechanism. **2015**. https://doi.org/10.1021/jacs.5b00281.

(74) Yamada, I.; Kinoshita, M.; Oda, S.; Tsukasaki, H.; Kawaguchi, S.; Oka, K.; Mori, S.; Ikeno, H.; Yagi, S. Enhanced Catalytic Activity and Stability of the Oxygen Evolution Reaction on Tetravalent Mixed Metal Oxide. *Cite This Chem. Mater* **2020**, *32*, 3903. https://doi.org/10.1021/acs.chemmater.0c00061.

(75) Ahn, I. K.; Joo, W.; Lee, J. H.; Kim, H. G.; Lee, S. Y.; Jung, Y.; Kim, J. Y.; Lee, G. B.; Kim, M.; Joo, Y. C. Metal-Organic Framework-Driven Porous Cobalt Disulfide Nanoparticles Fabricated by Gaseous Sulfurization as Bifunctional Electrocatalysts for Overall Water Splitting. *Sci. Rep.* **2019**, *9* (1), 1–10. https://doi.org/10.1038/s41598-019-56084-9.

(76) Dou, Y.; He, C.-T.; Zhang, L.; Chen, X.-M.; Yin, H.; Zhao, H. How Cobalt and Iron Doping Determine the Oxygen Evolution Electrocatalytic Activity of NiOOH. https://doi.org/10.1016/j.xcrp.2020.100077.

(77) Lin, Z.; Cai, L.; Lu, W.; Chai, Y. Phase and Facet Control of Molybdenum Carbide Nanosheet Observed by In Situ TEM. *Small* **2017**, *13* (35). https://doi.org/10.1002/SMLL.201700051.

(78) Sevilla, M.; Sanchís, C.; Valdés-Soh, T.; Morallón, E.; Fuertes, A. B. Synthesis of Graphitic Carbon Nanostructures from Sawdust and Their Application as Electrocatalyst Supports. *J. Phys. Chem. C* **2007**, *111* (27), 9749–9756. https://doi.org/10.1021/JP072246X/ASSET/IMAGES/LARGE/JP072246XF00009.JPEG.

(79) Chen, Z.; Song, J.; Zhang, R.; Li, R.; Hu, Q.; Wei, P.; Xi, S.; Zhou, X.; T Nguyen, P. T.; Duong, H. M.; Seng Lee, P.; Zhao, X.; Joo Koh, M.; Yan, N.; Ping Loh, K. Addressing the Quantitative Conversion Bottleneck in Single-Atom Catalysis. https://doi.org/10.1038/s41467-022-30551-w.

(80) Zhang, P.; Cheng, N.; Li, M.; Zhou, B.; Bian, C.; Wei, Y.; Wang, X.; Jiang, H.; Bao, L.; Lin, Y.; Hu, Z.; Du, Y.; Gong, Y. Transition-Metal Substitution-Induced Lattice Strain and Electrical Polarity Reversal in Monolayer WS2. *ACS Appl. Mater. Interfaces* **2020**, *12* (16), 18650–18659. https://doi.org/10.1021/ACSAMI.9B22004/ASSET/IMAGES/MEDIUM/AM9B22004_M001.GIF.

(81) Gu, L. F.; Li, C. F.; Zhao, J. W.; Xie, L. J.; Wu, J. Q.; Ren, Q.; Li, G. R. Dual Modulation of Lattice Strain and Charge Polarization Induced by Co(OH)2/Ni(OH)2 Interfaces for Efficient Oxygen Evolution Catalysis. *J. Mater. Chem. A* **2021**, *9* (22), 13279–13287. https://doi.org/10.1039/D1TA01866C.

(82) Zhang, F.; He, L.; Lian, S.; Wang, M.; Chen, X.; Yin, J.; Pan, H.; Ren, J.; Chen, M. Investigation of Strain and Transition-Metal Doping Effect on Hydrogen Evolution Reaction Catalysts of Mo2C, MoP, and Ni2P. *J. Phys. Chem. C* **2021**, *125* (35), 19119–19130. https://doi.org/10.1021/ACS.JPCC.1C04745/ASSET/IMAGES/LARGE/JP1C04745_0010.JPEG.

(83) Ramadhan, Z. R.; Poerwoprajitno, A. R.; Cheong, S.; Webster, R. F.; Kumar, P. V.; Cychy, S.; Gloag, L.; Benedetti, T. M.; Marjo, C. E.; Muhler, M.; Wang, D. W.; Gooding, J. J.; Schuhmann, W.; Tilley, R. D. Introducing Stacking Faults into Three-Dimensional Branched Nickel Nanoparticles for Improved Catalytic Activity. *J. Am. Chem. Soc.* **2022**, *144* (25), 11094–11098. https://doi.org/10.1021/JACS.2C04911/ASSET/IMAGES/LARGE/JA2C04911_0004.JPEG.

(84) Abu Hatab, A. S.; Ahmad, Y. H.; Ibrahim, M.; Elsafi Ahmed, A.; Abdul Rahman, M. B.; Al-Qaradawi, S. Y. MOF-Derived Cobalt@Mesoporous Carbon as Electrocatalysts for Oxygen Evolution Reaction: Impact of Organic Linker. *Langmuir* **2022**, *16*, 8. https://doi.org/10.1021/ACS.LANGMUIR.2C02873/ASSET/IMAGES/LARGE/LA2C02873_0007.JPEG.

(85) Kneer, A.; Wagner, N.; Sadeler, C.; Scherzer, A.-C.; Gerteisen, D. Effect of Dwell Time and Scan Rate during Voltage Cycling on Catalyst Degradation in PEM Fuel Cells. *J. Electrochem. Soc.* **2018**, *165* (10), F805–F812. https://doi.org/10.1149/2.0651810JES/XML.

(86) El-Sayed, H. A.; Weiß, A.; Olbrich, L. F.; Putro, G. P.; Gasteiger, H. A. OER Catalyst Stability Investigation Using RDE Technique: A Stability Measure or an Artifact? *J. Electrochem. Soc.* **2019**, *166* (8), F458–F464. https://doi.org/10.1149/2.0301908JES/XML.

(87) Kuo, D. Y.; Eom, C. J.; Kawasaki, J. K.; Petretto, G.; Nelson, J. N.; Hautier, G.; Crumlin, E. J.; Shen, K. M.; Schlom, D. G.; Suntivich, J. Influence of Strain on the Surface-Oxygen Interaction and the Oxygen Evolution Reaction of SrIrO3. *J. Phys. Chem. C* **2018**, *122* (8), 4359–4364. https://doi.org/10.1021/ACS.JPCC.7B12081/ASSET/IMAGES/LARGE/JP-2017-12081P_0005.JPEG.

(88) Müllner, M.; Riva, M.; Kraushofer, F.; Schmid, M.; Parkinson, G. S.; Mertens, S. F. L.; Diebold, U. Stability and Catalytic Performance of Reconstructed Fe 3 O 4 (001) and Fe 3 O 4 (110) Surfaces during Oxygen Evolution Reaction. *J. Phys. Chem. C* **2019**, *123* (13), 8304–8311. https://doi.org/10.1021/ACS.JPCC.8B08733/ASSET/IMAGES/LARGE/JP-2018-087334_0007.JPEG.

(89) Lee, W. H.; Han, M. H.; Ko, Y. J.; Min, B. K.; Chae, K. H.; Oh, H. S. Electrode Reconstruction Strategy for Oxygen Evolution Reaction: Maintaining Fe-CoOOH Phase with Intermediate-Spin State during Electrolysis. *Nat. Commun. 2022 131* **2022**, *13* (1), 1–10. https://doi.org/10.1038/s41467-022-28260-5.

(90) Dutta, A.; Pradhan, N. Developments of Metal Phosphides as Efficient OER Precatalysts. *J. Phys. Chem. Lett.* **2017**, *8* (1), 144–152. https://doi.org/10.1021/ACS.JPCLETT.6B02249/ASSET/IMAGES/LARGE/JZ-2016-02249W_0007.JPEG.

(91) Gao, D.; Zhang, J.; Wang, T.; Xiao, W.; Tao, K.; Xue, D.; Ding, J. Metallic Ni 3 N Nanosheets with Exposed Active Surface Sites for Efficient Hydrogen Evolution. *J. Mater. Chem. A* **2016**, *4* (44), 17363–17369. https://doi.org/10.1039/C6TA07883D.

(92) Zhou, Y.; Zhang, W.; Hu, J.; Li, D.; Yin, X.; Gao, Q. Inherent Oxygen Vacancies Boost Surface Reconstruction of Ultrathin Ni-Fe Layered-Double-Hydroxides toward Efficient Electrocatalytic Oxygen Evolution. *ACS Sustain. Chem. Eng.* **2021**, *9* (21), 7390–7399. https://doi.org/10.1021/ACSSUSCHEMENG.1C02256/ASSET/IMAGES/LARGE/SC1C02256_0006.JPEG.

(93) Zhuang, L.; Jia, Y.; He, T.; Du, A.; Yan, X.; Ge, L.; Zhu, Z.; Yao, X. Tuning Oxygen Vacancies in Two-Dimensional Iron-Cobalt Oxide Nanosheets through Hydrogenation for Enhanced Oxygen Evolution Activity. *Nano Res.* **2018**, *11* (6), 3509–3518. https://doi.org/10.1007/S12274-018-2050-8/METRICS.

(94) Nocera, D. G. Solar Fuels and Solar Chemicals Industry. *Acc. Chem. Res.* **2017**, *50* (3), 616–619. https://doi.org/10.1021/ACS.ACCOUNTS.6B00615/ASSET/IMAGES/LARGE/AR-2016-00615F_0003.JPEG.

(95) Zhou, P.; Navid, I. A.; Ma, Y.; Xiao, Y.; Wang, P.; Ye, Z.; Zhou, B.; Sun, K.; Mi, Z. Solar-to-Hydrogen Efficiency of More than 9% in Photocatalytic Water Splitting. *Nat. 2023 6137942* **2023**, *613* (7942), 66–70. https://doi.org/10.1038/s41586-022-05399-1.

(96) Ehlers, J. C.; Feidenhans'l, A. A.; Therkildsen, K. T.; Larrazábal, G. O. Affordable Green

Hydrogen from Alkaline Water Electrolysis: Key Research Needs from an Industrial Perspective. *ACS Energy Lett.* **2023**, *8* (3), 1502–1509. https://doi.org/10.1021/ACSENERGYLETT.2C02897/ASSET/IMAGES/LARGE/NZ2C02897_0005.JPEG.

(97) Sun, J.; Li, S.; Zhang, Q.; Guan, J. Iron–Cobalt–Nickel Trimetal Phosphides as High-Performance Electrocatalysts for Overall Water Splitting. *Sustain. Energy Fuels* **2020**, *4* (9), 4531–4537. https://doi.org/10.1039/D0SE00694G.

(98) Görlin, M.; Halldin Stenlid, J.; Koroidov, S.; Wang, H. Y.; Börner, M.; Shipilin, M.; Kalinko, A.; Murzin, V.; Safonova, O. V.; Nachtegaal, M.; Uheida, A.; Dutta, J.; Bauer, M.; Nilsson, A.; Diaz-Morales, O. Key Activity Descriptors of Nickel-Iron Oxygen Evolution Electrocatalysts in the Presence of Alkali Metal Cations. *Nat. Commun. 2020 111* **2020**, *11* (1), 1–11. https://doi.org/10.1038/s41467-020-19729-2.

(99) Li, Y. F.; Selloni, A. Mechanism and Activity of Water Oxidation on Selected Surfaces of Pure and Fe-Doped NiOx. *ACS Catal.* **2014**, *4* (4), 1148–1153. https://doi.org/10.1021/CS401245Q/SUPPL_FILE/CS401245Q_SI_001.PDF.

(100) Trotochaud, L.; K. Ranney, J.; N. Williams, K.; W. Boettcher, S. Solution-Cast Metal Oxide Thin Film Electrocatalysts for Oxygen Evolution. *J. Am. Chem. Soc.* **2012**, *134* (41), 17253–17261. https://doi.org/10.1021/ja307507a.

(101) Yang, J.; Wang, T.; Li, Y.; Pu, X.; Chen, H.; Li, Y.; Yang, B.; Zhang, Y.; Zhao, J.; Cao, Q.; Chen, X.; Ghasemi, S.; Hagfeldt, A.; Li, X. Overcome Low Intrinsic Conductivity of NiOx Through Triazinyl Modification for Highly Efficient and Stable Inverted Perovskite Solar Cells. *Sol. RRL* **2022**, *6* (9), 2200422. https://doi.org/10.1002/SOLR.202200422.

(102) Etzi Coller Pascuzzi, M.; Man, A. J. W.; Goryachev, A.; Hofmann, J. P.; Hensen, E. J. M. Investigation of the Stability of NiFe-(Oxy)Hydroxide Anodes in Alkaline Water Electrolysis under Industrially Relevant Conditions. *Catal. Sci. Technol.* **2020**, *10* (16), 5593–5601. https://doi.org/10.1039/D0CY01179G.

(103) Chen, R.; Hung, S.-F.; Zhou, D.; Gao, J.; Yang, C.; Tao, H.; Bin Yang, H.; Zhang, L.; Zhang, L.; Xiong, Q.; Ming Chen, H.; Liu, B.; Chen, R.; Zhou, D.; Gao, J.; Yang, C.; Tao, H.; Yang, H. B.; Zhang, L.; Liu, B.; Hung, S.; Chen, H. M.; Xiong, Q. Layered Structure Causes Bulk NiFe Layered Double Hydroxide Unstable in Alkaline Oxygen Evolution Reaction. *Adv. Mater.* **2019**, *31* (41), 1903909. https://doi.org/10.1002/ADMA.201903909.

(104) Stern, L. A.; Feng, L.; Song, F.; Hu, X. Ni2P as a Janus Catalyst for Water Splitting: The Oxygen Evolution Activity of Ni2P Nanoparticles. *Energy Environ. Sci.* **2015**, *8* (8), 2347–2351. https://doi.org/10.1039/C5EE01155H.

(105) Li, S.; Wang, L.; Su, H.; Hong, A. N.; Wang, Y.; Yang, H.; Ge, L.; Song, W.; Liu, J.; Ma, T.; Bu, X.; Feng, P. Electron Redistributed S-Doped Nickel Iron Phosphides Derived from One-Step Phosphatization of MOFs for Significantly Boosting Electrochemical Water

Splitting. *Adv. Funct. Mater.* **2022**, *32* (23), 2200733. https://doi.org/10.1002/ADFM.202200733.

(106) Munir, A.; Haq, T. ul; Saleem, M.; Qurashi, A.; Hussain, S. Z.; Sher, F.; Ul-Hamid, A.; Jilani, A.; Hussain, I. Controlled Engineering of Nickel Carbide Induced N-Enriched Carbon Nanotubes for Hydrogen and Oxygen Evolution Reactions in Wide PH Range. *Electrochim. Acta* **2020**, *341*, 136032. https://doi.org/10.1016/J.ELECTACTA.2020.136032.

(107) Seok, S.; Choi, M.; Lee, Y.; Jang, D.; Shin, Y.; Kim, Y. H.; Jo, C.; Park, S. Ni Nanoparticles on Ni Core/N-Doped Carbon Shell Heterostructures for Electrocatalytic Oxygen Evolution. *ACS Appl. Nano Mater.* **2021**, *4* (9), 9418–9429. https://doi.org/10.1021/ACSANM.1C01908/ASSET/IMAGES/LARGE/AN1C01908_0009.JPEG.

(108) Das, D.; Santra, S.; Nanda, K. K. In Situ Fabrication of a Nickel/Molybdenum Carbide-Anchored N-Doped Graphene/CNT Hybrid: An Efficient (Pre)Catalyst for OER and HER. *ACS Appl. Mater. Interfaces* **2018**, *10* (41), 35025–35038. https://doi.org/10.1021/ACSAMI.8B09941/ASSET/IMAGES/LARGE/AM-2018-09941Q_0006.JPEG.

(109) Hall, D. S.; Lockwood, D. J.; Poirier, S.; Bock, C.; MacDougall, B. R. Raman and Infrared Spectroscopy of α and β Phases of Thin Nickel Hydroxide Films Electrochemically Formed on Nickel. *J. Phys. Chem. A* **2012**, *116* (25), 6771–6784. https://doi.org/10.1021/JP303546R/ASSET/IMAGES/LARGE/JP-2012-03546R_0011.JPEG.

(110) Bo, X.; Li, Y.; Chen, X.; Zhao, C. Operando Raman Spectroscopy Reveals Cr-Induced-Phase Reconstruction of NiFe and CoFe Oxyhydroxides for Enhanced Electrocatalytic Water Oxidation. *Chem. Mater.* **2020**, *32* (10), 4303–4311. https://doi.org/10.1021/ACS.CHEMMATER.0C01067/ASSET/IMAGES/LARGE/CM0C01067_0005.JPEG.

(111) Dong, J.; Qian, Z.; Xu, P.; Yue, M. F.; Zhou, R. Y.; Wang, Y.; Nan, Z. A.; Huang, S.; Dong, Q.; Li, J. F.; Fan, F. R.; Tian, Z. Q. In Situ Raman Spectroscopy Reveals the Structure Evolution and Lattice Oxygen Reaction Pathway Induced by the Crystalline–Amorphous Heterojunction for Water Oxidation. *Chem. Sci.* **2022**, *13* (19), 5639–5649. https://doi.org/10.1039/D2SC01043G.

(112) Yeo, S.; Bell, A. T. In Situ Raman Study of Nickel Oxide and Gold-Supported Nickel Oxide Catalysts for the Electrochemical Evolution of Oxygen. **2012**. https://doi.org/10.1021/jp3007415.

(113) Lai, W.; Ge, L.; Li, H.; Deng, Y.; Xu, B.; Ouyang, B.; Kan, E. In Situ Raman Spectroscopic Study towards the Growth and Excellent HER Catalysis of Ni/Ni(OH)2 Heterostructure. *Int. J. Hydrogen Energy* **2021**, *46* (53), 26861–26872. https://doi.org/10.1016/J.IJHYDENE.2021.05.158.

(114) Al Samarai, M.; Hahn, A. W.; Beheshti Askari, A.; Cui, Y. T.; Yamazoe, K.; Miyawaki, J.; Harada, Y.; Rüdiger, O.; Debeer, S. Elucidation of Structure-Activity Correlations in a Nickel Manganese Oxide Oxygen Evolution Reaction Catalyst by Operando Ni L-Edge X-Ray Absorption Spectroscopy and 2p3d Resonant Inelastic X-Ray Scattering. *ACS Appl. Mater. Interfaces* **2019**, *11* (42), 38595–38605. https://doi.org/10.1021/ACSAMI.9B06752/ASSET/IMAGES/LARGE/AM9B06752_0001.JPEG.

(115) Gallenberger, J.; Moreno Fernández, H.; Alkemper, A.; Li, M.; Tian, C.; Kaiser, B.; Hofmann, J. P. Stability and Decomposition Pathways of the NiOOH OER Active Phase of NiOx Electrocatalysts at Open Circuit Potential Traced by Ex Situ and in Situ Spectroscopies. *Catal. Sci. Technol.* **2023**, *13* (16), 4693–4700. https://doi.org/10.1039/D3CY00674C.

(116) Lin, C.; Zhao, Y.; Zhang, H.; Xie, S.; Li, Y. F.; Li, X.; Jiang, Z.; Liu, Z. P. Accelerated Active Phase Transformation of NiO Powered by Pt Single Atoms for Enhanced Oxygen Evolution Reaction. *Chem. Sci.* **2018**, *9* (33), 6803–6812. https://doi.org/10.1039/C8SC02015A.

(117) Bediako, D. K.; Lassalle-Kaiser, B.; Surendranath, Y.; Yano, J.; Yachandra, V. K.; Nocera, D. G. Structure-Activity Correlations in a Nickel-Borate Oxygen Evolution Catalyst. *J. Am. Chem. Soc.* **2012**, *134* (15), 6801–6809. https://doi.org/10.1021/JA301018Q/SUPPL_FILE/JA301018Q_SI_001.PDF.

(118) Xiao, H.; Shin, H.; Goddard, W. A. Synergy between Fe and Ni in the Optimal Performance of (Ni,Fe)OOH Catalysts for the Oxygen Evolution Reaction. *Proc. Natl. Acad. Sci. U. S. A.* **2018**, *115* (23), 5872–5877. https://doi.org/10.1073/PNAS.1722034115/SUPPL_FILE/PNAS.1722034115.SAPP.PDF.

(119) Klaus, S.; Cai, Y.; Louie, M. W.; Trotochaud, L.; Bell, A. T. Effects of Fe Electrolyte Impurities on Ni(OH)2/NiOOH Structure and Oxygen Evolution Activity. *J. Phys. Chem. C* **2015**, *119* (13), 7243–7254. https://doi.org/10.1021/ACS.JPCC.5B00105/SUPPL_FILE/JP5B00105_SI_001.PDF.

(120) Trotochaud, L.; Young, S. L.; Ranney, J. K.; Boettcher, S. W. Nickel-Iron Oxyhydroxide Oxygen-Evolution Electrocatalysts: The Role of Intentional and Incidental Iron Incorporation. *J. Am. Chem. Soc.* **2014**, *136* (18), 6744–6753. https://doi.org/10.1021/JA502379C/SUPPL_FILE/JA502379C_SI_001.PDF.

(121) Yang, F.; Lopez Luna, M.; Haase, F. T.; Escalera-López, D.; Yoon, A.; Rüscher, M.; Rettenmaier, C.; Jeon, H. S.; Ortega, E.; Timoshenko, J.; Bergmann, A.; Chee, S. W.; Roldan Cuenya, B. Spatially and Chemically Resolved Visualization of Fe Incorporation into NiO Octahedra during the Oxygen Evolution Reaction. *J. Am. Chem. Soc.* **2023**, *145* (39), 21465–21474. https://doi.org/10.1021/JACS.3C07158/SUPPL_FILE/JA3C07158_SI_002.AVI.

(122) Valizadeh, A.; Najafpour, M. M. Is Nickel Phosphide an Efficient Catalyst for the

Oxygen-Evolution Reaction at Low Overpotentials? *New J. Chem.* **2020**, *44* (45), 19630–19641. https://doi.org/10.1039/D0NJ03701J.

(123) Raveendran, A.; Chandran, M.; Dhanusuraman, R. A Comprehensive Review on the Electrochemical Parameters and Recent Material Development of Electrochemical Water Splitting Electrocatalysts. *RSC Adv.* **2023**, *13* (6), 3843–3876. https://doi.org/10.1039/D2RA07642J.

(124) Feng, C.; Bilal Faheem, M.; Fu, J.; Xiao, Y.; Li, C.; Li, Y. Fe-Based Electrocatalysts for Oxygen Evolution Reaction: Progress and Perspectives. *ACS Catal.* **2020**, *10* (7), 4019–4047. https://doi.org/10.1021/acscatal.9b05445.

(125) Kang, Q.; Lai, D.; Tang, W.; Lu, Q.; Gao, F. Intrinsic Activity Modulation and Structural Design of NiFe Alloy Catalysts for an Efficient Oxygen Evolution Reaction. *Chem. Sci.* **2021**, *12* (11), 3818–3835. https://doi.org/10.1039/D0SC06716D.

(126) Mendoza-Garcia, A.; Su, D.; Sun, S. Sea Urchin-like Cobalt–Iron Phosphide as an Active Catalyst for Oxygen Evolution Reaction. *Nanoscale* **2016**, *8* (6), 3244–3247. https://doi.org/10.1039/C5NR08763E.

(127) Wang, Y.; Yan, D.; El Hankari, S.; Zou, Y.; Wang, S. Recent Progress on Layered Double Hydroxides and Their Derivatives for Electrocatalytic Water Splitting. *Adv. Sci.* **2018**, *5* (8), 1800064. https://doi.org/10.1002/ADVS.201800064.

(128) Li, Z.; Dou, X.; Zhao, Y.; Wu, C. Enhanced Oxygen Evolution Reaction of Metallic Nickel Phosphide Nanosheets by Surface Modification. *Inorg. Chem. Front.* **2016**, *3* (8), 1021–1027. https://doi.org/10.1039/C6QI00078A.

(129) Han, C.; Li, W.; Shu, C.; Guo, H.; Liu, H.; Dou, S.; Wang, J. Catalytic Activity Boosting of Nickel Sulfide toward Oxygen Evolution Reaction via Confined Overdoping Engineering. *ACS Appl. Energy Mater.* **2019**, *2* (8), 5363–5372. https://doi.org/10.1021/ACSAEM.9B00932/ASSET/IMAGES/LARGE/AE9B00932_0006.JPEG.

(130) Schäfer, H.; Beladi-Mousavi, S. M.; Walder, L.; Wollschläger, J.; Kuschel, O.; Ichilmann, S.; Sadaf, S.; Steinhart, M.; Küpper, K.; Schneider, L. Surface Oxidation of Stainless Steel: Oxygen Evolution Electrocatalysts with High Catalytic Activity. *ACS Catal.* **2015**, *5* (4), 2671–2680. https://doi.org/10.1021/ACSCATAL.5B00221/ASSET/IMAGES/LARGE/CS-2015-002219_0005.JPEG.

(131) Zamanizadeh, H. R.; Sunde, S.; Pollet, B. G.; Seland, F. Tailoring the Oxide Surface Composition of Stainless Steel for Improved OER Performance in Alkaline Water Electrolysis. *Electrochim. Acta* **2022**, *424*, 140561. https://doi.org/10.1016/J.ELECTACTA.2022.140561.

(132) Gomes, A. S. O.; Yaghini, N.; Martinelli, A.; Ahlberg, E. A Micro-Raman Spectroscopic

Study of Cr(OH)3 and Cr2O3 Nanoparticles Obtained by the Hydrothermal Method. *J. Raman Spectrosc.* **2017**, *48* (10), 1256–1263. https://doi.org/10.1002/JRS.5198.

(133) Bo, X.; Li, Y.; Hocking, R. K.; Zhao, C. NiFeCr Hydroxide Holey Nanosheet as Advanced Electrocatalyst for Water Oxidation. *ACS Appl. Mater. Interfaces* **2017**, *9* (47), 41239–41245. https://doi.org/10.1021/ACSAMI.7B12629/ASSET/IMAGES/AM-2017-126299_M003.GIF.

(134) Örnek, C.; Payam, B.; Gloskovskii, A.; Kazmanlı, K.; Mohamed, N.; Derin, B.; Ürgen, M.; Chou, C. E.; Yen, H. W.; Avcı, B.; Ooi, S. Understanding the Passive Behaviour of Low-Chromium High-Strength Hybrid Steel in Corrosive Environments. *npj Mater. Degrad. 2023 71* **2023**, *7* (1), 1–15. https://doi.org/10.1038/s41529-023-00392-z.

(135) Auguste, R.; Chan, H. L.; Romanovskaia, E.; Qiu, J.; Schoell, R.; Liedke, M. O.; Butterling, M.; Hirschmann, E.; Attallah, A. G.; Wagner, A.; Selim, F. A.; Kaoumi, D.; Uberuaga, B. P.; Hosemann, P.; Scully, J. R. A Multimodal Approach to Revisiting Oxidation Defects in Cr2O3. *npj Mater. Degrad. 2022 61* **2022**, *6* (1), 1–13. https://doi.org/10.1038/s41529-022-00269-7.

(136) Mironova-Ulmane, N.; Kuzmin, A.; Steins, I.; Grabis, J.; Sildos, I.; Pärs, M. Raman Scattering in Nanosized Nickel Oxide NiO. *J. Phys. Conf. Ser.* **2007**, *93* (1), 012039. https://doi.org/10.1088/1742-6596/93/1/012039.

(137) Abdullah, H.; Jurait, J.; Singh, R.; Singh, S. A.; Bhushan, M.; Kumar, Y.; Periyasamy, L.; Viswanath, A. K. Fabrication and a Detailed Study of Antibacterial Properties of α-Fe2O3/NiO Nanocomposites along with Their Structural, Optical, Thermal, Magnetic and Cytotoxic Features. *Nanotechnology* **2019**, *30* (18), 185101. https://doi.org/10.1088/1361-6528/AB0124.

(138) Dutta, A.; Mutyala, S.; Samantara, A. K.; Bera, S.; Jena, B. K.; Pradhan, N. Synergistic Effect of Inactive Iron Oxide Core on Active Nickel Phosphide Shell for Significant Enhancement in Oxygen Evolution Reaction Activity. *ACS Energy Lett.* **2018**, *3* (1), 141–148. https://doi.org/10.1021/ACSENERGYLETT.7B01141/ASSET/IMAGES/LARGE/NZ-2017-011415_0005.JPEG.

(139) Kawashima, K.; Márquez-Montes, R. A.; Li, H.; Shin, K.; Cao, C. L.; Vo, K. M.; Son, Y. J.; Wygant, B. R.; Chunangad, A.; Youn, D. H.; Henkelman, G.; Ramos-Sánchez, V. H.; Mullins, C. B. Electrochemical Behavior of a Ni3N OER Precatalyst in Fe-Purified Alkaline Media: The Impact of Self-Oxidation and Fe Incorporation. *Mater. Adv.* **2021**, *2* (7), 2299–2309. https://doi.org/10.1039/D1MA00130B.

(140) Batchellor, A. S.; Boettcher, S. W. Pulse-Electrodeposited Ni-Fe (Oxy)Hydroxide Oxygen Evolution Electrocatalysts with High Geometric and Intrinsic Activities at Large Mass Loadings. *ACS Catal.* **2015**, *5* (11), 6680–6689. https://doi.org/10.1021/ACSCATAL.5B01551/ASSET/IMAGES/LARGE/CS-2015-015515_0007.JPEG.

(141) Davydov, S. V. Phase Equilibria in the Carbide Region of Iron–Carbon Phase Diagram. *Steel Transl.* **2020**, *50* (12), 888–896. https://doi.org/10.3103/S0967091220120025/FIGURES/6.

(142) Nguyen, E. T.; McBride, J. R.; Mao, K.; Martin, P. A.; Strouse, G. F. Metal Carbide Nanocrystal Nucleation and Growth in a Transition Metal Coordination Polymer. *J. Phys. Chem. C* **2022**, *126* (48), 20636–20643. https://doi.org/10.1021/ACS.JPCC.2C06036/ASSET/IMAGES/LARGE/JP2C06036_0006.JPEG.

(143) Raghavan, V. C-Co-Fe (Carbon-Cobalt-Iron). https://doi.org/10.1007/s11669-009-9547-5.

(144) Cheng, J.; Hu, P.; Ellis, P.; French, S.; Kelly, G.; Lok, C. M. Density Functional Theory Study of Iron and Cobalt Carbides for Fischer-Tropsch Synthesis. *J. Phys. Chem. C* **2010**, *114* (2), 1085–1093. https://doi.org/10.1021/JP908482Q/ASSET/IMAGES/LARGE/JP-2009-08482Q_0010.JPEG.

(145) Wezendonk, T. A.; Sun, X.; Dugulan, A. I.; van Hoof, A. J. F.; Hensen, E. J. M.; Kapteijn, F.; Gascon, J. Controlled Formation of Iron Carbides and Their Performance in Fischer-Tropsch Synthesis. *J. Catal.* **2018**, *362*, 106–117. https://doi.org/10.1016/J.JCAT.2018.03.034.

(146) Li, S.; Yang, J.; Song, C.; Zhu, Q.; Xiao, D.; Ma, D.; Li, S.; Song, C.; Ma, D.; Yang, J.; Zhu, Q.; Xiao, D. Iron Carbides: Control Synthesis and Catalytic Applications in COx Hydrogenation and Electrochemical HER. *Adv. Mater.* **2019**, *31* (50), 1901796. https://doi.org/10.1002/ADMA.201901796.

(147) Yang, C.; Zhao, B.; Gao, R.; Yao, S.; Zhai, P.; Li, S.; Yu, J.; Hou, Y.; Ma, D. Construction of Synergistic Fe5C2/Co Heterostructured Nanoparticles as an Enhanced Low Temperature Fischer-Tropsch Synthesis Catalyst. *ACS Catal.* **2017**, *7* (9), 5661–5667. https://doi.org/10.1021/ACSCATAL.7B01142/ASSET/IMAGES/LARGE/CS-2017-011425_0005.JPEG.

(148) Chang, Q.; Zhang, C.; Liu, C.; Wei, Y.; Cheruvathur, A. V; Dugulan, ‖ A Iulian; Niemantsverdriet, J. W.; Liu, X.; He, Y.; Qing, M.; Zheng, L.; Yun, Y.; Yang, Y.; Li, Y. Supporting Information Relationship between Iron Carbide Phases (ϵ-Fe2C, Fe7C3, and χ-Fe5C2) and Catalytic Performances of Fe/SiO2 Fischer-Tropsch Catalyst.

(149) De Smit, E.; Cinquini, F.; Beale, A. M.; Safonova, O. V.; Van Beek, W.; Sautet, P.; Weckhuysen, B. M. Stability and Reactivity of ε-X-θ Iron Carbide Catalyst Phases in Fischer-Tropsch Synthesis: Controlling Mc. *J. Am. Chem. Soc.* **2010**, *132* (42), 14928–14941. https://doi.org/10.1021/JA105853Q/SUPPL_FILE/JA105853Q_SI_001.PDF.

(150) Liu, Q. Y.; Shang, C.; Liu, Z. P. In Situ Active Site for Fe-Catalyzed Fischer-Tropsch Synthesis: Recent Progress and Future Challenges. *J. Phys. Chem. Lett.* **2022**, *13* (15), 3342–3352. https://doi.org/10.1021/ACS.JPCLETT.2C00549/ASSET/IMAGES/LARGE/JZ2C00549_

0005.JPEG.

(151) Louw, J. D.; Van Den Berg, J. P.; Ferreira, L. C.; Pienaar, J. J. Appearance of FeC in a Hydrocarbon Synthesis Catalyst. *J. Am. Chem. Soc.* **1957**, *79* (22), 5899–5902. https://doi.org/10.1021/JA01579A018/ASSET/JA01579A018.FP.PNG_V03.

(152) Liu, X. W.; Cao, Z.; Zhao, S.; Gao, R.; Meng, Y.; Zhu, J. X.; Rogers, C.; Huo, C. F.; Yang, Y.; Li, Y. W.; Wen, X. D. Iron Carbides in Fischer-Tropsch Synthesis: Theoretical and Experimental Understanding in Epsilon-Iron Carbide Phase Assignment. *J. Phys. Chem. C* **2017**, *121* (39), 21390–21396. https://doi.org/10.1021/ACS.JPCC.7B06104/ASSET/IMAGES/LARGE/JP-2017-061044_0002.JPEG.

(153) Wang, H.; Zhu, S.; Deng, J.; Zhang, W.; Feng, Y.; Ma, J. Transition Metal Carbides in Electrocatalytic Oxygen Evolution Reaction. *Chinese Chem. Lett.* **2021**, *32* (1), 291–298. https://doi.org/10.1016/j.cclet.2020.02.018.

(154) Mu, A.; Scheu, C.; Pokharel, A.; Bo, S.; Bein, T.; Fattakhova-rohlfing, D. Iron-Doped Nickel Oxide Nanocrystals Alkaline Water Splitting. *ACS Nano* **2015**, *9* (5), 5180–5188.

(155) Chuang, C. H.; Hsiao, L. Y.; Yeh, M. H.; Wang, Y. C.; Chang, S. C.; Tsai, L. D.; Ho, K. C. Prussian Blue Analogue-Derived Metal Oxides as Electrocatalysts for Oxygen Evolution Reaction: Tailoring the Molar Ratio of Cobalt to Iron. *ACS Appl. Energy Mater.* **2020**, *3* (12), 11752–11762. https://doi.org/10.1021/ACSAEM.0C01903/ASSET/IMAGES/LARGE/AE0C01903_0008.JPEG.

(156) Huang, J.; Xu, P.; Gao, T.; Huangfu, J.; Wang, X. jie; Liu, S.; Zhang, Y.; Song, B. Controlled Synthesis of Hollow Bimetallic Prussian Blue Analog for Conversion into Efficient Oxygen Evolution Electrocatalyst. *ACS Sustain. Chem. Eng.* **2020**, *8* (2), 1319–1328. https://doi.org/10.1021/acssuschemeng.9b07122.

(157) Wang, J.; Hou, Y. Iron Carbide Nanostructures: An Emerging Material for Tumor Theranostics. *Accounts Mater. Res.* **2022**, *3* (1), 89–99. https://doi.org/10.1021/ACCOUNTSMR.0C00018/ASSET/IMAGES/LARGE/MR0C00018_0007.JPEG.

(158) Ye, Z.; Zhang, P.; Lei, X.; Wang, X.; Zhao, N.; Yang, H. Iron Carbides and Nitrides: Ancient Materials with Novel Prospects. *Chem. – A Eur. J.* **2018**, *24* (36), 8922–8940. https://doi.org/10.1002/CHEM.201706028.

(159) Naraghi, R.; Selleby, M.; Ågren, J. Thermodynamics of Stable and Metastable Structures in Fe-C System. *Calphad Comput. Coupling Phase Diagrams Thermochem.* **2014**, *46*, 148–158. https://doi.org/10.1016/j.calphad.2014.03.004.

(160) Dey, G. R.; Soliman, S. S.; McCormick, C. R.; Wood, C. H.; Katzbaer, R. R.; Schaak, R. E. Colloidal Nanoparticles of High Entropy Materials: Capabilities, Challenges, and

Opportunities in Synthesis and Characterization. *ACS Nanosci. Au* **2023**. https://doi.org/10.1021/ACSNANOSCIENCEAU.3C00049.

(161) Soliman, S. S.; Dey, G. R.; McCormick, C. R.; Schaak, R. E. Temporal Evolution of Morphology, Composition, and Structure in the Formation of Colloidal High-Entropy Intermetallic Nanoparticles. *ACS Nano* **2023**, *17* (16), 16147–16159. https://doi.org/10.1021/ACSNANO.3C05241/SUPPL_FILE/NN3C05241_SI_001.PDF.

(162) Dey, G. R.; Soliman, S. S.; McCormick, C. R.; Wood, C. H.; Katzbaer, R. R.; Schaak, R. E. Colloidal Nanoparticles of High Entropy Materials: Capabilities, Challenges, and Opportunities in Synthesis and Characterization. *ACS Nanosci. Au* **2024**, *4* (1), 3–20. https://doi.org/10.1021/ACSNANOSCIENCEAU.3C00049/ASSET/IMAGES/LARGE/NG3C00049_0008.JPEG.

(163) Hardy, D. A.; Nguyen, E. T.; Parrish, S. E.; Schriber, E. A.; Schlicker, L.; Gili, A.; Kamutzki, F.; Hohman, J. N.; Strouse, G. F. Prussian Blue Iron−Cobalt Mesocrystals as a Template for the Growth of Fe/Co Carbide (Cementite) and Fe/Co Nanocrystals. **2019**. https://doi.org/10.1021/acs.chemmater.9b02957.

(164) Bhadeshia, H. K. D. H.; Chintha, A. R.; Lenka, S. Critical Assessment 34: Are χ (Hägg), η and ϵ Carbides Transition-Phases Relative to Cementite in Steels? *https://doi.org/10.1080/02670836.2019.1625526* **2019**, *35* (11), 1301–1305. https://doi.org/10.1080/02670836.2019.1625526.

(165) Okamoto, H. The C-Fe (Carbon-Iron) System. *J. Phase Equilibria* **1992**, *13* (5), 543–565. https://doi.org/10.1007/BF02665767/METRICS.

(166) Ishlda, K.; Nishlzawa, T. Phase Diagram Evaluations: Section II The C-Co (Carbon-Cobalt) System Equilibrium Diagram.

(167) Tang, T.; Duan, Z.; Baimanov, D.; Bai, X.; Liu, X.; Wang, L.; Wang, Z.; Guan, J. Synergy between Isolated Fe and Co Sites Accelerates Oxygen Evolution. *Nano Res.* **2023**, *16* (2), 2218–2223. https://doi.org/10.1007/S12274-022-5001-3/METRICS.

(168) Ali Ehsan, M.; Saeed Hakeem, A.; Rehman, A. Synergistic Effects in Bimetallic Pd-CoO Electrocatalytic Thin Films for Oxygen Evolution Reaction. **2020**, *10*, 14469. https://doi.org/10.1038/s41598-020-71389-w.

(169) Jiang, J.; Zhou, X. L.; Lv, H. G.; Yu, H. Q.; Yu, Y. Bimetallic-Based Electrocatalysts for Oxygen Evolution Reaction. *Adv. Funct. Mater.* **2023**, *33* (10). https://doi.org/10.1002/ADFM.202212160.

(170) Bai, L.; Hsu, C. S.; Alexander, D. T. L.; Chen, H. M.; Hu, X. A Cobalt-Iron Double-Atom Catalyst for the Oxygen Evolution Reaction. *J. Am. Chem. Soc.* **2019**, *141* (36), 14190–14199. https://doi.org/10.1021/JACS.9B05268/SUPPL_FILE/JA9B05268_SI_001.PDF.

(171) Li, K.; Li, Y.; Peng, W.; Zhang, G.; Zhang, F.; Fan, X. Bimetallic Iron-Cobalt Catalysts

and Their Applications in Energy-Related Electrochemical Reactions. **2019**. https://doi.org/10.3390/catal9090762.

(172) Wang, J.; Hou, Y. Iron Carbide Nanostructures: An Emerging Material for Tumor Theranostics. *Accounts Mater. Res.* **2022**, *3* (1), 89–99. https://doi.org/10.1021/ACCOUNTSMR.0C00018/ASSET/IMAGES/LARGE/MR0C00018_0007.JPEG.

(173) Nikitenko, S. I.; Koltypin, Y.; Palchik, O.; Felner, I.; Xu, X. N.; Gedanken, A.; Blackmond, D. G.; Lightfoot, A.; Pfaltz, A.; Rosner, T.; Schnider, P.; Zimmermann, N.; Powell, M. T.; Hou, D.; Perry, M. C.; Cui, X.; Burgess, K.; Reibenspies, J. H.; Hou, -r; Colacot, T. A. Synthesis of Highly Magnetic, Air-Stable Iron ± Iron Carbide Nanocrystalline Particles by Using Power Ultrasound**. *Halterman Compr. Asymmetric Catal.* **2001**, *113* (23), 206–215. https://doi.org/10.1002/1521-3757(20011203)113:23<4579::AID-ANGE4579>3.0.CO;2-D.

(174) El-Gendy, A. A.; Bertino, M.; Clifford, D.; Qian, M.; Khanna, S. N.; Carpenter, E. E. Experimental Evidence for the Formation of CoFe2C Phase with Colossal Magnetocrystalline-Anisotropy. *Appl. Phys. Lett.* **2015**, *106* (21), 213109. https://doi.org/10.1063/1.4921789/27454.

(175) Neeli, S. T.; Ramsurn, H.; Ng, C. Y.; Wang, Y.; Lu, J. Removal of Cr (VI), As (V), Cu (II), and Pb (II) Using Cellulose Biochar Supported Iron Nanoparticles: A Kinetic and Mechanistic Study. *J. Environ. Chem. Eng.* **2020**, *8* (5), 103886. https://doi.org/10.1016/J.JECE.2020.103886.

(176) Yuan, X.; Zhou, Y.; Huo, C.; Guo, W.; Yang, Y.; Li, Y.; Wen, X. Crystal Structure Prediction Approach to Explore the Iron Carbide Phases: Novel Crystal Structures and Unexpected Magnetic Properties. *J. Phys. Chem. C* **2020**, *124* (31), 17244–17254. https://doi.org/10.1021/ACS.JPCC.0C05129/ASSET/IMAGES/LARGE/JP0C05129_0008.JPEG.

(177) Raghavan, V. C-Co-Fe (Carbon-Cobalt-Iron). *J. Phase Equilibria Diffus.* **2009**, *30* (4), 378. https://doi.org/10.1007/s11669-009-9547-5.

(178) Li, S. J.; Ishihara, M.; Yumoto, H.; Aizawa, T.; Shimotomai, M. Characterization of Cementite Films Prepared by Electron-Shower-Assisted PVD Method. *Thin Solid Films* **1998**, *316*, 100104.

(179) Dong, X. L.; Zhang, Z. D.; Xiao, Q. F.; Zhao, X. G.; Chuang, Y. C.; Jin, S. R.; Sun, W. M.; Li, Z. J.; Zheng, Z. X.; Yang, H. Characterization of Ultrafine γ-Fe(C), α-Fe(C) and Fe3C Particles Synthesized by Arc-Discharge in Methane. *J. Mater. Sci.* **1998**, *33* (7), 1915–1919. https://doi.org/10.1023/A:1004369708540/METRICS.

(180) Yang, C.; Zhao, H.; Hou, Y.; Ma, D. Fe5C2 Nanoparticles: A Facile Bromide-Induced Synthesis and as an Active Phase for Fischer–Tropsch Synthesis. *J. Am. Chem. Soc.* **2012**, *134* (38), 15814–15821. https://doi.org/10.1021/ja305048p.

(181) Li, S.; Yang, C.; Yin, Z.; Yang, H.; Chen, Y.; Lin, L.; Li, M.; Li, W.; Hu, G.; Ma, D.; Berlin, S.-V. Wet-Chemistry Synthesis of Cobalt Carbide Nanoparticles as Highly Active and Stable Electrocatalyst for Hydrogen Evolution Reaction. https://doi.org/10.1007/s12274-017-1425-6.

(182) Williams, B.; Clifford, D.; El-Gendy, A. A.; Carpenter, E. E. Solvothermal Synthesis of Fe7C3 and Fe3C Nanostructures with Phase and Morphology Control. *J. Appl. Phys.* **2016**, *120* (3), 33904. https://doi.org/10.1063/1.4958972/143672.

(183) Huba, Z. J.; Carpenter, E. E. Size and Phase Control of Cobalt-Carbide Nanoparticles Using OH - and Cl - Anions in a Polyol Process. *J. Appl. Phys.* **2012**, *111* (7), 7–529. https://doi.org/10.1063/1.3677816/370898.

(184) Yang, Z.; Zhao, T.; Huang, X.; Chu, X.; Tang, T.; Ju, Y.; Wang, Q.; Hou, Y.; Gao, S. Modulating the Phases of Iron Carbide Nanoparticles: From a Perspective of Interfering with the Carbon Penetration of Fe@Fe3O4 by Selectively Adsorbed Halide Ions. *Chem. Sci.* **2016**, *8* (1), 473–481. https://doi.org/10.1039/C6SC01819J.

(185) Li, S.; Yang, C.; Yin, Z.; Yang, H.; Chen, Y.; Lin, L.; Li, M.; Li, W.; Hu, G.; Ma, D. Wet-Chemistry Synthesis of Cobalt Carbide Nanoparticles as Highly Active and Stable Electrocatalyst for Hydrogen Evolution Reaction. *Nano Res. 2017 104* **2017**, *10* (4), 1322–1328. https://doi.org/10.1007/S12274-017-1425-6.

(186) Kresse, G.; Furthmü, J. Efficient Iterative Schemes for Ab Initio Total-Energy Calculations Using a Plane-Wave Basis Set. **1996**.

(187) Kresse, G.; Hafner, J. Ab. Initio Molecular Dynamics for Liquid Metals. *47*.

(188) Perdew, J. P.; Burke, K.; Ernzerhof, M. Generalized Gradient Approximation Made Simple. **1996**.

(189) Blochl, P. E. Projector Augmented-+rave Method. *Phys. Rev. B Vol. 50*, 24.

(190) Pack, J. D.; Monkhorst, H. J. "Special Points for Brillonln-Zone Integrations"-a Reply*. **1977**.

(191) Nguyen, E. T.; Mcbride, J. R.; Mao, K.; Martin, P. A.; Strouse, G. F. Metal Carbide Nanocrystal Nucleation and Growth in a Transition Metal Coordination Polymer. *J. Phys. Chem. C* **2063**, *2022*, 2024. https://doi.org/10.1021/acs.jpcc.2c06036.

(192) Sun, H.; Dimagno, S. G. Anhydrous Tetrabutylammonium Fluoride. **2005**. https://doi.org/10.1021/ja0440497.

(193) Charette, A. B.; Chinchilla, R.; Nájera, C. Tetrabutylammonium Bromide. *Encycl. Reagents Org. Synth.* **2007**. https://doi.org/10.1002/047084289X.RT011.PUB2.

(194) Li, Z.; Zhao, T.-T.; Jiang, W.-J.; Niu, S.; Wu, M.; Hu, J.-S. Bimetal Prussian Blue as a

Continuously Variable Platform for Investigating the Composition–Activity Relationship of Phosphides-Based Electrocatalysts for Water Oxidation. *ACS Appl. Mater. & Interfaces* **2018**, *10* (42), 35904–35910. https://doi.org/10.1021/acsami.8b10257.

(195) Wu, Z.-P.; Lu, F.; Zang, S.-Q.; Wen, X.; Lou, D.; Wu, Z.-P.; Lu, X. F.; Lou, X. W.; Zang, S.-Q. Non-Noble-Metal-Based Electrocatalysts toward the Oxygen Evolution Reaction. *Adv. Funct. Mater.* **2020**, *30* (15), 1910274. https://doi.org/10.1002/ADFM.201910274.

(196) Zhang, L.; Ren, X.; Guo, X.; Liu, Z.; Asiri, A. M.; Li, B.; Chen, L.; Sun, X. Efficient Hydrogen Evolution Electrocatalysis at Alkaline PH by Interface Engineering of Ni2P-CeO2. *Inorg. Chem.* **2018**, *57* (2), 548–552. https://doi.org/10.1021/ACS.INORGCHEM.7B02665/ASSET/IMAGES/LARGE/IC-2017-02665B_0004.JPEG.

(197) Ghosh, S.; Manna, L. The Many "Facets" of Halide Ions in the Chemistry of Colloidal Inorganic Nanocrystals. *Chem. Rev.* **2018**, *118* (16), 7804–7864. https://doi.org/10.1021/ACS.CHEMREV.8B00158/ASSET/IMAGES/LARGE/CR-2018-00158Z_0035.JPEG.

(198) Sun, H.; Zhu, Y.; Jung, W. Tuning Reconstruction Level of Precatalysts to Design Advanced Oxygen Evolution Electrocatalysts. *Mol. 2021, Vol. 26, Page 5476* **2021**, *26* (18), 5476. https://doi.org/10.3390/MOLECULES26185476.

(199) Saad, A.; Cheng, Z.; Zhang, X.; Liu, S.; Shen, H.; Thomas, T.; Wang, J.; Yang, M.; Saad, A.; Cheng, Z.; Zhang, X.; Liu, S.; Shen, H.; Yang, M.; Thomas, T.; Wang, J. Ordered Mesoporous Cobalt–Nickel Nitride Prepared by Nanocasting for Oxygen Evolution Reaction Electrocatalysis. *Adv. Mater. Interfaces* **2019**, *6* (20), 1900960. https://doi.org/10.1002/ADMI.201900960.

(200) Fan, K.; Zou, H.; Lu, Y.; Chen, H.; Li, F.; Liu, J.; Sun, L.; Tong, L.; Toney, M. F.; Sui, M.; Yu, J. Direct Observation of Structural Evolution of Metal Chalcogenide in Electrocatalytic Water Oxidation. *ACS Nano* **2018**, *12* (12), 12369–12379. https://doi.org/10.1021/ACSNANO.8B06312/ASSET/IMAGES/MEDIUM/NN-2018-06312G_M005.GIF.

(201) Liu, K.; Wang, F.; He, P.; Shifa, T. A.; Wang, Z.; Cheng, Z.; Zhan, X.; He, J. The Role of Active Oxide Species for Electrochemical Water Oxidation on the Surface of 3d-Metal Phosphides. *Adv. Energy Mater.* **2018**, *8* (15), 1703290. https://doi.org/10.1002/AENM.201703290.

(202) Tan, Z.; Sharma, L.; Kakkar, R.; Meng, T.; Jiang, Y.; Cao, M. Arousing the Reactive Fe Sites in Pyrite (FeS2) via Integration of Electronic Structure Reconfiguration and in Situ Electrochemical Topotactic Transformation for Highly Efficient Oxygen Evolution Reaction. *Inorg. Chem.* **2019**, *58* (11), 7615–7627. https://doi.org/10.1021/ACS.INORGCHEM.9B01017/ASSET/IMAGES/LARGE/IC-2019-010172_0008.JPEG.

(203) McCrory, C. C. L.; Jung, S.; Ferrer, I. M.; Chatman, S. M.; Peters, J. C.; Jaramillo, T. F. Benchmarking Hydrogen Evolving Reaction and Oxygen Evolving Reaction Electrocatalysts for Solar Water Splitting Devices. *J. Am. Chem. Soc.* **2015**, *137* (13), 4347–4357. https://doi.org/10.1021/JA510442P/SUPPL_FILE/JA510442P_SI_001.PDF.

(204) Cao, L. M.; Lu, D.; Zhong, D. C.; Lu, T. B. Prussian Blue Analogues and Their Derived Nanomaterials for Electrocatalytic Water Splitting. *Coord. Chem. Rev.* **2020**, *407*, 213156. https://doi.org/10.1016/j.ccr.2019.213156.

(205) Li, H.; Li, Q.; Wen, P.; Williams, T. B.; Adhikari, S.; Dun, C.; Lu, C.; Itanze, D.; Jiang, L.; Carroll, D. L.; Donati, G. L.; Lundin, P. M.; Qiu, Y.; Geyer, S. M. Colloidal Cobalt Phosphide Nanocrystals as Trifunctional Electrocatalysts for Overall Water Splitting Powered by a Zinc–Air Battery. *Adv. Mater.* **2018**, *30* (9), 1705796. https://doi.org/10.1002/ADMA.201705796.

(206) Soliman, S. S.; Dey, G. R.; Mccormick, C. R.; Schaak, R. E. Temporal Evolution of Morphology, Composition, and Structure in the Formation of Colloidal High-Entropy Intermetallic Nanoparticles. *ACS Nano* **2023**, *17*, 16147–16159. https://doi.org/10.1021/acsnano.3c05241.

(207) Xin, Y.; Li, S.; Qian, Y.; Zhu, W.; Yuan, H.; Jiang, P.; Guo, R.; Wang, L. High-Entropy Alloys as a Platform for Catalysis: Progress, Challenges, and Opportunities. **2020**. https://doi.org/10.1021/acscatal.0c03617.

(208) Sun, Y.; Dai, S. High-Entropy Materials for Catalysis: A New Frontier. *Sci. Adv* **2021**, *7*.

(209) Löffler, T.; Savan, A.; Garzón-Manjón, A.; Meischein, M.; Scheu, C.; Ludwig, A.; Schuhmann, W. Toward a Paradigm Shift in Electrocatalysis Using Complex Solid Solution Nanoparticles. *ACS Energy Lett.* **2019**, *4* (5), 1206–1214. https://doi.org/10.1021/ACSENERGYLETT.9B00531.

(210) Dey, G. R.; McCormick, C. R.; Soliman, S. S.; Darling, A. J.; Schaak, R. E. Chemical Insights into the Formation of Colloidal High Entropy Alloy Nanoparticles. *ACS Nano* **2023**, *17* (6), 5943–5955. https://doi.org/10.1021/ACSNANO.3C00176/SUPPL_FILE/NN3C00176_SI_001.PDF.

(211) Zhang, S.; Liu, X.; Luo, H.; Wu, Z.; Wei, B.; Shao, Z.; Huang, C.; Hua, K.; Xia, L.; Li, J.; Liu, L.; Ding, W.; Wang, H.; Sun, Y. Morphological Modulation of Co2C by Surface-Adsorbed Species for Highly Effective Low-Temperature CO2 Reduction. *ACS Catal.* **2022**, *12* (14), 8544–8557. https://doi.org/10.1021/ACSCATAL.2C02020.

(212) Chang, Q.; Zhang, C.; Liu, C.; Wei, Y.; Cheruvathur, A. V.; Dugulan, A. I.; Niemantsverdriet, J. W.; Liu, X.; He, Y.; Qing, M.; Zheng, L.; Yun, Y.; Yang, Y.; Li, Y. Relationship between Iron Carbide Phases (ε-Fe2C, Fe7C3, and χ-Fe5C2) and Catalytic Performances of Fe/SiO2 Fischer-Tropsch Catalysts. *ACS Catal.* **2018**, *8* (4), 3304–3316. https://doi.org/10.1021/acscatal.7b04085.

(213) Lin, Y. H.; Huang, P. C.; Wang, S. C.; Huang, J. L. Highly Active Electrocatalyst Cobalt-Carbide Nanoparticles Synthesized by Wet-Chemistry Method for Hydrogen Evolution Reaction. *Mod. Phys. Lett. B* **2020**, *34* (7–9), 1–7. https://doi.org/10.1142/S0217984920400229.

(214) Tang, Y. J.; Liu, C. H.; Huang, W.; Wang, X. L.; Dong, L. Z.; Li, S. L.; Lan, Y. Q. Bimetallic Carbides-Based Nanocomposite as Superior Electrocatalyst for Oxygen Evolution Reaction. *ACS Appl. Mater. Interfaces* **2017**, *9* (20), 16977–16985. https://doi.org/10.1021/acsami.7b01096.

(215) Zu, M. Y.; Wang, C.; Zhang, L.; Zheng, L. R.; Yang, H. G. Reconstructing Bimetallic Carbide Mo6Ni6C for Carbon Interconnected MoNi Alloys to Boost Oxygen Evolution Electrocatalysis. *Mater. Horizons* **2019**, *6* (1), 115–121. https://doi.org/10.1039/C8MH00664D.

(216) Xin, Y.; Li, S.; Qian, Y.; Zhu, W.; Yuan, H.; Jiang, P.; Guo, R.; Wang, L. High-Entropy Alloys as a Platform for Catalysis: Progress, Challenges, and Opportunities. *ACS Catal.* **2020**, *10* (19), 11280–11306. https://doi.org/10.1021/ACSCATAL.0C03617/ASSET/IMAGES/MEDIUM/CS0C03617_0016.GIF.

(217) Buckingham, M. A.; Skelton, J. M.; Lewis, D. J. Synthetic Strategies toward High Entropy Materials: Atoms-to-Lattices for Maximum Disorder. *Cryst. Growth Des.* **2023**, *23* (10), 6998–7009. https://doi.org/10.1021/ACS.CGD.3C00712.

(218) Wang, Z.; Li, Z.-T.; Shi, ·; Zhao, J.; Wu, Z.-G. High-Entropy Carbide Ceramics: A Perspective Review. *Tungsten* **123AD**, *3*, 131–142. https://doi.org/10.1007/s42864-021-00085-7.

(219) Aamlid, S. S.; Oudah, M.; Rottler, J.; Hallas, A. M. Understanding the Role of Entropy in High Entropy Oxides. *J. Am. Chem. Soc.* **2023**, *145* (11), 5991–6006. https://doi.org/10.1021/JACS.2C11608/ASSET/IMAGES/MEDIUM/JA2C11608_0008.GIF.

(220) Dey, G. R.; McCormick, C. R.; Soliman, S. S.; Darling, A. J.; Schaak, R. E. Chemical Insights into the Formation of Colloidal High Entropy Alloy Nanoparticles. *ACS Nano* **2023**, *17* (6), 5943–5955. https://doi.org/10.1021/ACSNANO.3C00176/SUPPL_FILE/NN3C00176_SI_001.PDF.

(221) Huang, J.; Xu, P.; Gao, T.; Huangfu, J.; Wang, X. jie; Liu, S.; Zhang, Y.; Song, B. Controlled Synthesis of Hollow Bimetallic Prussian Blue Analog for Conversion into Efficient Oxygen Evolution Electrocatalyst. *ACS Sustain. Chem. Eng.* **2020**, *8* (2), 1319–1328. https://doi.org/10.1021/ACSSUSCHEMENG.9B07122/SUPPL_FILE/SC9B07122_SI_001.PDF.

(222) Du, M.; Geng, P.; Pei, C.; Jiang, X.; Shan, Y.; Hu, W.; Ni, L.; Pang, H. High-Entropy

Prussian Blue Analogues and Their Oxide Family as Sulfur Hosts for Lithium-Sulfur Batteries. **2022**. https://doi.org/10.1002/anie.202209350.

(223) Yao, Y.; Wang, S.; Wang, C.; Wu, Z.; Xiao, C.; Guo, X.; Yan, X.; Qi, J.; Zhou, Y.; Zhu, Z.; Yang, Y.; Li, X.; Li, J. Prussian Blue Analogue-Derived High-Entropy Alloy Nanoarchitectonics for Efficient Fenton-like Catalysis †. **2024**. https://doi.org/10.1039/d3ta07737c.

(224) Bornamehr, B.; Presser, V.; Zarbin, A. J. G.; Yamauchi, Y.; Husmann, S. Prussian Blue and Its Analogues as Functional Template Materials: Control of Derived Structure Compositions and Morphologies. **2023**. https://doi.org/10.1039/d2ta09501g.

(225) Xiao, Y.; Xiao, J.; Zhao, H.; Li, J.; Zhang, G.; Zhang, D.; Guo, X.; Gao, H.; Wang, Y.; Chen, J.; Wang, G.; Liu, H. Prussian Blue Analogues for Sodium-Ion Battery Cathodes: A Review of Mechanistic Insights, Current Challenges, and Future Pathways. **2024**. https://doi.org/10.1002/smll.202401957.

(226) Jiang, W.; Wang, T.; Chen, H.; Suo, X.; Liang, J.; Zhu, W.; Li, H.; Dai, S. Room Temperature Synthesis of High-Entropy Prussian Blue Analogues. *Nano Energy* **2021**, *79*, 105464. https://doi.org/10.1016/J.NANOEN.2020.105464.

(227) Fan, Q.; Liu, K.; Liu, Z.; Liu, H.; Zhang, L.; Zhong, P.; Gao, C. A Ligand-Exchange Route to Nobel Metal Nanocrystals with a Clean Surface for Enhanced Optical and Catalytic Properties. *Part. Part. Syst. Charact.* **2017**, *34* (8). https://doi.org/10.1002/ppsc.201700075.

(228) Yu, F.; Zhou, H.; Zhu, Z.; Sun, J.; He, R.; Bao, J.; Chen, S.; Ren, Z. Three-Dimensional Nanoporous Iron Nitride Film as an Efficient Electrocatalyst for Water Oxidation. *ACS Catal.* **2017**, *7* (3), 2052–2057. https://doi.org/10.1021/ACSCATAL.6B03132/ASSET/IMAGES/LARGE/CS-2016-03132H_0004.JPEG.

(229) Aamlid, S. S.; Oudah, M.; Rottler, J.; Hallas, A. M. Understanding the Role of Entropy in High Entropy Oxides. *J. Am. Chem. Soc.* **2023**, *145* (11), 5991–6006. https://doi.org/10.1021/JACS.2C11608.

(230) Sarkar, A.; Velasco, L.; Wang, D.; Wang, Q.; Talasila, G.; de Biasi, L.; Kübel, C.; Brezesinski, T.; Bhattacharya, S. S.; Hahn, H.; Breitung, B. High Entropy Oxides for Reversible Energy Storage. https://doi.org/10.1038/s41467-018-05774-5.

(231) Harrington, T. J.; Gild, J.; Sarker, P.; Toher, C.; Rost, C. M.; Dippo, O. F.; McElfresh, C.; Kaufmann, K.; Marin, E.; Borowski, L.; Hopkins, P. E.; Luo, J.; Curtarolo, S.; Brenner, D. W.; Vecchio, K. S. Phase Stability and Mechanical Properties of Novel High Entropy Transition Metal Carbides. *Acta Mater.* **2019**, *166*, 271–280. https://doi.org/10.1016/J.ACTAMAT.2018.12.054.

(232) Moskovskikh, D.; Vorotilo, S.; Buinevich, V.; Sedegov, A.; Kuskov, K.; Khort, A.;

Shuck, C.; Zhukovskyi, M.; Mukasyan, A. Extremely Hard and Tough High Entropy Nitride Ceramics. **2020**. https://doi.org/10.1038/s41598-020-76945-y.

(233) Sarker, P.; Harrington, T.; Toher, C.; Oses, C.; Samiee, M.; Maria, J.-P.; Brenner, D. W.; Vecchio, K. S.; Curtarolo, S. High-Entropy High-Hardness Metal Carbides Discovered by Entropy Descriptors. https://doi.org/10.1038/s41467-018-07160-7.

(234) Stern, L. A.; Feng, L.; Song, F.; Hu, X. Ni2P as a Janus Catalyst for Water Splitting: The Oxygen Evolution Activity of Ni2P Nanoparticles. *Energy Environ. Sci.* **2015**, *8* (8), 2347–2351. https://doi.org/10.1039/C5EE01155H.

(235) Liang, H.; Xu, M.; Asselin, E. Corrosion of Monometallic Iron- and Nickel-Based Electrocatalysts for the Alkaline Oxygen Evolution Reaction: A Review. *J. Power Sources* **2021**, *510*, 230387. https://doi.org/10.1016/J.JPOWSOUR.2021.230387.

(236) Callejas, J. F.; Read, C. G.; Popczun, E. J.; McEnaney, J. M.; Schaak, R. E. Nanostructured Co2P Electrocatalyst for the Hydrogen Evolution Reaction and Direct Comparison with Morphologically Equivalent CoP. *Chem. Mater.* **2015**, *27* (10), 3769–3774. https://doi.org/10.1021/ACS.CHEMMATER.5B01284/SUPPL_FILE/CM5B01284_SI_001.PDF.

(237) Wang, T.; Wang, C.; Jin, Y.; Sviripa, A.; Liang, J.; Han, J.; Huang, Y.; Li, Q.; Wu, G. Amorphous Co–Fe–P Nanospheres for Efficient Water Oxidation. *J. Mater. Chem. A* **2017**, *5* (48), 25378–25384. https://doi.org/10.1039/C7TA08720A.

(238) Liu, J.; Li, X.; Liu, B.; Zhao, C.; Kuang, Z.; Hu, R.; Liu, B.; Ao, Z.; Wang, J. Shape-Controlled Synthesis of Metal-Organic Frameworks with Adjustable Fenton-Like Catalytic Activity. *ACS Appl. Mater. Interfaces* **2018**, *10* (44), 38051–38056. https://doi.org/10.1021/acsami.8b12686.

(239) Shiba, F.; Nito, M.; Kawakita, K.; Okawa, Y. Size Control of Monodisperse Prussian Blue Nanoparticles by Enforced-Nucleation and Additional-Growth Procedures in a Citrate Reduction System. *Part. Sci. Technol.* **2015**, *33* (6), 671–676. https://doi.org/10.1080/02726351.2015.1020181.

(240) Hu, M.; Furukawa, S.; Ohtani, R.; Sukegawa, H.; Nemoto, Y.; Reboul, J.; Kitagawa, S.; Yamauchi, Y. Synthesis of Prussian Blue Nanoparticles with a Hollow Interior by Controlled Chemical Etching. *Angew. Chemie - Int. Ed.* **2012**, *51* (4), 984–988. https://doi.org/10.1002/anie.201105190.

(241) Yang, W.; Wu, X.; Yu, Y.; Yang, C.; Xu, S.; Li, H. Controlled Synthesis and Magnetic Properties of Iron–Cobalt–Phosphide Nanorods. *Nanoscale* **2016**, *8* (36), 16187–16191. https://doi.org/10.1039/C6NR04810B.

(242) Zhang, S.; Jiang, G.; Filsinger, G. T.; Wu, L.; Zhu, H.; Lee, J.; Wu, Z.; Sun, S. Halide Ion-Mediated Growth of Single Crystalline Fe Nanoparticles. *Nanoscale* **2014**, *6* (9), 4852–

4856. https://doi.org/10.1039/C4NR00193A.

(243) Bhadeshia, H. K. D. H.; Chintha, A. R.; Lenka, S. Critical Assessment 34: Are χ (Hägg), η and ϵ Carbides Transition-Phases Relative to Cementite in Steels? *Mater. Sci. Technol. (United Kingdom)* **2019**, *35* (11), 1301–1305. https://doi.org/10.1080/02670836.2019.1625526.

(244) Gangwar, A.; Singh, G.; Shaw, S. K.; Mandal, R. K.; Sharma, A.; Meena, S. S.; Prajapat, C. L.; Prasad, N. K. Synthesis and Structural Characterization of CoxFe3−xC ($0 \leq x \leq 0.3$) Magnetic Nanoparticles for Biomedical Applications. *New J. Chem.* **2019**, *43* (8), 3536–3544. https://doi.org/10.1039/C8NJ05240A.

(245) Liu, X. W.; Cao, Z.; Zhao, S.; Gao, R.; Meng, Y.; Zhu, J. X.; Rogers, C.; Huo, C. F.; Yang, Y.; Li, Y. W.; Wen, X. D. Iron Carbides in Fischer-Tropsch Synthesis: Theoretical and Experimental Understanding in Epsilon-Iron Carbide Phase Assignment. *J. Phys. Chem. C* **2017**, *121* (39), 21390–21396. https://doi.org/10.1021/ACS.JPCC.7B06104/ASSET/IMAGES/LARGE/JP-2017-061044_0002.JPEG.

(246) Yang, Z.; Zhao, T.; Huang, X.; Chu, X.; Tang, T.; Ju, Y.; Wang, Q.; Hou, Y.; Gao, S. Modulating the Phases of Iron Carbide Nanoparticles: From a Perspective of Interfering with the Carbon Penetration of Fe@Fe3O4 by Selectively Adsorbed Halide Ions. *Chem. Sci.* **2016**, *8* (1), 473–481. https://doi.org/10.1039/C6SC01819J.

BIOGRAPHICAL SKETCH

Isabella A. Bertini
ORCID: https://orcid.org/0000-0001-8365-7259

Education

Ph.D. in Materials Chemistry | Florida State University |
| Graduation Date: Aug 2nd 2024 | | Concentration in Nanoscience |

M.S. in Materials Chemistry (In-Flight) | Florida State University |
| Graduated: Dec 2021 | | Concentration in Nanoscience |

B.S. in Biology | University of North Georgia − Dahlonega |
| Graduated: May 2019 | | Minor: Chemistry |

Research Experience

Graduate Student Research in Nanomaterial Chemistry

| Geoffrey F. Strouse Ph.D. | Florida State University: Aug 2019 – Present |

Investigation of first-row transition metal nanocarbides for electrochemical water splitting

- Design, synthesis, and full (structural, elemental, chemical, and morphological) characterization of novel Fe, Co, Ni based (monometallic, bimetallic, and trimetallic) nanocarbides from Prussian Blue Analogue (PBA) single source precursors for application in the oxygen evolution reaction (OER) and hydrogen evolution reactions (HER)
- Elementary electrochemical analyses (LSV, CV, chronopotentiometry) to assess electrocatalyst performance in the water splitting reaction (OER/HER)
- Study of OER kinetics through Tafel analysis
- Collaboration with local computational chemists to probe the thermodynamics and energetics of nanocarbide catalysts for OER
- Post OER physical and chemical characterizations to observe material transformation events under OER conditions

Investigation of halide incorporation on resultant nanocrystal phase

- Synthesis and full (structural, elemental, chemical, and morphological) characterization of pure phase FeCo nanocarbides
- Use of synthetic parameters: temperature, time, metal ratio, halide concentration, and halide species to target unique nanocrystal phases
- Collaboration with local computational chemists for mechanistic insight into the effect of halides in our synthetic route

Investigation of the structure – property relationship in nano metal-xides (x = C,P,O,S,N) for applications in catalysis and magnetism

- Synthesis and full (structural, elemental, chemical, and morphological) characterization of multi-metallic first row transition metal-xides (Cr, Mn, Fe, Co, Ni, Cu, Zn)
- Elementary electrochemical analyses (LSV, CV, chronopotentiometry) to assess electrocatalyst performance in the water splitting reaction (OER/HER)
- Study of OER kinetics through Tafel analysis
- Determination of catalytic performance dependence on crystal phase in these new materials

Undergraduate Student Research in Polymer Chemistry

| N. Eric Huddleston Ph.D. | University of North Georgia – Dahlonega: Aug 2018 – May 2019 |

- Perform and research classical and modern synthesis reactions for plant derived polymers
- Small scale synthesis of pre-polymers/polymers via photocycloaddition reactions using fumaric acid and derivatives
- Analysis of crude products and starting material with ^{1}H-NMR and IR techniques
- Record of mechanisms, reactions, and procedures executed
- Literature research for modern green chemistry protocols

Undergraduate Student Research in Nanomaterial Chemistry

| Megan Foley Ph.D. | University of North Georgia – Dahlonega: Jan 2019 – May 2019 |

- Synthesis of fluorescent and magnetic nanoparticles
- Characterization of synthesized materials via XRD (through collaboration)
- Literature research on biological applications of materials of interest (weekly assignments were discussed at group meetings 1x a week)
- Development and production of elementary lab procedures for Materials chemistry course based on relevant literature

Lab Techniques and Instrumentation Experience

- Microwave synthesis of nanoparticles
- Round bottom synthesis of nanoparticles
- Schlenk line technique
- Powder X-ray Diffraction (pXRD)
- Single Crystal X-Ray Diffraction (SCXRD)
- X-ray fluorescence (XRF)
- X-Ray Photoelectron Spectroscopy (XPS)
- Transmission and ATR FTIR Absorption Spectroscopy
- Raman Spectroscopy
- UV-Vis Absorption Spectroscopy
- Thermogravimetric Analysis (TGA)
- Differential Scanning Calorimetry (DSC)
- Cyclic Voltammetry (CV)

- Linear Sweep Voltammetry (LSV)
- Chronopotentiometry (CP)
- Inductively Coupled Plasma Mass Spectrometry (ICP-MS)
- Proton and Carbon (Solution) NMR Spectroscopy
- Scanning electron microscopy (SEM)
- Light and dissection microscopy
- Column/affinity/size exclusion chromatography
- SDS-PAGE
- Agarose and polyacrylamide gel-electrophoresis
- PCR
- RotoVap
- Aseptic inoculation of agar plates and broths
- Knowledge of selective and growth media to isolate an organism
- DNA/RNA/protein extractions
- Dissection techniques
- Restriction enzymes and molecular cloning
- Titration

Software Skills

- All Microsoft software, ChemDraw, PYMOL, GenBank, Molecular EvolutionaryO Genetics Analysis (MEGA), mVista, clustal sequence alignment, SciFinder, ImageJ, SWISS-MODEL, Smartlab Studio II, Igor, casaXPS, Smartlab Studio II, crystalmaker, crystaldiffract, originpro.

Publications

1. **Title:** "A Single Source, Scalable Route for Direct Isolation of Earth Abundant Nano − Metal Carbide Water Splitting Electrocatalysts"

   Authors: Nguyen, E.T.; **Bertini, I.A.**; Ritz, A.J.; Lazenby, R.A.; Mao, K.; McBride, J.R.; Mattia, A.V.; Kuszynski, J.E.; Wenzel, S.F.; Bennett, S.D.; Strouse, G.F.

   Journal: Inorganic Chemistry, 2022, 61, 35, 13836-13845

   DOI: 10.1021/acs.inorgchem.2c01713
2. **Title:** "Electrocatalytic activity and surface oxide reconstruction of bimetallic iron–cobalt nanocarbide electrocatalysts for the oxygen evolution reaction"

   Authors: Bertini, I.A.‡; Ritz, A. ‡; Nguyen, E.T.; Strouse, G.F.; Lazenby, R.A.

   Journal: Royal Chemistry Society Advances 2023,**13**, 33413-33423

   DOI: 10.1039/D3RA07003D
3. **Title:** "Microwave Inhibition of the Hydrogenation of CO2 for Methane Formation"

Authors: Hsu, C.; **Bertini, I.A.**; Bogle, M.; Lochner, E.; Strouse, G.F.; Stiegman, A.E.*
Journal: ACS J. Phys. Chem. C, 2023 127, 19, 9067–9075
DOI: 10.1021/acs.jpcc.3c01599

4. **Title:** "Influence of Al2O3 Overlayers on Intermolecular Interactions between Metal Oxide Bound Molecules"
   Authors: Knorr E. S.; Basquill, C.T.; **Bertini, I.A**.; Arcidiacono, A.; Beery, D.; Wheeler, J.P.; Winfred, J.S.R.; Strouse, G.F.; Hanson, K.
   Journal: Molecules 2023, 28(12), 4835
   DOI: 10.3390/molecules28124835
5. **Title:** "Halide − Mediated Phase Control of PBA − Derived $Fe_xCo_{1-x}C_y$ Nanocarbides"
   Authors: Bertini, I.A.; Bell, S.; Lamichhane, B.; Kattel, S.; Strouse, G.F
   Journal: under revision to ACS Chemistry of Materials
   DOI: TBD
6. **Title:** "Prussian Blue Analogue Derived First Row Transition Metal High-Entropy Nanocarbides"
   Authors: Bertini, I.A.; Bell, S.; Johnpoll, D.; Strouse G.F.
   Journal: under preparation
   DOI: TBD
7. **Title:** "Synthesis of First-Row Transition Metal High-Entropy Nano MX-ides for OER"
   Authors: Bertini, I.A.; Bell, S.; Johnpoll, D.; Strouse G.F.
   Journal: under preparation
   DOI: TBD
8. **Title:** "Tracking surface oxide formation in FeNi-containing nanocarbides: insights into carbide catalyst degradation in alkaline OER conditions"
   Authors: Ritz, A. ‡; **Bertini, I.A.‡;** Bourque, M.R.; Weissberger, R.D.; Castro, S.; Barton, D.; Wysel, S.; Gorman, J.; Strouse G.F.; Lazenby, RA.
   Journal: under preparation
   DOI: TBD
9. **Title:** "PBA − Derived FeCoNi Trimetallic Nanocarbides for Electrocatalytic Water Splitting"
   Authors: Ritz, A.; **Bertini, IA.**; Bell, S.; Gorman, J.; Strouse, G.F.; Lazenby, R.A.

Journal: under preparation

DOI: TBD

Research Presentations

American Chemical Society Spring National Meeting New Orleans, LA

"Halide-mediated phase control in Fe, Co, and Ni nano M-xides (x = C, O, P, S) for applications in catalysis and magnetism"

03/20/2024 Oral Presentation

American Chemical Society Spring National Meeting Indianapolis, IN

"Investigating the effect of crystal phase and bimetallic ratio modulation in FeCo and FeNi nanocarbides for applications in catalysis and magnetism"

03/28/2023 Oral Presentation

Florida State University Departmental Materials Seminar

Tallahassee, FL

"A Study of Structure − Property Relations in 3d Transition Metal Nanocarbides"

03/23/2023 Oral Presentation

American Chemical Society Spring National Meeting San Diego, CA

"Stoichiometric control, Optimization, and Electrocatalytic Performance of Various Bimetallic MX-ides (X= carbides, phosphides, nitrides, sulfides, oxides) for the Oxygen Evolution Reaction"

03/23/2022 Oral Presentation

Doctoral Candidacy Oral Presentation Tallahassee, FL

"Rational Design of Earth-Abundant Electrocatalysts for the Oxygen Evolution Reaction"

11/19/2021 Oral Presentation

American Chemical Society Fall National Meeting

Atlanta, GA

"Synthesis and Optimization of $Fe_{3-x}Co_xC$ for the Oxygen Evolution Reaction (OER)"

8/25/2021 Oral Presentation

University of North Georgia Departmental Seminar

Dahlonega, GA

"Mesoscale Templated Growth of Iron-Cobalt Nanomaterials: A Study of Size, Phase, and Composition"

2/19/2021 Oral Presentation

Florida State University Departmental Materials Seminar

Tallahassee, FL

"Designing Nanoscale First-Row Transition Metal Carbide and Alloys for the Oxygen Evolution Reaction"

10/1/2020 Oral Presentation

American Chemical Society Spring National Meeting Orlando, FL

"From Nature to Materials: Progress towards the Synthesis of Reversible Crosslinking Materials via the [2+2] Photocycloaddition of Fumaric Acid and its Derivatives"

04/03/2019 Poster Presentation Session: Green Chemistry

- Capstone project for two semesters of research on plant-derived polymers

Teaching Experience

Graduate Teaching Assistant Florida State University Aug 2019 – Present

Lecture Teaching Assignments

General Chemistry I and II (7 semesters, lead TA for 6 semesters)

Roles and Responsibilities

- Engaged with students directly 5.5 hours a week
  - 3 – 1.5 hr lecture classes (330+ students)
  - 1 – 1 hr recitation classes (3 sections of 30 students each)
- Plan and execute weekly recitation exercises
  - a mixture of short lectures, discussions, workshops, Q&A sessions, and/or kahoot or competitive/teamwork activities
- Facilitated learning of subject matter via hands on assistance in active learning assignments during lecture classes
- Encouraged collaborative learning during class and recitation
- Monitored one-on-one student progress during office hours held 2x/wk
- Prepared exam (4-5x/semester) and quiz (10-15x/semester) questions

- Edited and proofed exams (4-5x/semester)
- Graded exams (4-5x/semester) and quizzes (10-15x/semester)

Lead TA (TA Supervisor) Responsibilities

- Organize and coordinate weekly TA meetings to discuss lesson plans
- Serve as liaison for communication of course information between professor on record and TAs
- Delegate tasks (grading and question writing) to TAs handed down from professor on record
- Train and mentor new TAs
    - Provide a key for workshops/activities (1/wk)
    - Walk through workshops/activities for recitation (1/wk)
    - Explain in detail how "active learning" and "facilitating learning" differ from just providing answers to students
    - "Open door" policy- new TAs can always reach me in my office or via text/email
    - Mentor new TAs on their journey through the graduate program by checking in on mental health throughout the semester

Inorganic Chemistry (1 semester)

- Engaged with students directly 5 hours a week
    - 4 – 1 hr lecture classes (30 students)
    - 1 – 1 hr recitation classes (30 students)
- Edited and proofed exams (4-5x/semester)
- Graded exams (4-5x/semester) and quizzes (10-15x/semester)
- Monitored one-on-one student progress during office hours held 2x/wk

Laboratory Teaching Assignments

General Chemistry I and II Laboratory (2 semesters)

Organic Chemistry Laboratory (1 semester)

One-Semester Condensed Organic Laboratory for Pre-Professional Majors (1 semester)

- General Roles and Responsibilities for all labs (10 labs/semester)
    - Engage with students via hand-on lab training and supervision for 3 hr lab 1/wk (3 sections of 30 students)
    - Implement and ensure safety protocol by enforcement of wearing proper PPE and waste disposal
    - Plan and lead pre-lab discussions and demonstrations on related course materials (3/wk)
    - Monitor one-on-one student progress during office hours held 2x/wk
    - Grade midterm and final exams (2x/semester)

Tutoring Experience

Freelance – Aug 2015 – Present

Classes offered: General Biology I and II, Genetics and Cell Biology, General Chemistry I and II, Organic Chemistry I, Biochemistry I and II, Algebra, Pre-Calc, Trigonometry

Pedagogy at a glance:

- Engaged with students in 1-3 1 hr sessions per week, depending on students need
- Plan and prepare practice problems and worksheets for each session
- Discuss a brief synopsis of the subject matter with students to assess where strengths and weaknesses are
- Facilitate learning by first working on a practice problem together and then allowing student to try on their own and when they get stuck work through the thought process they should use to solve the problem at hand

Mentorship Experience

Undergraduate Research Opportunity Program (UROP) Mentor

Florida State University: Aug 2021-Present

Mentees: Sebastian Castro (Chem-Engineering), Dylan Barton (Chem-Engineering), James Gorman (Biochemistry), Samantha Bell (Biochemistry), Dorian Johnpoll (Biochemistry)

Mentorship at a glance:

- Educate students on the nanomaterial research field and increase scientific literacy via weekly literature discussions
- Plan and execute hands - on research
    - Develop and strategize a research project for each student to work on
    - Educate students on the fundamentals of nanomaterial research
    - Explain in detail the rationale for synthetic procedures, characterization methods, and each students research project
    - Plan weekly experiments for students to execute (1-3x/wk)
    - Assist with synthetic apparatus set-up and clean-up
    - Explain and train students in physical and chemical characterization techniques of synthesized nanomaterials
    - Provide opportunities for students to present research findings at local or national conferences (all mentored students presented at the FSU UROP symposiums (SP 2022-2024), James Gorman (SP 2023) and Samantha Bell (SP 2024) presented at the ACS national meetings)

- Provide advice and encouragement for continuing education
- Assist in applications for REU, graduate degree programs, and professional degree programs
    - Sebastian Castro received a summer REU for SU 2023 at California Tech
    - James Gorman received a travel award for the ACS SP 2023 conference to present his research
- Provide letters of support/recommendations for future endeavors

Leadership/Awards

- Excellence in graduate teaching department of chemistry awardee Spring 2024
- Excellence in graduate teaching- nominee 2021, 2022, 2023
- Scholarship Chair Committee Head 2 semester for UNG CO-ED National Honor Fraternity: Phi Sigma Pi
- Peer Health Educators 1 semester
- Sales manager for 5 years in the retail industry